Syntheses, Properties, and Self-assembling Behavior of Dehydroannulenes Fused with Phenanthrene or Benzene Moieties

Nobutaka Takahashi

2016

Department of Chemistry and Chemical Biology

Graduate School of Science and Technology

Gunma University

Contents

Abbreviations and Symbols

Å	angstrom (1 Å = 10^{-10} m)
ABM	arylene–butadiynylene macrocycle
AEM	arylene–ethynylene macrocycle
AFM	atomic force microscope
a.u.	arbitrary unit
brs	broad singlet (NMR)
Bu	butyl
ca.	*circa*
C_T	total concentration
CV	cyclic voltammetry
d	doublet (NMR)
δ	chemical shift
D	diffusion coefficient
δ_{agg}	chemical shifts of aggregated species
δ_{calcd}	calculated chemical shift
$\Delta\delta$	change in resonance
ΔE_{calcd}	calculated HOMO–LUMO gap
decomp.	decomposition
ΔE_{opt}	optical HOMO–LUMO gap
ΔE_{redox}	electrochemical HOMO–LUMO gap
DFT	density functional theory
ΔH	enthalpy
dith	dithranol

δ_{mon}	chemical shifts of monomer
δ_{obs}	observed chemical shift
DP_N	number average aggregate
DPV	differential pulse voltammetry
ΔS	entropy
DSC	differential scanning calorimetry
ε	molar absorption coefficient
ε_{agg}	molar absorption coefficient for aggregated species
ε_{mon}	molar absorption coefficient for a monomer
ε_{obs}	observed molar absorption coefficient
E_{onset}^{ox}	oxidation onset
E_{onset}^{red}	reduction onset
E_{pa}	oxidation potential
E_{pc}	reduction potential
ESPs	electrostatic-potential surface
EtOH	ethanol
eV	electron volt
f	oscillator strength (DFT calculations)
Fc/Fc^+	ferrocene/ferrocenium ion
Φ_f	fluorescence quantum yield
FMO	frontier molecular orbital
GPC	gel-permeation chromatography
HOMO	highest occupied molecular orbital
HR	high resolution
Hz	hertz (s^{-1})
J	coupling constant

K	association constant
k_b	Boltzmann's constant
k_f	fluorescence rate constant
k_{nr}	nonradiative rate constant
λ	wavelength
λ_{ex}	excitation wavelength
λ_{max}^{abs}	absorption maxima
λ_{max}^{fl}	fluorescence maxima
λ_{max}^{pho}	0-0 origin of the phosphorescence spectrum
λ_{onset}	absorption onset
LUMO	lowest unoccupied molecular orbital
m	multiplet (NMR)
MALDI	matrix-assisted laser desorption ionization
MCH	methylcyclohexane
Me	methyl
MeOH	methanol
MEPs	molecular electrostatic potentials
M.p.	melting point
MS	mass spectrometry
N/A	not applicable
NBA	*m*-nitrobenzyl alcohol
NBO	natural bond orbital
N.D.	not determined
[*n*]DA	dehydro[*n*]annulene
[*n*]DBA	dehydrobenzo[*n*]annulene
NICS	nucleus-independent chemical shift

NMR	nuclear magnetic resonance
o-DCB	*o*-dichlorobenzene
Ph	phenyl
POM	polarizing optical microscopy
ppm	parts per million
q	quartet (NMR)
qui	quintet (NMR)
R	substituent
R	gas constant
RT	room temperature
S_1	lowest excited singlet
SA	sinapinic acid
SEM	scanning electron microscope
sep	septet (NMR)
sex	sextet (NMR)
sh	shoulder peak
t	triplet (NMR)
T	temperature
T_1	lowest excited triplet
TBAF	tetrabutylammonium fluoride
TD-DFT	time-dependent density functional theory
τ_f	fluorescence lifetime
THF	tetrahydrofuran
TIPS	triisopropylsilyl
TLC	thin-layer chromatography
T_m	melting temperature

TMEDA	*N,N,N',N'*-tetramethylethylenediamine
TMS	trimethylsilyl
TMSA	trimethylsilylacetylene
UV	ultraviolet
vis	visible
WAXD	wide-angle X-ray diffraction

Chapter 1. General Introduction

1-1. Dehydroannulenes and Dehydrobenzoannulenes

An [*n*]annulene (*e.g.*, [18]annulene,[1] Figure1-1a) is defined as a monocyclic hydrocarbon comprised of alternating single and double bonds where the number in brackets denotes the number of π-electrons associated with cyclic conjugation.[2] Replacement of one or more of double bonds of an [*n*]annulene with triple bonds affords a dehydro[*n*]annulene ([*n*]DA, *e.g.*, [18]DA,[3] Figure 1-1b). Benzannulation of annulene and DA leads to benzo[*n*]annulene (*e.g.*, benzo[18]annulene,[4] Figure 1-1c) and dehydrobenzo[*n*]annulene ([*n*]DBA, *e.g.*, [18]DBA,[5] Figure 1-1d), respectively.

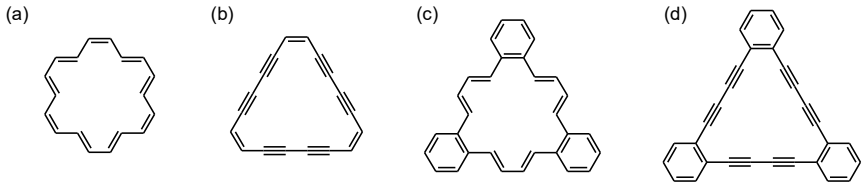

Figure 1-1. (a) [18]Annulene (cyclooctadecanonaene), (b) [18]DA (cyclooctadecatriene-hexayne), (c) benzo[18]annulene (tribenzo[*a,g,m*]cyclooctadecanonaene), and (d) [18]DBA (dodecadehydro-tribenzo[*a*,*g*,*m*]cyclooctadecatriene).

The concepts of aromaticity and antiaromaticity are of fundamental importance in classifying physical and chemical properties of planar and cyclic π-conjugated compounds.[6–10] Throughout the 1960s and 1970s, the above four classes of closely related molecules were investigated extensively in connection with the study on the aromaticity/antiaromaticity of cyclic π-conjugated system.[11] The ^{1}H NMR chemical shifts have been one of the most widely employed measure as the elucidation of aromaticity/antiaromaticity. According to Hückel's rule, planar and cyclic conjugated systems containing $(4n+2)\pi$ electrons induce diamagnetic ring current (diatropicity) under an external magnetic field. On the other hand, those containing $4n\pi$ electrons induce

paramagnetic ring current (paratropicity) under an external magnetic field. The research groups of Sondheimer, Staab, and Nakagawa, the three pioneers of this area of chemistry, prepared an impressive array of annulenic structures such as [14]DBA (Figure 1-2a),[12] [12]DBA (Figure 1-2b),[13,14] and acetylene–cumulene [14]DBA containing acetylenic and cumulenic linkages (Figure 1-2c),[15] respectively. The historical findings of the aromaticity/antiaromaticity of [*n*]annulenes, [*n*]DAs, benzo[*n*]annulenes, and [*n*]DBAs will not be dealt with in this Chapter; the reader is referred to the comprehensive reviews and books.[16–19]

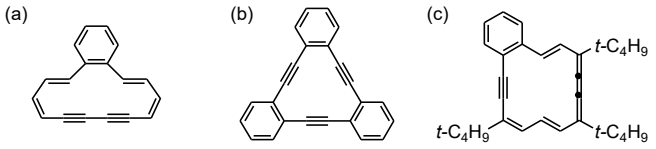

Figure 1-2. Structures of representative classic DBAs. (a) [14]DBA, (b) [12]DBA, and (c) acetylene–cumulene [14]DBA

The incorporation of triple bonds into an [*n*]annulene ring restricts the possible *cis–trans* isomerization of C=C double bonds and the rotation around C–C single bonds, and thereby the geometrical freedom of [*n*]DAs becomes lower than that of [*n*]annulenes. Therefore, the assessment of tropicity is more straightforward in [*n*]DAs than [*n*]annulenes; however, the incorporation of triple bonds lowers the extent of cyclic π-conjugation because the localization of π-electrons in the triple bonds in [*n*]DAs is more pronounced than that in the double bonds in [*n*]annulenes.[20] Benzannulation to an annulene ring not only suppresses the geometrical freedom but also dramatically increases the chemical stability,[21] yet it generally lowers the extent of cyclic π-conjugation because of the tendency of π-electron localization in the fused benzene rings.[22]

After the discovery[23] and isolation of bulk quantities[24] of various fullerene including buckminsterfullerene (C_{60}), their properties and covalent modification were extensively investigated in subsequent years. In parallel, vigorous researches on carbon nanotubes for their application into optoelectronic materials were carried out.[25–27] More recently, the extraordinarily facile access to graphene, which is a single layer of graphite, has drawn enormous interest among the physics and chemistry communities owing to its intriguing electronic and magnetic properties.[28]

In parallel with the developments on the study on carbon allotropes in the field of physics mentioned above, organic chemists have been interested in the design and chemical synthesis of carbon allotropes and carbon-rich materials. Cyclo[*n*]carbon was proposed as the first carbon allotrope in 1966 (*e.g.*, cyclo[18]carbon, Figure 1-3a),[29] and then various 2D and 3D carbon networks were proposed one after another since the late 1980s, which was apparently inspired by the discovery of fullerenes.[30] Among the proposed 2D and 3D carbon networks, the 2D carbon networks composed of benzene rings and acetylenic units, namely ethyne and butadiyne units were named as graphyne[31] (Figure 1-3b) and graphdiyne[5,32] (Figure 1-3c), respectively, and they have been hitherto unknown 2D networks and the representative targets of synthetic and computational works. Thus, since [12]- and [18]DBAs are the smallest substructure of graphyne and graphdiyne, respectively, a variety of larger congeners of [12]-[33–37] and [18]DBAs[38–40] have been synthesized as model compounds of graphyne and graphdiyne, respectively (Figure 1-4). The historical overview of carbon-rich materials is summarized in a recent review,[41] and the work on DBAs has been the subject of recent review.[42]

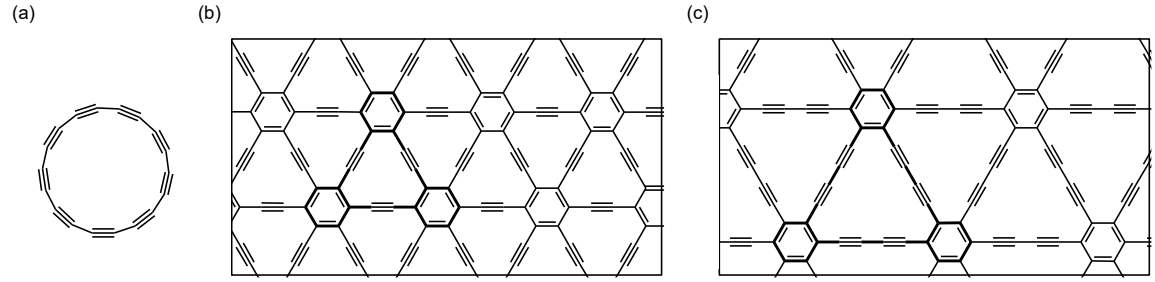

Figure 1-3. Structures of (a) cyclo[18]carbon, (b) graphyne, and (c) graphdiyne. The bold lines denote the [12]DBA and [18]DBA units as the smallest substructure of graphyne and graphdiyne, respectively.

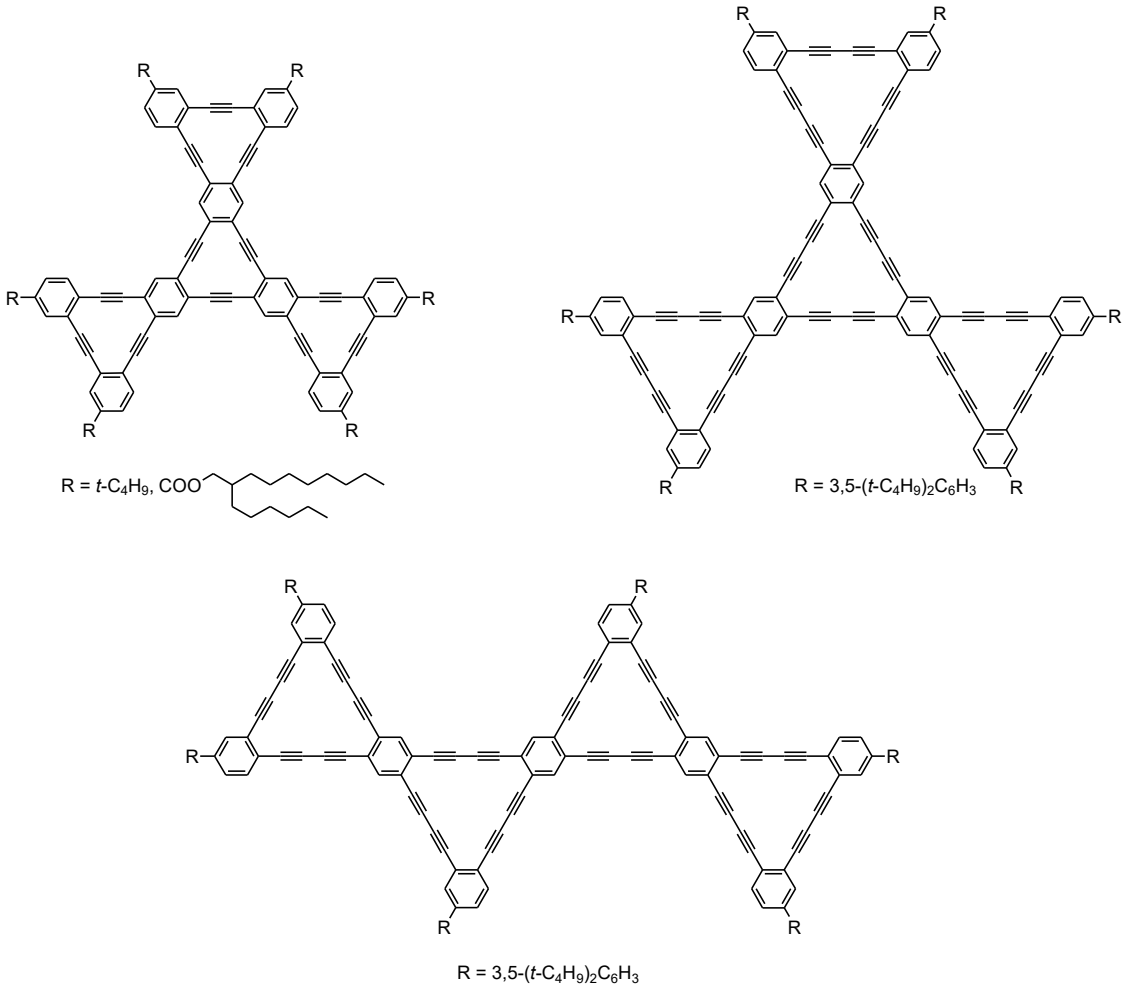

Figure 1-4. Representative substructures of graphyne and graphdiyne.

The reactivities of DAs and DBAs have attracted much interest from the viewpoint of their potential precursor as novel all-carbon allotropes and carbon-rich materials. In fact, the generation of cyclo[*n*]carbons by the [2 + 2] cycloreversion of [*n*]DA precursors containing [4.3.2]propellatriene moieties was achieved (Scheme 1-1), however, their generation was only successful in the gas phase and bulk quantities have not been isolated to date.[43] The formation of carbon-rich materials by polymerization of DAs and DBAs in the solid state was also reported. For instance, photoinduced topochemical polymerization of [14]DBA formed poly(butadiyne)s (Scheme 1-2a)[44] and thermally induced polymerization of [20]DBA afforded ordered onion- and tube-type carbon nanostructures (Scheme 1-2b).[45]

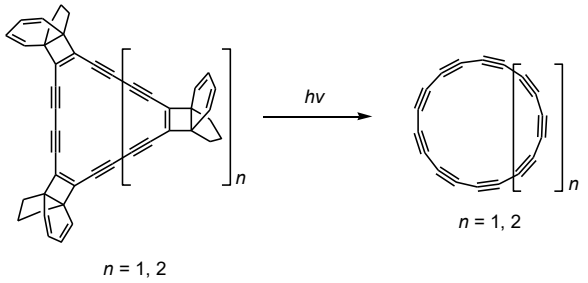

Scheme 1-1. Example of the generation of cyclo[*n*]carbons.

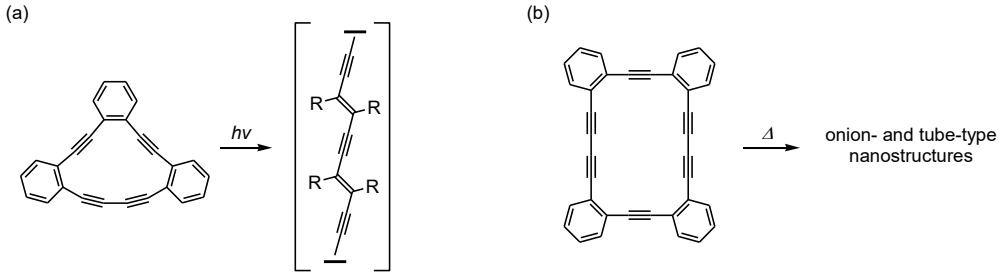

Scheme 1-2. Examples of polymerization of (a) [14]- and (b) [20]DBAs in the solid state.

Recently, the reactivity of acetylenic linkages in DAs and DBAs has been exploited to form polycyclic compounds by multiple bond formations via tandem reactions. Indeed, [8]-,[46–48] [12]-,[49–52] and [14]DBAs[53,54] were converted into unsaturated polycyclic compounds containing five-membered rings via transannular cyclizations induced by either nucleophiles

or electrophiles (Scheme 1-3a–c). More recently, the transformation of thiophene-[55] and thiophene-*S*,*S*-dioxide-fused[56] [12]DAs into polycyclic compounds containing biphenylene skeleton has been reported, and it has been pointed out that the reactivity of the DAs increases with decreasing aromaticity of the fused rings (Scheme 1-3d).

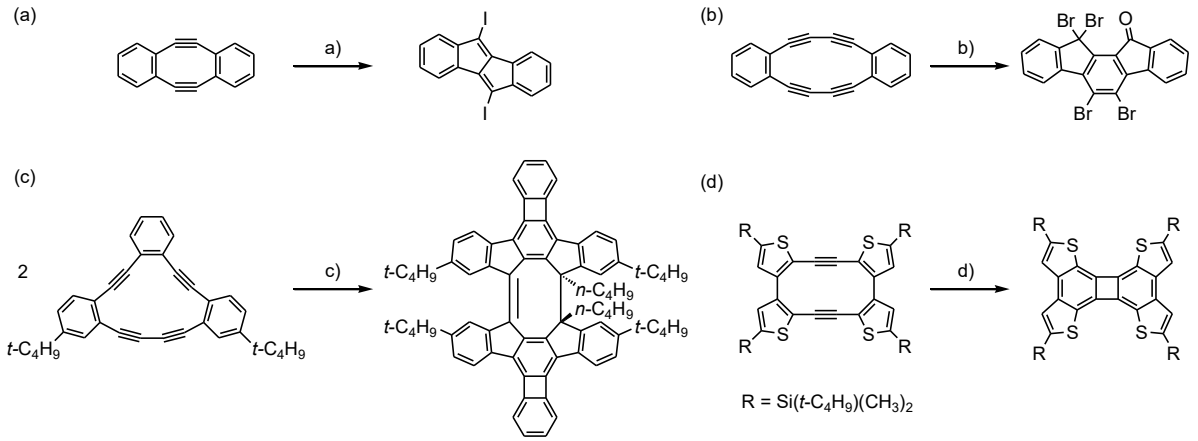

Scheme 1-3. Transannular cyclization of (a) [8]-, (b) [12]-, and (c) [14]DBAs and (d) thiophene-fused [12]DAs. Reagents and conditions: a) I_2, CH_3CH_2CN, −78 °C to RT; b) Br_2, Air, CH_2Cl_2, RT; c) 1) *n*-BuLi, THF, −78 °C to RT; 2) H_2O, THF, RT; d) heat, CH_2Cl_2.

From the viewpoint of photofunctional materials application, DAs and DBAs have attracted a great deal of interest during the last two decades owing to their intriguing optical and optoelectronic properties.[57] The key to the conception of high-performance optoelectronic materials is based on the insight of clear structure–property relationships, which can be used to understand the properties of existing materials and predict the ideal materials.[58] A large number of DBAs have been synthesized and their properties were investigated to establish their structure–property relationship; the congeners, to which aromatic rings are not annulated, are less known owing to their instability (Figure 1-5).[59] The introduction of donor and/or acceptor functional groups on the benzene rings of the DBA systems is nowadays regarded as the effective way to control the electronic and optoelectronic properties of the resulting compounds (Figure 1-6).[60–63] [*n*]DBAs possessing large π-conjugated circuit ($n > 20$) have been extensively synthesized (Figure 1-7),[64–70] and their properties and tropicity

(aromaticity/antiaromaticity) have been explored;[71,72] because of the nonplanar and flexible structures, most of them show nonaromaticity and possess ineffective macrocyclic π-conjugation.

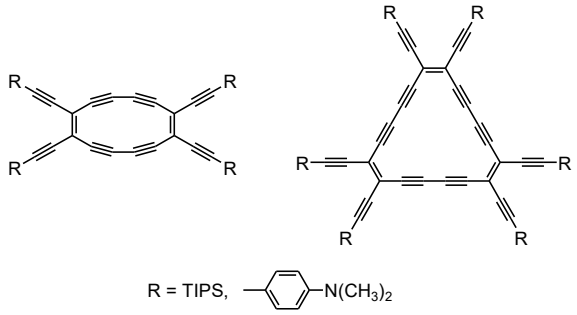

Figure 1-5. Representative structures of functionalized DA derivatives.

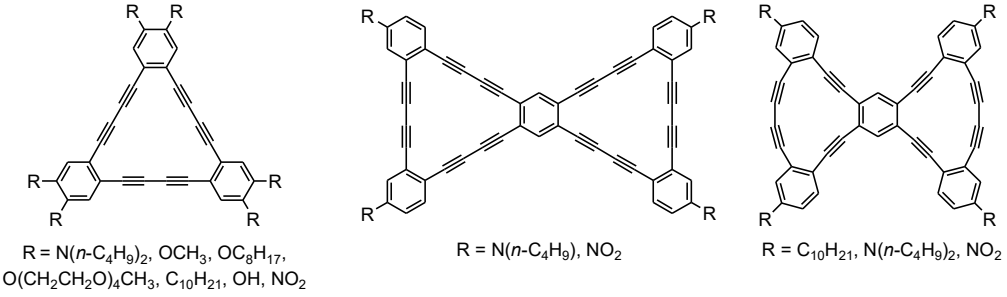

Figure 1-6. Structures of donor- and/or acceptor-substituted DBAs.

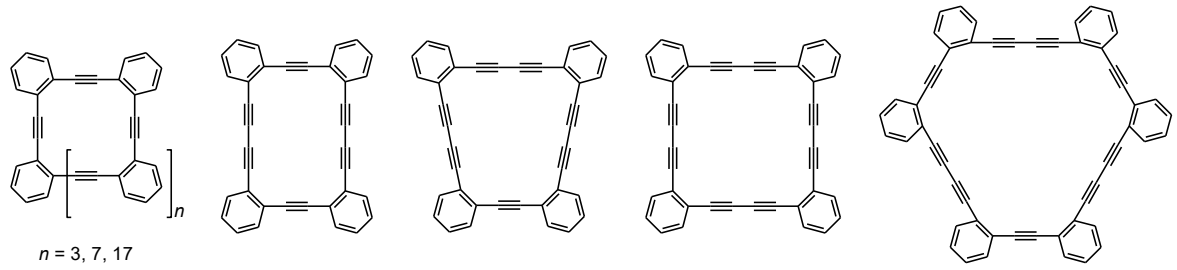

Figure 1-7. Structures of higher [*n*]DBAs (*n* > 20) composed of benzene rings and ethyne and/or butadiyne linkages.

Supramolecular chemistry is defined as ”chemistry beyond the molecule”, which focuses on the study on molecular assemblies formed by various noncovalent interactions.[73] Self-assembly is one of the key concept of supramolecular chemistry. Planar and rigid

π-conjugated compounds tend to form self-assemblies, such as liquid crystals, gels, and 1D crystalline nanostructures, by π–π stacking interactions and/or other intermolecular interactions (*e.g.*, hydrogen bond, dipole–dipole interactions, and van der Waals interactions).[74] The self-assemblies have intriguing photophysical and electrical properties reflecting not only the intrinsic electronic properties of the molecules but also the macroscopic order of the molecules in the self-assemblies.[75] For example, since π-stacked 1D columns provide a pathway for charge and/or exciton migration to display functional properties, the fabrication of well-defined 1D self-assembled clusters, such as nanometer- or micrometer-sized fibers, belts, and rods, with π-stacked 1D columns are hot topics mainly due to their potential applications for the next generation of organic electronic nanodevices. In this context, the properties of DBAs in the solid state have been recently exploited, and some well-defined supramolecular architectures based on functionalized DBAs have been reported in single crystals,[76–80] liquid crystals,[81] vesicles,[82,83] gels,[84] nanofibers,[85,86] and 2D crystals on surface[87,88] (Figure 1-7).

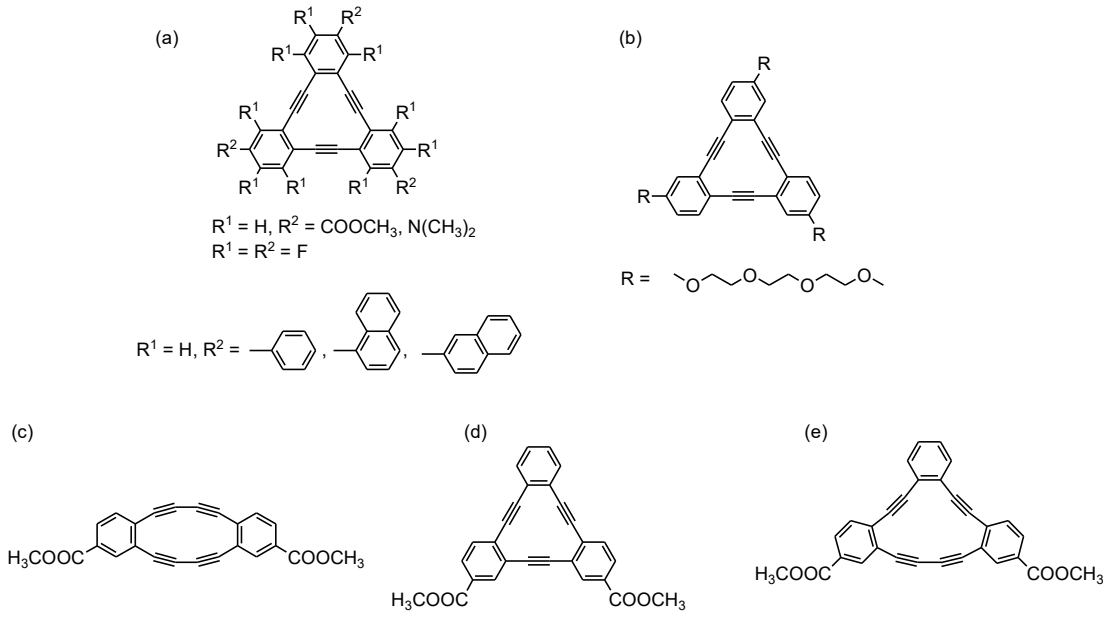

Figure 1-8. Examples of DBAs to form (a) single crystals, (b) liquid crystals, and (c–d) gels with π-stacked 1D arrangement.

1-2. Research Strategy

Octadehydrodibenzo[12]annulene ([12]DBA) and dodecadehydrotribenzo[18]annulene ([18]DBA) have rigid and planar 4*n*π and (4*n* + 2)π circuits, respectively, and become very popular π-scaffolding in the DBA chemistry; a variety of their derivatives such as **1a** and **2a** have so far been synthesized because the metal-mediated or metal-catalyzed homocoupling reactions of readily accessible diethynyl benzene derivatives have been well established. In view of the previous findings as summarized above, the author was stimulated to develop higher analogues of **1a** and **2a** systematically by the replacement of fused aromatics from a benzene ring to a condensed aromatic system and/or the extension of acetylenic linkages from butadiyne to octatetrayne units. Thus, as shown in Figure 1-9, the author planned to synthesize tetraalkoxyphenanthrene-fused DAs **3**–**5** possessing butadiyne linkages (Chapter 2), DBAs **6**–**8** possessing octatetrayne linkages (Chapter 3), and tetraalkoxyphenanthrene-fused DAs **9** and **10** possessing octatetrayne linkages (Chapter 4) and investigate their properties and self-assembling behavior; their design principle is described at the beginning parts of Chapters 2, 3, and 4. DAs **3**–**5**, **9**, and **10** and DBAs **6**–**8** were targeted to 1) enhance the understanding of π-conjugation and tropicity (*i.e.*, aromaticity/antiaromaticity) in DA and DBA systems, 2) expand the knowledge about the rational design of self-assembling acetylenic macrocycles, and 3) eventually generate new electronic, photophysical, electrochemical, and self-assembling properties. In this thesis, the author will present the synthesis, properties, and self-assembling behavior of **3**–**10**, and these studies are described in the following three chapters.

Chapter 2. Tetraalkoxyphenanthrene-Fused Octadehydro[12]- and Dodecadehydro[18]annulenes: Syntheses, Self-assembly, and Electronic, Optical, and Electrochemical Properties

Chapter 3. Hexadecadehydrodibenzo[20]-, Tetracosadehydrotribenzo[30]-, and

Dotriacontadehydrotetrabenzo[40]annulenes: Syntheses, Characterizations, Electronic Properties, and Self-associations

Chapter 4. Tetraalkoxyphenanthrene-Fused Hexadecadehydro[20]- and Tetracosadehydro[30]annulenes: Syntheses, Self-assembly, and Electronic, Optical, and Electrochemical Properties

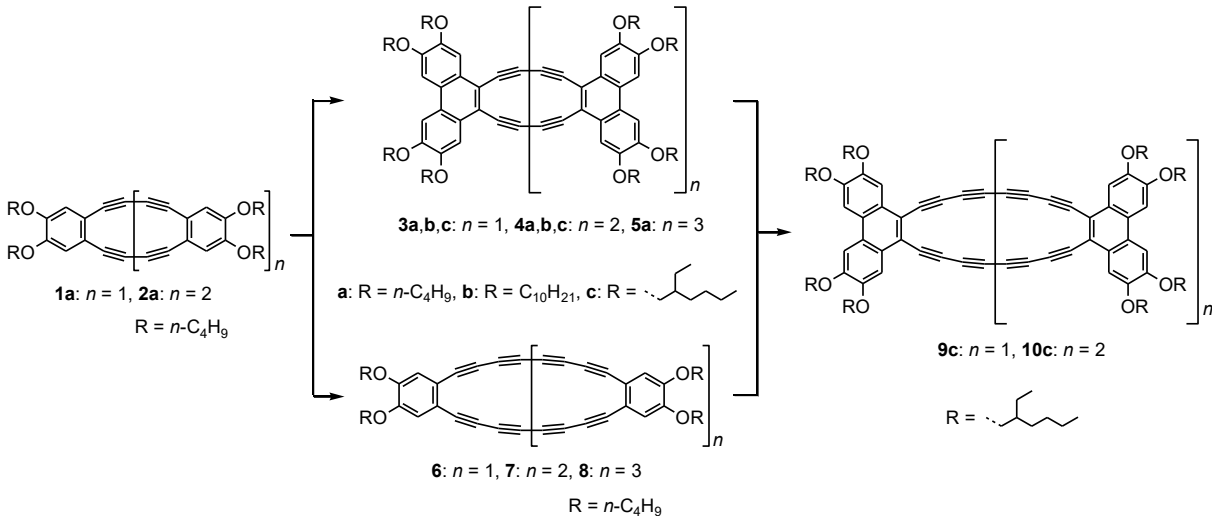

Figure 1-9. Molecular designs of DAs fused with phenanthrene or DBAs.

Chapter 2. Tetraalkoxyphenanthrene-Fused Octadehydro[12]- and Dodecadehydro[18]annulenes: Syntheses, Self-assembly, and Electronic, Optical, and Electrochemical Properties

2-1. Introduction

The appropriate annulation of aromatic and conjugated heterocyclic systems larger than benzene to a dehydro[*n*]annulene ([*n*]DA) ring would give rise to high thermal, light, and/or air stability and fascinating electronic and aggregating properties in the resulting molecules owing to the structural and electronic features of the annulated moiety. Indeed, [*n*]DAs fused with phenanthrene,[89] dimethoxynaphthalene,[90] quinoxaline,[91] Ru(II)-coordinated dipyridophenazine,[92] phthalocyanine,[93–95] subphthalocyanine,[96] tetrathiafulvalene,[97,98] or [4]helicene[99] have been synthesized (Figure 2-1). However, the elucidation of the correlation of annulated moieties with physicochemical properties still remains to be carried out; moreover, the studies on the formation of 1D superstructures have been quite limited.[97,98] In this context, the author undertook the synthesis of [12]- and [18]DAs **3a**,**b** and **4a**,**b** annulated at the 9,10-positions of 2,3,6,7-tetraalkoxyphenanthrene (Figure 2-2); although the synthesis of unsubstituted phenanthrene-fused [12]DA was reported by Nakagawa and co-workers in 1962 (Figure 2-1a), a detailed investigation on the structure and electronic properties was not carried out.[89] The following three major structural features are of importance in this design.

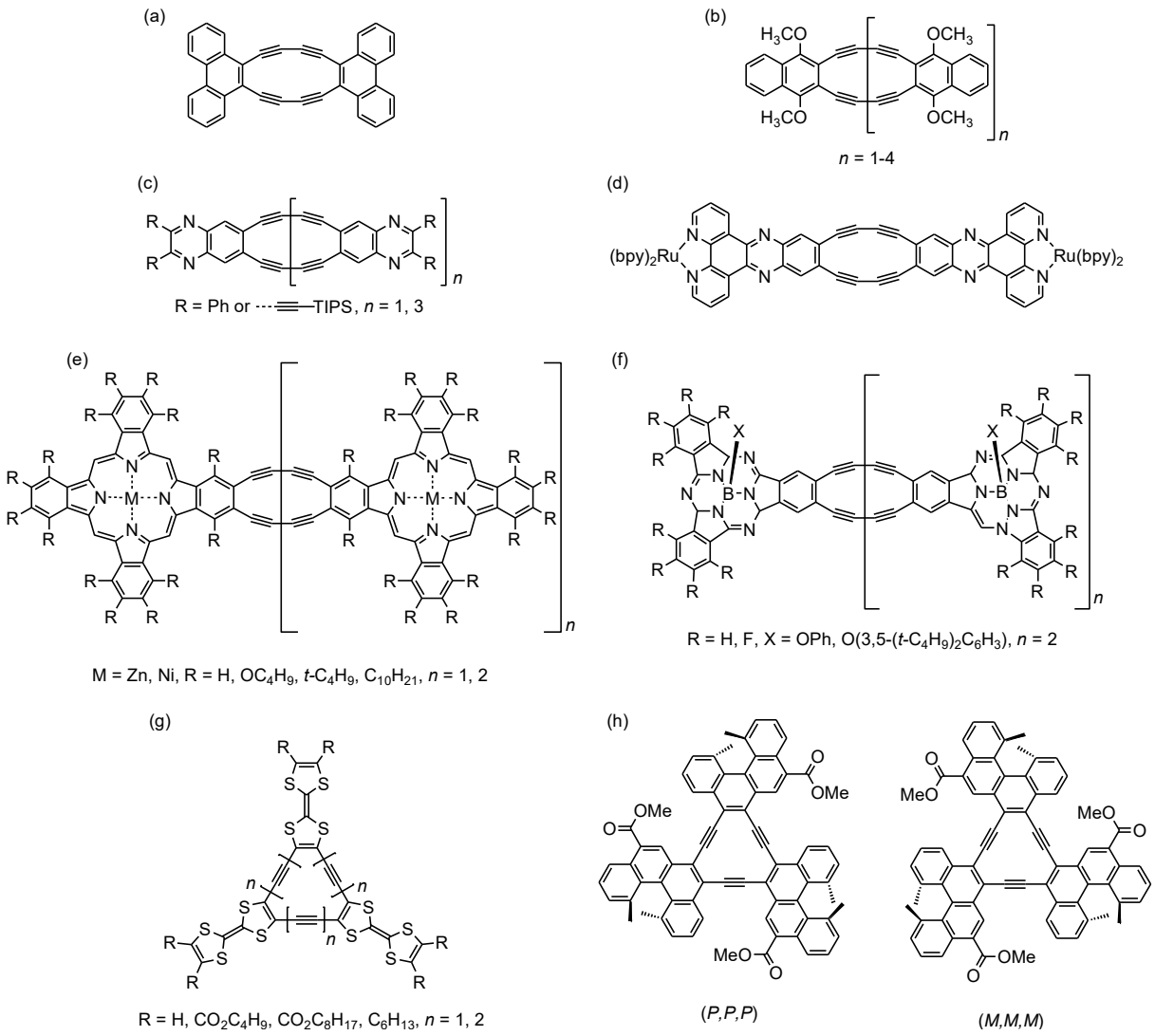

Figure 2-1. Structures of (a) phenanthrene-, (b) dimethoxynaphthalene-, (c) quinoxaline-, (d) Ru(II)-coordinated dipyridophenazine-, (e) phthalocyanine- (f) subphthalocyanine-, (g) tetrathiafulvalene-, and (h) [4]helicene-fused DA derivatives.

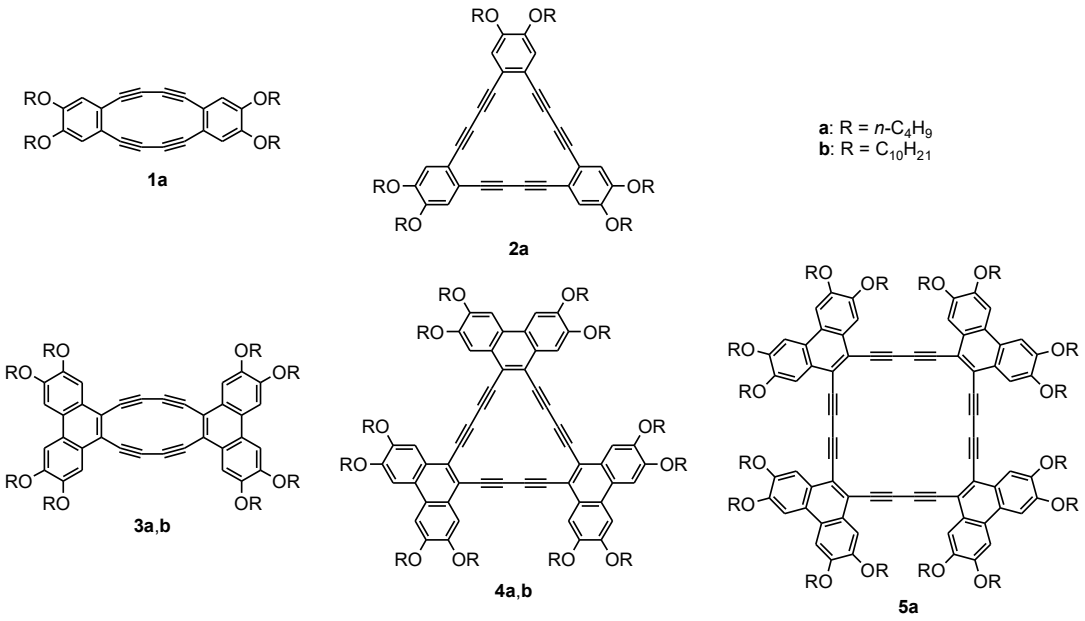

Figure 2-2. Structures of DBAs **1a** and **2a** and phenanthrene-fused DAs **3a**,**b**, **4a**,**b**, and **5a**.

First, the bond order of the C9–C10 bond is higher than that of the C–C bond in benzene; the Wiberg bond indexes were calculated to be 1.69 and 1.43 for phenanthrene and benzene, respectively, by natural bond orbital (NBO) analyses at the B3LYP/6-311G(d,p)//B3LYP/6-31G(d) level (Figure 2-3).[100] The annulation at the 9,10-positions of phenanthrene to a DA ring would enhance the extent of macrocyclic conjugation relative to the benzannulation, and thereby phenanthrene-fused [12]- and [18]DAs **3** and **4** should feature higher tropicity and smaller HOMO–LUMO gaps than the corresponding DBAs **1** and **2**.[90,101,102] Second, the annulation with phenanthrene expands the π-frameworks, which would bring about the self-association properties for planar **3** and **4** in solution through effective π–π stacking interactions derived from large π-surfaces. Third, the alkoxy chains added to aromatic nuclei were expected to not only ensure the solubility of the compounds in common organic solvents but also promote 1D self-assembly through cooperative van der Waals interactions to provide self-assembled superstructures.

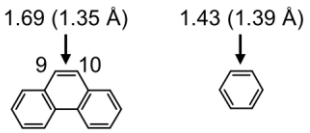

Figure 2-3. Wiberg bond indexes calculated by NBO analysis at the B3LYP/6-311G(d,p)//B3LYP/6-31G(d) level. The values in parentheses are the bond lengths.

In Chapter 2, the author describes the syntheses of [12]-, [18]-, and [24]DAs **3a**,**b**, **4a**,**b**, and **5a** and their unique properties. Although **5a** was not the targeted compound initially, its synthesis and characterization made it possible to elucidate the relationship between the topology of a DA ring and its properties. The electronic properties of **3a**,**b**, **4a**,**b**, and **5a** were exploited on the basis of UV–vis and fluorescence spectroscopies, cyclic and differential pulse voltammetry (CV and DPV), and theoretical calculations and compared with those of DBAs **1a** and **2a** from a viewpoint of the structure–property relationships. The tropicity of **3a**,**b**, **4a**,**b**, and **5a** is discussed on the basis of the ^{1}H NMR chemical shifts and nucleus-independent chemical shift (NICS). The author also reports the self-association behavior of **3a**,**b** and **4a**,**b** in solution and their formation of self-assembled superstructures, such as micrometer- and nanometer-sized 1D clusters and liquid crystals.

2-2. Syntheses and Structures

The synthesis of **3a**,**b**, **4a**,**b**, and **5a** was accomplished by using Cu-mediated or Pd-catalyzed oxidative macrocyclization reactions as key steps (Scheme 2-1). The author planned to introduce butoxy or decyloxy groups to phenanthrene-fused DAs because the length of alkoxy groups was anticipated to affect the solubility and self-assembling properties of the compounds. A Friedel–Crafts acylation of the readily available **11a**,**b** with oxalyl chloride in CH_2Cl_2 in the presence of $AlCl_3$ and urea afforded **12a**,**b**, which were converted into diketones **13a**,**b** by intramolecular oxidative cyclization with VOF_3 in the presence of $BF_3{\cdot}Et_2O$.[103] The addition of the lithiated acetylide of trimethylsilylacetylene (TMSA) to

13a,**b** and subsequent removal of the TMS groups with K_2CO_3 gave diols **14a**,**b**; this reaction gave only one isomer but the stereochemistry was not determined. A reductive aromatization of diols **14a**,**b** with $SnCl_2 \cdot 2H_2O$ in tetrahydrofuran (THF) was carried out to prepare the key intermediates **15a**,**b**. Monitoring of the reaction mixture with thin-layer chromatography (TLC) revealed the appearance of blue fluorescent spots along with consumption of the diols; however, the desired diynes **15a**,**b** were not isolated. Thus, following the workup, the crude materials explosively decomposed in the solid state to become black materials that were insoluble in any organic solvent, thus indicating that polymerization of the formed **15a**,**b** had taken place. Therefore, to avoid the decomposition of these products, the author employed the following procedure: 1) The reaction mixture was concentrated to a small volume, 2) the residue was subjected to column chromatography and eluted with CH_2Cl_2 to afford a colorless solution of the product, and 3) the solvent was carefully replaced with the solvent used in the next macrocyclization reaction by evaporation followed by dilution, and the resulting solution was used in the reaction immediately.

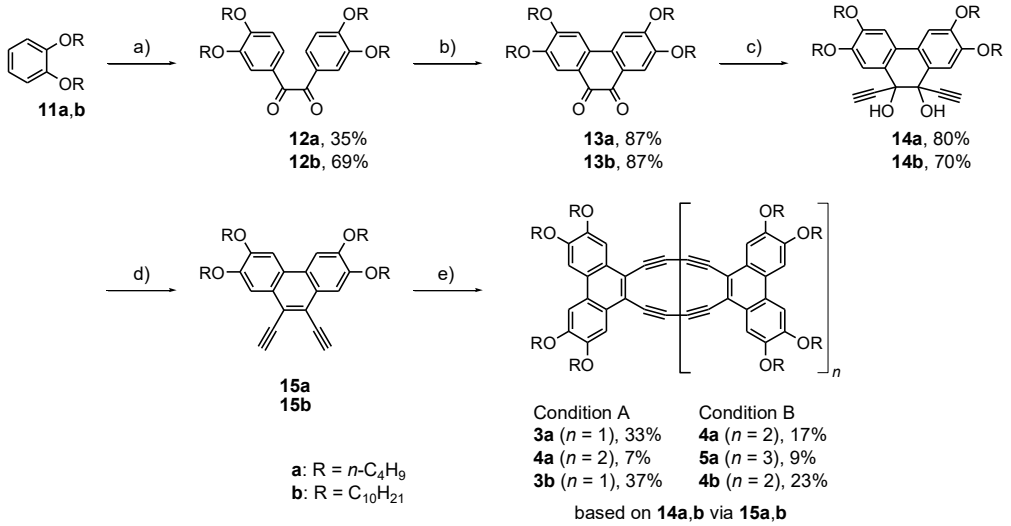

Scheme 2-1. Synthesis of DAs **3a**,**b**, **4a**,**b**, and **5a**. Reagents and conditions: a) $(COCl)_2$, $AlCl_3$, urea, CH_2Cl_2, 0 °C to RT; b) VOF_3, $BF_3 \cdot EtO_2$, CH_2Cl_2, RT; c) 1) TMS−C≡CLi, THF, −78 °C to RT; 2) H_2O; 3) K_2CO_3, THF/MeOH (1:1 v/v), RT; d) $SnCl_2 \cdot 2H_2O$, THF, 60 °C; e) conditions A: CuCl, TMEDA, *o*-DCB, 50 °C, conditions B: $[PdCl_2(PPh_3)_2]$, CuI, *p*-benzoquinone, THF/Et_3N (1:1 v/v), RT. *o*-DCB = *o*-dichlorobenzene, TMEDA = *N*,*N*,*N'*,*N'*-tetramethylethylenediamine.

The author first examined the oxidative Hay coupling reaction of **15a** by using CuCl and *N,N,N',N'*-tetramethylethylenediamine (TMEDA) in *o*-dichlorobenzene (*o*-DCB),[104,105] which furnished **3a** as a red solid and **4a** as a yellow solid in 33 and 7% yields, respectively, over two steps from **14a**. Likewise, **3b** was obtained as a red solid by means of the Hay coupling reaction of **15b**. Although the TLC analysis indicated the formation of a small amount of **4b**, its isolation was not attempted because the synthesis of **4b** was achieved in a moderate yield by the alternative Pd-catalyzed macrocyclization. Thus, when homocoupling reactions of **15a**,**b** with [$PdCl_2(PPh_3)_2$], CuI, and *p*-benzoquinone were performed,[106] **3a**,**b** were not detected by TLC and ^{1}H NMR spectroscopic analysis of the reaction mixture; consequently, **4a**,**b** were isolated in 17 and 23% yields, respectively, over two steps.[107] The Pd-catalyzed reaction with **15a** also afforded [24]DA **5a** in 9% yield. Compounds **3a**,**b**, **4a**,**b**, and **5a** were undoubtedly identified by mass spectrometric (FAB or MALDI-TOF) analysis together with their highly symmetric NMR spectra described below. The TMS-protected diyne **17a**, as a reference compound of the present DAs, was synthesized in two steps from **13a** (Scheme 2-2). Thus, the addition of the lithiated acetylide of TMSA to **13a** gave diol **16a**, which was converted into **17a** by the treatment with $SnCl_2 \cdot 2H_2O$ in THF. Compound **17a** was stable in the solid state in sharp contrast to **15a**,**b**. DBAs **1a** and **2a** as a reference compound of the present DAs were also synthesized according to the literature procedures (Scheme 2-3).[108] Iodation of **11a** with H_5IO_6 and I_2 in EtOH afforded diiodide **18**, which was converted into **19** by Sonogashira coupling reaction with TMSA using [$PdCl_2(PPh_3)_2$] and CuI. Desilylation of **19** with K_2CO_3 afforded terminal alkyne **20**, which was subjected to the Hay coupling reaction to afford DBAs **1a** and **2a** in 41 and 13% yields, respectively.

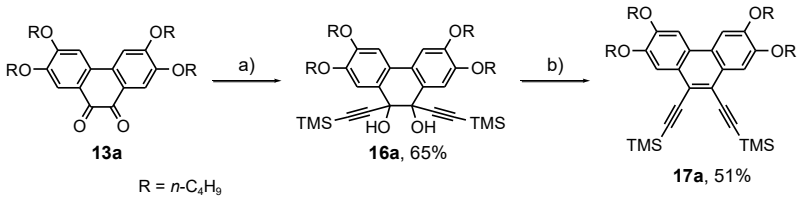

Scheme 2-2. Synthesis of reference compound **17a** for DAs. Reagents and conditions: a) 1) TMS−C≡CLi, THF, −78 °C to RT; 2) H_2O; b) $SnCl_2 \cdot 2H_2O$, THF, 60 °C.

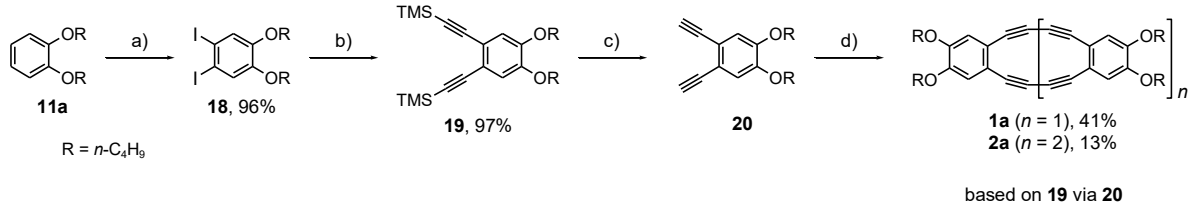

Scheme 2-3. Synthesis of DBAs **1a** and **2a**. Reagents and conditions: a) H_5IO_6, I_2, EtOH, 50 °C; b) $[PdCl_2(PPh_3)_2]$, CuI, TMSA, THF/Et_3N (3:1 v/v), 60 °C; c) K_2CO_3, THF/MeOH (1:1 v/v); d) CuCl, TMEDA, *o*-DCB, 50 °C. TMSA = trimethylsilylacetylene, *o*-DCB = *o*-dichlorobenzene, TMEDA = *N*,*N*,*N*′,*N*′-tetramethylethylenediamine.

Weakly diffracting crystals of **3a** for X-ray diffraction analysis were obtained by very slow evaporation of a solution in $CHCl_3$ at room temperature (Figure 2-4). The crystals proved to contain no solvent molecules. The deviation from the mean plane composed of carbon atoms of the phenanthrene moieties and butadiyne linkages is at most 0.02 Å, thus indicating the remarkably planar structure. The oligoyne linkages are strained with bond angles 165.5, 167.3, 166.7, and 165.2 for C1–C2–C3, C2–C3–C4, C3–C4–C5, and C4–C5–C6, respectively, which are almost the same as the corresponding angles of [12]DBA **21**, which has four butyl substituents, as reported by Swager and co-workers (Figure 2-5).[48] Noticeably, the C6–C7 bond of 1.395 Å is shorter than the C–C bond of 1.413 Å shared by the benzene moieties and the annulene ring in [12]DBA **21** as expected. The molecules arrange longitudinally in a slipped π-stacked fashion, and thus the phenanthrene moieties overlap with the DA cores to form a 1D column (Figure 2-4b,c). The intermolecular distance between the center of the DA core and the plane of facing molecules is approximately 3.4 Å, and the angle between the plane of the DA core and the stacking axis is 43°.

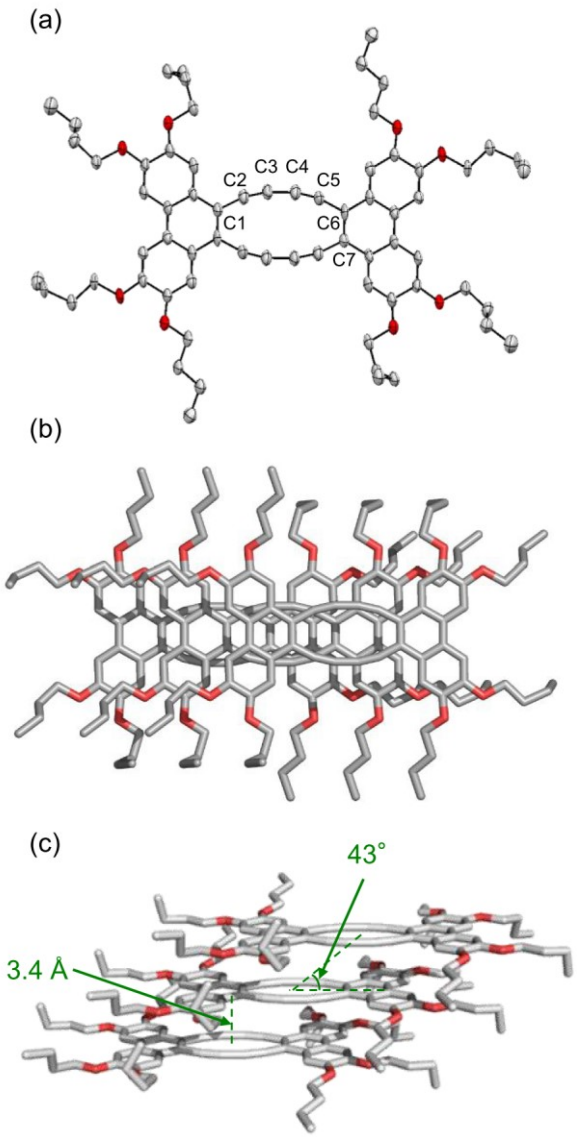

Figure 2-4. (a) ORTEP plot of **3a** with displacement ellipsoid at 50% probability level. Hydrogen are omitted for clarity. (b) Top and (c) side views of the packing diagram.

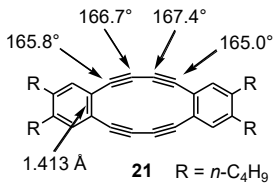

Figure 2-5. Structure of [12]DBA **21**. Bond lengths and angles determined by X-ray crystallographic analysis.

2-3. ^{1}H NMR Spectra and NICS Calculations

The author calculated the molecular structures of **1'**–**5'**, in which the butoxy groups in the corresponding derivatives **1a**–**5a** were replaced with methoxy groups to decrease the calculation time (Figure 2-6). The optimization of **1'**–**4'** was performed by density functional theory (DFT) calculations at the B3LYP/6-31G(d) level, whereas the PM7 calculation was conducted for **5'**; the large molecular size of **5'** prevented the use of DFT. The optimized structures of [12]annulenes **1'** and **3'** have planar D_{2h} symmetry, whereas the structures of [18]annulenes **2'** and **4'** are also planar with D_{3h} symmetry. The structure of [24]annulene **5'** was calculated to have a nonplanar, saddle-shaped D_{2d}-symmetric structure akin to that of cyclooctatetraene. The bond angles and lengths in the experimentally determined structure of **3a** mentioned above were virtually reproduced in the calculated structure of **3'** (bond angles: ±1°; bond lengths: ±0.02 Å).

The partial ^{1}H NMR spectra of DAs **3a**–**5a**, and acyclic **17a** in $CDCl_3$ at 20 °C are shown in Figure 2-7. Planar and rigid DAs **3a**,**b** and **4a**,**b** exhibit very simple NMR signals, namely a pair of two singlets in the aromatic region owing to their highly symmetrical structures. Nonplanar DA **5a** also exhibits simple and sharp NMR signals. The temperature-dependent ^{1}H NMR spectra of **5a** in CD_2Cl_2 displayed a broadening of some signals and no coalescence was observed down to −60 °C, thus suggesting that the conformational change in **5a** at room temperature is rapid on the NMR timescale and that **5a** is quite flexible.[109]

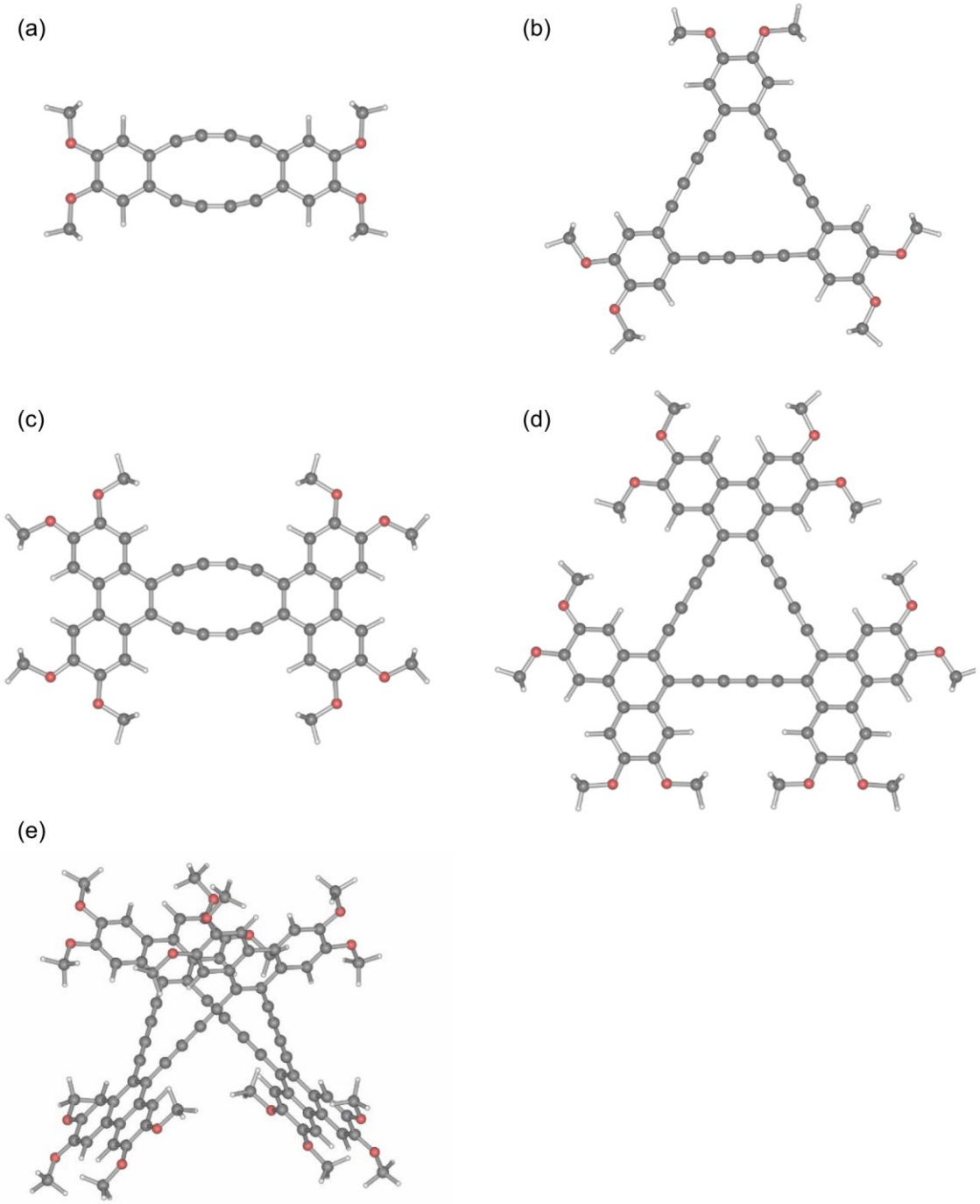

Figure 2-6. Optimized molecular structures of (a) **1'**, (b) **2'**, (c) **3'**, and (d) **4'**, where the butoxy groups in **1a**–**4a** are replaced with methoxy groups (B3LYP/6-31G(d)). (e) PM7-optimized structure of **5'**, where the butoxy groups in **5a** are replaced with methoxy groups.

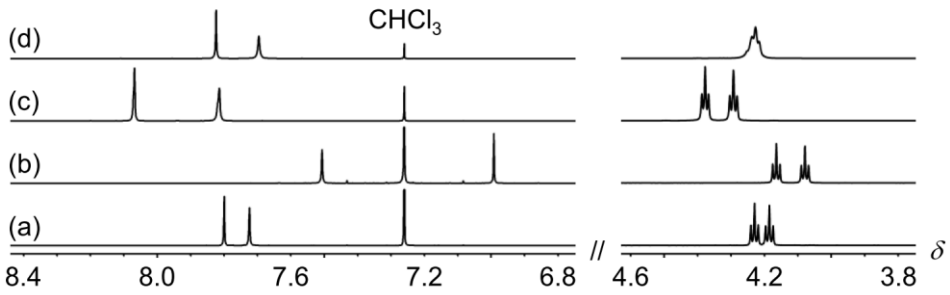

Figure 2-7. Partial ^{1}H NMR spectra of (a) **17a**, (b) **3a** (1.28×10^{-3} mol dm^{-3}), (c) **4a** (1.45×10^{-2} mol dm^{-3}), and (d) **5a** in $CDCl_3$ at 20 °C.

The ^{1}H NMR chemical shifts are a good measure for the elucidation of tropicity, namely diatropicity, paratropicity, or atropicity. Thus, the author compared the changes in the chemical shifts of the aromatic protons in **3a**–**5a** from those signals in **17a** (Table 2-1). The arene proton environments in **17a** are used as a reference standard because of the structural similarity, yet this simple DA subunit may lack the anisotropic effects attributable to distortion of acetylenic linkages.[110] The aromatic protons in **3a** resonate at δ = 7.50 and 6.99, which are shifted upfield relative to those of **17a** (δ = 7.80 and 7.72, Figure 2-7). In sharp contrast, the resonances of the aromatic protons in **4a** (δ = 8.07 and 7.82) are shifted downfield. The aromatic protons in **3b** and **4b** show almost the same NMR chemical shifts as those in **3a** and **4a**, respectively. For nonplanar **5a**, almost no shift is observed (δ = 7.82 and 7.69) relative to **17a**. Notably, the resonances of the –OCH_2– protons in **3a** and **4a** are also distinctively shifted upfield and downfield, respectively, relative to **17a**, whereas those signals in **5a** have hardly shifted. Overall, these results imply paratropic, diatropic, and atropic characters of **3**, **4**, and **5**, respectively.

Table 2-1. Observed ^{1}H NMR Chemical Shifts and NICS Values for **1a**–**5a**, **17a**, **22**, and **23**

	Chemical shifts for aromatic and –OCH_2– protons δ_{obs}[a]	NICS(0)[b,c]	NICS(1)[b,c]
1a	6.39, 3.87	+3.8	+3.7
2a	7.10, 3.87	−0.09	−0.08
3a	7.50, 6.99, 4.16, 4.08[d]	+6.6	+6.0
4a	8.07, 7.82, 4.38, 4.30[e]	−0.7	−0.4
5a	7.82, 7.69, 4.22	N/A	N/A
17a	7.80, 7.72, 4.23, 4.18	N/A	N/A
22[f]	N/A	+9.1	+8.1
23	7.02[g]	−3.6	−3.2

[a] In $CDCl_3$ at 20 °C. [b] Calculated by using GIAO/HF//6-31G(d)//B3LYP/6-31G(d) for **1'**–**4'**, **22**, and **23**. [c] For **1'**–**4'**, in which the butoxy groups in **1a**–**4a** replaced with methoxy groups. [d] [**3a**] = 1.28×10^{-3} mol dm^{-3}. [e] [**4a**] = 1.45×10^{-2} mol dm^{-3}. [f] Unknown compound. [g] In CCl_4 (reported in Ref. 3)

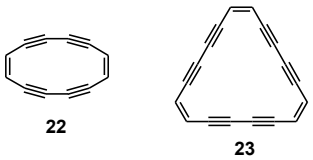

Figure 2-8. Structures of [12]DA **22** and [18]DA **23**.

To obtain insight into the relationships between the aromatic nuclei annulated into a DA ring, namely phenanthrene and benzene, and the tropicity, the author calculated the NICS(0) (and NICS(1)) values (GIAO/HF/6-31(d)//B3LYP/6-31G(d)) of the planar compounds **1'**–**4'** together with the parent [12]DA **22** and [18]DA **23** (Figure 2-8).[111,112] The NICS(0) (and NICS(1)) values of **3'** are +6.6 (+6.0), respectively, which are considerably more positive than those of DBA **1'** (+3.8 (+3.7)). The NICS(0) (and NICS(1)) values of **4'** (−0.7 (−0.4)) are not large, but distinctively more negative than those of **2'** (−0.09 (−0.08)). These results suggest that **3a**,**b** are more paratropic than **1a**, whereas **4a**,**b** are more diatropic than **2a**.[5] This outcome probably reflects the finding that the Wiberg bond indexes

(B3LYP/6-311G(d,p)//B3LYP/6-31G(d)) of the C–C bonds (1.38 and 1.36 for **3'** and **4'**, respectively) shared by the phenanthrene moieties and the DA ring are larger than those (1.25 and 1.26 for **1'** and **2'**, respectively) shared by the benzene moieties and the DA ring. Noticeably, the NICS(0) (and NICS(1)) values of **3'** still remain about 70% of values of antiaromatic **22** (+9.1 (+8.1)). This finding indicates substantially strong paratropicity, namely, the antiaromaticity of **3a**,**b**, which is further supported by UV–vis and fluorescence spectroscopic and cyclic voltammetric analysis (see below). On the other hand, the NICS values of **4'** are drastically less than those of aromatic **23** (−3.6 (−3.2)), and hence the tropicity of **4a**,**b** is very weak.

2-4. Electronic and Photophysical Properties

The author measured the UV–vis spectra of **1a**–**5a** in $CHCl_3$ (Figure 2-9), and the results are summarized in Table 2-2. The absorption spectra of **3a** and **3b** are very similar to each other, as are those spectra of **4a** and **4b**. The solutions of **3a**,**b** in $CHCl_3$ are orange, whereas the solutions of **4a**,**b** and **5a** are yellow (Figure 2-10). The longest absorption maxima (λ_{max}^{abs}) and absorption onsets (λ_{onset}) of **3a** and **4a** are remarkably red-shifted relative to those of the corresponding **1a** and **2a** (Figure 2-9). This finding should be attributable to the high extent of macrocyclic conjugation in **3a** and **4a** relative to **1a** and **2a**, respectively, as judged from the Wiberg bond indexes of the C–C bonds shared by the aromatic nuclei and the DA rings in **1'**–**4'** (see above). The larger π surface of phenanthrene than benzene may also contribute to the observed bathochromic shifts in **3a** and **4a** relative to **1a** and **2a**, respectively. Interestingly, the longest λ_{max}^{abs} and λ_{onset} values of **3a** are clearly red-shifted relative to **4a** and **5a**, despite the smallest ring size of **3a**, thus probably reflecting the antiaromatic character and distortion of the π system of **3a**.[113] The blue-shifted longest λ_{max}^{abs} and λ_{onset} values of **5a** relative to **4a** are explained by the marked nonplanarity of **5a**, which should make its macrocyclic conjugation insufficient.

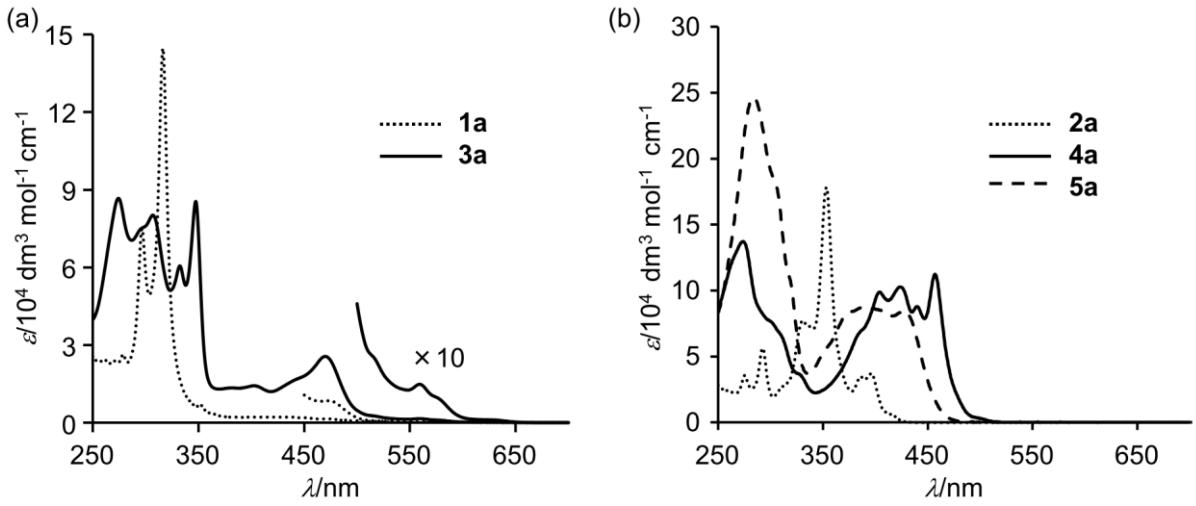

Figure 2-9. UV–vis absorption spectra of (a) **1a** and **3a** and (b) **2a**, **4a**, and **5a** in $CHCl_3$ at 25 °C.

Table 2-2. Photophysical Data of **1a**–**5a**[a]

	λ_{max}^{abs} [nm]	λ_{onset}[b] [nm]	λ_{max}^{fl} [nm]	Φ_f[c]
1a	297, 316, 352, 409, 435, 472	450	N.D.	~0
2a	275, 292, 330, 353, 386, 396, 415[d]	425	430	0.36
3a	274, 306, 332, 347, 381, 402, 470, 559	575	N.D.	~0
4a	274, 404, 424, 440, 457	510	509	0.20
5a	284, 390, 427	480	481	0.07

[a] In $CHCl_3$ at 25 °C. [b] The longest absorption wavelength with a molar absorptivity ε = 1000 dm^3 mol^{-1} cm^{-1}. [c] Fluorescence quantum yields. [d] A peak as a shoulder.

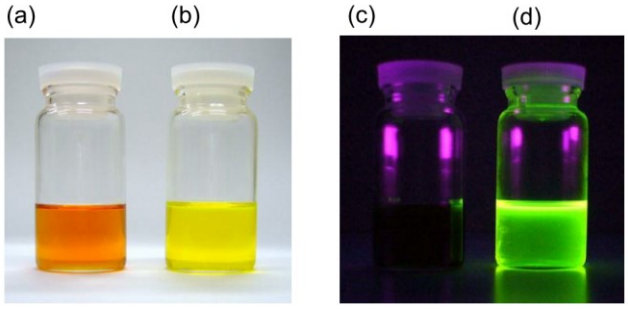

Figure 2-10. Optical photographs of (a) **3a**, (b) **4a**, (c) **3a** (under irradiation at 365 nm), and (d) **4a** (under irradiation at 365 nm).

Noticeably, [12]annulenes **1a** and **3a,b** feature characteristic broad and weak absorption bands in the longer wavelength region. The spectrum of **3a** has an intense absorption band at λ = 470 nm (ε = 25500 dm^3 mol^{-1} cm^{-1}) and weak absorption bands from λ = 500 to 600 nm with the distinctive longest absorption at λ_{max}^{abs} = 559 nm (ε = 1480 dm^3 mol^{-1} cm^{-1}), whereas the spectrum of **1a** has weak absorption bands from λ = 380 to 500 nm and a sharp absorption band at λ_{max}^{abs} = 352 nm (Figure 2-9a). To elucidate the features of the absorption spectra of planar **3** and **4** together with **1** and **2**, the single-point calculations at the B3LYP/6-31+G(d,p)//B3LYP/6-31G(d) level for **1'**–**4'** were performed. The obtained frontier molecular orbital (FMO) plots for **1'**–**4'** are shown in Figure 2-11. Both the HOMOs and LUMOs of [12]annulenes **1'** and **3'** are *ungerade* orbitals (Figure 2-11), and hence the longest absorption bands ($S_0 \rightarrow S_1$ bands) of **1** and **3** are reasonably assigned as symmetrically forbidden HOMO→LUMO transitions, which are typical of 4*n*π-electron systems.[35,58,114] This assignment is supported by time-dependent DFT (TD-DFT) calculations at the B3LYP/6-31G(d) level for **1'** and **3'**,[115] which estimate the oscillator strength of the HOMO→LUMO transition to be 0 (λ_{max}^{calcd} = 589 and 716 nm for **1'** and **3'**, respectively). The HOMOs and HOMO−1s of [18]annulenes **2'** and **4'** are degenerate, as are the LUMOs and LUMO+1s (Figure 2-11). According to the TD-DFT calculations for **2'** and **4'**, the HOMO−1→LUMO+1, HOMO−1→LUMO, HOMO→LUMO, and HOMO→LUMO+1 transitions are allowed for **2** and **4**, and thus the oscillator strengths are 0.94 at λ_{max}^{calcd} = 392 nm and 1.23 at λ_{max}^{calcd} = 463 nm for **2'** and **4'**, respectively.

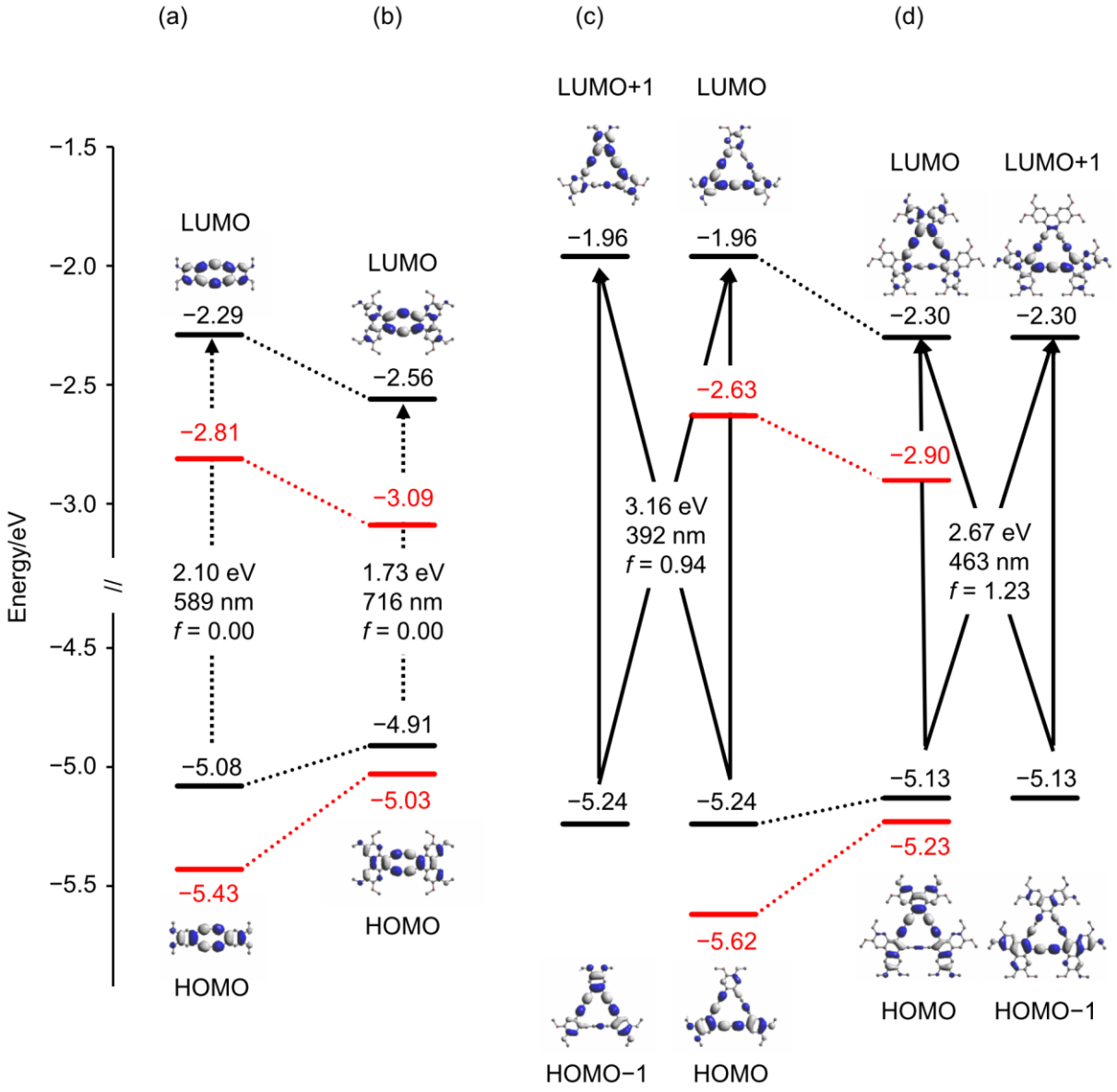

Figure 2-11. (Black) energy diagrams and frontier molecular orbital (FMO) plots of (a) **1'**, (b) **3'**, (c) **2'**, and (d) **4'** by using the B3LYP/6-31+G(d,p)//B3LYP/6-31G(d) method, and their transitions estimated by TD-DFT calculations at B3LYP/6-31G(d)//B3LYP/6-31G(d). (Red) HOMO and LUMO levels of (a) **1a**, (b) **3b**, (c) **2a**, and (d) **4a** deduced from the oxidation onset (E_{onset}^{ox}) and reduction onset (E_{onset}^{red}) values according to the following equation: HOMO = −(4.8 + E_{onset}^{ox}) eV, LUMO = −(4.8 + E_{onset}^{red}) eV.

Compounds **1a** and **3a**,**b** are nonfluorescent, whereas **2a**, **4a**,**b**, and **5a** are fluorescent. The author measured the fluorescence spectra of **2a**, **4a**,**b**, and **5a** in $CHCl_3$ at the dilute regime (10^{-5}–10^{-6} mol dm^{-3}; Figure 2-12). Their fluorescence maxima (λ_{max}^{fl}) follow the trend of the corresponding λ_{max}^{abs} values (Table 2-2). The spectrum of **5a** is substantially broad relative to **2a** and **4a**, thus implying a somewhat large structural change between the

ground and excited states in **5a**. The author determined the absolute fluorescence quantum yields (Φ_f) by an integrating sphere system.[116] The Φ_f values of **4a**,**b** are 0.20 and 0.19, respectively, which are smaller than that of the corresponding DBA **2a** with $\Phi_f = 0.36$. DA **5a** displays the low Φ_f value of 0.07. The nonfluorescent nature of **3a**,**b** is remarkable in view of the highly fluorescent nature of some phenanthrene-based oligomers and polymers.[117,118] The lack of fluorescence is usually the case with $4n\pi$-electron systems,[119,120] and hence these results together with the UV–vis spectroscopic data support the antiaromaticity of **3a**,**b**.

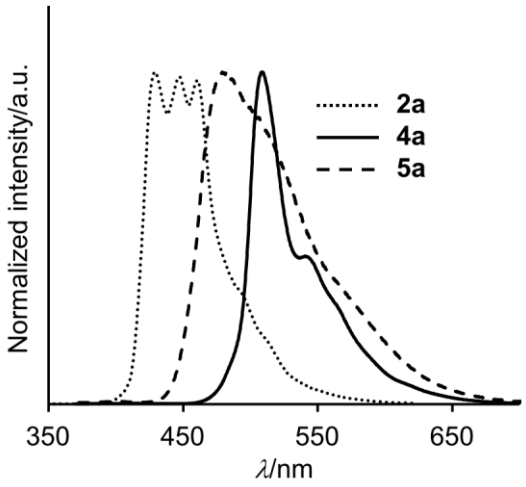

Figure 2-12. Fluorescence spectra of **2a**, **4a**, and **5a** in $CHCl_3$ at 25 °C. The excitation wavelengths λ_{ex} = 320, 360, and 360 nm for **2a**, **4a**, and **5a**, respectively.

2-5. Electrochemical Properties

The electrochemical properties of **3b**, **4a**,**b**, and **5a** together with **1a** and **2a** were examined by using CV in *o*-DCB (0.1 mol dm^{-3} *n*-Bu_4NPF_6, standard ferrocene/ferrocenium ion (Fc/Fc^+)); the results are summarized in Table 2-3. The electrochemical property of **3a** could not be investigated due to the low solubility in *o*-DCB. All the compounds displayed amphoteric behavior within the available potential window, and the redox processes for most

compounds are irreversible (Figures 2-13 and 2-14). The redox behavior of **4a** and **4b** are very similar to each other, indicating that of the length of the alkoxy groups hardly affects electrochemical properties. It is considered that the DA rings in **3b**, **4a**,**b**, and **5a** behave as redox centers due to no splitting of the redox processes and the large contribution of both HOMOs and LUMOs from the DA rings. The oxidation potentials (E_{pa}) and the oxidation onsets (E_{onset}^{ox}) of **3b** and **4a** are more negative than those of **1a** and **2a**, respectively. Moreover, the reduction potentials (E_{pc}) and the reduction onsets (E_{onset}^{red}) of **3b** and **4a** are more positive than those of **1a** and **2a**, respectively. Thus, the annulation of phenanthrene to the DA ring relative to the benzannulation clearly brings about the decrease in the HOMO–LUMO gaps, as expected from the results obtained by the absorption spectra. Indeed, the single-point calculations for **1'**–**4'** predict that the HOMO–LUMO gaps of **3'** and **4'** are smaller than those of the corresponding compounds **1'** and **2'**, respectively. The E_{onset}^{ox} values are negatively shifted from **5a** and **4a** to **3b**, whereas the E_{onset}^{red} values are positively shifted from **4a** and **5a** to **3b**. It is worth stating that the E_{onset}^{ox} and E_{onset}^{red} values for **3b** are negative and positive relative to **4a** and **5a**, respectively, although **3b** has a smaller DA ring than **4a** and **5a**. The observed readiness of **3b** to release and gain electrons should reflect an electronic structure characteristic of antiaromaticity. Accordingly, the electrochemical HOMO–LUMO gaps decrease from **5a** and **4a** to **3b**. A good correlation exists between the optical HOMO–LUMO gaps (ΔE_{opt}) and the electrochemical HOMO–LUMO gaps (ΔE_{redox}) in **3b**, **4a**, and **5a**.

Table 2-3. Oxidation and Reduction Potentials of **1a**, **2a**, **3b**, **4a,b**, and **5a**,[a] and Theoretically Calculated HOMO and LUMO Levels, Electrochemical HOMO–LUMO Gaps, and Optical HOMO–LUMO Gaps

	E_{onset}^{ox} (E_{pa})	E_{onset}^{red} (E_{pc})	HOMO[b]	LUMO[b]	ΔE_{redox}[c]	ΔE_{calcd}[b]	ΔE_{opt}[d]
	[V]	[V]	[eV]	[eV]	[V]	[eV]	[eV]
1a	+0.63	−1.99	−5.08	−2.29	2.62	2.79	2.74
	(+0.78)[f]	(−2.16)[g]					
	(+1.21)[f]	(−2.51)[e]					
2a	+0.82	−2.17	−5.24	−1.96	2.99	3.28	2.91
	(+0.96)[e]	(−2.43)[h]					
3b	+0.23	−1.71	−4.91	−2.56	1.94	2.35	2.15
	(+0.44)[e]	(−1.92)[f]					
	(+0.98)[e]	(−2.16)[g]					
4a	+0.43	−1.90	−5.13	−2.30	2.38	2.83	2.43
	(+0.58)[e]	(−2.04)[g]					
	(+0.79)[e]	(−2.31)[e]					
		(−2.55)[e]					
5a	+0.52	−1.92	–[i]	–[i]	2.44	–[i]	2.58
	(+0.65)[e]	(−2.04)[f]					
	(+1.00)[e]	(−2.42)[e]					

[a] Measuring by using CV in *o*-DCB (0.1 mol dm^{-3} *n*-Bu_4NPF_6). All the potentials are given versus the Fc/Fc^+ couple as an external standard. Scan rate = 100 mV s^{-1}. [b] B3LYP/6-31+G(d,p)//B3LYP/6-31G(d) for **1'**–**4'**, where the butoxy groups in **1a**, **2a**, and **4a** and the decyloxy groups in **3b** were replaced by methoxy groups. [c] The electrochemical gap (ΔE_{redox}) is defined as the potential difference between E_{onset}^{ox} and E_{onset}^{red}. [d] The optical gap (ΔE_{opt}) is defined as the longest energy absorption wavelength with a molar absorptivity ε = 1000 dm^3 mol^{-1} cm^{-1}. [e] Irreversible wave. [f] Reversible wave. [g] Quasireversible wave. [h] Unresolved wave. [i] Not calculated.

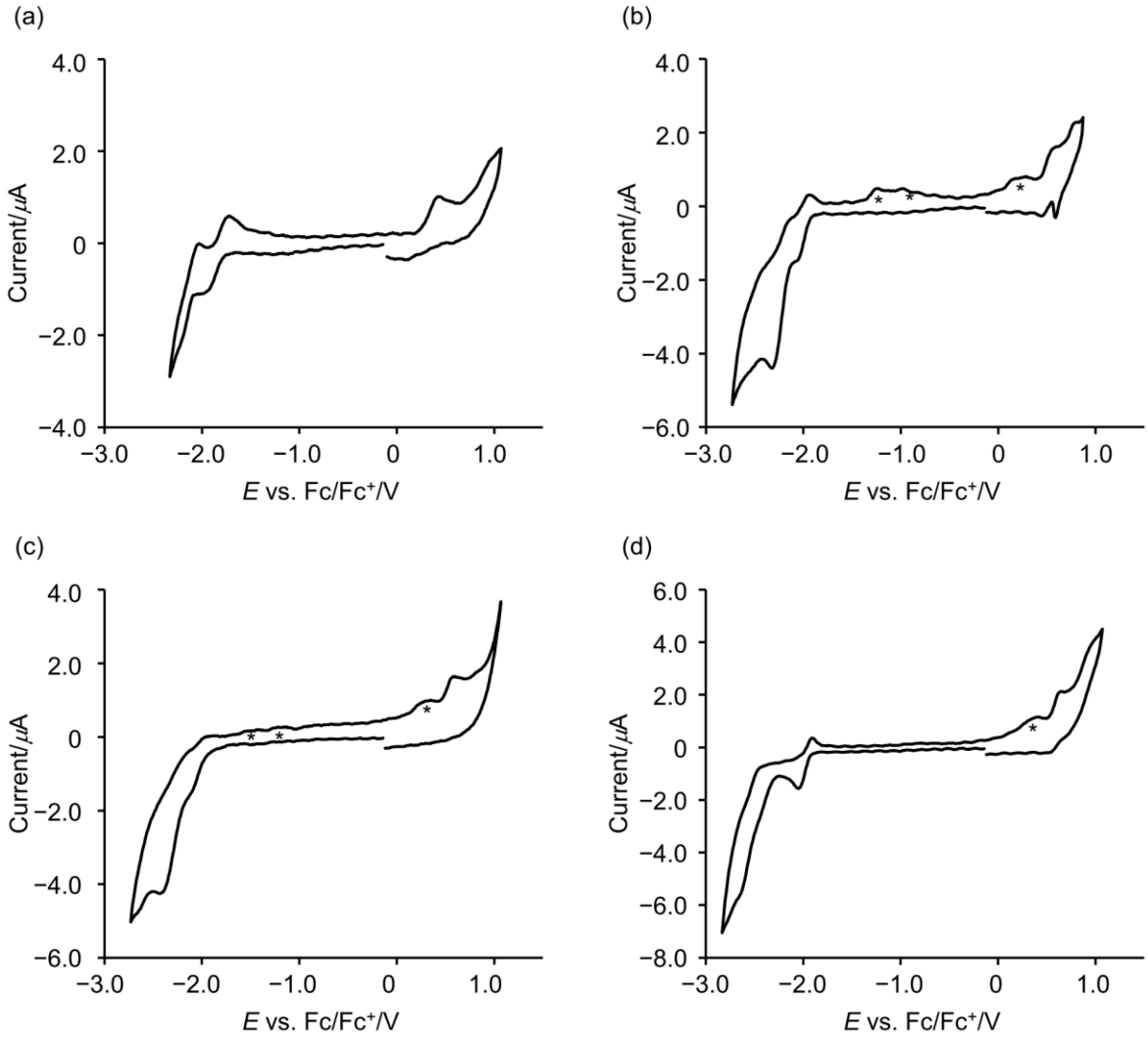

Figure 2-13. Cyclic voltammograms of (a) **3b**, (b) **4a**, (c) **4b**, and (d) **5a** measured in *o*-DCB (0.1 mol dm^{-3} *n*-Bu_4NPF_6) at a scan rate of 100 mV s^{-1}. The peaks attributed to the decomposed species formed by reduction are labeled with an asterisk.

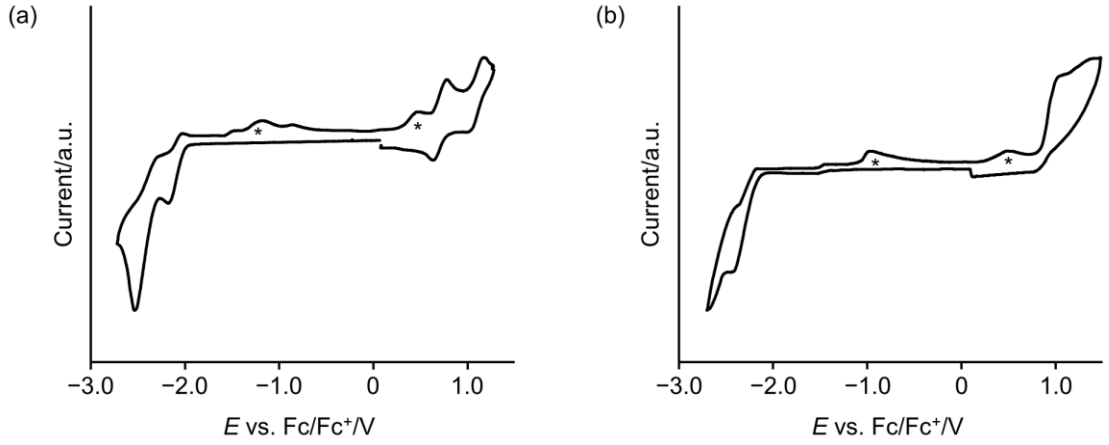

Figure 2-14. Cyclic voltammograms of (a) **1a** and (b) **2a** measured in *o*-DCB (0.1 mol dm^{-3} *n*-Bu_4NPF_6) at a scan rate of 100 mV s^{-1}. The peaks attributed to the decomposed species formed by reduction are labeled with an asterisk.

The redox behaviors of **3b**, **4a**,**b**, and **5a** were further investigated by DPV in *o*-DCB (0.1 mol dm^{-3} *n*-Bu_4NPF_6, standard Fc/Fc^+; Figure 2-15). DAs **3b**, **4a**,**b**, and **5a** basically experience multiple $1e^-$ redox steps. Interestingly, the current values of the second reduction peaks at approximately −2.3 V for **4a**,**b** are almost twice as large as those of the first reduction and oxidation peaks (Figure 2-15b,c), thus suggesting that the simultaneous $2e^-$ reduction occurs at approximately −2.3 V. This observation may be interpreted as follows: dianions of **4a**,**b** generated by the $2e^-$ reduction are antiaromatic with 20π electrons, and accordingly the following $1e^-$ reduction readily proceeds.

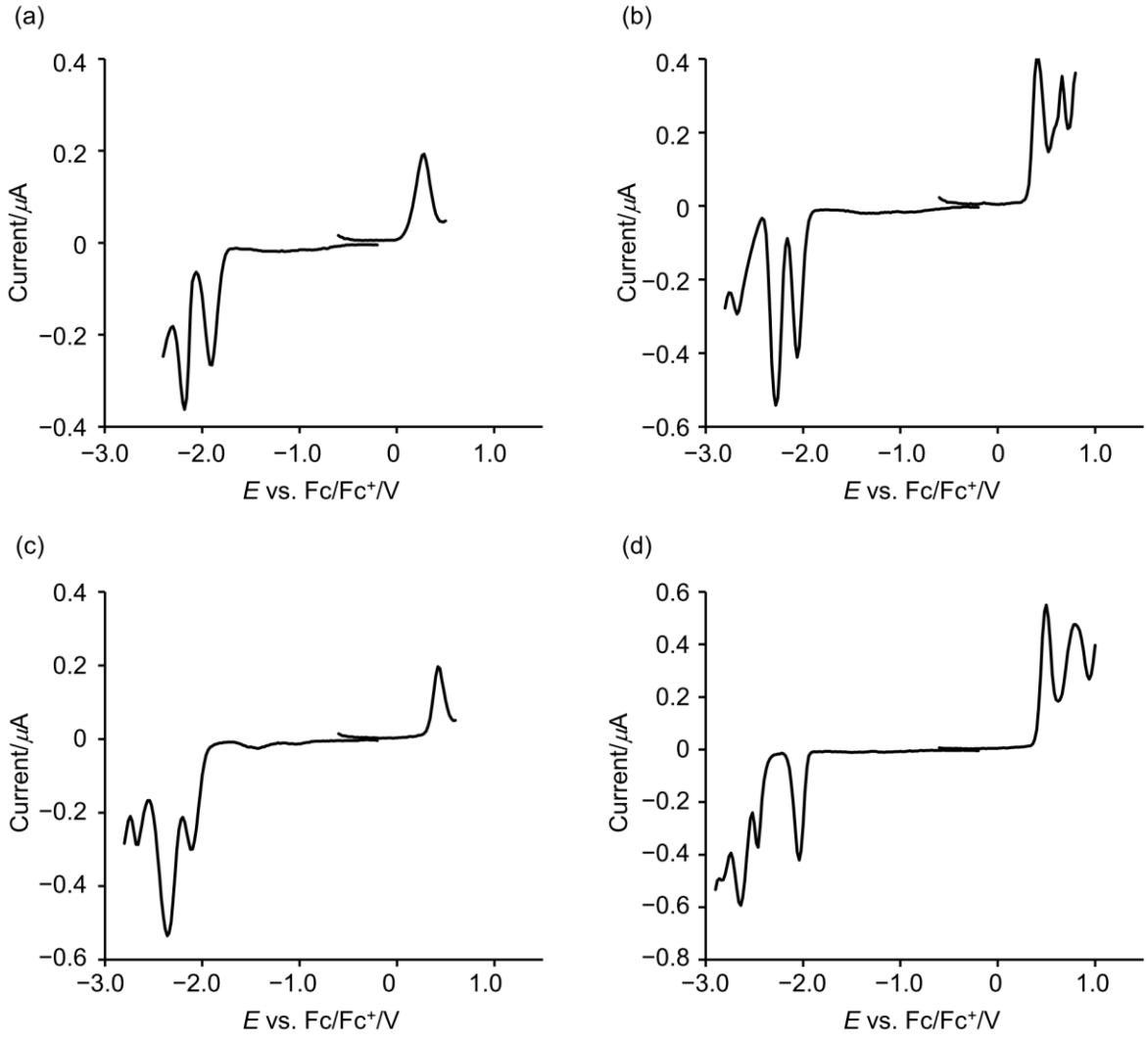

Figure 2-15. Differential pulse voltammograms of (a) **3b**, (b) **4a**, (c) **4b**, and (c) **5a** measured in *o*-DCB (0.1 mol dm^{-3} *n*-Bu_4NPF_6) at a pulse width of 100 ms over a period of 200 ms.

2-6. Self-association

During the ^{1}H NMR spectroscopic measurements of **3a**,**b** and **4a**,**b** in $CDCl_3$, the subtle but unequivocal upfield shifts of their aromatic protons were found upon increasing the concentration ($\Delta\delta$ = 0.03–0.06 ppm for the range of 10^{-5}–10^{-2} mol dm^{-3}; Figure 2-16), thus suggesting the occurrence of self-association in solution by effective π–π stacking interactions to form aggregates. On the other hand, the resonances for the aromatic protons in **1a** and **2a** hardly change at any concentrations, and thus the self-association of **1a** and **2a** in $CDCl_3$ is almost negligible. These results confirm that the self-association behaviors of **3a**,**b** and **4a**,**b** are reasonably attributed to the expanded contact areas for π–π stacking interactions as a consequence of the annulation with phenanthrene. The chemical shifts of the aromatic protons in **5a** were concentration independent, thus indicating no self-association, as expected from its nonplanarity. The diffusion coefficients (*D*) for **3a**,**b** and **4a**,**b** were almost independent of the concentrations on the basis of the diffusion NMR experiments, thus suggesting that a monomer–dimer equilibrium predominantly exists.[121] The plots of the chemical shifts of the aromatic protons versus the concentrations of **3a**,**b** and **4a**,**b** were fitted to a curve for the monomer–dimer model (Figure 2-16), which produced the self-association constants (*K*) of **3a**, **3b**, **4a**, and **4b** to be 20 ± 9, 51 ± 10, 6 ± 1, and < 5 dm^3 mol^{-1}, respectively; as for the determination of *K* values, the reader is referred to Chapter 6.[122] The chemical-shift changes for **4b** were so small that an accurate *K* value was not obtained. The *K* values of **3a**,**b** are larger than those of **4a**,**b** although the π framework of the former is smaller than the latter. According to the PM7 calculations, there is steric hindrance from the alkoxy groups in **4a**,**b** in contrast to **3a**,**b** (Figure 2-17). This finding may account for the smaller *K* values of **4a**,**b** than **3a**,**b**; such steric hindrance in **4a**,**b** may prevent the π surfaces of the molecules from approaching each other to some extent. Noticeably, **3a**,**b** and **4a**,**b** undergo self-association in $CDCl_3$, although the observed *K* values are small. The aggregation in $CDCl_3$ that results from arylene–ethynylene macrocycles (AEMs) and

arylene–butadiynylene macrocycles (ABMs) with only apolar alkyl or alkoxy substituents is scarce. Most AEMs and ABMs that exhibit the self-association behavior in $CDCl_3$ reported to date have ester or donor/acceptor functionalization, which can assist aggregation by additional dipole–dipole or π donor–π acceptor interactions.[123–127]

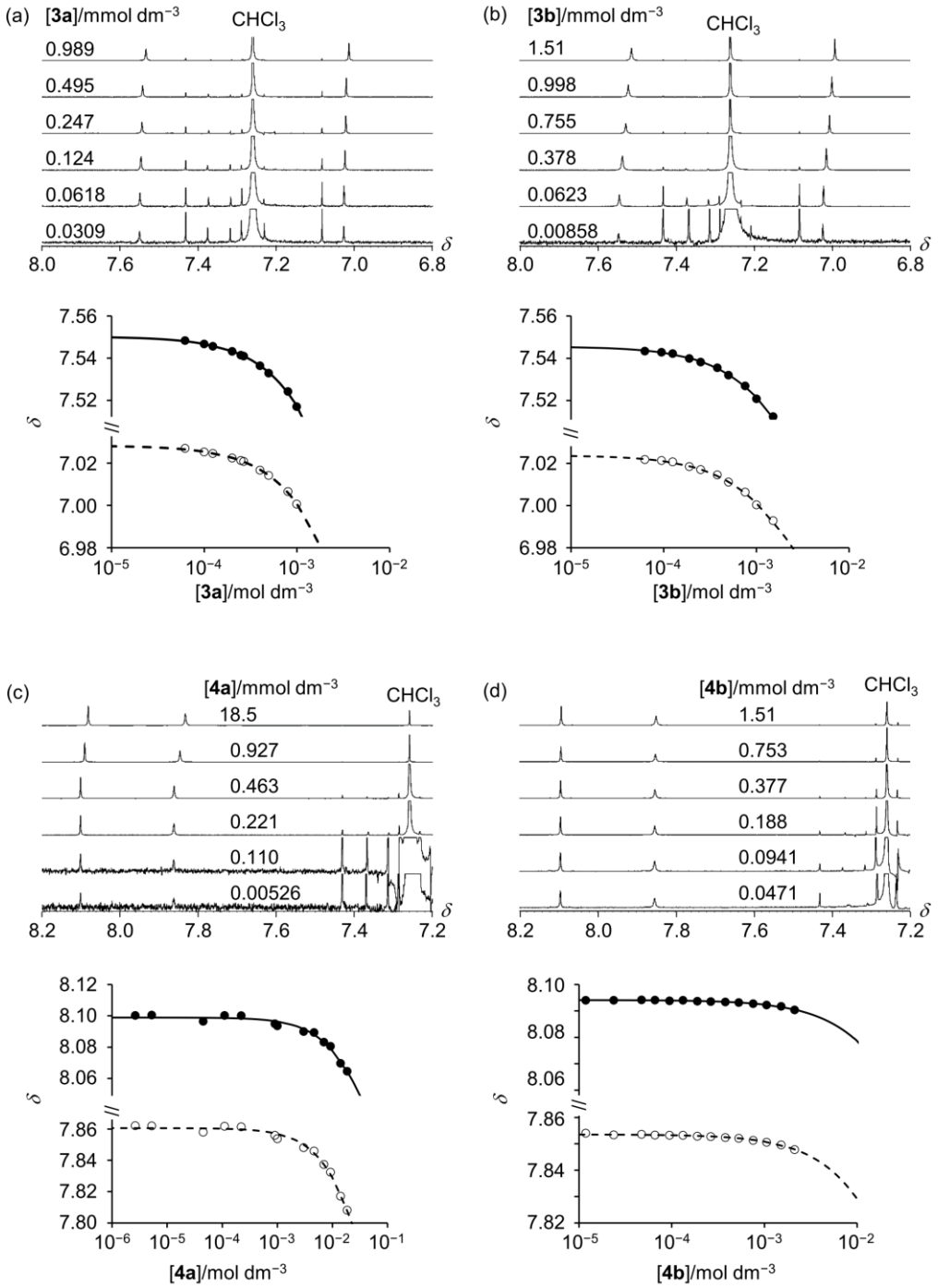

Figure 2-16. Partial ^{1}H NMR spectra of (a) **3a**, (b) **3b**, (e) **4a**, and (f) **4b** in $CDCl_3$ in various concentrations at 20 °C (top) and the corresponding nonlinear curve-fitting plots of the concentration dependence of the chemical shifts of the aromatic protons (bottom).

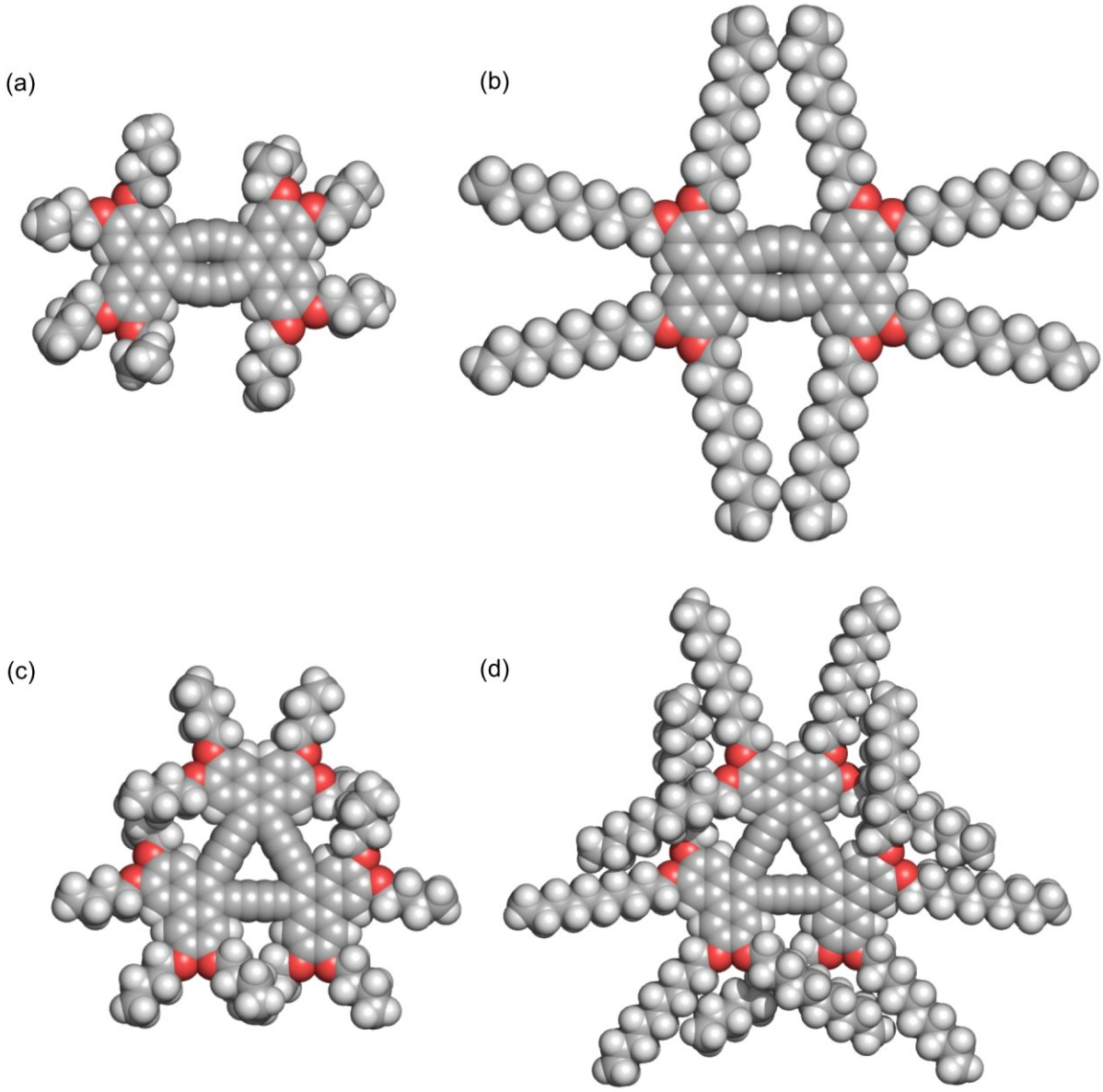

Figure 2-17. (a) X-ray crystal structure of **3a**. PM7-optimized structures of (b) **3b**, (c) **4a**, and (d) **4b**.

2-7. Self-assembled Superstructures

Because **3a**,**b** and **4a**,**b** show aggregation properties in solution, the author anticipated the fabrication of large-sized superstructures through self-assembly from **3a**,**b** and **4a**,**b**. The author investigated their self-assembly through a phase-transfer method, in which the molecules in solution experience solubility change during a slow diffusion of a poor solvent into the solution, thus initiating the formation of assembled clusters. To each solution of **3a**,**b** and **4a**,**b** in $CHCl_3$ (1.7×10^{-3} mol dm^{-3}), 40–50 vol.% of EtOH was slowly added to

maintain two phases. The resulting mixtures were allowed to stand at room temperature, and orange fibrous materials for **3a**,**b** and yellow jelly materials for **4a**,**b** formed (Figure 2-18). To investigate the morphology of the materials obtained, scanning electron microscopic (SEM) experiments were conducted, which revealed that well-defined structures with high aspect ratios were obtained from both **3a**,**b** and **4a**,**b** (Figure 2-19). [12]DAs **3a**,**b** basically formed significantly long 1D microbelts more than 300 mm in length. The widths and thicknesses of the microbelts obtained from **3a** are 1–1.5 μm and 300–500 nm, respectively (Figure 2-19a,b). A small number of prismatic structures with widths of 2–4 μm also coexisted. In the case of **3b**, only 1D microbelts with widths and thicknesses of 0.2–1 μm and 50–100 nm, respectively, were formed (Figure 2-19e,f). The microbelts are generally bundled with different widths. Meanwhile, [18]DAs **4a**,**b** produced more flexible superstructures than [12]DAs **3a**,**b**. Thus, **4a** produced helically twisted nanofibers with widths of 200–300 nm, thicknesses of 30–50 nm, and lengths of more than 50 μm (Figure 2-19c,d). The extensively entangled nanofibers with widths of 50–100 nm were formed from **4b** (Figure 2-19g,h). These flexible fibers further formed a 3D network reminiscent to fiber networks typically seen in organogels.[128,129] The author also prepared the assemblies of **3a**,**b** and **4a**,**b** from $CHCl_3$/hexane system (1.7×10^{-3} mol dm^{-3}) (Figure 2-20); the SEM measurements showed that the morphology of the assemblies were almost independent of the solvents used. The reason why **3b** and **4b** with decyloxy side chains provided narrower self-assembled clusters than **3a** and **4a** with butoxy chains, respectively, is in part the higher solubility of the former in $CHCl_3$, thus leading to slower aggregation.[130]

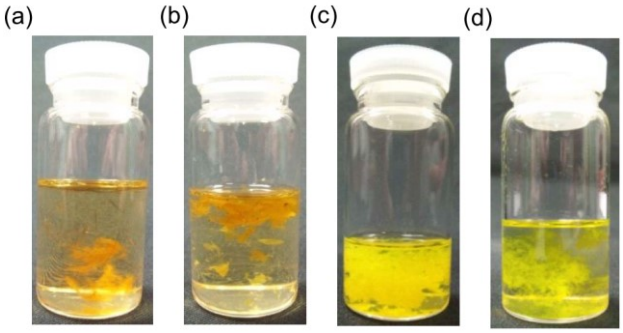

Figure 2-18. Optical photographs of the precipitate of (a) **3a**, (b) **3b**, (c) **4a**, and (d) **4b** formed in $CHCl_3$/EtOH system.

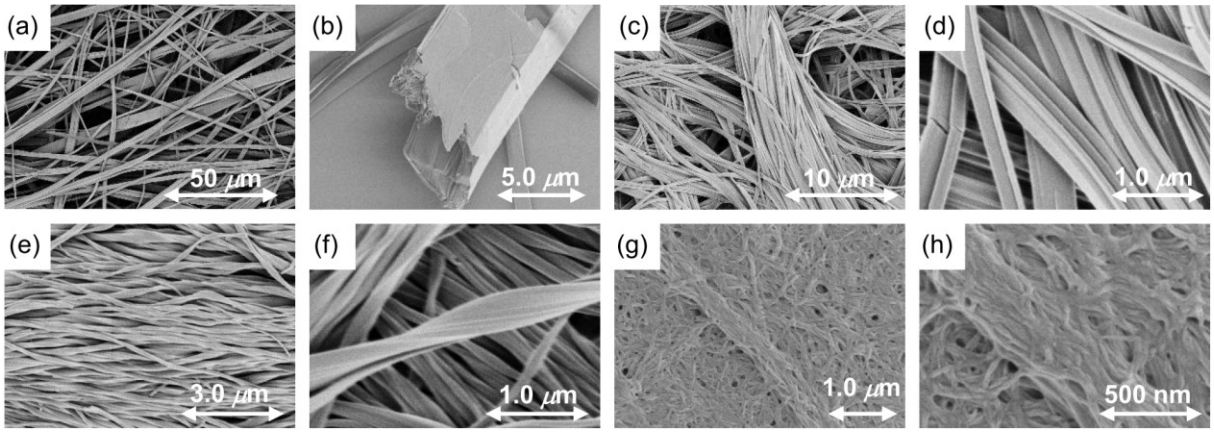

Figure 2-19. SEM images of 1D clusters of (a,b) **3a**, (c,d) **3b**, (e,f) **4a**, and (g,h) **4b** obtained from $CHCl_3$/EtOH system.

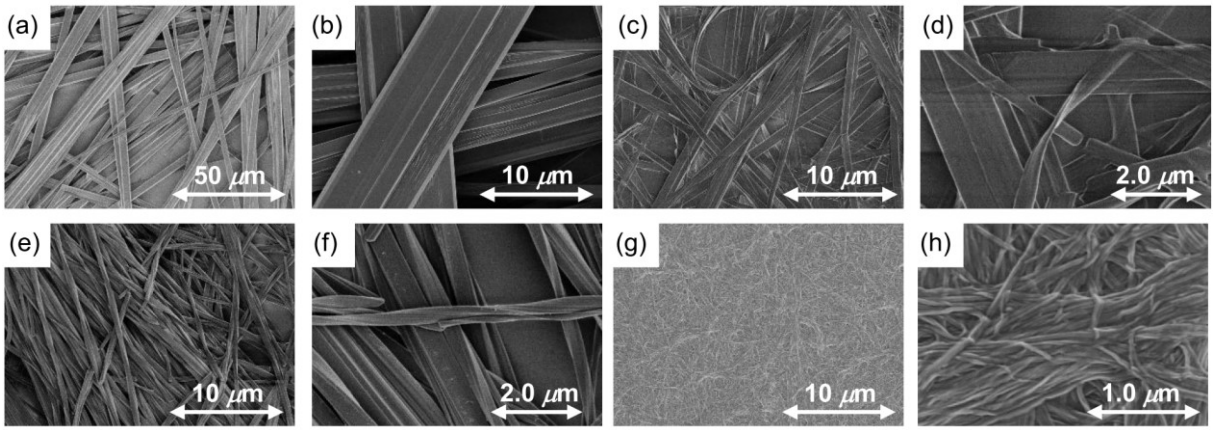

Figure 2-20. SEM images of 1D clusters of (a,b) **3a**, (c,d) **3b**, (e,f) **4a**, and (g,h) **4b** obtained from $CHCl_3$/hexane system.

The self-assembled clusters of **3a**,**b** and **4a**,**b** were further investigated by wide-angle X-ray diffraction (WAXD) measurements (Figure 2-21). Among a number of peaks present in the patterns, the peaks of interest are over approximately 2θ = 23° (*d* spacing = 3.8 Å), which corresponds to the π–π stacking distance along the growth direction of the clusters.[131,132] The author could not deduce the molecular-packing mode from the WAXD patterns; however, the effects of the topology of the DA ring and the length of the alkoxy chains on the crystallinity of the self-assembled clusters are noticeably visible, and the results are consistent with those in the SEM measurements. The diffraction pattern of assembled **3a** showed sharp, intense peaks at 22.9, 24.8, and 27.6° (*d* spacing = 3.9, 3.6, and 3.3 Å, respectively), which is indicative of high crystallinity. The assembled **3b** also exhibited well defined peaks at 23.5, 25.0, and 26.18 (*d* spacing = 3.8, 3.6, and 3.4 Å, respectively). Relative to the assembled **3a**,**b**, the WAXD patterns of the assembled **4a** exhibited broad peaks at 22.9, 23.5, 25.1, and 26.3° (*d* spacing = 3.9, 3.8, 3.6, and 3.4 Å, respectively), thus indicating the less crystalline character. The assembled **4b** showed amorphous character, and thus only one significantly broad peak was observed at 19–23° (*d* spacing = 4.5–3.8 Å). Overall, it is likely that the [12]DA ring is responsible for the high crystallinity of the clusters relative to the [18]DA ring, and the elongation of the alkoxy chains decreases the crystallinity.

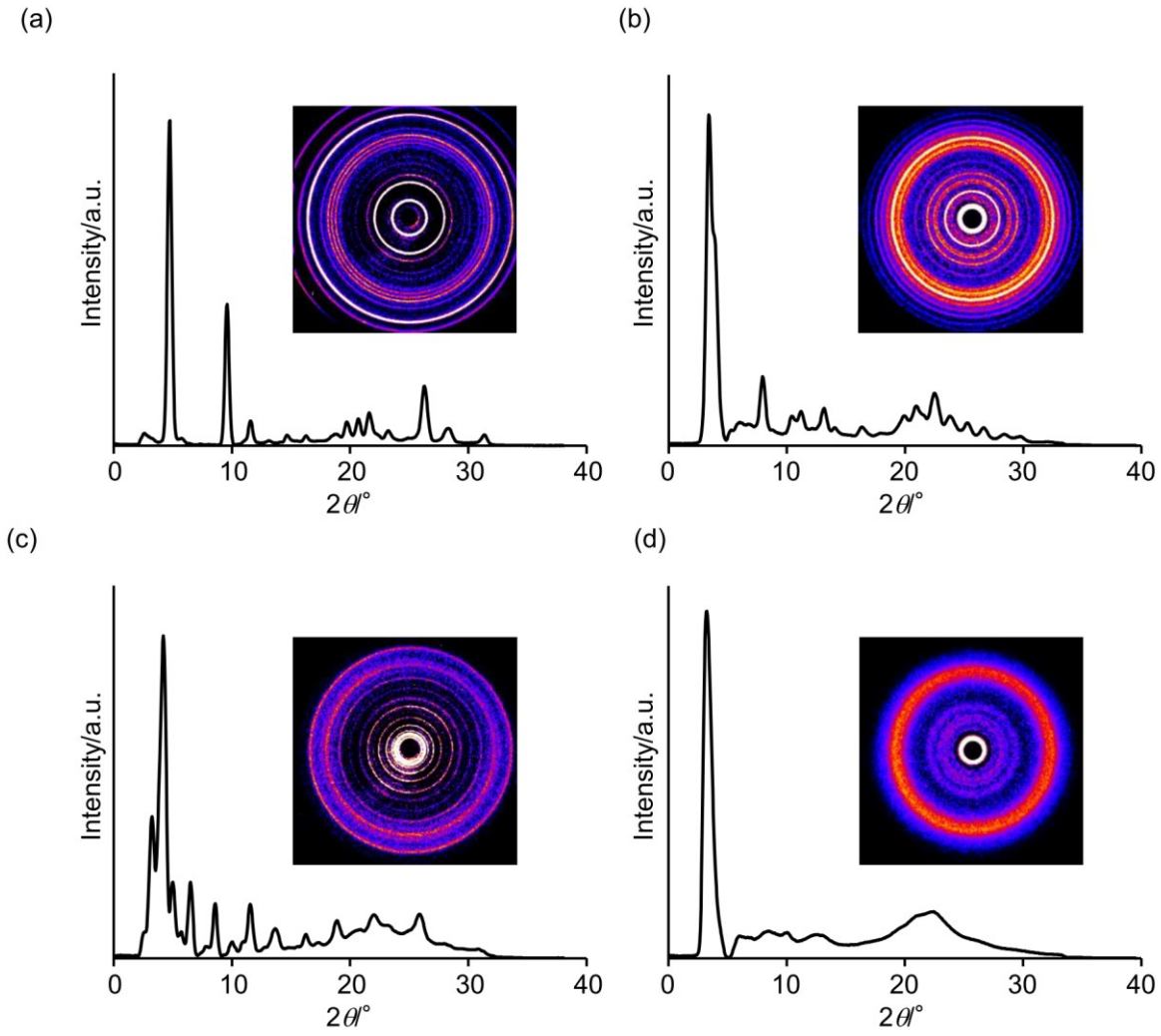

Figure 2-21. WAXD patterns of superstructures of (a) **3a**, (b) **3b**, (c) **4a**, and (d) **4b** obtained from $CHCl_3$/EtOH system at 25 °C.

Thermal behaviors of **3b** and **4b** were investigated by differential scanning calorimetry (DSC) and polarizing optical microscopy (POM) measurements. The DSC investigation of **3b** revealed two phase transitions at 111 and 165 °C on heating, thus indicating the formation of a mesophase (Figure 2-22). In POM, **3b** is an isotropic fluid above 165 °C, and the material appears completely dark under crossed polarizers. On cooling, the material becomes birefringent and a liquid-crystalline texture readily develops under crossed polarizers (Figure 2-23). The DSC trace of **4b** exhibited a single peak at 110 °C upon heating up to 170 °C. POM revealed that the material is birefringent over 110 °C, thus suggesting the formation of a liquid-crystalline phase (Figure 2-23). Shearing converts the structured

texture into an unspecific birefringent texture, which is indicative of the fluidlike nature of the material. Below 90 °C, no clear textural change is observed, and the texture is hardly damaged by shearing. In contrast to **3b** and **4b**, no phase transition was observed for **3a** and **4a** in the range 25–170 °C.

The formation of liquid crystals from **3b** and **4b** was confirmed by simultaneous variable-temperature WAXD and DSC measurements. The WAXD patterns of **3b** and **4b** recorded at approximately 130 and 25 °C, taken as representative examples, are shown in Figure 2-23. In the WAXD patterns of **3b**, most multiple peaks observed at 25 °C became significantly broadened when the temperature reached approximately 110 °C, at which point a clear endothermic peak was observed in the DSC trace. When the sample was cooled from 170 to 25 °C, the sharp peaks recovered at approximately 110 °C associated with the apparent exothermic peak in the DSC trace. Compound **4b** also showed similar WAXD profiles and DSC trace. The diffraction patterns and thermal behaviors of **3b** and **4b** were reproducible over multicycle measurements after the first heating. At approximately 130 °C, both **3b** and **4b** showed characteristic, amorphous halo peaks at approximately 19.5° (*d* spacing = 4.5 Å) for the liquid-crystalline phase, which could be attributed to the molten decyloxy chains with a liquid like conformation. The observed peaks reached over 25° corresponding to *d* spacing of approximately 3.5 Å, thus indicating that the aggregates of **3b** and **4b** are stabilized by π–π stacking interactions. On the basis of these observations, the liquid crystals from **3b** and **4b** are assumed to form in the following way: the aggregation of the molecules of **3b** and **4b** is driven by effective π–π stacking interactions of the phenanthrene-fused DA core. The flexible decyloxy side chains contribute to facilitate phase separation and lead to a liquid-crystalline mesophase. The butoxy chains in **3a** and **4a** are probably not long enough to facilitate phase separation. Unfortunately, due to the unresolved broad peaks in the small-angle region, the author cannot assign the liquid-crystalline organization of **3b** and **4b** from the WAXD measurements.

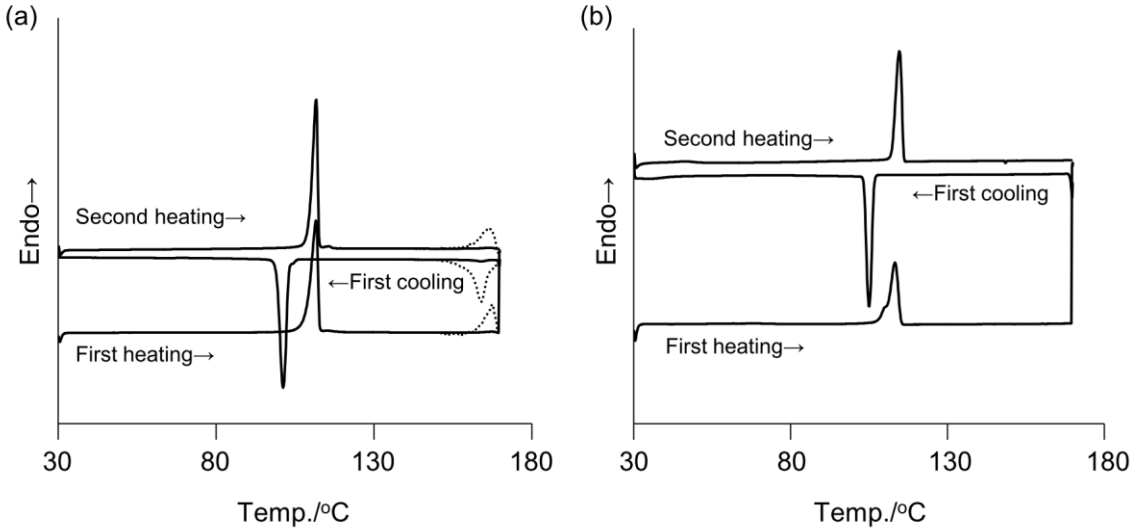

Figure 2-22. DSC measurement results of (a) **3b** and (b) **4b**.

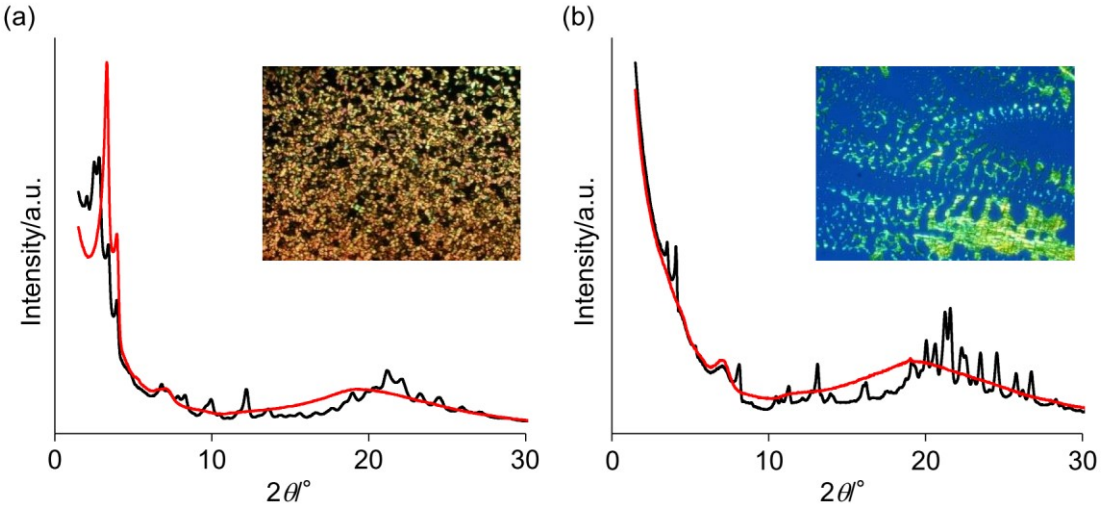

Figure 2-23. POM and WAXD patterns of (a) **3b** and (b) **4b** at approximately 130 and 25 °C (red and black lines, respectively) on cooling.

2-8. Conclusions

The author has synthesized tetraalkoxyphenanthrene-fused DAs **3a**,**b**, **4a**,**b**, and **5a** by using Cu-mediated or Pd-catalyzed oxidative cyclization reactions as key steps. By investigating the properties of **3a**,**b**, **4a**,**b**, and **5a** together with DBAs **1a** and **2a**, it was found that the annulation at the 9,10-positions of phenanthrene into a DA ring enhances the tropicities and decreases the HOMO–LUMO gaps of the molecules relative to the benzannulation. A noticeable degree of antiaromaticity of **3a**,**b** was demonstrated based on spectroscopic, electrochemical, and computational data. In sharp contrast to DBAs **1a** and **2a**, the phenanthrene-fused DAs **3a**,**b** and **4a**,**b** showed self-association properties in solution through effective π–π stacking interactions as a result of their extended π-surfaces. Both **3a**,**b** and **4a**,**b** produced 1D self-assembled clusters with high aspect ratios, which differed in the morphology and crystallinity depending on the topology of the DA ring and the chain length appended to the phenanthrene moieties. The formation of liquid crystals by self-assembling **3b** and **4b** has been also demonstrated. To the best of our knowledge, there has been no example of liquid crystals that have a [12]- or [18]DA derivatives possessing butadiyne linkages.

2-9. Experimental Section

Preparation of 12a: To a suspension of **11a** (1.00 g, 4.50 mmol), urea (257 mg, 4.28 mmol), and $AlCl_3$ (900 mg, 6.75 mmol) in CH_2Cl_2 (10 mL) was added dropwise oxalyl chloride (0.19 mL, 2.25 mmol) at 0 °C under argon atmosphere. After the mixture was stirred at room temperature for 18 h, the resulting brown mixture was poured into H_2O. The organic phase was separated, and the aqueous phase was extracted with CH_2Cl_2. The combined organic phase was washed with aqueous $NaHCO_3$, dried over anhydrous $MgSO_4$, and evaporated under reduced pressure. The residue was purified by washing with MeOH and subsequent silica gel column chromatography (CH_2Cl_2) to afford **12a** (390 mg, 0.78 mmol, 35%) as white

solids, which was fully characterized by the ^{1}H NMR spectroscopy.[133] ^{1}H NMR ($CDCl_3$, 300 MHz): δ 0.98 (t, 6H, J = 7.4 Hz), 0.99 (t, 6H, J = 7.4 Hz) 1.46–1.58 (m, 8H), 1.78–1.88 (m, 8H), 4.06 (t, 4H, J = 6.5 Hz), 4.07 (t, 4H, J = 6.5 Hz), 6.85 (d, 2H, J = 8.4 Hz), 7.43 (dd, 2H, J = 1.9, 8.4 Hz), 7.57 (d, 2H, J = 1.9 Hz).

Preparation of 12b: Compound **11b** (500 mg, 1.28 mmol) was allowed to react with oxalyl chloride (0.055 mL, 0.64 mmol) in the presence of urea (73 mg, 1.21 mmol) and $AlCl_3$ (257 mg, 1.93 mmol) in CH_2Cl_2 (2 mL) according to the synthetic procedure of **12a**. The crude material was purified by washing with MeOH and subsequent silica gel column chromatography (CH_2Cl_2) to afford **12b** (370 mg, 0.44 mmol, 69%) as white solids, which was fully characterized by the ^{1}H NMR spectroscopy.[103] ^{1}H NMR ($CDCl_3$, 300 MHz): δ 0.88 (t, 12H, J = 6.0 Hz), 1.27–1.51 (m, 56H), 1.84 (qui, 8H, J = 6.9 Hz), 4.06 (t, 8H, J = 6.9 Hz), 6.84 (d, 2H, J = 8.3 Hz), 7.43 (dd, 2H, J = 1.9, 8.3 Hz), 7.57 (d, 2H, J = 1.9 Hz).

Preparation of 13a: To a solution of **12a** (3.00 g, 6.00 mmol) and $BF_3{\cdot}Et_2O$ (1.68 mL, 13.5 mmol) in CH_2Cl_2 (100 mL) was added VOF_3 (2.57 g, 20.7 mmol) at room temperature under argon atmosphere. After the mixture was stirred for 2 h, aqueous citric acid (3.5%, 100 mL) was added to the mixture. The organic phase was separated, and the aqueous phase was extracted with CH_2Cl_2. The combined organic phase was washed with H_2O, dried over anhydrous $MgSO_4$, and evaporated under reduced pressure. The residue was purified by silica gel column chromatography (toluene/EtOAc, 10:1) to afford **13a** (2.57 g, 5.23 mmol, 87%) as red solids. M.p. 123–127 °C; ^{1}H NMR ($CDCl_3$, 300 MHz): δ 1.00 (t, 6H, J = 7.4 Hz), 1.03 (t, 6H, J = 7.4 Hz), 1.48–1.60 (m, 8H), 1.82–1.92 (m, 8H), 4.09 (t, 4H, J = 6.6 Hz), 4.20 (t, 4H, J = 6.5 Hz), 7.12 (s, 2H), 7.55 (s, 2H); ^{13}C NMR ($CDCl_3$, 125 MHz): δ 13.94, 19.16, 19.25, 31.11, 31.13, 68.55, 68.92, 106.34, 112.37, 124.02, 130.77, 148.97, 155.29, 178.85 (14 signals out of 15 expected); UV–vis (CH_2Cl_2): λ_{max}^{abs} (relative intensity) = 519 (0.01), 484 (0.01), 365 (0.65), 299 (1.0) nm; HR-FAB-MS (NBA, positive): m/z calcd for $C_{30}H_{40}O_6^+$ 496.2825, found 496.2805 $[M]^+$.

Preparation of 13b: Compound **12b** (3.00 g, 6.00 mmol) was oxidized with VOF_3 (2.57 g, 20.7 mmol) in the presence of $BF_3{\cdot}Et_2O$ (1.68 mL, 13.5 mmol) in CH_2Cl_2 (100 mL) according to the synthetic procedure of **13a**. The crude material was purified by silica gel column chromatography (toluene/EtOAc, 10:1) to afford **13b** (2.57 g, 5.23 mmol, 87%) as deeply red solids, which was fully characterized by the ^{1}H NMR spectroscopy.[103] ^{1}H NMR ($CDCl_3$, 300 MHz): δ 0.88 (t, 12H, J = 6.8 Hz), 1.28–1.58 (m, 56H), 1.80–1.95 (m, 8H), 4.19 (t, 4H, J = 6.6 Hz), 4.19 (t, 4H, J = 6.5 Hz), 7.10 (s, 2H), 7.54 (s, 2H).

Preparation of 14a: A solution of *n*-BuLi in hexane (2.64 mol dm^{-3}, 1.40 mL, 3.69 mmol) was added dropwise to a solution of TMSA (0.58 mL, 4.00 mmol) in THF (10 mL) at −78 °C under argon atmosphere. After stirring at −78 °C for 30 min, a solution of **13a** (500 mg, 1.00 mmol) in THF (5 mL) was added dropwise to the reaction mixture. After the mixture was stirred at room temperature for 18 h, the resulting mixture was diluted with saturated aqueous NH_4Cl. The organic phase was separated, and the aqueous phase was extracted with $CHCl_3$. The combined organic phase was washed with aqueous NH_4Cl, dried over anhydrous $MgSO_4$, and evaporated under reduced pressure. The residue was purified by column chromatography on silica gel (toluene/EtOAc, 10:1 to 5:1) to give the crude diol (439 mg).

A mixture of the crude diol and K_2CO_3 (300 mg, 2.17 mmol) in THF/MeOH (1:1, 10 mL) was stirred at room temperature for 2 h. The resulting mixture was diluted with THF, and the insoluble material was removed by filtration. The filtrate was diluted with CH_2Cl_2, washed with H_2O, dried over anhydrous $MgSO_4$, and evaporated under reduced pressure. The residue was purified by column chromatography on silica gel (toluene/EtOAc, 20:3) to afford **14a** (443 mg, 0.80 mmol, 80%) as a yellow oil. ^{1}H NMR ($CDCl_3$, 300 MHz): δ = 1.00 (t, 12H, J = 7.3 Hz), 1.47–1.60 (m, 8H), 1.79–1.89 (m, 8H), 2.51 (s, 2H), 3.02 (s, 2H), 4.10 (t, 8H, J = 6.5 Hz), 7.15 (s, 2H), 7.39 s, 2H); ^{13}C NMR ($CDCl_3$, 75 MHz): δ = 14.06, 19.41, 31.48, 31.56, 69.06, 69.64, 74.94, 75.67, 82.30, 110.15, 111.47, 124.72, 127.71, 149.32,

149.93 (15 signals out of 17 expected); UV–vis (CH_2Cl_2): λ_{max}^{abs} = 318 nm; HR-FAB-MS (NBA, positive): *m/z* calcd for $C_{34}H_{44}O_6^+$: 548.3138; found: 548.3136 $[M]^+$.

Preparation of 14b: A solution of *n*-BuLi in hexane (2.64 mol dm^{-3}, 0.85 mL, 2.22 mmol) was added dropwise to a solution of TMSA (0.35 mL, 2.40 mmol) in THF (20 mL) at −78 °C under argon atmosphere. After the mixture had been stirred at −78 °C for 30 min, a solution of **13b** (500 mg, 0.60 mmol) in THF (5 mL) was added dropwise. The mixture was then stirred at room temperature for 18 h, and subsequently the resulting mixture was diluted with saturated aqueous NH_4Cl. The organic phase was separated, and the aqueous phase was extracted with $CHCl_3$. The combined organic phase was washed with aqueous NH_4Cl, dried over anhydrous $MgSO_4$, and evaporated under reduced pressure. The residue was purified by column chromatography on silica gel (toluene/EtOAc, 10:1 to 5:1) to give the crude diol (439 mg).

A mixture of the crude diol and K_2CO_3 (102 mg, 0.74 mmol) in THF/MeOH (1:1, 10 mL) was stirred at room temperature for 2 h, the resulting mixture was diluted with THF, and the insoluble material was removed by filtration. The filtrate was diluted with CH_2Cl_2, washed with H_2O, dried over anhydrous $MgSO_4$, and evaporated under reduced pressure. The residue was purified by column chromatography on silica gel (toluene/EtOAc, 10:1) to afford **14b** (369 mg, 0.41 mmol, 70%) as a yellow solid. M.p. 57–59 °C; ^{1}H NMR ($CDCl_3$, 300 MHz): δ = 0.89 (t, 12H, *J* = 6.6 Hz), 1.23–1.58 (m, 56H), 1.85 (qui, 8H, *J* = 6.8 Hz), 2.51 (s, 2H), 2.97 (s, 2H), 4.08 (t, 8H, *J* = 6.8 Hz), 7.14 (s, 2H), 7.38 (s, 2H); ^{13}C NMR ($CDCl_3$, 125 MHz): δ = 14.15, 22.73, 26.11, 26.13, 29.33, 29.42, 29.44, 29.50, 29.53, 29.57, 29.66, 29.71, 31.94, 31.96, 69.16, 69.83, 74.64, 75.52, 82.50, 110.03, 111.24, 124.59, 127.82, 149.12, 149.63 (25 signals out of 29 expected); UV–vis (CH_2Cl_2): λ_{max}^{abs} = 318 nm; HR-FAB-MS (NBA, positive): *m/z* calcd for $C_{56}H_{92}O_6^+$: 884.6894; found: 884.6885 $[M]^+$.

Preparation of 3a and 4a (Cu-mediated method): A suspension of **14a** (100 mg, 0.18 mmol) and $SnCl_2 \cdot 2H_2O$ (205 mg, 0.91 mmol) in THF (10 mL) was stirred at 60 °C for 13 h

under argon atmosphere. After the reaction mixture was concentrated under reduced pressure to approximately 1 mL, the resulting mixture was purified by column chromatography on silica gel (CH_2Cl_2) to give a colorless solution of aromatized diyne **15a**. The solvent was replaced with *o*-DCB by evaporation followed by immediate dilution, and the solution was used in the next reaction immediately.

CuCl (29 mg, 0.29 mmol) and TMEDA (0.7 mL, 4.9 mmol) were added to a solution of **15a** in *o*-DCB (130 mL). The resulting mixture was stirred at 50 °C for 11 h under supply of air. After the solvent was removed under reduced pressure, the residue was suspended in $CHCl_3$, and the resulting solution was washed with H_2O. The organic phase was dried over anhydrous $MgSO_4$ and evaporated under reduced pressure. The residue was suspended in CH_2Cl_2, and insoluble material was collected by filtration, which was purified by column chromatography on silica gel ($CHCl_3$) to afford **3a** (32 mg, 0.031 mmol, 33%) as a red solid. The filtrate was concentrated under reduced pressure, and the residue was purified by column chromatography on silica gel (hexane/$CHCl_3$, 1:2) and reprecipitation from CH_2Cl_2/hexane to afford **4a** (7 mg, 0.0046 mmol, 7%) as a yellow solid. **3a**: M.p. > 250 °C; ^{1}H NMR ($CDCl_3$, 500 MHz, 1.28×10^{-3} mol dm^{-3}): δ = 1.03 (t, 24H, J = 7.3 Hz), 1.52–1.58 (m, 16H), 1.86–1.92 (m, 16H), 4.08 (t, 8H, J = 6.4 Hz), 4.16 (t, 8H, J = 6.4 Hz), 6.99 (s, 4H), 7.50 (s, 4H); ^{13}C NMR was not available due to the low solubility of **3a**; UV–vis ($CHCl_3$): λ_{max}^{abs} (ε) = 559 (1480), 470 (25500), 402 (14200), 381 (13400), 347 (85400), 332 (60500), 306 (80000), 274 nm (86600 dm^3 mol^{-1} cm^{-1}); HR-FAB-MS (NBA, positive): *m/z* calcd for $C_{68}H_{80}O_8^+$: 1024.5853; found: 1024.5859 $[M]^+$. **4a**: M.p. > 250 °C; ^{1}H NMR ($CDCl_3$, 500 MHz, 1.45×10^{-2} mol dm^{-3}): δ = 1.08 (t, 36H, J = 7.5 Hz), 1.62–1.71 (m, 24H), 1.95–2.01 (m, 24H), 4.30 (t, 12H, J = 6.4 Hz), 4.38 (t, 12H, J = 6.4 Hz), 7.82 (s, 6H), 8.07 (s, 6H); ^{13}C NMR ($CDCl_3$, 125 MHz): δ = 14.14, 14.23, 19.52, 19.79, 31.46, 31.66, 68.79, 69.22, 82.47, 83.21, 105.18, 109.45, 120.81, 124.66, 126.07, 149.78, 150.84; UV–vis ($CHCl_3$): λ_{max}^{abs} (ε) = 457 (67100), 440 (53200), 423 (62500), 404 (60100), 274 nm (84500 dm^3 mol^{-1} cm^{-1}); HR-FAB-MS

(NBA, positive): *m/z* calcd for $C_{102}H_{120}O_{12}^{+}$: 1536.8780; found: 1536.8777 $[M]^{+}$.

Preparation of 4a and 5a (Pd-catalyzed method): A suspension of **14a** (443 mg, 0.81 mmol) and $SnCl_2 \cdot 2H_2O$ (909 mg, 4.03 mmol) in THF (10 mL) was stirred at 60 °C for 13 h under argon atmosphere. After the reaction mixture was concentrated under reduced pressure to approximately 1 mL, the resulting mixture was purified by column chromatography on silica gel (CH_2Cl_2) to give a colorless solution of aromatized diyne **15a**. The solvent was replaced with THF by evaporation followed by immediate dilution, and the solution was used in the next reaction immediately.

Et_3N (40 mL) was added to a solution of **15a** in THF (120 mL), and the resulting solution was bubbled with argon with stirring for 30 min. $[PdCl_2(PPh_3)_2]$ (56 mg, 0.081 mmol), CuI (30 mg, 0.16 mmol), and *p*-benzoquinone (88 mg, 0.81 mmol) were added to the solution. After the reaction mixture had been stirred at room temperature for 18 h, the suspension was filtered through a bed of silica gel, and the filtrate was evaporated under reduced pressure. The residue was diluted with CH_2Cl_2, washed with aqueous NH_4Cl, dried over anhydrous $MgSO_4$, and evaporated under reduced pressure. The residue was purified by column chromatography on silica gel ($CHCl_3$) and recycling GPC ($CHCl_3$) to afford **4a** (71 mg, 0.046 mmol, 17%) and **5a** (38 mg, 0.019 mmol, 9%) as yellow solids. **5a**: M.p. > 250 °C; ^{1}H NMR ($CDCl_3$, 600 MHz): δ = 0.98 (t, 24H, J = 7.4 Hz), 1.04 (t, 24H, J = 7.4 Hz), 1.52–1.63 (m, 32H), 1.88–1.96 (m, 32H), 4.23 (t, 32H, J = 6.7 Hz), 7.70 (s, 8H), 7.82 (s, 8H); ^{13}C NMR ($CDCl_3$, 150 MHz): δ = 14.11, 19.49, 31.27, 31.41, 68.97, 69.23, 81.78, 82.86, 105.07, 108.90, 121.44, 124.65, 126.11, 149.81, 150.63 (15 signals out of 17 expected); UV–vis ($CHCl_3$): λ_{max}^{abs} (ε) = 427 (84600), 390 (87600), 284 nm (246000 dm^3 mol^{-1} cm^{-1}); MALDI-TOF-MS (dith, positive): *m/z* 2050.2 $[M+H]^{+}$; elemental analysis calcd (%) for $C_{136}H_{160}O_{16} \cdot 0.3CHCl_3$: C 78.45, H 7.74; found: C 78.46, H 8.01.

Preparation of 3b (Cu-mediated method): A suspension of **14b** (157 mg, 0.18 mmol) and $SnCl_2 \cdot 2H_2O$ (193 mg, 0.82 mmol) in THF (10 mL) was stirred at 60 °C for 13 h under argon.

After the reaction mixture was concentrated under reduced pressure to approximately 1 mL, the resulting mixture was purified by column chromatography on silica gel (CH_2Cl_2) to give a colorless solution of aromatized diyne **15b**. The solvent was replaced with *o*-DCB by evaporation followed by immediate dilution, and the solution was used immediately.

CuCl (48 mg, 0.36 mmol) and TMEDA (0.43 mL, 3.0 mmol) were added to a solution of **15b** in *o*-DCB (40 mL), and the resulting mixture was stirred at 50 °C for 11 h under supply of air. After the solvent was removed under reduced pressure, the residue was suspended in $CHCl_3$, and the resulting mixture was washed with H_2O. The organic phase was dried over anhydrous $MgSO_4$ and evaporated under reduced pressure. The residue was suspended in CH_2Cl_2, and the insoluble material was collected by filtration, which was subjected to column chromatography on silica gel ($CHCl_3$) to afford **3b** (56 mg, 0.032 mmol, 37%) as a red solid. M.p. 167–168 °C; ^{1}H NMR ($CDCl_3$, 500 MHz, 1.51 × 10^{-3} mol dm^{-3}): δ = 0.87–0.89 (m, 24H), 1.29–1.40 (m, 96H), 1.52–1.56 (m, 16H), 1.87–1.94 (m, 16H), 4.06 (t, 8H, J = 6.4 Hz), 4.15 (t, 8H, J = 6.4 Hz), 6.98 (s, 4H), 7.50 (s, 4H); ^{13}C NMR ($CDCl_3$, 125 MHz, 40 °C): δ = 14.22, 14.23, 22.86, 26.40, 29.53, 29.57, 29.62, 29.77, 29.83, 29.88, 29.90, 32.12, 32.13,68.93, 69.52, 88.65, 93.96, 105.00, 108.32, 124.59, 124.69, 127.04, 149.72, 150.57 (24 signals out of 29 expected); UV–vis ($CHCl_3$): λ_{max}^{abs} (ε) = 559 (1600), 470 (27100), 403 (14800), 381 (13700), 347 (89400), 332 (63000), 306 (82900), 274 nm (89500 dm^3 mol^{-1} cm^{-1}); MALDI-TOF-MS (dith, positive): 1698.0 $[M+H]^+$; elemental analysis calcd (%) for $C_{116}H_{176}O_8 \cdot 1.7\ CHCl_3$: C 74.34, H 9.41; found: C 74.37, H 9.67. The author could not obtain satisfactory elemental analysis for this compound because this compound probably contains solvent molecules in the solid state. The author believe that the compound is undoubtedly pure on the basis of the ^{1}H NMR spectrum.

Preparation of 4b (Pd-catalyzed method): A suspension of **14b** (326 mg, 0.37 mmol) and $SnCl_2 \cdot 2H_2O$ (415 mg, 1.84 mmol) in THF (10 mL) was stirred at 60 °C for 13 h under argon atmosphere. After the reaction mixture was concentrated under reduced pressure to

approximately 1 mL, the resulting mixture was purified by column chromatography on silica gel (CH_2Cl_2) to give a colorless solution of aromatized diyne **15b**. The solvent was replaced with THF by evaporation followed by dilution, and the solution was used in the next reaction. Et_3N (30 mL) was added to a solution of **15b** in THF (30 mL), and the resulting solution was bubbled with an argon with stirring for 30 min. $[PdCl_2(PPh_3)_2]$ (26 mg, 0.037 mmol), CuI (14 mg, 0.074 mmol), and *p*-benzoquinone (36 mg, 0.33 mmol) were added to the solution. After the mixture had been stirred at room temperature for two days, the suspension was filtered through a bed of silica gel, and the filtrate was evaporated under reduced pressure. The residue was diluted with $CHCl_3$, washed with aqueous NH_4Cl, dried over anhydrous $MgSO_4$, and evaporated under reduced pressure. The residue was purified by column chromatography on silica gel (hexane/$CHCl_3$, 1:2), reprecipitation from $CHCl_3$/hexane, and recycling GPC ($CHCl_3$) to afford **4b** (72 mg, 0.028 mmol, 23%) as a yellow solid. M.p. > 250 °C; ^{1}H NMR ($CDCl_3$, 500 MHz, 6.05 × 10^{-3} mol dm^{-3}): δ = 0.85 (t, 18H, J = 6.8 Hz), 0.89 (t, 18H, J = 6.8 Hz), 1.24–1.45 (m, 144H), 1.58–1.68 (m, 24H), 1.95–2.02 (m, 24H), 4.29 (t, 12H, J = 6.1 Hz), 4.38 (t, 12H, J = 6.1 Hz), 7.83 (s, 6H), 8.08 (s, 6H); ^{13}C NMR (CDCl3, 125 MHz, 40 °C): δ = 14.20, 14.22, 22.84, 22.86, 26.43, 26.76, 29.56, 29.58, 29.66, 29.76, 29.83, 29.89, 29.91, 29.93, 29.99, 32.12, 69.16, 69.80, 82.55, 83.36, 105.75, 109.74, 120.96, 124.77, 126.26, 150.01, 151.00 (27 signals out of 29 expected); UV–vis ($CHCl_3$): λ_{max}^{abs} (ε) = 457 (115000), 440 (90000), 424 (105200), 404 (101200), 273 nm (140600 dm^3 mol^{-1} cm^{-1}); MALDI-TOF-MS (dith, positive): *m/z* 2547.1 $[M+H]^+$; elemental analysis calcd (%) for $C_{174}H_{264}O_{12}\cdot 0.25\ CHCl_3$: C 81.18, H 10.33; found: C 81.18, 10.44.

Preparation of 16a: To a solution of TMSA (0.11 mL, 0.77 mmol) in THF (20 mL) was added dropwise a *n*-BuLi hexane solution (2.64 mol dm^{-3}, 0.28 mL, 0.73 mmol) at −78 °C under argon atmosphere. After stirring at −78 °C for 30 min, a solution of **13a** (50 mg, 0.10 mmol) in THF (5 mL) was added dropwise to the mixture. After the mixture was stirred at room temperature for 10 min, the resulting mixture was diluted with saturated aqueous NH_4Cl.

The organic phase was separated, and the aqueous phase was extracted with CH_2Cl_2. The combined organic phase was washed with aqueous NH_4Cl, dried over anhydrous $MgSO_4$, and evaporated under reduced pressure. The residue was purified by silica gel column chromatography (hexane/CH_2Cl_2, 1:1 to 0:1) to afford **16a** (45 mg, 0.06 mmol, 65%) as yellow solids. M.p. 105–107 °C; ^{1}H NMR ($CDCl_3$, 300 MHz): δ 0.21 (s, 18H), 0.99 (t, 12H, J = 7.4 Hz), 1.48–1.56 (m, 8H), 1.80–1.87 (m, 8H), 2.82 (s, 2H), 4.09 (t, 8H, J = 5.9 Hz), 7.15 (s, 2H), 7.48 (s, 2H); ^{13}C NMR ($CDCl_3$, 75 MHz): δ −0.04, 13.99, 14.02, 19.37, 31.42, 31.52, 68.91, 69.76, 75.88, 93.30, 104.22, 110.32, 113.95, 124.93, 126.33, 148.96, 149.97 (17 signals out of 18 expected); UV–vis (CH_2Cl_2): λ_{max}^{abs} = 318 nm; HR-FAB-MS (NBA, positive): *m*/*z* calcd for $C_{40}H_{60}O_6Si_2^+$ 692.3928, found 692.3923 $[M]^+$.

Preparation of 17a: A suspension of **16** (12 mg, 0.018 mmol) and $SnCl_2 \cdot 2H_2O$ (25 mg, 0.11 mmol) in THF (1 0 mL) was stirred at 60 °C for 13 h under argon atmosphere. After brine was added into the mixture, the organic phase was separated, and the aqueous phase was extracted with CH_2Cl_2. The combined organic phase was dried over anhydrous $MgSO_4$ and evaporated under reduced pressure. The residue was purified by silica gel column chromatography (CH_2Cl_2) to afford **17a** (6 mg, 0.009 mmol, 51%) as yellow solids. M.p. 123–127 °C; ^{1}H NMR ($CDCl_3$, 300 MHz): δ 0.37 (s, 18H), 1.03 (t, 6H, J = 7.4 Hz), 1.04 (t, 6H, J = 7.3 Hz), 1.53–1.63 (m, 8H), 1.90–1.95 (m, 8H), 4.19 (t, 4H, J = 6.6 Hz), 4.23 (t, 4H, J = 6.6 Hz), 7.73 (s, 2H), 7.80 (s, 2H); ^{13}C NMR ($CDCl_3$, 150 MHz): δ 0.38, 14.08, 14.12, 19.47, 31.25, 31.43, 68.57, 69.34, 103.17, 103.38, 105.22, 109.04, 120.82, 124.23, 125.68, 149.37, 150.06 (17 signals out of 18 expected); UV–vis (CH_2Cl_2): λ_{max}^{abs} (relative intensity) = 396 (0.10), 359 (0.37), 344 (0.30), 302 (0.64), 296 (0.63), 266 (1.00) nm; HR-FAB-MS (NBA, positive) *m/z* calcd for $C_{40}H_{58}O_4Si_2^+$ 658.3874, found 658.3881 $[M]^+$.

Preparation of 1a and 2a: To a solution of **19** (350 mg, 0.845 mmol) in THF/MeOH (1:1, 10 mL) was added K_2CO_3 (467 mg, 3.38 mmol). After the mixture was stirred at room temperature for 30 min, H_2O was added into the mixture. The organic phase was separated,

and the aqueous phase was extracted with Et_2O. The combined organic phase was washed with aqueous NH_4Cl, dried over anhydrous $MgSO_4$, and evaporated under reduced pressure. The residue was purified by silica gel column chromatography ($CHCl_3$) to give desilylated diyne **20**, which was used in the next cyclization reaction without further purification due to the instability.

A mixture of **20**, CuCl (100 mg, 1.01 mmol), and TMEDA (3.0 mL, 20.2 mmol) in *o*-DCB (170 mL) was stirred at 50 °C for 11 h under air supply. After the solvent was removed under reduced pressure, the residue was dissolved in $CHCl_3$. The resulting solution was washed with H_2O, dried over anhydrous $MgSO_4$, and evaporated under reduced pressure. The residue was chromatographed over silica gel (hexane/$CHCl_3$, 1:1) to afford **1a**[50] (93 mg, 0.173 mmol, 41%) as yellow solids and crude **2a**, which was further purified by reprecipitation from $CHCl_3$/MeOH to afford pure **2a** (30 mg, 0.04 mmol, 13%) as yellow solids. **2a**: M.p. 283 °C (decomp.); ^{1}H NMR ($CDCl_3$, 500 MHz): δ 0.99 (t, 18H, J = 7.3 Hz), 1.47–1.54 (m, 12H), 1.83 (tt, 12H, J = 6.8 Hz), 4.03 (t, 12H, J = 6.8 Hz), 7.10 (s, 6H); ^{13}C NMR ($CDCl_3$, 125 MHz): δ 13.97, 19.30, 31.10, 69.00, 77.05, 81.05, 115.89, 118.38, 149.78; UV–vis ($CHCl_3$): λ_{max}^{abs} (ε) = 396 (37100), 386 (34500), 353 (178300), 330 (76900), 292 (56300), 275 nm (35500 dm^3 mol^{-1} cm^{-1}); MALDI-TOF-MS (dith, positive): m/z 805.36 $[M+H]^+$; Elemental analysis calcd (%) for $C_{54}H_{60}O_6 \cdot 0.18CHCl_3$: C 78.73, H, 7.33, found: C 78.76, H 7.03.

X-ray crystal structure analysis of 3a: Crystal data at −180 °C for $C_{68}H_{80}O_8$, M_r = 1025.38, Triclinic, space group P-1, D_{calcd} = 1.211 g cm^{-3}, Z = 1, a = 5.063(3) Å, b = 15.140(11) Å, c = 18.661(16) Å, α = 92.93(4)°, β = 96.93(5)°, γ = 97.28(4)°, V = 1405.3(18) Å^3; Mo-$K\alpha$ radiation, λ = 0.71075, μ = 0.776 cm^{-1}. A red crystal (linear dimensions *ca.* 0.38 × 0.02 × 0.01 mm) was obtained from $CHCl_3$ at 25 °C. Numbers of measured and unique reflections were 13672 and 4784, respectively (R_{int} = 0.152). Final $R(F)$ = 0.121, $wR(F^2)$ = 0.206 for

343 parameters and 4784 reflections with $I > 2\sigma(I)$ (corresponding R values are 0.344 for all data). CCDC-892383 contains the supplementary crystallographic data.

Chapter 3. Hexadecadehydrodibenzo[20]-, Tetracosadehydrotribenzo[30]-, and Dotriacontadehydrotetrabenzo[40]annulenes: Syntheses, Characterizations, Electronic Properties, and Self-associations

3-1. Introduction

Acetylenic macrocycles, particularly dehydro[*n*]annulenes ([*n*]DAs) and dehydrobenzo[*n*]annulenes ([*n*]DBAs), have received long-lasting attention in not only the basic aspect of aromaticity/antiaromaticity but also materials science because of their particularly interesting optoelectronic and self-assembling properties as described in Chapter 1. Because the Cu-mediated homocoupling reactions of ene-diynes or diethynylbenzenes, which are available with relative ease, have been well established, a variety of [*n*]DAs and [*n*]DBAs that consist of alkene or benzene moieties, respectively, and butadiyne linkages at the unsaturated bond were synthesized, including [12]DBA **1b**,[134–136] [18]DBA **2b**,[21] and their derivatives (Figure 3-1). Moreover, advances in the field of Pd-catalyzed alkyne cross-coupling reactions have brought about the synthesis of related DBAs with more sophisticated functionality and the construction of larger and more complex DBA systems.[21,40,62]

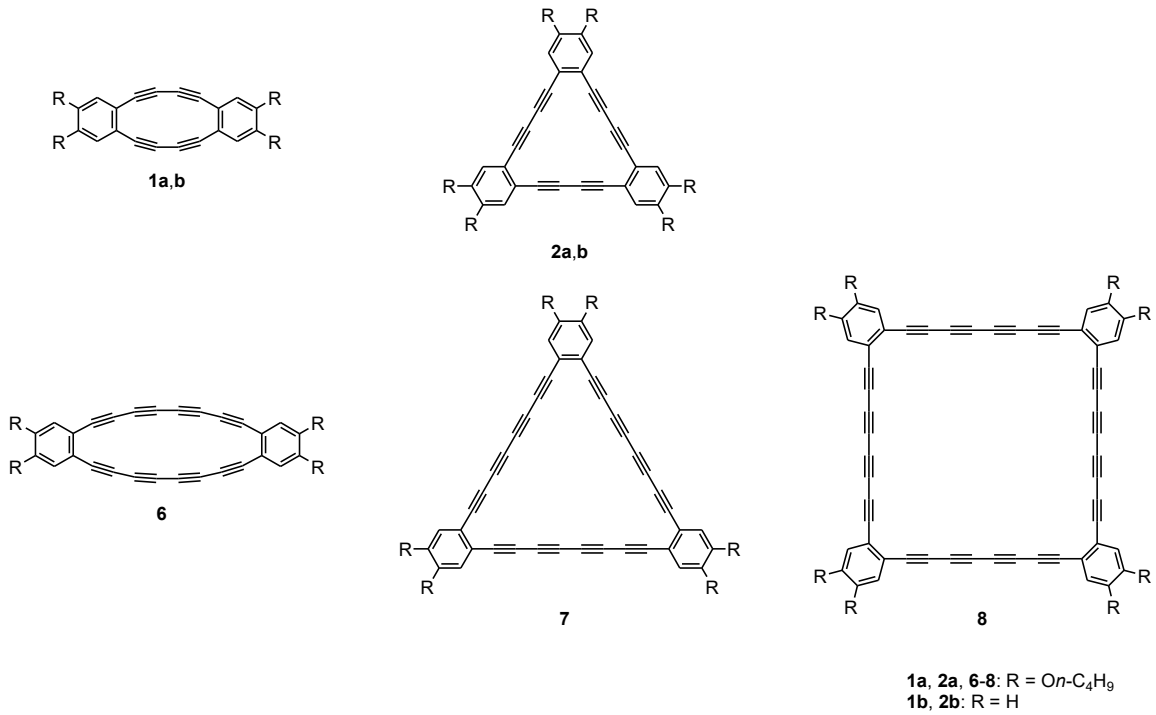

Figure 3-1. Structures of [12]- and [18]DBAs **1a**,**b** and **2a**,**b** possessing butadiyne linkages and [20]-, [30]-, and [40]DBAs **6**–**8** possessing octatetrayne linkages.

The incorporation of oligoyne linkages that are longer than butadiyne linkages into DA and DBA systems would allow us to obtain valuable insight into relevant structure–property relationships, namely, the effects of the ring expansion on the stability, tropicity, and electronic properties. However, examples of [*n*]DAs and [*n*]DBAs possessing oligoyne linkages are quite limited to date, and a summary of those in particular resulting from the groups of Haley,[72,137,138] Tobe,[110,139] and Diederich[62] is included in Figure 3-2. One of the reasons for the lack of [*n*]DAs and [*n*]DBAs possessing oligoyne linkages may be that acetylenic compounds become unstable with an increasing number of conjugated C≡C–C bonds.[21,140–144] In Chapter 3, the author describes the syntheses, characterizations, and properties of hitherto unknown [20]-, [30]-, and [40]DBAs **6**–**8** possessing octatetrayne linkages. By comparing the properties of **6**–**8** with those of [12]DBA **1a** and [18]DBA **2a**, the elucidation of the relationship between the ring size and the properties in the present DBA systems was focused on.

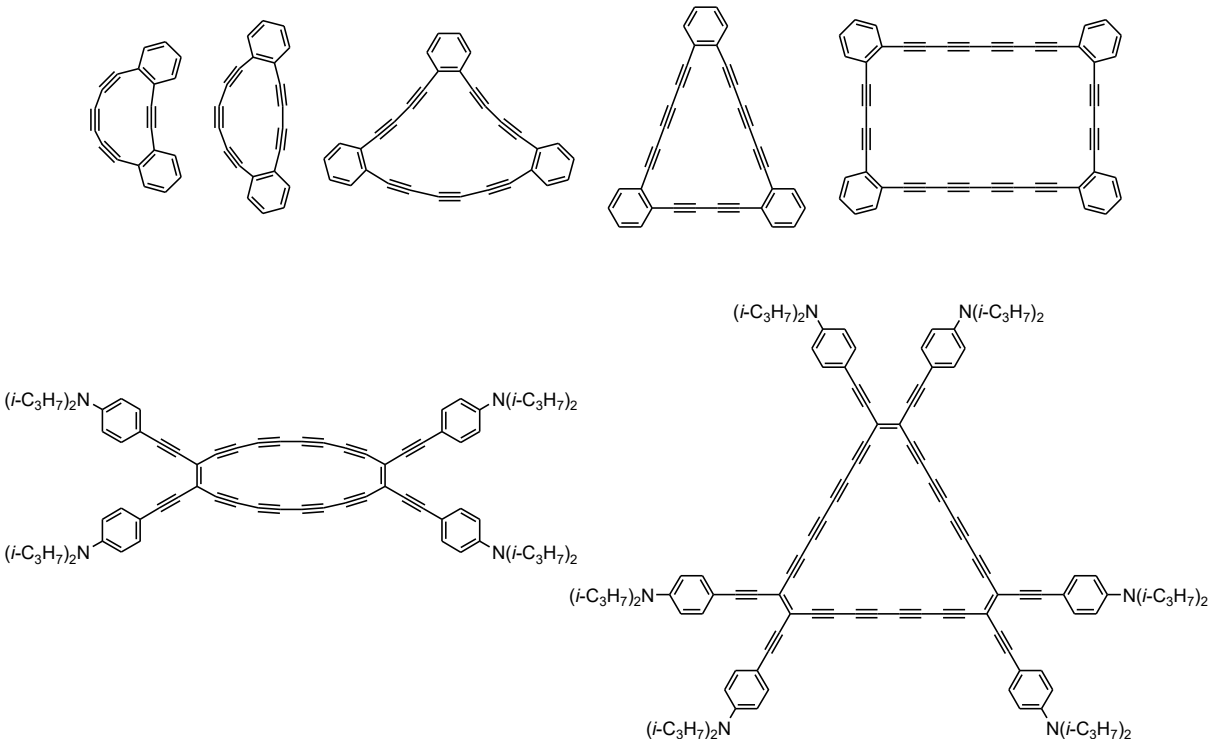

Figure 3-2. Examples of DAs and DBAs possessing hexatriyne or octatetrayne linkages.

3-2. Syntheses and Structures

The synthesis of DBAs **6**–**8** is outlined in Scheme 3-1. Compound **19** was converted into bromoalkyne **24** via desilylation with K_2CO_3 followed by silver catalyzed bromination. The Cadiot-Chodkiewicz coupling of **24** with trimethylsilylacetylene (TMSA) provided silyl-protected bisbutadiynyl arene **25**. Desilylation of **25** with K_2CO_3 afforded the terminal alkyne **26** that showed only limited stability in its neat form, which was rapidly placed under the Hay coupling condition in acetone. The careful separation of the crude mixture obtained in the macrocyclization afforded [20]DBA **6** and [30]DBA **7** in 5% yield, over two steps. The yield of **6** could not be determined because **6** could be handled only in solution; a neat sample rapidly decomposed to furnish black, intractable materials. The Pd-catalyzed coupling reaction was also investigated, and **8** and **7** were isolated in 6 and 7% yields, respectively. The low yields from the macrocyclization are probably due to the decomposition of the terminal alkyne during the reactions and/or the formation of oligomeric

or polymeric products. DBAs **6**–**8** were undoubtedly identified by mass spectrometric (FAB or MALDI-TOF) analysis together with their highly symmetric NMR spectra as described below. DBAs **7** and **8** showed higher stability than **6** and could be stored in the solid state at −15 °C for over a year; however, at room temperature, the solid sample of **7** gradually decomposed within a few months. [40]DBA **8** did not show any sign of decomposition when kept in the solid state at room temperature for over a year.

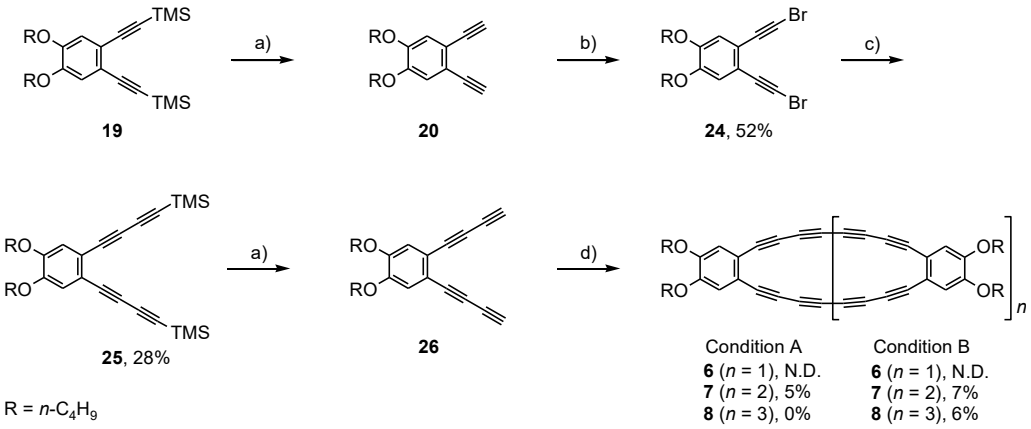

Scheme 3-1. Synthesis of DBAs **6**–**8**. Reagents and conditions: a) K_2CO_3, THF/MeOH (1:1 v/v), RT; b) $AgNO_3$, *N*-bromosuccinimide, THF/MeOH (1:1 v/v), RT; c) CuCl, $NH_2OH{\cdot}HCl$, *n*-$BuNH_2$, TMSA, CH_2Cl_2/H_2O (7:5 v/v), 0 °C; d) conditions A: CuCl, TMEDA, acetone, −5 °C to RT, conditions B: $[PdCl_2(PPh_3)_2]$, CuI, *p*-benzoquinone, THF/Et_3N (1:2 v/v), RT. TMSA = trimethylsilylacetylene. *o*-DCB = *o*-dichlorobenzene, TMEDA = *N*,*N*,*N'*,*N'*-tetramethylethylenediamine.

The author calculated the molecular structures of **6'**−**8'**, in which the butoxy groups in **6**–**8** were replaced with methoxy groups, at the B3LYP/6-31G(d) level of theory (Figure 3-3).[100] The optimized structures **1'**, **2'**, **6'**, and **7'** are planar (D_{2h} symmetry for **1'** and **6'**, D_{3h} symmetry for **2'** and **7'**). The structure of **8'** was calculated to be a nonplanar D_{2d}-symmetric structure. Unlike **2'**, **7'**, and **8'**, the C≡C–C bonds in **1'** and **6'** are apparently deformed from linearity. The bending angles of the C≡C–C bonds in **6'** are 170.3–175.2°, whereas those in **1'** are 164.1–167.5°; thus, the strain in C≡C–C bonds in **6'** is predicted to be released in comparison to that of **1'**. The evidence for the moderate strain in the C≡C–C bonds of **6** is manifested by the downfield shifts of the ^{13}C NMR peaks of the sp carbons by

ca. 4–5 ppm for **6** compared to **7**. Nevertheless, **6** shows drastically reduced stability as compared to **1a**. Although the reason for this finding is unclear at present, a similar severe instability in cyclic alkyl octatetraynes was reported by Tykwinski and co-workers.[145]

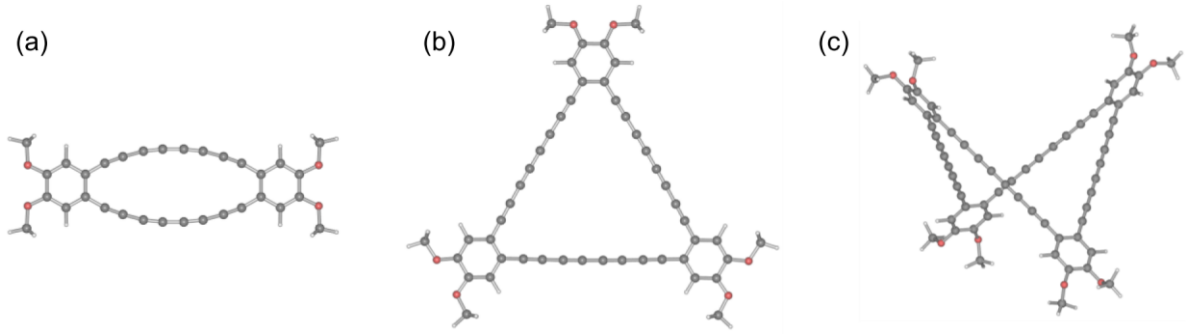

Figure 3-3. Optimized molecular structures of (a) **6'**, (b) **7'**, and (c) **8'**, where the butoxy groups in **6**–**8** are replaced with methoxy groups (B3LYP/6-31G(d)).

Single crystals of **7** suitable for X-ray diffraction analysis were obtained by recrystallization from a *p*-xylene solution as a clathrate, with *p*-xylene having a 2:5 stoichiometry (Figure 3-4a,b). The C≡C–C bond angles are 176.5–179.8°, and the deviation from the mean plane composed of the benzene moieties and octatetrayne linkages is at most 0.21 Å. Interestingly, the molecules of **7** and *p*-xylene form a 2D sheetlike structure in which the [30]DBA cores roughly align within the plane (Figure 3-4c). The butoxy groups and *p*-xylene molecules occupy the spaces between the π-core within the plane suggesting that CH–π and van der Waals interactions play an important role for the formation of the 2D-sheet. Thus, each benzene moiety of **7** adopts typical parallel displaced packing, where one corner of benzene hexagon locates above the center of the adjacent benzene ring, to form the triple-layered structure (Figure 3-4d,e). Consequently, the octatetrayne linkages are highly overlapped with close distances of *ca.* 3.45–3.50 Å.

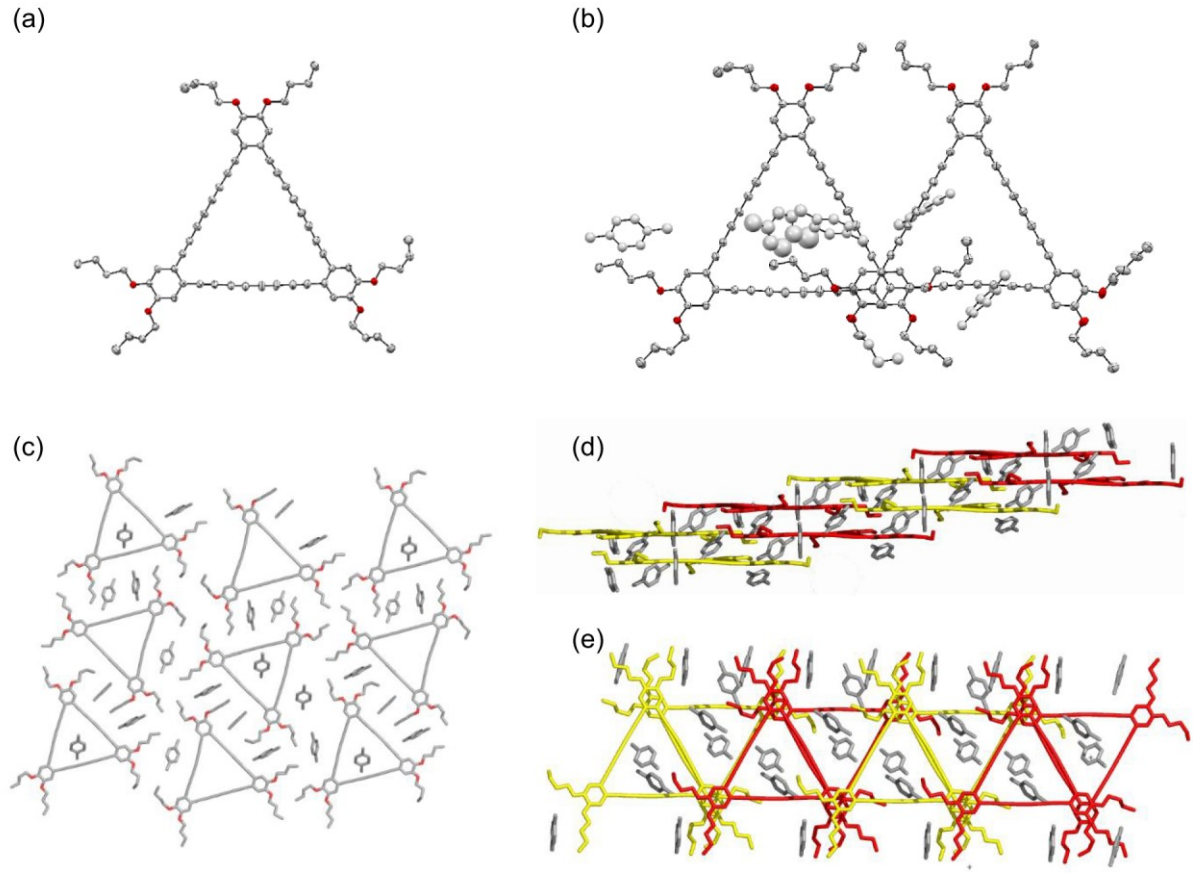

Figure 3-4. ORTEP plots of (a) DBA **7** and (b) (DBA **7**)$_2$·(*p*-xylene)$_5$ with displacement ellipsoid at 50% probability level. Hydrogen atoms and *p*-xylene molecules are omitted for clarity. Packing structures of (DBA **7**)$_2$·(*p*-xylene)$_5$ of (c) 2D sheetlike structure and 1D column structure from (d) bird-eye view and (e) top view.

3-3. ^{1}H NMR Spectra and NICS Calculations

DBAs **6**–**8** displayed very simple ^{1}H NMR spectra; thus, one singlet signal for aromatic protons was observed (Figures 3-5). Planar [20]- and [30]DBAs **6** and **7** are formally antiaromatic and aromatic, respectively. The change in resonance ($\Delta\delta$) of aromatic protons is a good indicator of the elucidation of tropicity. The signal of the aromatic protons for **6** is upfield shifted by $\Delta\delta$ = 0.28 ppm with respect to the signal for acyclic **25**. The signal for **7** is only slightly downfield shifted by $\Delta\delta$ = 0.05 ppm, which is almost comparable to the shift ($\Delta\delta$ = 0.02 ppm) for nonplanar, apparently nonaromatic **8**. The observed chemical shift changes from acyclic **25** to **6** and **7** are apparently small as compared to those from **19** to **1a** and **2a**, respectively; the $\Delta\delta$ values are 0.51 ppm for **1a** and 0.20 ppm for **2a** with respect to **19**. This

finding indicates that the tropicity of **6** and **7** substantially decreases as compared to the corresponding **1a** and **2a** owing to the expansion of the DA ring. Vollhardt and Matzger first reported the attenuating effect of the increase in the size of DBA rings on the nucleus-independent chemical shift (NICS) values.[111,112,135] Indeed, the NICS(0) (and NICS(1)) values of **6'** calculated at the GIAO/HF/6-31G(d)//B3LYP/6-31G(d) level are +1.1 (+1.1), which are only *ca.* 30% of those of **1'** (+3.8 (+3.7)); the NICS(0) (and NICS(1)) values for parent [12]DA **22** are calculated to be +9.2 (+8.1). The NICS(0) (and NICS(1)) of **7'** are calculated to be +0.1 (+0.1), which are obviously paradoxical values for compounds with macrocyclic diatropicity. Thus, it is considered that the paratropicity of **6** is significantly weak and the diatropicity of **7** is negligible.

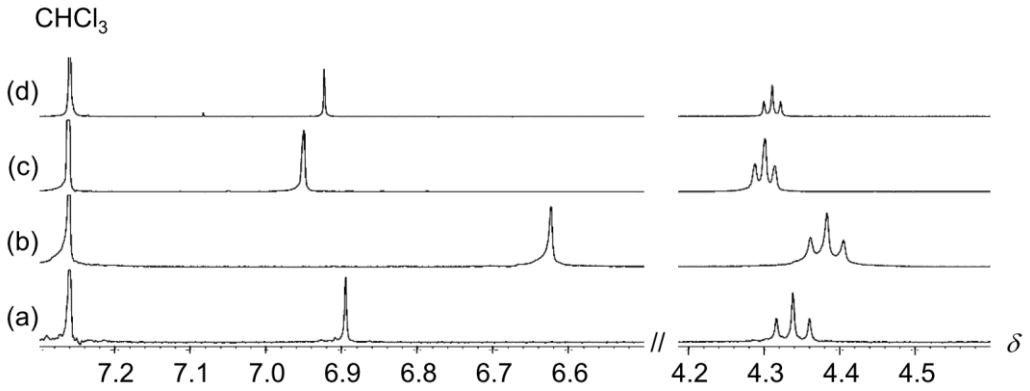

Figure 3-5. Partial ^{1}H NMR spectra of (a) **25**, (b) **6**, (c) **7**, and (d) **8** in $CDCl_3$ at 20 °C.

3-4. Electronic and Electrochemical Properties

In the UV–vis spectra (Figure 3-6, Table 3-1), the red shifts of the longest absorption maxima (λ_{max}^{abs}) are observed in **6** and **7** compared with **1a** and **2a**, respectively, which are attributed to the extension of π conjugation as a result of the extension of the oligoyne linkages; the longest λ_{max}^{abs} of **1a**, **2a**, **6**, and **7** are 472, 396, 490, and 451 nm, respectively. Notably, the λ_{max}^{abs} and absorption onsets (λ_{onset}) are red shifted from **8** and **7** to **6** in spite of **6** having the smallest ring size. Considering that the paratropicity of **6** is significantly weak and the conjugation pathway of **6** is shorter than that of **7** and **8**, the smaller HOMO–LUMO gap of **6** compared to **7** and **8** may derive from the strained oligoyne linkages in **6**.[113] The blue-shifted longest λ_{max}^{abs} (418 nm) and λ_{onset} in **8** relative to **6** and **7** are readily explained by the considerable nonplanarity of **8**, which should suppress the π conjugation to some extent in the macrocyclic framework composed of the benzene moieties and octatetrayne linkages. DBAs **1a** and **6**–**8** are nonfluorescent, whereas **2a** is fluorescent with an absolute fluorescence quantum yield (Φ_f) of 0.36 in $CHCl_3$ as described in Chapter 2.

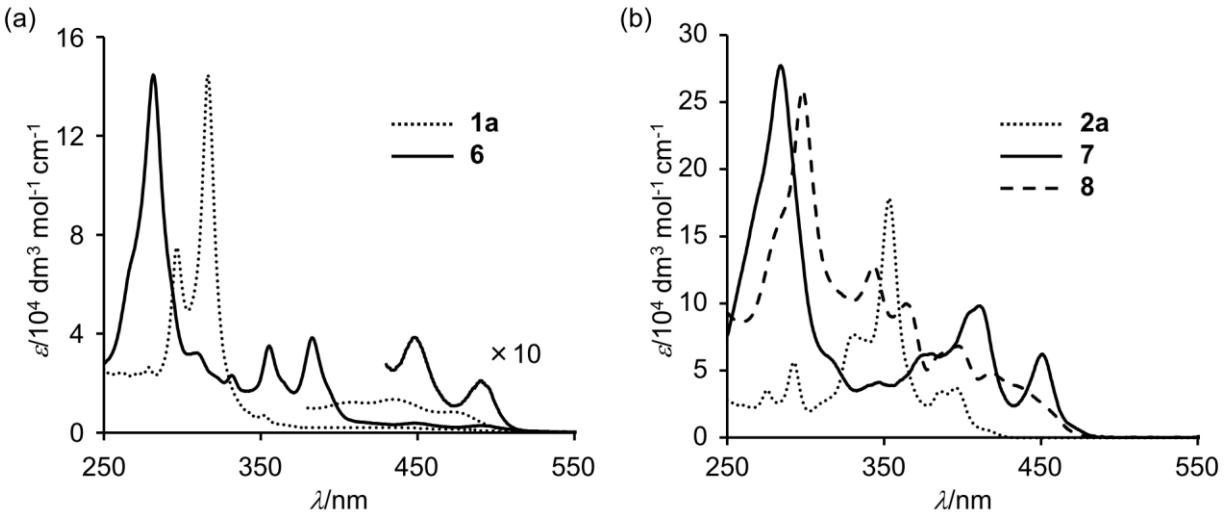

Figure 3-6. UV–vis absorption spectra of (a) **1a** and **6** and (b) **2a**, **7**, and **8** in $CHCl_3$ at 25 °C.

Table 3-1. The Longest λ_{max}^{abs} of **1a**, **2a**, and **6**–**8** and Calculated Lowest Excitation Wavelengths of **1'**, **2'**, **6'**, and **7'**

	$\lambda_{max}^{abs[a]}$ [nm]	$\lambda_{max}^{calcd[b]}$ [nm] (*f*)	Composition of band
1a	472	589 (0.000)	H → L, 91%
2a	415[c]	450 (0.000)	H–1 → L, 43%; H–1 → L+1, 8%; H → L, 8%; H–1 → L+1, 43%
	396	392 (0.948)	H–1 → L, 5%; H–1 → L+1, 33%; H → L, 33%, H–1 → L+1, 5%
		392 (0.948)	H–1 → L, 33%; H–1 → L+1, 5%; H → L, 5%; H–1 → L+1, 33%
6	490	676 (0.000)	H → L, 98%
7	475[c]	523 (0.000)	H–1 → L, 13%; H–1 → L+1, 32%; H → L, 32%; H–1 → L+1, 13%
	451	493 (0.869)	H–5 → L+2, 4%; H–2 → L+3, 4%; H–1 → L, 12%; H–1 → L+1, 31%; H → L, 30%; H → L+1, 13%
		493 (0.869)	H–4 → L+2, 4%; H–2 → L+4, 4%; H–1 → L, 31%; H–1 → L+1, 12%; H → L, 12%; H → L+1, 30%
8	418	—[d]	—[d]

[a] In $CDCl_3$ at 25 °C. [b] TD-DFT (TD/B3LYP/6-31(d)) calculations were carried out with uses of optimized structures at the B3LYP/6-31G(d) level of theory; *f* = oscillator strength; H = HOMO, L = LUMO. [c] Shoulder peak. [d] Not calculated.

The author carried out the density functional theory (DFT) calculations for **6'**–**8'**. The frontier molecular orbital (FMO) plots for **6'**–**8'** were obtained by the single-point calculations at the B3LYP/6-31+G(d,p)//B3LYP/6-31G(d) level (Figure 3-7). Similar to **2'**, the HOMO and HOMO–1 of **7'** are degenerate, as are the LUMO and LUMO+1. Time-dependent DFT (TD-DFT) calculations at the B3LYP/6-31G(d)//B3LYP/6-31G(d) level for **6'** and **7'** revealed that the molecular orbitals associated with the absorptions in the longer wavelength region for **6** and **7** are the same as those for the corresponding **1a** and **2a** (Table 3-1). Thus, as is the case with **1a**, the absorption of **6** is assigned to be symmetrically forbidden HOMO–LUMO transition and the absorption of **7** is related to the mixed transitions from HOMO and HOMO–1 to LUMO and LUMO+1.

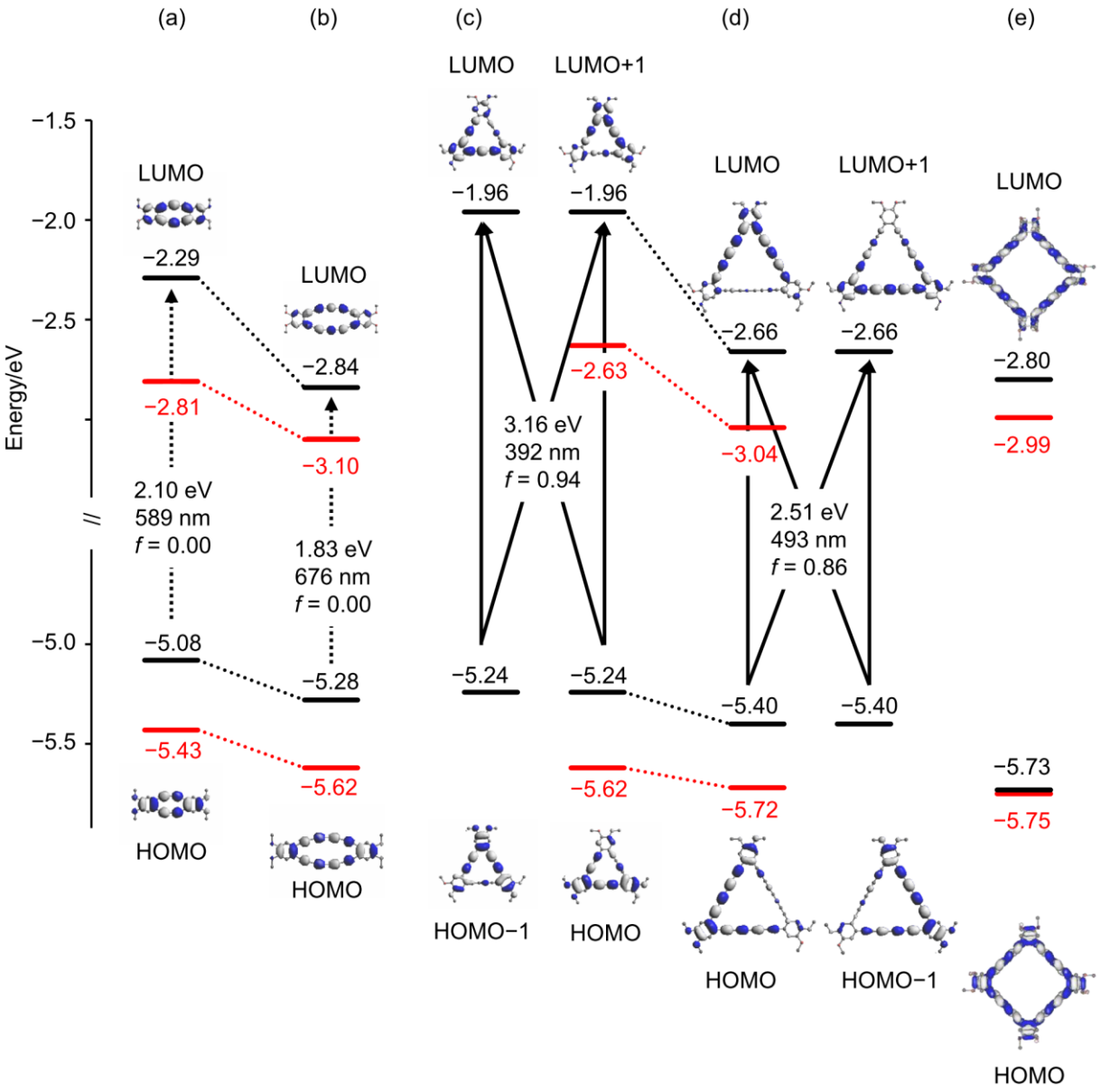

Figure 3-7. (Black) energy diagrams and frontier molecular orbital (FMO) plots of (a) **1'**, (b) **6'**, (c) **2'**, (d) **7'**, and (e) **8'** by using the B3LYP/6-31+G(d,p)//B3LYP/6-31G(d) method, and their transitions estimated by TD-DFT calculations at B3LYP/6-31G(d)//B3LYP/6-31G(d). (Red) HOMO and LUMO levels of (a) **1a**, (b) **6**, (c) **2a**, (d) **7**, and (e) **8** deduced from the oxidation onset (E_{onset}^{ox}) and reduction onset (E_{onset}^{red}) values according to the following equation: HOMO = −(4.8 + E_{onset}^{ox}) eV, LUMO = −(4.8 + E_{onset}^{red}) eV.

To gain insight into the frontier orbital energy of DBAs **6**–**8** as well as **1a** and **2a** in experiment, cyclic voltammetry (CV) analysis in *o*-dichlorobenzene (*o*-DCB) was conducted (0.1 mol dm^{-3} *n*-Bu_4NPF_6, standard ferrocene/ferrocenium ion (Fc/Fc^+)); the results are summarized in Table 3-2. All of the DBAs displayed amphoteric behavior within the available potential window (Figure 3-8). Both the oxidation onsets (E_{onset}^{ox}) and reduction onsets (E_{onset}^{red}) for **6** and **7** are positively shifted as compared to those for **1a** and **2a**, respectively, reflecting the stronger electron-withdrawing ability of an octatetrayne unit compared to that of a butadiyne unit.[146] The E_{onset}^{red} values are more positively shifted than the E_{onset}^{ox} values; hence, **6** and **7** have smaller potential differences between the E_{onset}^{ox} and E_{onset}^{red} values, namely, the smaller electrochemical HOMO–LUMO gaps (ΔE_{redox}) compared to those of **1a** and **2a**, respectively. The ΔE_{redox} become apparently small from **8** and **7** to **6**, as expected from the absorption spectra. These trends are well reproduced by the calculations; the ΔE_{redox} values for **1a**, **2a**, and **6**–**8** match the calculated HOMO–LUMO gaps (ΔE_{calcd}) for corresponding **1'**, **2'**, and **6'**–**8'**.

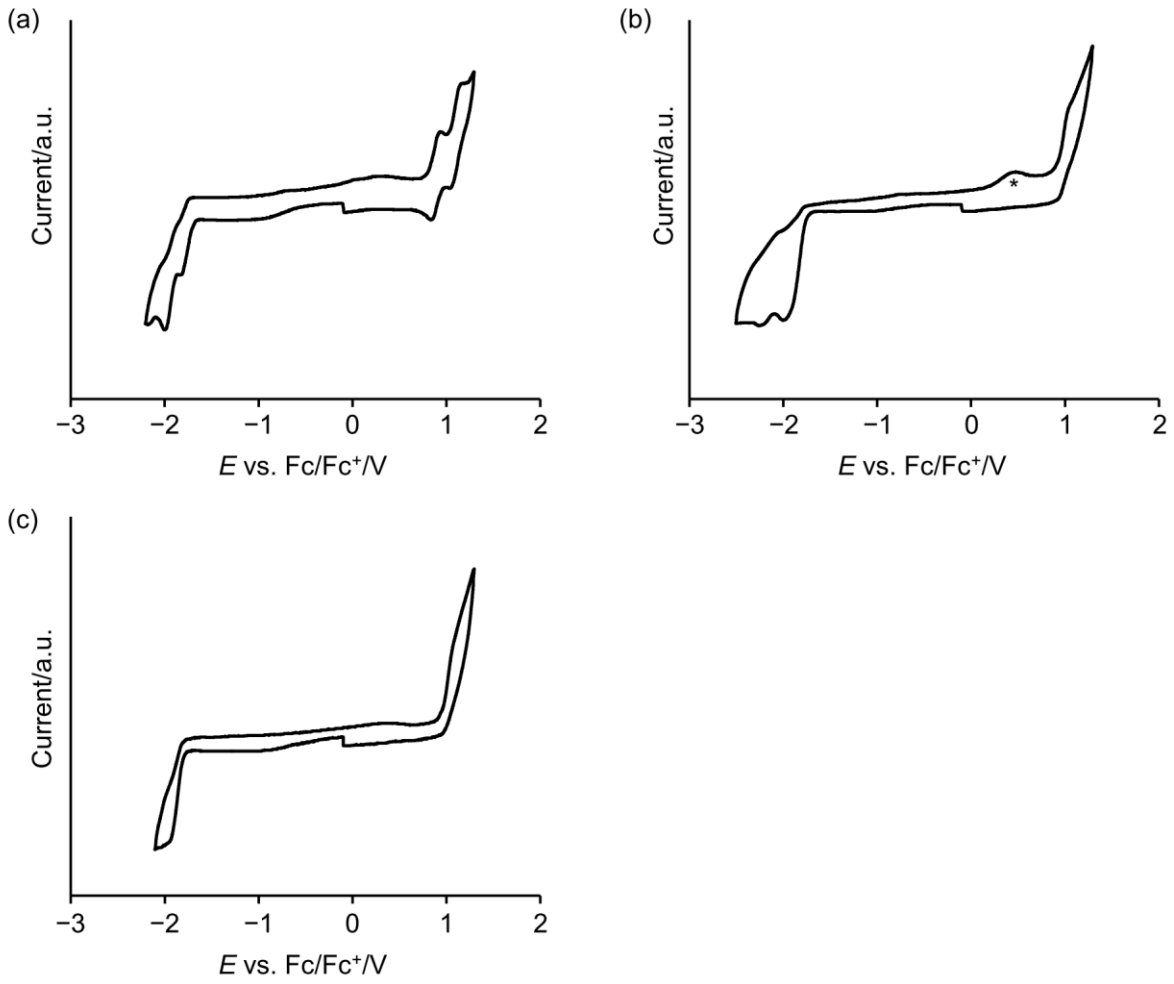

Figure 3-8. Cyclic voltammograms of (a) **6**, (b) **7**, and (c) **8** measured in *o*-DCB (0.1 mol dm^{-3} *n*-Bu_4NPF_6) at a scan rate of 100 mV s^{-1}. The peak attributed to the decomposed species formed by reduction are labeled with an asterisk.

Table 3-2. Oxidation and Reduction Potentials of **1a**, **2a**, and **6**–**8** by CV in *o*-DCB[a], Electrochemical HOMO–LUMO Gaps,[b] and Theoretically Calculated HOMO and LUMO Levels

	E_{onset}^{ox} (E_{pa}) [V]	E_{onset}^{red} (E_{pc}) [V]	ΔE_{redox}[c] [V]	HOMO [eV]	LUMO [eV]	ΔE_{calcd} [eV]
1a	+0.63	−1.99	2.62	−5.08	−2.29	2.79
	(+0.78)[d]	(−2.16)[e]				
	(+1.21)[d]	(−2.51)[f]				
2a	+0.82	−2.17	2.99	−5.24	−1.96	3.28
	(+0.96)[f]	(−2.43)[f]				
6	+0.82	−1.70	2.52	−5.28	−2.84	2.44
	(+0.92)[d]	(−1.81)[e]				
	(+1.14)[d]	(−1.99)[f]				
7	+0.92	−1.76	2.68	−5.40	−2.66	2.74
	(+1.03)[f]	(−1.99)[f]				
8	+0.95	−1.81[g]	2.76	−5.73	−2.80	2.93
	(+1.05)[f]					

[a] Measuring by using CV in *o*-DCB (0.1 mol dm^{-3} *n*-Bu_4NPF_6). All the potentials are given versus the Fc/Fc^+ couple as an external standard. Scan rate = 100 mV s^{-1}. [b] B3LYP/6-31+G(d,p)//B3LYP/6-31G(d) for **1'**, **2'**, and **6'**–**8'**, where the butoxy groups in **1a**, **2a**, and **6**–**8** are replaced with methoxy groups. [c] The electrochemical gap (ΔE_{redox}) is defined as the potential difference between E_{onset}^{ox} and E_{onset}^{red}. [d] Reversible wave. [e] Quasireversible wave. [f] Irreversible wave. [g] Unresolved wave.

3-5. Self-association

The ^1H NMR spectra of **7** in $CDCl_3$ showed subtle but distinctive upfield shifts of the aromatic protons upon increasing the concentration unexpectedly (Figure 3-9a). This indicates the occurrence of self-association in solution by π–π stacking interactions. The diffusion coefficients (*D*) for **7** were almost independent of the concentrations on the basis of the diffusion NMR experiments, suggesting that a monomer–dimer equilibrium predominantly exists.[121] The plots of the chemical shifts of the aromatic protons as a function of concentration was fitted to a curve for the monomer–dimer model (Figure 3-9a)[122] and yielded the self-association constant (*K*) of 4 ± 1 dm^3 mol^{-1}. In contrast to **7**, the resonance for the aromatic protons in **2a** was independent of the concentrations in $CDCl_3$.

These results demonstrate that the extension of the oligoyne linkages from **2a** to **7** enhances the self-association ability. To investigate the effect of solvent polarity on the self-association of **7**, the author performed the NMR experiments in $CDCl_3/CD_3CN$ solvent system. The *K* values in $CDCl_3/CD_3CN$ ratios of 2:1 and 1:1 were 56 ± 5 and 112 ± 45 dm^3 mol^{-1}, respectively (Figure 3-9b,c), which indicate that the self-association is enhanced by the solvophobic effects in the mixed-solvent system.

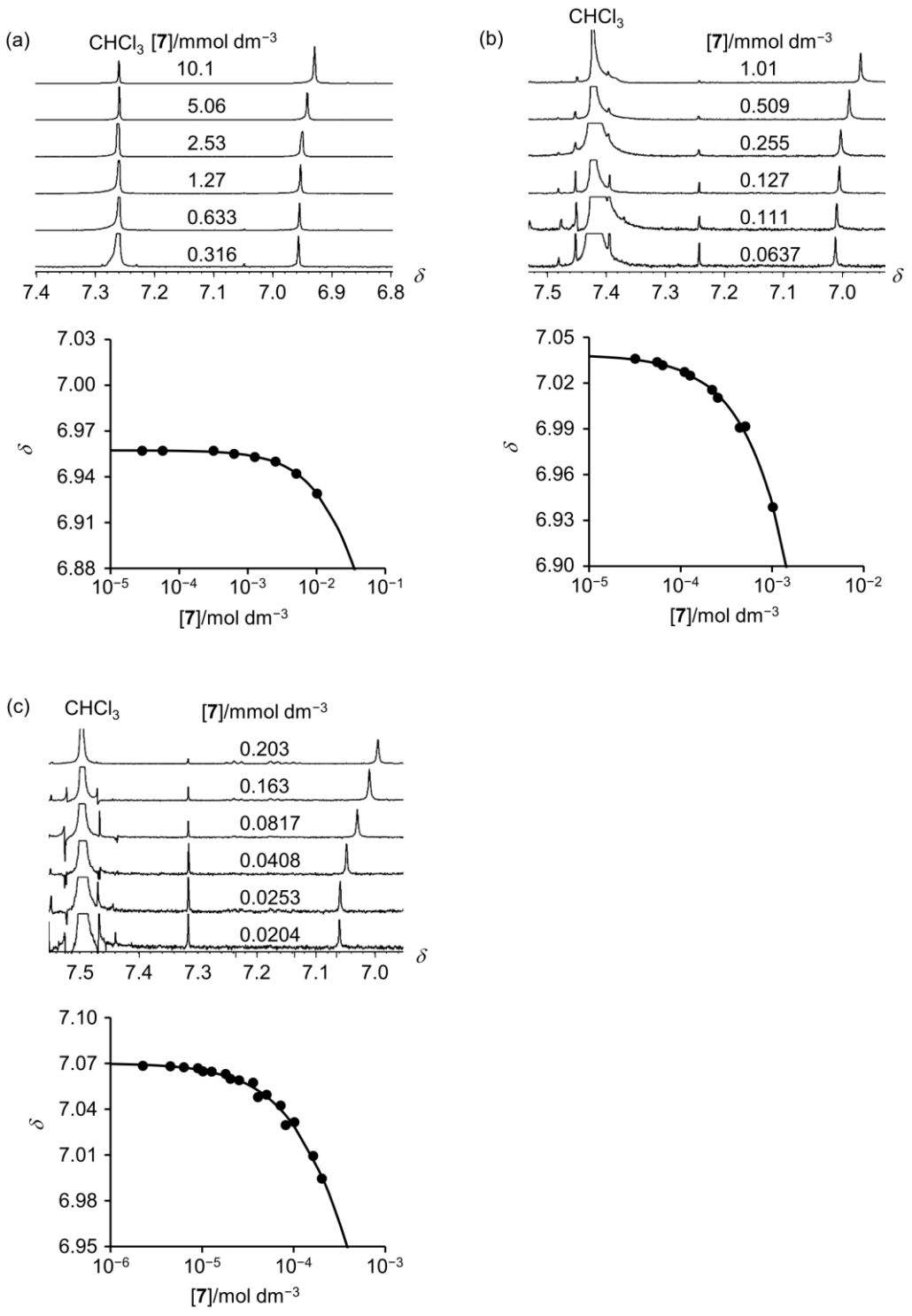

Figure 3-9. Partial ^{1}H NMR spectra of **7** in various concentrations at 20 °C in (a) $CHCl_3$, (b) $CDCl_3/CD_3CN$ = 2:1, and (c) $CDCl_3/CD_3CN$ = 1:1 (top) and the corresponding nonlinear curve-fitting plots of the concentration dependence of the chemical shifts of the aromatic protons (bottom).

To examine the electronic effect of the oligoyne linkages on the self-association, the author calculated the electrostatic-potential surfaces (ESPs) and molecular electrostatic potentials (MEPs) of **1'** and **7'** at the B3LYP/6-31+G(d,p)//B3LYP/6-31G(d) level (Figure 3-10). The MEPs at 2 Å above the center of the benzene rings are −8.8 and −4.0 kcal mol^{-1} for **1'** and **7'**, respectively, which clearly indicates a less-negative character for the benzene rings of **7** than **1a**. The polar/π model predicts that electron-withdrawing aromatic rings favor effective π−π stacking interactions.[147,148] In addition, it was pointed out by Tobe and co-workers that arylene–butadiynylene macrocycles (ABMs) possess a higher self-association ability than arylene–ethynylene macrocycles (AEMs) because of the strong electron-withdrawing effect of the butadiyne units in the former.[125] Therefore, it is reasonable to conclude that the octatetrayne linkages in **7** promote π–π stacking interactions effectively owing to their strong electron-withdrawing effect.

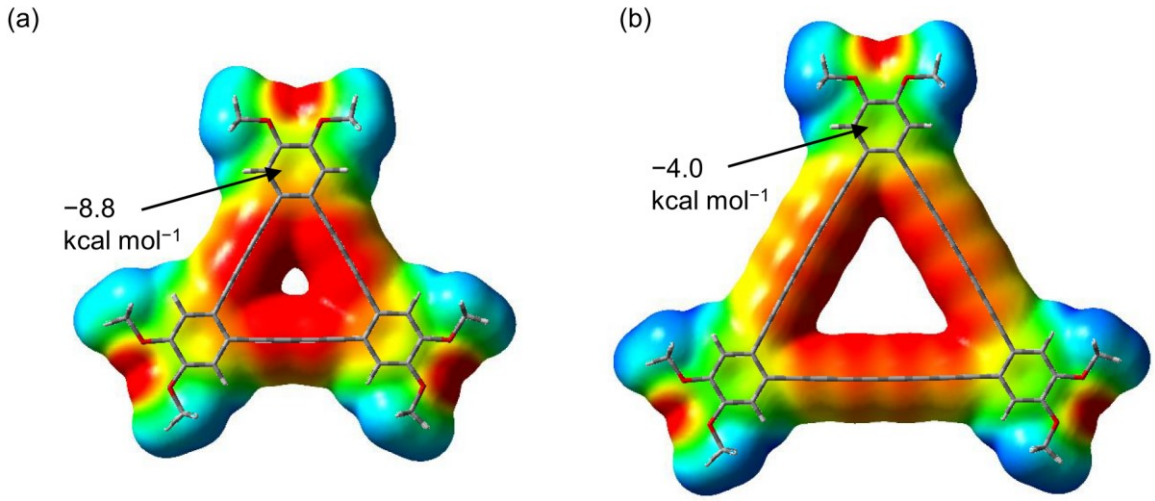

Figure 3-10. EPSs and values of the MEPs; the calculated position of the MEPs are 2 Å above the center of the benzene rings of (a) **2'** and (b) **7'** at the level of B3LYP/6-31+G(d,p)//B3LYP/6-31G(d). The Potentials are drawn in the same color scale, with red indicating more-negative electrostatic potentials and blue, more-positive potentials.

3-6. Conclusions

The author has synthesized hitherto unknown [20]-, [30]-, and [40]DBAs **6**–**8** possessing octatetrayne linkages. The unique 2D sheetlike network of (DBA **7**)$_2$·(*p*-xylene)$_5$ in the solid state was revealed. The expansion of the DBA cores by extension of the oligoyne linkages from butadiyne to octatetrayne units significantly decreases tropicity; thus, the paratropicity of **6** should be extremely weak, and the diatropicity of **7** should be negligible. The octatetrayne linkages are responsible for small HOMO–LUMO gaps compared to the butadiyne linkages. The effective self-association properties of **7** in solution suggest that octatetrayne linkages facilitate π–π stacking interactions.

3-7. Experimental Section

Preparation of 24: To a solution of **19** (800 mg, 1.93 mmol) in THF/MeOH (1:1, 10 mL) was added K_2CO_3 (528 mg, 3.82 mmol). After the mixture was stirred at room temperature for 50 min, the suspension was evaporated under reduced pressure. The residue was purified by silica gel column chromatography (acetone) to give desilylated diyne **20**, which was used in the next reaction without further purification because of the instability.

To a solution of **20** in acetone (10 mL) were added *N*-bromosuccinimide (784 mg, 4.40 mmol) and $AgNO_3$ (96 mg, 0.57 mmol). After the mixture was stirred at room temperature for 6 h, the suspension was evaporated under reduced pressure. The residue was suspended with hexane and filtered, and the filtrate was evaporated under reduced pressure. The residue was purified by silica gel column chromatography (hexane/CH_2Cl_2, 10:1) to afford **24** (430 mg, 1.00 mmol, 52%) as a red solid. M.p. 64–66 °C; ^{1}H NMR ($CDCl_3$, 300 MHz): δ 0.97 (t, 6H, J = 7.4 Hz), 1.48 (tq, 4H, J = 7.4, 7.2 Hz), 1.78 (tt, 4H, J = 7.2, 6.8 Hz), 3.95 (t, 4H, J = 6.8 Hz), 6.86 (s, 2H); ^{13}C NMR ($CDCl_3$, 75 MHz): δ 13.8, 19.2, 31.1, 51.9, 68.8, 78.6, 116.1, 118.4, 149.2; UV−vis (CH_2Cl_2): λ_{max}^{abs} = 290 nm; MALD-TOF-MS (dith, positive): *m/z* 451.00 $[M+Na]^+$; elemental analysis calcd (%) for $C_{18}H_{20}Br_2O_2$: C, 50.49, H, 4.71; Found: C,

50.03; H, 4.71.

Preparation of 25: To a suspension of CuCl (50 mg, 0.50 mmol) and *n*-$BuNH_2$ (3.6 mL, 35 mmol) in H_2O (5 mL) and CH_2Cl_2 (5 mL) was added $NH_2OH{\cdot}HCl$ (5 mg, 0.1 mmol) at 0 °C. A solution of **24** (430 mg, 1.00 mmol) and TMSA (0.42 mL, 3.0 mmol) in CH_2Cl_2 (2 mL) was added dropwise to the mixture at 0 °C. After the resulting mixture was stirred at 0 °C for 40 min, aqueous NH_4Cl was added. The organic phase was successively washed with aqueous NH_4Cl and H_2O, dried over anhydrous $MgSO_4$, and evaporated under reduced pressure. The residue was purified by silica gel column chromatography (hexane/CH_2Cl_2, 5:1) and recycling GPC ($CHCl_3$) to afford **25** (130 mg, 0.28 mmol, 28%) as yellow oil. ^{1}H NMR ($CDCl_3$, 300 MHz): δ 0.24 (s, 18H), 0.97 (t, 6H, J = 7.4 Hz), 1.43−1.51 (m, 4H), 1.79 (qui, 4H, J = 6.8 Hz), 3.96 (t, 4H, J = 6.8 Hz), 6.90 (s, 2H); ^{13}C NMR ($CDCl_3$, 125 MHz): δ −0.2, 13.9, 19.2, 31.0, 68.9, 75.2, 76.8, 88.2, 91.8, 116.9, 117.9, 149.9; UV−vis ($CHCl_3$): λ_{max}^{abs} (relative intensity) = 255 (0.31), 270 (0.60), 286 (1.00), 329 (0.35), 352 (0.36) nm; MALDI-TOF-MS (dith, positive): *m/z* 462.58 $[M]^+$; elemental analysis calcd (%) for $C_{28}H_{38}O_2Si_2{\cdot}0.04CHCl_3$: C, 72.03, H, 8.20; Found: C, 71.78, H, 7.85.

Preparation of DBAs 6 and 7 (Cu-mediated method): A mixture of **25** (656 mg, 1.42 mmol) and K_2CO_3 (392 mg, 2.84 mmol) in THF/MeOH (1:1, 10 mL) was stirred at room temperature for 1 h. After the mixture was diluted with acetone (20 mL), the insoluble material was removed by filtration, and the filtrate was evaporated under reduced pressure. The residue was purified by silica gel column chromatography (acetone) to give desilylated alkyne **26**, which was used in the next coupling reaction without further purification because of the instability.

To a mixture of **26** and TMEDA (1.0 mL, 7.1 mmol) in acetone (250 mL) was added CuCl (700 mg, 7.10 mmol) at −5 °C, and the resulting mixture was stirred at room temperature for 22 h. The mixture was filtered through a bed of silica gel, and the filtrate was evaporated under reduced pressure to *ca.* 1 mL. The mixture was purified by silica gel column

chromatography (hexane/toluene, 1:1) to afford unstable **6** and **7** (22 mg, 0.023 mmol, 5%) as yellow solids. [20]DBA **6** decomposed upon concentration to give an insoluble black material. A dilute solution of **6** can be stored for over a year at −15 °C. **6**: ^{1}H NMR ($CDCl_3$, 600 MHz) δ 0.96 (t, 12H, J = 7.3 Hz), 1.45 (sex, 8H, J = 7.3 Hz), 1.76 (tt, 8H, J = 7.3, 6.9 Hz), 3.91 (t, 8H, 6.9 Hz), 6.62 (s, 4H); ^{13}C NMR ($CDCl_3$, 150 MHz): δ 13.9, 19.2, 31.0, 67.7, 69.0, 70.8, 80.3, 82.2, 114.0, 122.0, 150.5; UV−vis ($CHCl_3$): λ_{max}^{abs} (relative intensity) = 490 (0.02), 447 (0.03), 383 (0.27), 356 (0.24), 332 (0.16), 309 (0.22), 282 (1.00) nm; HR-FAB-MS (NBA, positive) *m/z* calcd for $C_{44}H_{40}O_4^+$: 632.2927; found, 632.2927 $[M]^+$. **7**: M.p. 155 °C (decomp.); ^{1}H NMR ($CDCl_3$, 500 MHz, 2.53 × 10^{-3} mol dm^{-3}) δ 0.98 (t, 18H, J = 7.5 Hz), 1.50 (tq, 12H, J = 7.5, 7.3 Hz), 1.81 (tt, 12H, J = 7.3, 6.8 Hz), 4.00 (t, 12H, J = 6.8 Hz), 6.95 (s, 6H); ^{13}C NMR ($CDCl_3$, 125 MHz): δ 13.9, 19.2, 31.0, 64.4, 68.93, 69.04, 75.7, 77.6, 116.5, 118.3, 150.4; UV−vis ($CHCl_3$) λ_{max}^{abs} (ε) = 451 (62200), 411 (98100), 380 (62600), 347 (41200), 284 nm (277300 dm^3 mol^{-1} cm^{-1}); HR-FAB-MS (NBA, positive) *m/z* calcd for $C_{66}H_{60}O_6^+$: 948.4390; found, 948.4380 $[M]^+$.

Preparation of DBAs 7 and 8 (Pd-catalyzed method): Compound **25** (322 mg, 0.88 mmol) was desilylated according to the same procedure used for the preparation of DBAs **6** and **7**. A solution of **26** in Et_3N/THF (1:2, 90 mL) was bubbled with argon with stirring for 30 min. $[PdCl_2(PPh_3)_2]$ (62 mg, 0.088 mmol), CuI (34 mg, 0.176 mmol), and *p*-benzoquinone (85 mg, 0.79 mmol) were added to the solution, and the resulting mixture was stirred at room temperature for 16 h under argon atmosphere. The mixture was filtered through a bed of silica gel, and the filtrate was evaporated under reduced pressure. The residue was subjected to silica gel column chromatography ($CHCl_3$). The collected material was suspended with CH_2Cl_2, and the insoluble material was collected by filtration, which was further washed with CH_2Cl_2 to afford **8** (16 mg, 0.013 mmol, 6%) as a yellow solid. An analytical sample was obtained by reprecipitation from $CHCl_3$/hexane. The filtrate was concentrated under reduced pressure. The residue was further purified by recycling GPC ($CHCl_3$) to afford **7**

(18 mg, 0.019 mmol, 7%). **8**: M.p. 148 °C (decomp.); ^{1}H NMR ($CDCl_3$, 600 MHz) δ 0.97 (t, 24H, J = 7.3 Hz), 1.41−1.52 (m, 16H), 1.80 (qui, 16H, J = 6.4 Hz), 3.99 (t, 16H, J = 6.4 Hz), 6.92 (s, 8H); ^{13}C NMR ($CDCl_3$, 125 MHz) δ 13.9, 19.2, 31.0, 64.5, 68.9, 69.1, 76.0, 77.7, 116.8, 118.3, 150.5; UV−vis ($CHCl_3$): λ_{max}^{abs} (ε) = 418 (48400), 397 (68200), 364 (99700), 343 (128300), 298 nm (259100 dm^3 mol^{-1} cm^{-1}); MALDI-TOF-MS (SA, positive) *m/z* 1273.87 $[M+H]^+$; elemental analysis calcd (%) for $C_{88}H_{80}O_8 \cdot 0.29\ CHCl_3$: C, 81.55, H, 6.22; Found: C, 81.55, H, 6.39. the author was unable to obtain satisfactory elemental analysis for this compound. This compound may tend to contain solvent molecules in the solid state. The author believe that the compound is pure on the basis of the ^{1}H NMR spectrum.

X-ray crystal structure analysis of 7: Crystal data at −120 °C for $C_{86}H_{85}O_6$, M_r = 1214.54, triclinic, space group *P*-1, D_{calcd} = 1.132 g cm^{-3}, Z = 4, a = 15.0672(3) Å, b = 1601877(3) Å, c = 33.1869(6) Å, α = 89.496(6)°, β = 77.803(5)°, γ = 64.751(5)°, V = 7125.5(2) $Å^3$; Mo-*K*α radiation, λ = 0.71070, μ = 0.539 mm^{-1}. A colorless crystal (linear dimensions *ca.* 0.10 × 0.08 × 0.06 mm) was obtained from *p*-xylene solution at 20 °C. Numbers of measured and unique reflections were 85594 and 25568, respectively (R_{int} = 0.061). Final $R(F)$ = 0.084, $wR(F^2)$ = 0.243 for 1670 parameters and 25568 reflections with $I > 2\sigma(I)$ and $3.03 < \theta < 68.20°$ (corresponding R values are 0.132 and 0.277 respectively, for all data). A high wR^2 value and a high maximum peak in the residual electron density plot derive from the dynamic disorder of the butoxy group and *p*-xylene molecules. CCDC-926926 contains the supplementary crystallographic data.

Chapter 4. Tetraalkoxyphenanthrene-Fused Hexadecadehydro[20]- and Tetracosadehydro[30]annulenes: Syntheses, Self-assembly, and Electronic, Optical, and Electrochemical Properties

4-1. Introduction

While a plethora of dehydro[*n*]annulenes ([*n*]DAs)[89–99] and dehydrobenzo[*n*]annulenes ([*n*]DBAs)[60–72,76–88] possessing ethyne and/or butadiyne linkages have been synthesized and their tropicity, electronic properties, and self-assembling behavior were extensively investigated to establish the structure–property relationships as described in Chapters 1 and 2, only a limited number of DAs and DBAs possessing oligoyne linkages longer than butadiyne linkages have been synthesized until now. The author succeeded in the syntheses and characterization of hitherto unknown DBAs possessing tetrayne linkages and the clarification of their properties as described in Chapter 3. The important finding obtained from this study is that the extension of acetylenic linkages potentially not only extends the cyclic π-conjugation, which affects tropicity and photophysical and electrochemical properties, but also enhances the self-association ability. Following the study described in Chapters 2 and 3, the author was motivated to extend acetylenic linkages of phenanthrene-fused DAs **3** and **4** from butadiyne to octatetrayne units and thus designed phenanthrene-fused [20]- and [30]DAs **9** and **10** possessing octatetrayne linkages to expand a family of conjugated macrocycles possessing oligoyne linkages (Figure 4-1). In Chapter 4, the author describes the syntheses of **9** and **10** and their unique properties. Their tropicity and physicochemical properties were assessed by various spectroscopies, cyclic and differential-pulse voltammetry (CV and DPV), and quantum chemical calculations and compared with those of **3** and **4** possessing butadiyne linkages. Concentration- and temperature-dependent ^{1}H NMR and UV–vis spectroscopies were applied for the quantitative analysis for the self-association of **3c, 4c**, **9c**, and **10c**; this is the first example of thermodynamic study on the self-association processes of conjugated

macrocycles possessing octatetrayne linkages. Moreover, the formation of self-assembled clusters from **3c, 4c**, **9c**, and **10c** were investigated by scanning electron microscopy (SEM), atomic force microscopy (AFM), and wide-angle X-ray diffraction (WAXD). Overall, the author focused on the elucidation of the effect of extending acetylenic linkages on tropicity, physicochemical and self-assembling properties, which should give valuable insight into the structure–property relationships in acetylenic macrocycles, and thus herein the significance of the incorporation of oligoyne linkages into the annulenic systems for the creation of π-functional systems is highlighted.

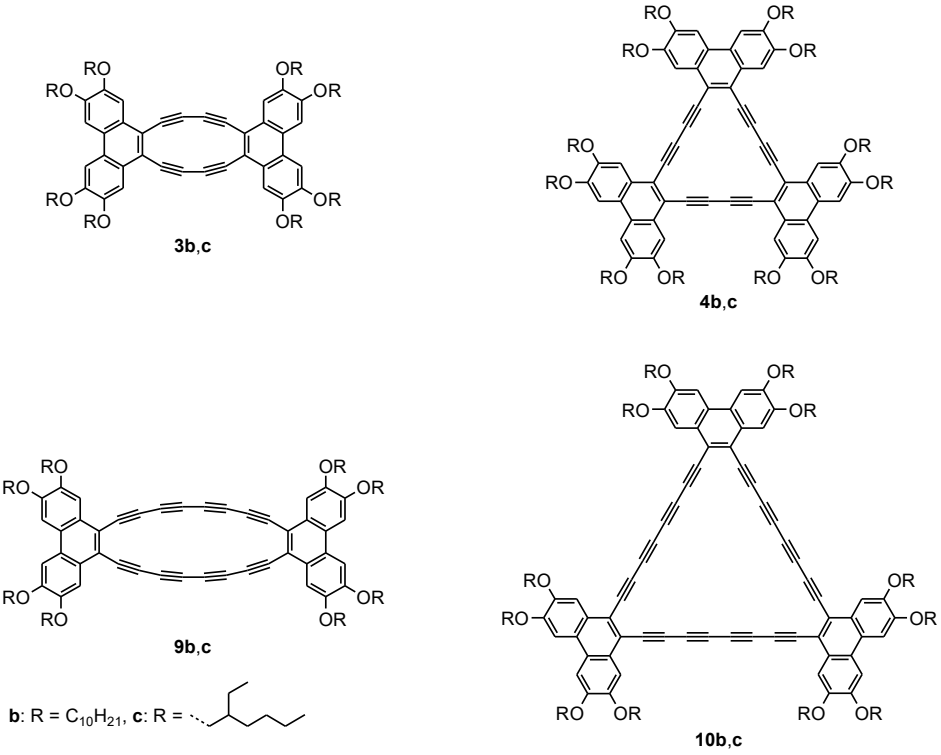

Figure 4-1. Structures of phenanthrene-fused DAs **3b**,**c**, **4b**,**c**, **9b**,**c**, and **10b**,**c**.

4-2. Syntheses

The synthetic route to [20]- and [30]DAs **9b**,**c** and **10c** is outlined in Scheme 4-1. The author planned to introduce decyloxy or 2-ethylhexyloxy groups to phenanthrene-fused DAs because the bulkiness of alkoxy groups was anticipated to affect the solubility and self-assembling behavior of the compounds. Intramolecular oxidative cyclization of benzils **12b**,**c** with $MoCl_5/TiCl_4$ mixture in CH_2Cl_2 afforded diketones **13b**,**c**. The addition of the lithiated acetylide of trimethylsilylacetylene (TMSA) to **13b**,**c**, followed by the treatment with $(MeO)_2SO_2$ gave methyl ethers **27b**,**c**. Desilylation of the TMS groups of **27b**,**c** with K_2CO_3 afforded **28b**,**c**, which were then placed on the Cadiot–Chodkiewicz coupling reaction condition with (2-bromoethynyl)triisopropylsilane to give **29b**,**c**. Reductive aromatization of **29b**,**c** with $SnCl_2 \cdot 2H_2O$ in THF in the presence of H_2SO_4 smoothly proceeded to afford **30b**,**c**. Removal of the triisopropylsilyl (TIPS) groups of **30b**,**c** with tetrabutylammonium fluoride (TBAF) gave the key intermediates **31b**,**c**, which were immediately subjected to macrocyclization reaction; terminal alkynes **31b**,**c** were unstable in contrast to **30b**,**c**.

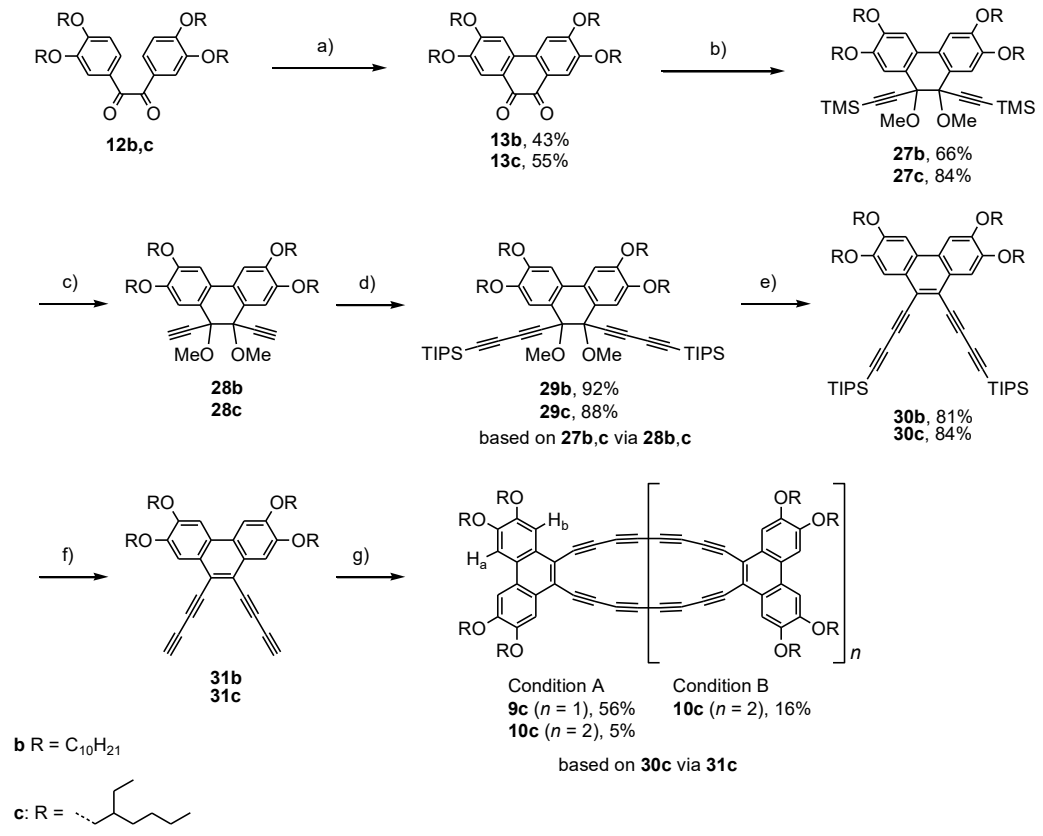

Scheme 4-1. Synthesis of DAs **9c** and **10c**. Reagents and conditions: a) $TiCl_4$, $MoCl_5$, CH_2Cl_2, 0 °C to RT; b) 1) TMS−C≡CLi, THF, −78 °C to RT; 2) $(MeO)_2SO_2$, THF, −78 °C to RT; c) K_2CO_3, THF/MeOH (1:1 v/v), RT; d) TIPS−C≡CBr, $NH_2OH{\cdot}HCl$, *n*-$BuNH_2$, CuCl, CH_2Cl_2/H_2O (1:1 v/v), 30 °C; e) $SnCl_2{\cdot}2H_2O$, H_2SO_4, THF, reflux; f) TBAF, THF, 0 °C; g) Condition A: CuCl, TMEDA, CH_2Cl_2, RT; Condition B: $[PdCl_2(PPh_3)_2]$, CuI, Et_3N, THF, RT. TBAF = tetrabutylammonium fluoride. TMEDA = *N*,*N*,*N*',*N*'-tetramethylethylenediamine.

First, the Hay coupling reaction of **31b** by using CuCl and *N*,*N*,*N'*,*N'*-tetramethylethylenediamine (TMEDA) in CH_2Cl_2 was examined. ^{1}H NMR and mass spectrometric analyses of the resulting material indicated the formation of **9b**, however, its isolation and characterization could not be accomplished due to the severe insolubility in organic solvents. Next, the author performed the Hay coupling reaction of **31c**, and gratifyingly isolated **9c** in 56% yield together with **10c** in 5% yield, over two steps from **30c**. DAs **9c** and **10c** are red solids that are readily soluble in common organic solvents, such as hexane, toluene, and $CHCl_3$, in sharp contrast to **9b** due to the bulky 2-ethylhexyloxy groups appended to the phenanthrene moieties in **9c** and **10c**. The Pd-mediated oxidative coupling reaction of **31c** with $[PdCl_2(PPh_3)_2]$ and CuI under air was also performed, and **10c** was

obtained in 16% yield. The formation of **9c** was not detected by the thin-layer chromatography (TLC) and the ^{1}H NMR spectroscopic analysis of the reaction mixture. The preferential formation of **10c** by the Pd-mediated homocoupling reaction of **31c** should reflect the difference of mechanism between the Cu- and Pd-mediated diyne-formation reactions.[149,150] DAs **9c** and **10c** were undoubtedly identified by MALDI-TOF-MS analyses together with their highly symmetric ^{1}H NMR spectra as described below. DAs **9c** and **10c** did not show any sign of decomposition when kept in the solid state for over a year. The solid-state stability of **9c** and **10c** is noteworthy, because macrocycles possessing octatetrayne units are known to be generally unstable in neat form; for instance, [20]- and [30]DBAs **6** and **7** decompose in the solid state as described in Chapter 3. The phenanthrene moieties and the bulky 2-ethylhexyloxy groups in **9c** and **10c** may contribute to their exceptional solid-state stability electronically and kinetically, respectively. Thermal gravimetric analyses (TGA) under nitrogen atmosphere showed that the 5% weight loss occurred at 328 °C and 273 °C for **9c** and **10c**, respectively, indicative of their high thermal stability (Figure 4-2). As reference compounds of **9c** and **10c**, [12]- and [18]DAs **3c** and **4c** possessing 2-ethylhexyloxy groups, were also prepared in similar manners for the synthesis of **3a**,**b** and **4a**,**b**, respectively, described in Chapter 2 (Scheme 4-2).

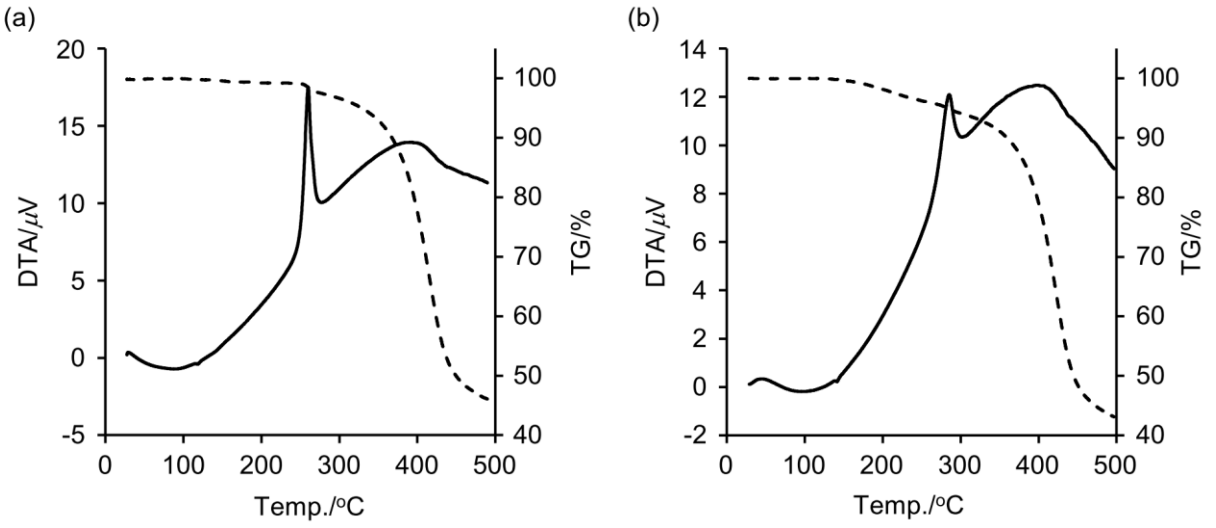

Figure 4-2. DTA (solid line) and TG (dashed line) curves of (a) **9c** and (b) **10c**.

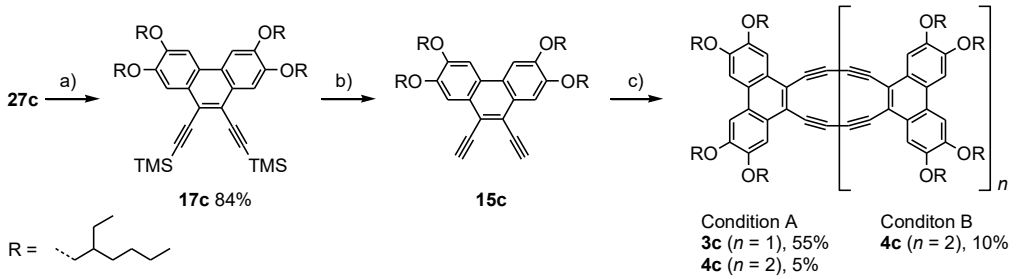

Scheme 4-2. Synthesis of DAs **3c** and **4c**. Reagents and conditions: a) $SnCl_2 \cdot 2H_2O$, H_2SO_4, THF, reflux; b) K_2CO_3, THF/MeOH (1:1 v/v), RT; c) Condition A: CuCl, TMEDA, CH_2Cl_2, reflux; Condition B: $[PdCl_2(PPh_3)_2]$, CuI, *p*-benzoquinone, Et_3N, THF, 70 °C. TMEDA = *N*,*N*,*N*',*N*'-tetramethylethylenediamine.

4-3. ^{1}H NMR Spectra and NICS Calculations

To gain insight into the structures of the DAs, the author optimized the ground-state structures of DAs **3'**, **4'**, **9'**, and **10'**, in which the 2-ethylhexyloxy groups in **3c**, **4c**, **9c**, and **10c** were replaced with methoxy groups, at the B3LYP/6-31G(d) level of theory.[100] The optimized structures of **3'** and **9'** have planar D_{2h} symmetry, whereas **4'** and **10'** are also planar with D_{3h} symmetry (Figure 4-3). The partial ^{1}H NMR spectra of **9c**, **10c**, and **30c** in $CDCl_3$ are shown in Figure 4-4. DAs **9c** and **10c** exhibit very simple NMR signals, namely a pair of two singlets in the aromatic region owing to their highly symmetrical structures. For the assignment of the ^{1}H NMR signals of the aromatic protons in **3c**, **4c**, **9c**, and **10c**, the

density functional theory (DFT) calculations for **3'**, **4'**, **9'** and **10'** at the GIAO/B3LYP/6-311++(2d,2p)//B3LYP/6-31G(d) level were conducted. The experimental and theoretical ^{1}H NMR chemical shifts are listed in Table 4-1. The theoretical chemical shifts of **3'**, **4'**, **9'** and **10'** show reasonable agreement with those of the corresponding **3c**, **4c**, **9c**, and **10c** observed experimentally.

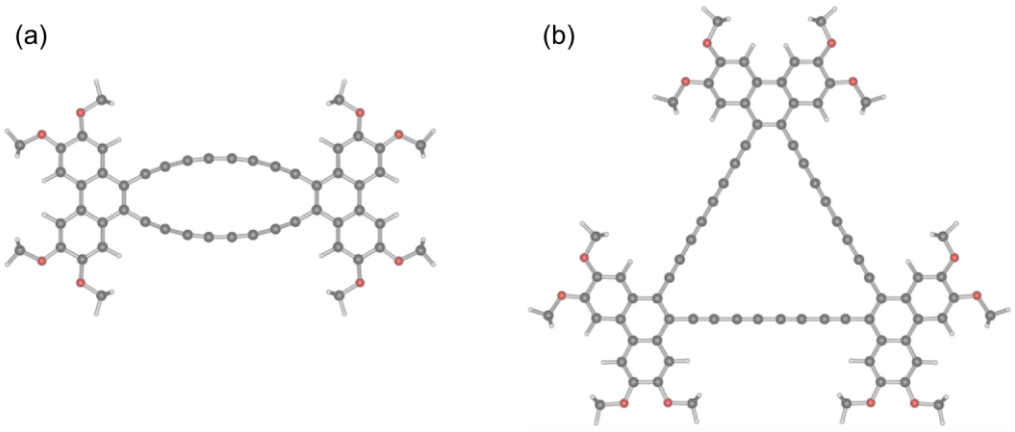

Figure 4-3. Optimized molecular structures of (a) **9'** and (b) **10'**, where the 2-ethylhexyloxy groups in **9c** and **10c** are replaced with methoxy groups (B3LYP/6-31G(d)).

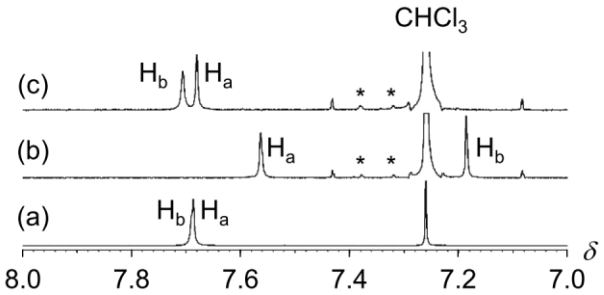

Figure 4-4. Partial ^{1}H NMR spectra of (a) **30c**, (b) **9c** (3.56×10^{-4} mol dm^{-3}), and (c) **10c** (1.68×10^{-4} mol dm^{-3}) in $CDCl_3$ at 20 °C. Peaks attributed to the impurity by solvent are labeled with asterisks.

Table 4-1. Observed and Calculated ^{1}H NMR Chemical Shifts and NICS Values for **3c**, **4c**, **9c**, **10c**, **17c**, and **30c**

	H_a		H_b			
	δ_{obs}[a]	δ_{calcd}[b]	δ_{obs}[a]	δ_{calcd}[b]	NICS(0)[c]	NICS(1)[c]
3c	7.52	7.55	7.00	6.94	+10.8	+9.5
4c	7.83	8.19	8.06	8.84	−2.3	−2.1
9c[d]	7.56	7.49	7.19	7.00	+6.0	+5.4
10c[e]	7.68	8.01	7.71	8.37	−0.8	−0.8
17c	7.70	7.84	7.79	8.10	N/A	N/A
30c	7.68	7.89	7.68	7.97	N/A	N/A

[a] In $CDCl_3$ at 25 °C. [b] Calculated by using GIAO/B3LYP/6-311++G(2d,2p)//B3LYP/6-31G(d) for **3'**, **4'**, **9'**, **10'**, **17'**, and **30'**, where the 2-ethylhexyloxy and TIPS groups in **3c**, **4c**, **9c**, **10c**, **17c**, and **30c** were replaced with methoxy and the TMS groups, respectively. [c] Calculated by using GIAO/B3LYP/6-311++G(2d,2p)//B3LYP/6-31G(d) for **3'**, **4'**, **9'**, and **10'**. [d] [**9c**] = 3.56×10^{-4} mol dm^{-3}. [e] [**10c**] = 8.43×10^{-4} mol dm^{-3}.

Planar [20]- and [30]DAs **9c** and **10c** are formally antiaromatic and aromatic, respectively. The ^{1}H NMR chemical shifts are a good measure for the elucidation of tropicity, namely paratropicity or diatropicity. Thus, the author compared the changes in the resonances ($\Delta\delta$) of the aromatic protons H_a and H_b in **9c** and **10c** from those signals in **30c**. The resonances of the aromatic protons for **9c** are upfield shifted relative to **30c** by $\Delta\delta$ = 0.12 and 0.49 ppm for H_a and H_b, respectively. The larger $\Delta\delta$ value of H_b than H_a implies the ring current of [20]DA moiety, that is, the paratropicity of **9c**. The resonances of the aromatic protons for **10c** are almost unchanged relative to **30c** by $\Delta\delta$ = 0 and 0.03 ppm for H_a and H_b, respectively, suggesting the atropicity of **10c**. The observed chemical shift changes from **30c** to **9c** and **10c** are apparently small as compared to those from **17c** to **3c** and **4c**; the $\Delta\delta$ values are 0.18 and 0.79 ppm for **3c** and 0.13 and 0.27 ppm for **4c** with respect to the signals of **17c**. These results clearly indicate the decrease of the tropicity of **9c** and **10c** relative to **3c** and **4c**, respectively. Indeed, the nucleus-independent chemical shift (NICS) (0) (and NICS(1)) values of **9'** calculated at the GIAO/B3LYP//6-311++G(2d,2p)//B3LYP/6-31G(d) level are calculated to be +6.0 (+5.4), which are less positive than those of **3'** (+10.8 (+9.5)) (Table

4-1).[111,112] The moderate NICS values of **9'** imply borderline character of **9c** between antiaromaticity and nonaromaticity. The NICS(0) (and NICS(1)) values of **10'** (−0.8 (−0.8)) are less negative than those of **4'** (−2.3 (−2.1)) and close to zero, indicating the lack of aromaticity of **10c**.

4-4. Electronic and Photophysical Properties

Figure 4-5 shows the absorption and emission spectra of **3c**, **4c**, **9c**, **10c**, **17c**, and **30c**. The longest wavelength absorption maxima (λ_{max}^{abs}) and the molar absorption coefficients (ε) of these compounds are listed in Table 4-2. The absorption bands of **3c**, **4c**, **9c**, and **10c** are located in the longer wavelength region than those of the corresponding **17c** and **30c**, reflecting the formation of the DA moieties. These observations indicate the extended π-conjugation of **3c**, **4c**, **9c**, and **10c** compared with **17c** and **30c**. The longest λ_{max}^{abs} value of **3c** (560 nm) is closely located to that of **9c** (552 nm), although the number of the tethering C≡C–C bonds differs from two to four. This similarity in the longest λ_{max}^{abs} values is originated from the combination of the extension of π-electron systems and the weakened antiaromaticity from **3c** to **9c**, which was recognized by the NMR spectroscopic investigations. In contrast, the longest λ_{max}^{abs} value of **10c** (504 nm) is red-shifted compared to that of **4c** (456 nm) apparently due to the extension of π-conjugation. Interestingly, the longest λ_{max}^{abs} value of **9c** is red-shifted relative to that of **10c** although the conjugation pathway of **9c** is shorter than that of **10c**. The difference in the longest λ_{max}^{abs} values between **9c** and **10c** may be derived from the distortion of the octatetrayne unit and/or the antiaromaticity in **9c**.[113]

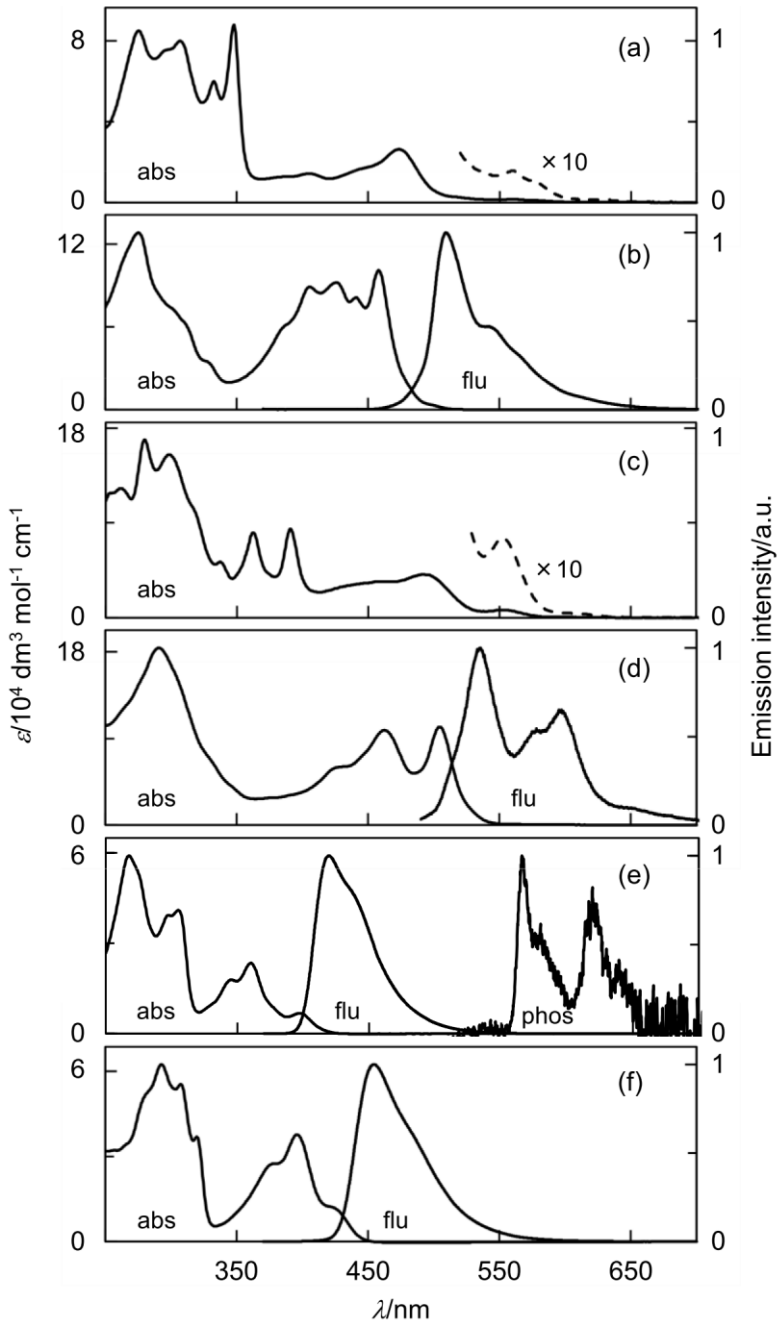

Figure 4-5. UV–vis and fluorescence spectra of (a) **3c**, (b) **4c**, (c) **9c**, (d) **10c**, (e) **17c**, and (f) **30c** in $CHCl_3$ at 25 °C, and phosphorescence spectra of **17c** in MTHF at −196 °C. Fluorescence from **3c** and **9c** in $CHCl_3$ at 25 °C, and phosphorescence from **3c**, **4c**, **9c**, **10c**, and **30c** in MTHF at −196 °C were absent.

Table 4-2. Photophysical Data of **3c**, **4c**, **9c**, **10c**, **17c**, and **30c**

	$\lambda_{max}^{abs[a]}$ [nm] (ε [dm^3 mol^{-1} cm^{-1}])	$\lambda_{max}^{fl[a]}$ [nm]	$\Phi_f^{[a,c]}$	$\tau_f^{[a,d]}$ [ns]	$k_f^{[a,e]}$ [10^7 s^{-1}]	$k_{nr}^{[a,f]}$ [10^7 s^{-1}]	$\lambda_{max}^{pho[g]}$ [nm]
3c	560 (1600)	N.D.	~0	N/A	N/A	N/A	N.D.
4c	456 (101000)	509	0.20	7.7	2.6	10.4	N.D.
9c	552 (7400)	N.D.	~0	N/A	N/A	N/A	N.D.
10c	504 (102200)	535	0.005	<0.2	N/A	N/A	N.D.
17c	397 (6900)	419	0.54	7.8	6.9	5.9	566
30c	426 (11400)	454	0.77	7.9	9.7	2.9	N.D.

[a] In $CHCl_3$ at 25 °C. [c] Fluorescence quantum yields. [d] Lifetime of fluorescence. [e] Fluorescence rate constant estimated by $k_f = \Phi_f \tau_f^{-1}$. [f] Non-radiative rate constant estimated by $k_{nr} = (1-\Phi_f)\tau_f^{-1}$. [g] In MTHF at −196 °C.

Fluorescence from **3c** and **9c** in $CHCl_3$ at 25 °C was absent, which is rationalized by considering the forbidden HOMO–LUMO transition characteristic of 4*n*π-electron systems as revealed by quantum chemical calculations (*vide infra*). Fluorescence quantum yields (Φ_f) and lifetimes (τ_f) for **4c**, **10c**, **17c**, and **30c** were determined, and based on these values, the fluorescence rates (k_f) and nonradiative rates (k_{nr}) were evaluated; these photophysical data are listed in Table 4-2. The Φ_f values of **4c** and **10c** are lower than that of **17c** and **30c**. The k_f values of **4c** and **10c** are relatively smaller than those of **17c** and **30c**, and the k_{nr} of **4c** is greater than that of **17c** and **30c**. Thus, the slower radiative and faster nonradiative processes in **4c** and **10c** than **17c** and **30c** result in lower Φ_f values of the former than the latter. Noticeably, **30c** possessing butadiyne units provides high Φ_f value of 0.77; aromatic compounds having butadiyne units are generally less fluorescent.[151–164] Very weak phosphorescence from **17c** was observed in 2-methyltetrahydrofuran (MTHF) at −198 °C, while that from **3c**, **4c**, **9c**, **10c**, and **30c** was absent. The wavelength of the 0–0 origin of the phosphorescence spectrum (λ_{max}^{pho}) is listed in Table 4-2. Observation of phosphorescence from **17c** indicates that intersystem crossing from the lowest excited singlet (S_1) state to the triplet (T_1) state is operative. Conversely, there would be two possibilities for the absence of phosphorescence in **3c**, **4c**, **9c**, **10c**, and **30c**. One is that the deactivation of the S_1 state is

governed by internal conversion to the ground state. The other is that the triplet state is nonphosphorescent in nature. Laser flash photolysis experiments of **3c**, **4c**, **9c**, **10c**, and **30c** using a 266 nm laser pulse were carried out to understand the photophysical and photochemical features of the triplet states.

Figure 4-6 shows a transient absorption spectrum obtained upon 266 nm laser pulsing in $CHCl_3$ solution of **9c**. The absorption spectrum is located from UV–vis to NIR region. The intensities of the absorption at 535 and 700 nm decreased with a rate of 2.1×10^5 s^{-1}. In the presence of the amount of oxygen, the decay was accelerated, indicating that the obtained transient signal is due to the triplet state. The transient signal data for **3c**, **4c**, **10c**, **17c**, and **30c** are deposited in Chapter 6. These transient signals for **3c**, **4c**, **10c**, and **30c** were also assigned to the triplet states. The transient signal for **17c** was not affected by the presence of the dissolved oxygen, and hence the transient species observed for **17c** may be formed by the chemical reaction from the S_1 state, though it is not identified yet. From the results of transient absorption measurements, it is inferred that the nonradiative process of the S_1 states involves the intersystem crossing to the triplet state for **3c**, **4c**, **9c**, **10c**, and **30c** and a chemical reaction for **17c** under the experimental conditions applied.

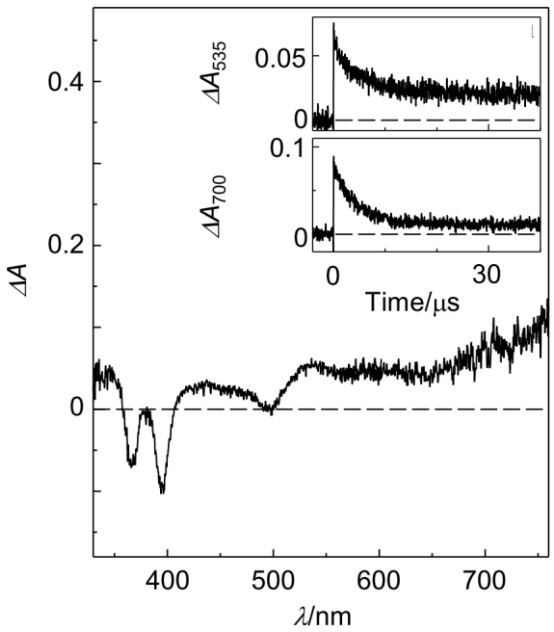

Figure 4-6. A transient absorption spectrum at 100 ns upon 266 nm laser pulsing in Ar–purged $CHCl_3$ solution of **9c** at 25 °C. Inset; traces at 535 nm (upper) and at 700 nm (lower).

Quantum chemical calculations for **9'** and **10'** were performed to investigate the electronic properties. The calculated surfaces of the molecular orbitals are depicted in Figure 4-7. The energy levels of HOMO and HOMO−1 for **4'** and **10'** are similar to each other, as are those of LUMO and LUMO+1. It can be seen for **3'**, **4'**, **9'**, and **10'** that the calculated electronic distribution is delocalized on the DA moieties. These results indicate that the extension of the oligoyne linkage does not inherently affect the delocalization of the electronic distribution on the studied molecular orbitals. The HOMOs and LUMOs of **3'** and **9'** are found to be of *ungerade*. From this result, it is inferred that the transition between HOMO and LUMO for **3'** and **9'** is symmetrically forbidden as seen for 4*n*π-electron systems.[35,58,114] By contrast, as for **4'** and **10'**, the HOMO−1s and HOMOs are of *gerade*, and the LUMOs and LUMO+1s are of *ungerade.* The transitions between HOMO or HOMO−1 and LUMO or LUMO+1 are symmetrically allowed. These considerations for the transition probability are supported from the viewpoint of the oscillator strength (*f*). The *f* values of the HOMO→LUMO transitions for **3'** and **9'** were calculated to be 0 with the

calculated longest absorption maxima (λ_{max}^{calcd}) of 716 and 783 nm for **3'** and **9'**, respectively, as listed in the Table 4-3. By contrast, the *f* values of HOMO−1→LUMO+1, HOMO−1→LUMO, HOMO→LUMO, and HOMO→LUMO+1 for **4'** and **10'** were calculated to be 1.23 (λ_{max}^{calcd} = 463 nm) and 1.36 (λ_{max}^{calcd} = 552 nm), respectively (Table 4-3); these *f* values are for allowed transitions.

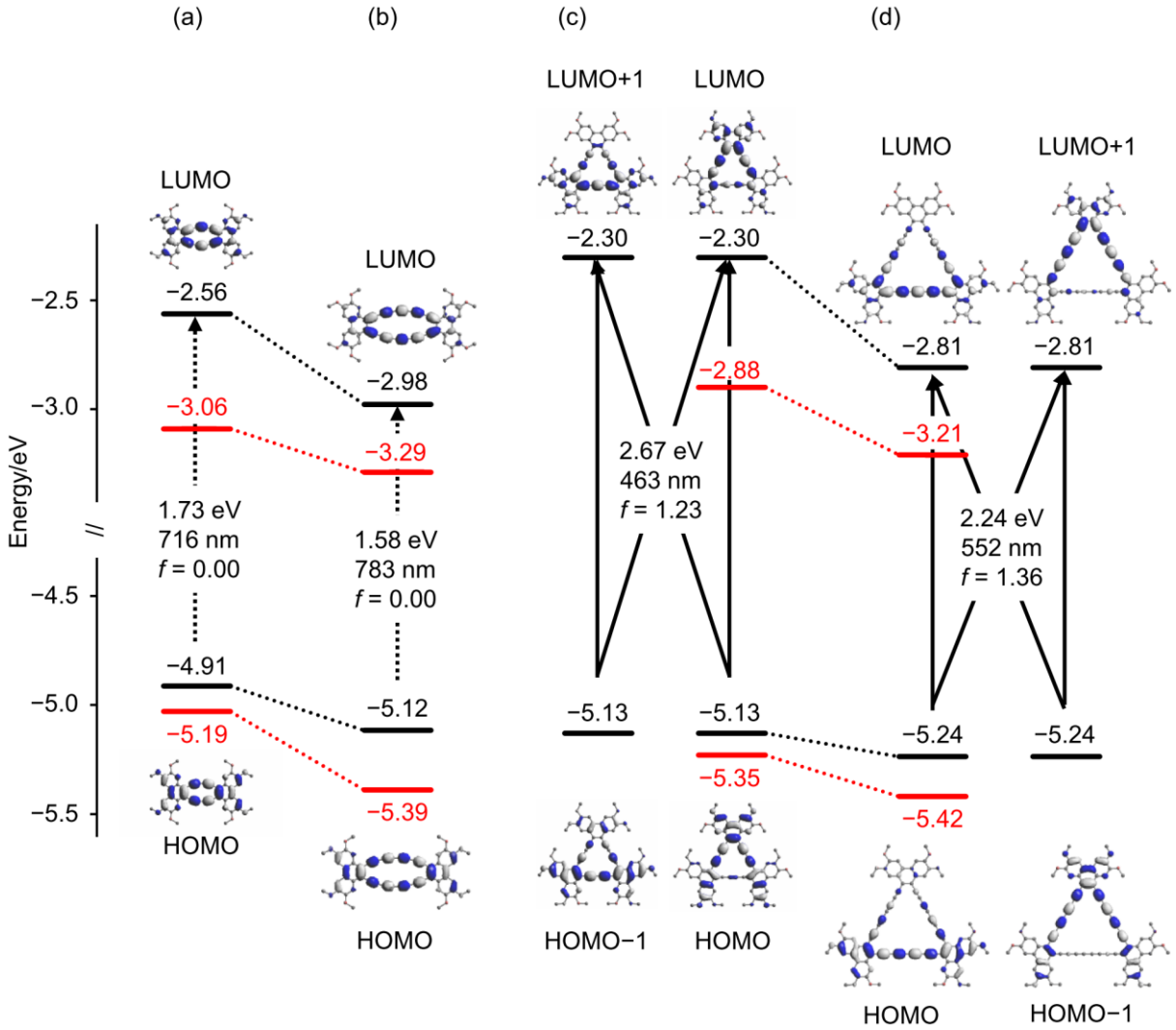

Figure 4-7. (Black) energy diagrams and frontier molecular orbital (FMO) plots of (a) **3'**, (b) **9'**, (c) **4'**, and (d) **10'** by using the B3LYP/6-31+G(d,p)//B3LYP/6-31G(d) method, and their transitions estimated by TD-DFT calculations at B3LYP/6-31G(d)//B3LYP/6-31G(d). (Red) HOMO and LUMO levels of (a) **3c**, (b) **9c**, (c) **4c**, and (d) **10c** deduced from the oxidation onset (E_{onset}^{ox}) and reduction onset (E_{onset}^{red}) values according to the following equation: HOMO = −(4.8 + E_{onset}^{ox}) eV, LUMO = −(4.8 + E_{onset}^{red}) eV.

Table 4-3. Calculated Lowest Excitation Energies of **3', 4', 9'**, and **10'**[a]

	λ_{max}^{calcd} [nm]	f[b]	Configuration
3'	716	0	H→L, 98%
4'	463	1.23	H→L, 0.45%; H−1→L+1, 45%
	463	1.23	H→L+1, 45%, H−1→L, 45%
9'	783	0	H→L, 98%
10'	552	1.36	H→L, 44%; H−1→L+1, 44%
	552	1.36	H→L+1, 44%; H−1→L, 44%

[a] TD-DFT (TD/B3LYP/6-31G(d)) calculations were carried out with the use of optimized structures at B3LYP/6-31G(d). [b] f = oscillator strength; H = HOMO; L = LUMO.

4-5. Electrochemical Properties

The electrochemical properties of **3c**, **4c**, **9c**, **10c**, **17c**, and **30c** were examined by using cyclic voltammetry (CV) and differential pulse voltammetry (DPV) in *o*-dichlorobenzene (*o*-DCB). Their oxidation onset (E_{onset}^{ox}) and reduction onset (E_{onset}^{red}) are summarized in Table 4-4. Acyclic **17c** displayed one irreversible oxidation step, and **30c** displayed two reversible oxidation waves (Figure 4-8). DAs **3c**, **4c**, **9c**, and **10c** displayed amphoteric multiredox behavior within the available potential window (Figure 4-8). The redox processes for **3c**, **4c**, **9c**, and **10c** were reversible except for the reduction processes for **4c**, whereas the redox processes for **3b** and **4b** were irreversible, as described in Chapter 2. This indicates that the cationic and anionic species of phenanthrene-fused DAs become kinetically stable by replacement of the linear decyloxy groups with the branched 2-ethylhexyloxy groups. The oxidation potentials (E_{pa}) and reduction potentials (E_{pc}) measured by CV matched the corresponding E_{pa} and E_{pc} measured by DPV; the reader is referred to Chapter 6.

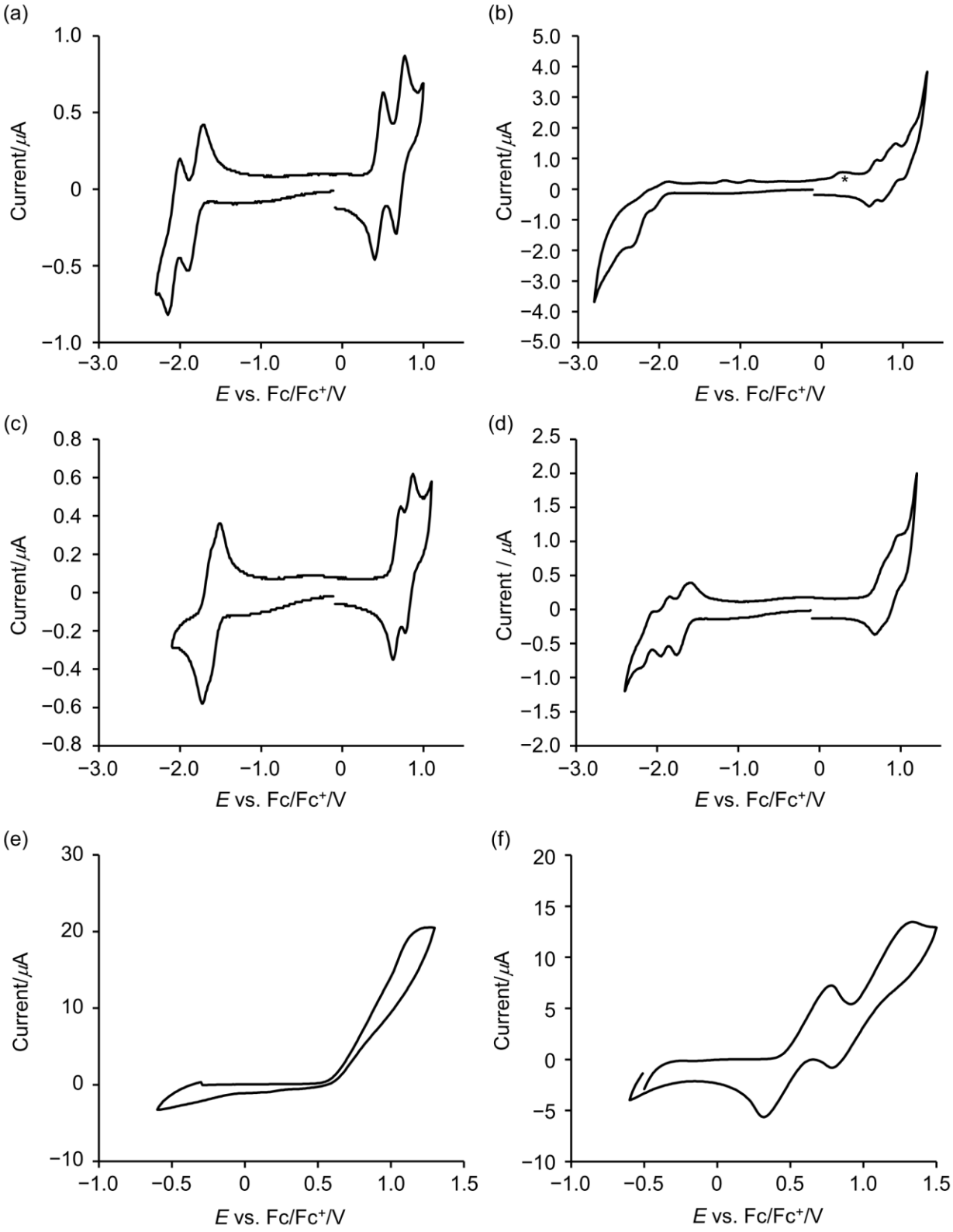

Figure 4-8. Cyclic voltammograms of (a) **3c**, (b) **4c**, (c) **9b**, (d) **10**, (e) **17b**, and (f) **30b** measured in *o*-DCB (0.1 mol dm^{-3} *n*-Bu_4NPF_6) at scan rate of 100 mV s^{-1}. The peaks attributed to the decomposed species formed by reduction are labelled with an asterisk.

Table 4-4. Oxidation and Reduction Potentials of **3c**, **4c**, **9c**, **10c**, **17c**, and **30c**,[a] Theoretically Calculated HOMO and LUMO Levels, Electrochemical HOMO–LUMO Gaps, and Optical HOMO–LUMO Gaps

	E_{onset}^{ox} (E_{pa}) [V]	E_{onset}^{red} (E_{pc}) [V]	HOMO[b] [eV]	LUMO[b] [eV]	ΔE_{redox}[c] [V]	ΔE_{calcd}[b] [eV]	ΔE_{opt}[d] [eV]
3c	+0.39	−1.74	−4.91	−2.56	2.13	2.35	2.21
	(+0.51)[e]	(−1.90)[e]					
	(+0.77)[e]	(−2.15)[e]					
4c	+0.55	−1.92	−5.13	−2.30	2.47	2.83	2.72
	(+0.68)[e]	(−2.10)[f]					
	(+0.93)[e]	(−2.33)[g]					
	(+1.15)[e]						
9c	+0.59	−1.51	−5.12	−2.98	2.10	2.14	2.25
	(+0.72)[e]	(−1.72)[e]					
	(+0.87)[e]						
10c	+0.62	−1.59	−5.24	−2.81	2.21	2.43	2.46
	(+0.79)[f]	(−1.76)[e]					
	(+0.95)[f]	(−1.95)[e]					
		(−2.19)[e]					
17c	+0.63	N.D.	−5.40	−1.75	N.A.	3.65	3.12
30c	+0.44	N.D.	−5.43	−2.21	N.A.	3.22	2.91
	(+0.78)[f]						
	(+1.33)[f]						

[a] Measuring by using CV in *o*-DCB (0.1 mol dm^{-3} *n*-Bu_4NPF_6). All the potentials are given versus the Fc^+/Fc couple as an external standard. Scan rate = 100 mV s^{-1}. [b] Calculated by using B3LYP/6-31+G(d,p)//B3LYP/6-31G(d) for **3'**, **4'**, **9'**, **10'**, **17'**, and **30'**, where the 2-ethylhexyloxy and TIPS groups in **3c**, **4c**, **9c**, **10c**, **17c**, and **30c** were replaced with methoxy and TMS groups, respectively. [c] The electrochemical gap (ΔE_{redox}) is defined as the potential difference between E_{onset}^{ox} and E_{onset}^{red}. [d] The optical gap (ΔE_{opt}) is defined as the longest maximal absorption wavelength. [e] Reversible wave. [f] Quasireversible wave. [g] Irreversible wave.

The E_{onset}^{ox} values for both **3c** and **4c** are more negative than that for **17c**, while the E_{onset}^{ox} values for both **9c** and **10c** are more positive than that for **30c**. Both the E_{onset}^{ox} and E_{onset}^{red} values for **9c** and **10c** are positively shifted as compared to those for **3c** and **4c**. The observed potential shifts should reflect the stronger electron-withdrawing ability of an octatetrayne unit than a butadiyne unit.[146] From **3c** to **9c**, the positive shift of the E_{onset}^{ox}

values is almost the same as that of the E_{onset}^{red} values, and thus the potential difference (ΔE_{redox}) between the E_{onset}^{ox} and E_{onset}^{red} values of **3c** and **9c** are similar to each other. On the other hand, from **4c** to **10c**, the positive shift of the E_{onset}^{red} value is pronounced relative to that of the E_{onset}^{ox} value, and hence the ΔE_{redox} of **10c** is smaller than that of **4c**. A good correlation exists between the optical gaps (ΔE_{opt}) and the ΔE_{redox} in **3c**, **4c**, **9c**, and **10c**, suggesting that the same orbitals, namely HOMO and LUMO, are involved in both optical and electrochemical gaps for **3c**, **4c**, **9c**, and **10c**. Thus, the oxidation and reduction of **3c**, **4c**, **9c**, and **10c** occurred on their DA moieties, which is supported by the finding that their HOMOs and LUMOs have large contribution from the DA rings (*vide supra*). The ΔE_{redox} values for **3c**, **4c**, **9c**, and **10c** match the calculated gaps (ΔE_{calcd}) for the corresponding **3'**, **4'**, **9'**, and **10'**.

An analysis of the influence of electron donating 2-ethylhexyloxy groups on the E_{pa} values of **3c**, **4c**, **9c**, and **10c** gives a deeper insight into the antiaromatic characteristic of **3c** and **9c**. Going form **3c** and **9c** to **4c** and **10c**, the number of 2-ethylhexyloxy groups increases from eight to twelve, however, both the first and second E_{pa} values of **3c** and **9c** are more negative than those of **4c** and **10c**, respectively. Thus, it seems that the antiaromatic character of **3c** and **9c** provides an explanation for the observed readiness to release electrons as compared to the corresponding **4c** and **10c**; it is easier to withdraw two electrons from antiaromatic $4n\pi$ systems. The difference of the first E_{pa} values between **9c** and **10c** (0.07 V) is smaller than that between **3c** and **4c** (0.17 V), suggesting the weaker antiaromaticity of **9c** than **3c**; this is in good agreement with the finding that the NICS values of **9'** are less positive than that of **3'** as described above.

4-6. Self-association

The author has described that **3b** and **4b** aggregate in $CDCl_3$ by effective π–π interactions in Chapter 2. In order to elucidate the effects of the bulkiness of alkoxy groups on the phenanthrene moieties and the length of oligoyne linkages on the self-association behavior of DAs, the ^{1}H NMR spectral measurements of **3c**, **4c**, **9c**, and **10c** in $CDCl_3$ were carried out at the concentration of 10^{-2}–10^{-5} mol dm^{-3}. Unlike **3b** and **4b**, the resonances of the aromatic protons in **3c** and **4c** were almost independent of concentrations, indicating that **3c** and **4c** are mainly present as a monomer under these conditions, which should be attributed to the bulky 2-ethylhexyloxy groups.[165,166] Noticeably, in contrast to **3c** and **4c**, the ^{1}H NMR signals of **9c** and **10c** are concentration-dependent with aromatic proton signals moving upfield upon increasing concentrations as shown in Figure 4-9. This demonstrates that **9c** and **10c** form stacked aggregates by π–π interactions and the extension of the oligoyne linkages apparently enhances the self-association ability. The diffusion coefficients (*D*) for **9c** and **10c** were almost independent of the concentrations on the basis of the diffusion NMR experiments, suggesting that a monomer–dimer equilibrium predominantly exists. The plots of the chemical shifts of the aromatic protons vs the concentrations of **9c** and **10c** were fitted to a curve for the monomer–dimer model (Figure 4-9), which produced the self-association constants (*K*) of **9c** and **10c** to be 9 and 62 dm^3 mol^{-1}, respectively (Table 4-5). The larger *K* value of **10c** than **9c** should reflect the larger number of phenanthrene moieties of the former than the latter.

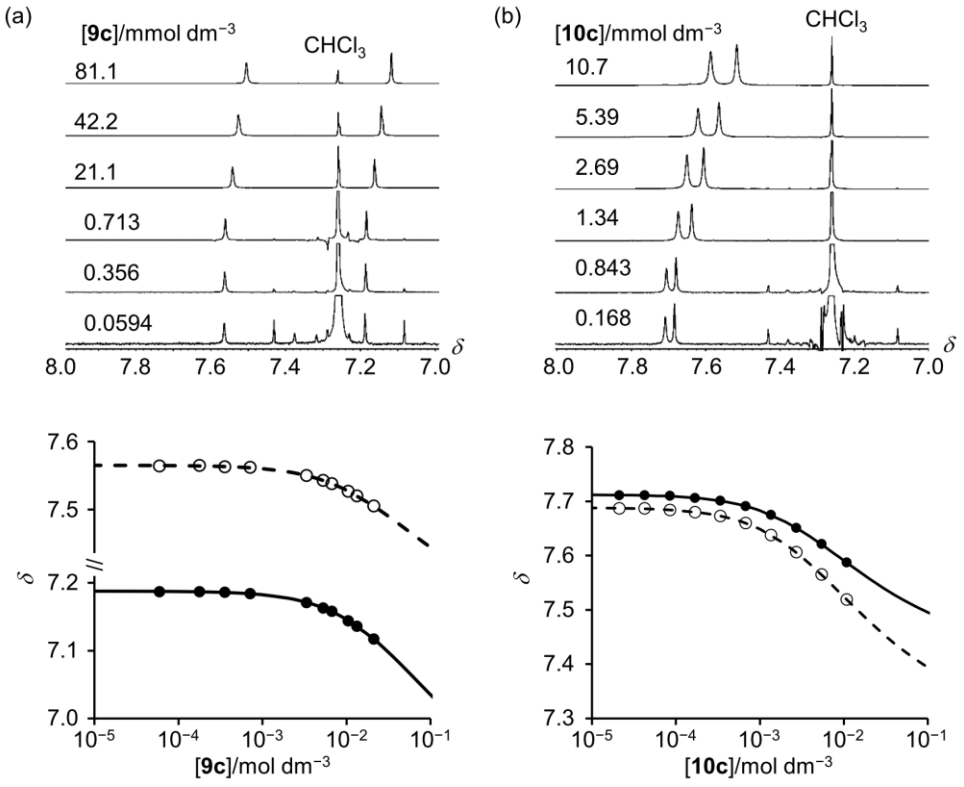

Figure 4-9. Partial ^{1}H NMR spectra of (a) **9c** and (b) **10c** in $CDCl_3$ in various concentrations at 20 °C (top) and the corresponding nonlinear curve-fitting plots of the concentration dependence of the chemical shifts of the aromatic protons (bottom).

Table 4-5. Association Constants and Thermodynamic Parameters of **3c**, **4c**, **9c**, and **10c**

	$CDCl_3$[a]			MCH[b]		
	K[c]	ΔH	ΔS	K	ΔH	ΔS
	[dm^3 mol^{-1}]	[kJ mol^{-1}]	[J K^{-1} mol^{-1}]	[dm^3 mol^{-1}]	[kJ mol^{-1}]	[J K^{-1} mol^{-1}]
3c	~0	N.D.	N.D.	400[c,d]	−23[d]	−26[d]
4c	~0	N.D.	N.D.	16[c,d]	−25[d]	−60[d]
9c	9	−8.8	−12	1400[c,e] (1600)[f]	−68[e]	−170[e]
10c	62	−19	−32	43000[c,e] (33000[f])	−75[e]	−167[e]

[a] Monomer–dimer model. [b] Isodesmic model. [c] At 20 °C. [d] ^{1}H NMR experiments (concentration dependence). [e] UV–vis experiments (temperature dependence). [f] UV–vis experiments (concentration dependence) at 25 °C.

It is well known that the self-association behavior of π-conjugated compounds is highly solvent-dependent.[167] The author analyzed the self-association behavior of **3c**, **4c**, **9b**, and **10c** in non-polar methylcyclohexane (MCH) by ^{1}H NMR spectroscopy at the concentration of 10^{-2}–10^{-5} mol dm^{-3}. Unlike in the case in $CDCl_3$, the ^{1}H NMR signals of **3c** and **4c** in MCH were concentration-dependent; their aromatic proton signals shifted upfield with increasing the concentrations. This indicates the occurrence of self-association of **3c** and **4c**, which hints a solvophobic contribution of MCH to their self-association. The *K* value of **4c** (16 dm^3 mol^{-1}), which were determined on the basis of the isodesmic model, is smaller than that of **3c** (400 dm^3 mol^{-1}), although the π framework of the former is larger than the latter; as for the determination of the *K* values, the reader is referred to Chapter 6. According to the PM7 calculations for **3c'** and **4c'**, in which the 2-ethylhexyloxy groups in **3c** and **4c** were replaced with the hexyloxy groups, there is steric hindrance from the alkoxy groups in **4c'** in contrast to **3c'** (Figure 4-10), which should result in the smaller *K* value of **4c** than **3c**. Pronounced concentration-dependent ^{1}H NMR chemical shift changes were observed for **9c**; the *K* value of **9c** in MCH was estimated to be 2200 dm^3 mol^{-1}. DA **10c** showed considerably broad proton signals even at the dilute concentration of 2.19×10^{-6} mol dm^{-3}, representing a high degree of self-association of **10c** as compared to **3c**, **4c**, and **9c**, however, the determination of the *K* value of **10c** in MCH was not possible.

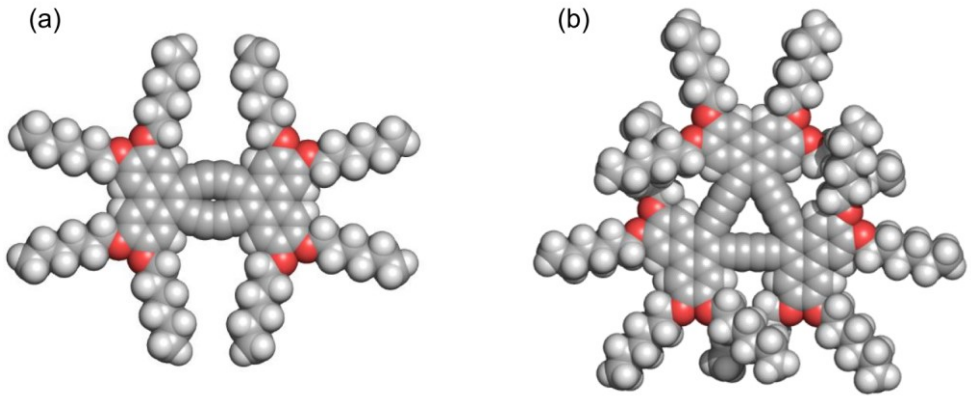

Figure 4-10. PM7-optimized structures of (a) **3c'** and (b) **4c'**, where the 2-ethylhexyloxy groups in **3c** and **4c** are replaced with hexyloxy groups.

Therefore, the author investigated the self-association behavior of **3c**, **4c**, **9c**, and **10c** in MCH by UV–vis spectroscopy in the concentration region of *ca.* 10^{-3}–10^{-7} mol dm^{-3}; broad concentration ranges are accessible by UV–vis spectroscopy relative to NMR spectroscopy. The UV–vis spectra of **3c** and **4c** were almost concentration-independent, indicating that **3c** and **4c** mainly exist as monomeric species under the dilute conditions measured. In stark contrast, the absorption bands of **9c** and **10c** became red-shifted through several isosbestic points upon increasing concentrations as shown in Figure 4-11a,b. These results indicate that **9c** and **10c** produce *J*-type assemblies by self-associations and equilibrate with their stacked assemblies. The *K* values of **9c** and **10c** were estimated to be 1600 and 33000 dm^3 mol^{-1}, respectively, according to the isodesmic model, and found to be hundreds of times as high as the *K* values in $CDCl_3$. The UV–vis spectra of **9c** and **10c** were also sensitive to temperature, and thus the λ_{max}^{abs} values were blue-shifted upon warming the solution from 5 °C to 60 °C (Figure 4-11c,d). The *K* values of **9c** and **10c** were estimated to be 1400 and 43000 dm^3 mol^{-1}, respectively, which are reasonably comparable to the values obtained by concentration-dependent UV–vis spectroscopic measurements.

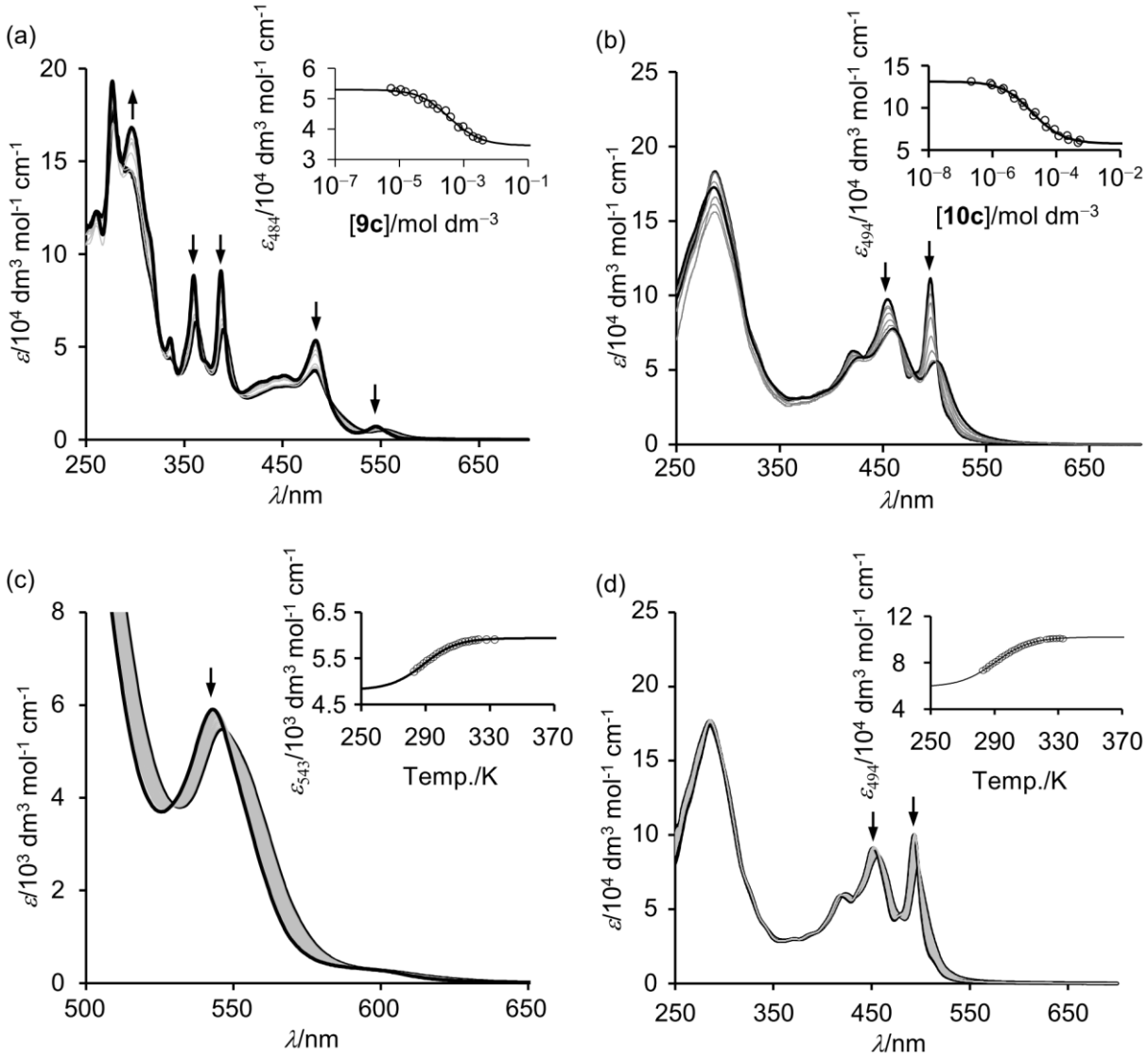

Figure 4-11. UV–vis spectra at various concentration of (a) **9c** ([**9c**] = 5.48 × 10^{-6}–3.87 × 10^{-3} mol dm^{-3}) and (b) **10c** ([**10c**] = 4.85 × 10^{-4}–2.21 × 10^{-7} mol dm^{-3}) in MCH. Arrows indicate the spectral changes with increasing concentration. Inset; Fitting of the change in the molar absorptivity at (a) 484 and (b) 494 nm to the isodesmic model. UV–vis spectra of (c) **9c** (2.04 × 10^{-3} mol dm^{-3}) and (d) **10c** (1.21 × 10^{-5} mol dm^{-3}) in MCH at various temperatures. Arrows indicate the spectral changes with decreasing temperature. Inset; Fitting of the change in the molar absorptivity at (c) 543 and (d) 494 nm to the isodesmic model.

The author investigated the thermodynamics of the self-association behavior of **3c**, **4c**, **9c**, and **10c**. The van't Hoff plots gave the thermodynamic parameters, namely enthalpic term (ΔH) and entropic term (ΔS), for the self-association as summarized in Table 4-5. In any cases, both the ΔH and ΔS values are negative, illustrating that their self-association processes are enthalpy-driven and entropy-opposed.

The self-association of **9c** and **10c** is enthalpically more favored than that of **3c** and **4c**, respectively; the ΔH values of **3c**, **4c**, **9c**, and **10c** are −23, −25, −68, and −75 kJ mol^{-1}, respectively. This suggests that the extension of oligoyne linkages from butadiyne to octatetrayne units enhances the π–π stacking interactions. The well-known polar/π model predicts that the introduction of electron-withdrawing substituents reduces the electron density of the π-system and thus decreases the electrostatic repulsion between π-electrons and promotes π-stacking interactions as briefly described in Chapter 3.[168] To examine the electronic effect of the oligoyne linkages on the self-association of DAs, the electrostatic-potential surface (ESPs) and molecular electrostatic potentials (MEPs) of **3'** and **9'** at the B3LYP//6-31+G(d,p)//B3LYP/6-31G(d) level were calculated (Figure 4-12). The MEPs at 2 Å above the center of the benzene rings of phenanthrene moieties are −10.7 and −11.3 kcal mol^{-1} for **3'** and −8.1 and −8.0 kcal mol^{-1} for **9'**. These results indicate a less-negative character for the phenanthrene moieties of **9c** than **3c**. Accordingly, it is likely that the self-association of **9c** and **10c** are greatly facilitated relative to **3c** and **4c**, respectively, due to the strong electron-withdrawing effect of octatetrayne linkages in **9c** and **10c**, which is in good agreement with the polar/π model. DAs **9c** and **10c** show large negative ΔS values compared to **3c** and **4c**, respectively; the ΔS values are −26, −60, −170, and −167 J K^{-1} mol^{-1} for **3c**, **4c**, **9c**, and **10c**, respectively. Interestingly, the trend of the ΔS values for **3c**, **4c**, **9c**, and **10c** follows that of their ΔH values, and thus the enthalpy–entropy compensation seems to apply. This finding supports that the molecular motion of **9c** and **10c** in the aggregates are restricted relative to that of **3c** and **4c**, respectively, reflecting the more effective π–π stacking interactions in the former than the latter. The more negative ΔH values of **4c** and **10c** than **3c** and **9c**, respectively, suggest that strong π–π stacking interactions are operative in **4c** and **10c** relative to **3c** and **9c**, respectively, which are probably due to larger π-electron systems of the former than the latter.

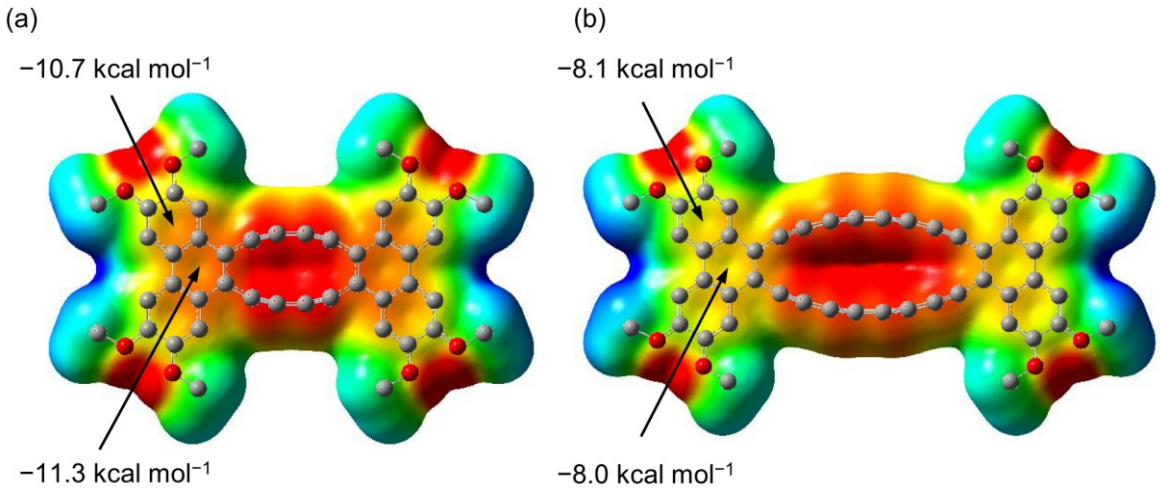

Figure 4-12. EPSs and values of the MEPs; the calculated position of the MEPs are 2 Å above the center of the benzene rings of (a) **3'** and (b) **9'** at the level of B3LYP/6-31+G(d,p)//B3LYP/6-31G(d). The Potentials are drawn in the same color scale, with red indicating more-negative electrostatic potentials and blue, more-positive potentials.

The self-association of **9c** and **10c** in MCH is enthalpically more favored but entropically less favored than that in $CDCl_3$. The enthalpic contributions are involved in desolvation as well as attractive electrostatic forces. A well-solvated solute commonly receives small enthalpic contribution during its association, because the desolvation of the solvent and the solute has to pay a large enthalpic cost. The author observed that **9c** and **10c** together with **3c** and **4c** are highly soluble in $CHCl_3$ relative to MCH, which should rationalize the finding that the ΔH values of **9c** and **10c** in MCH are significantly negative relative to those in $CHCl_3$.

4-7. Self-assembled Superstructures

In Chapter 2, the author has described that **3b** and **4b** formed 1D superstructures with high aspect ratio by self-assembly driven by π–π interactions; microbelts with lengths of > 300 μm and widths of 0.2–1 μm were obtained from **3b**, and nanofibers with lengths of > 1 μm and widths of 0.05–0.1 μm were obtained from **4b**. The author became interested in the elucidation of the influence of the bulkiness of alkoxy groups appended to the phenanthrene moieties and the size of the DA moiety on the morphology of superstructures and hence carried out the fabrication of self-assembled structures of **3c**, **4c**, **9c**, and **10c** through a phase-transfer method. Thus, to a solution of **3c**, **4c**, **9c**, and **10c** in $CHCl_3$ (5×10^{-3} mol dm^{-3}), *ca.* 80 vol. % EtOH was slowly added so that two phases can be maintained. The resulting mixtures were allowed to stand at room temperature for a day to afford the aggregates, which were visualized by scanning electron microscopy (SEM) as shown in Figure 4-13. DA **3c** formed microrods, namely prismatic structures with lengths of 5–100 μm and widths of 1–10 μm, while **4c** produced large platelet structures with lengths of 1–2 mm and widths of 100–200 μm. The lower self-association ability of **3c** and **4c** than **3b** and **4b** may give rise to the lower aspect ratio of self-assembled structures of the former than the latter. DAs **9c** and **10c** were found to form more flexible superstructures than **3c** and **4c**. Thus, **9c** produced slightly twisted microbelts with lengths of 10–1000 μm and widths of 0.3–3 μm. A number of microrods with lengths of 5–50 μm and widths of 0.3–2 μm also coexisted. DA **10c** formed microrods with lengths of 5–10 μm and widths of 0.5–1 μm and 0D microspheres with diameters of 4–10 μm. The microsphere was connected to the neighboring one or microrod to form irregular clusters.

Solvent is an important factor for molecular self-assembly in the solution-based process.[169] Therefore, the author conducted the fabrication of self-assembled clusters for **3c**, **4c**, **9c**, and **10c** by replacement of the good solvent from $CHCl_3$ to MCH. As shown in Figure 4-14, the morphology of superstructures of **3c**, **4c**, and **9c** obtained from MCH/EtOH system is

essentially similar to that obtained from a $CHCl_3$/EtOH system. Noticeably, the morphology of self-assembled clusters of **10c** obtained from MCH/EtOH system is quite different from that obtained from $CHCl_3$/EtOH system. Thus, helically twisted microrods with lengths of 10–20 μm and widths of 0.5–3 μm were observed together with microspheres (Figure 4–14g), and a straight microrods formed from $CHCl_3$/EtOH system was no longer observable. These results suggest that the self-assembling processes of **10c** in MCH/EtOH system are distinct from those in $CHCl_3$/EtOH system.

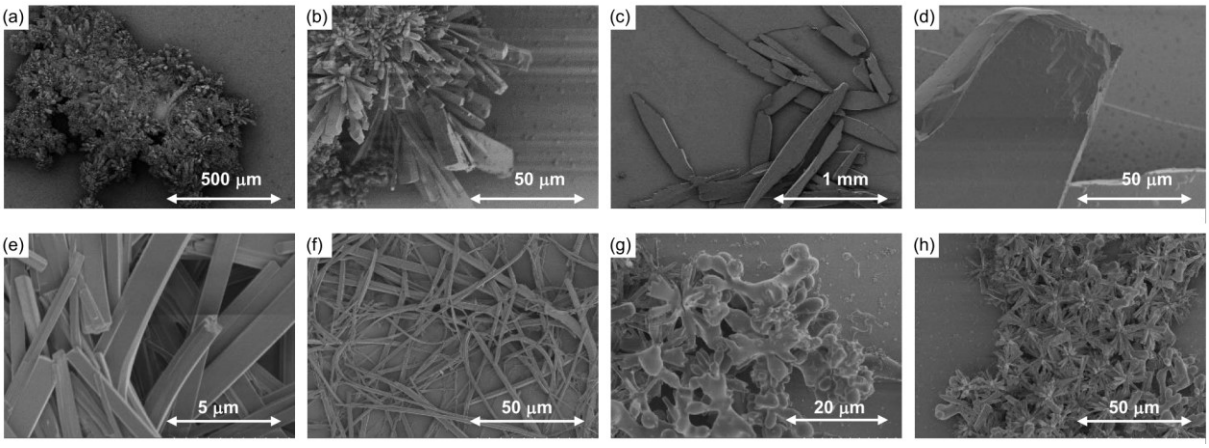

Figure 4-13. SEM images of (a,b) **3c**, (c,d) **4c**, (e,f) **9c**, and (g,h) **10c** obtained from $CHCl_3$/EtOH system.

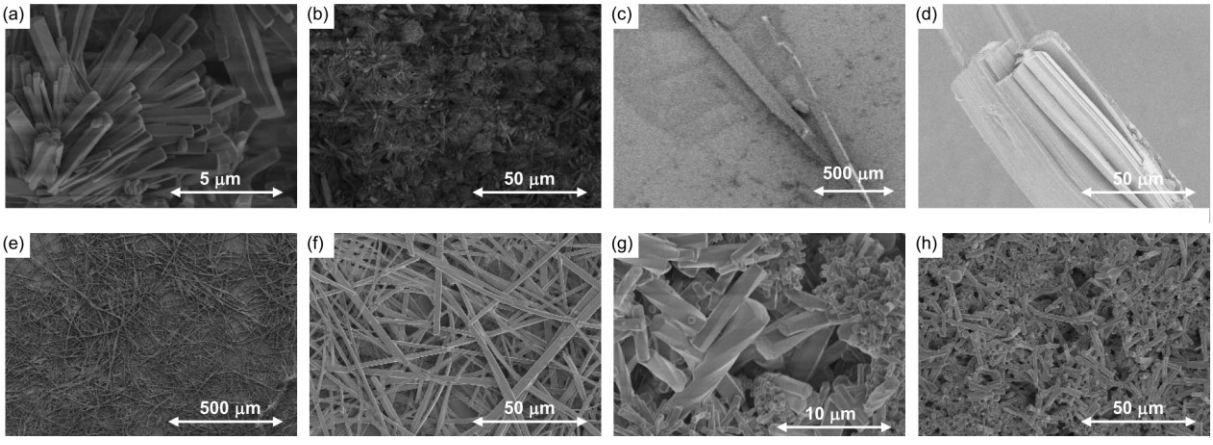

Figure 4-14. SEM images of (a,b) **3c**, (c,d) **4c**, (e,f) **9c**, and (g,h) **10c** obtained from MCH/EtOH system.

Ostwald's rule of order states that the less stable (namely metastable) polymorph forms first and then gets converted to a more stable polymorph;[170,171] it is possible that the initially formed metastable polymorph converts to the more stable one directly and/or by repetition of dissolution and adhesion of the molecules. From a closer inspection of the images obtained for **10c** (Figure 4-15), it is considered that the morphological changes of **10c** are as follows. In $CHCl_3$/EtOH system, molecules of **10c** formed metastable 0D microspheres at the beginning, which radiate to produce radially-connected, straight 1D microrods (Figure 4-15a–d), while in MCH/EtOH system initially formed microspheres deform elliptically (Figure 4-15e,f) and subsequently evolve into helically twisted microrods (Figure 4-15g,h). The observed supramolecular organization of **10c** depending on the solvents used, *i.e.* supramolecular polymorphism, is considered to stem from a combination of the difference of polarity between $CHCl_3$ and MCH and the difference of the solubility of **10c** toward $CHCl_3$ and MCH; however, the reason why only **10c** showed marked polymorphism is not clear at present. It is pointed out the rapid precipitation of compounds from the molecularly dispersed solutions tends to afford kinetically trapped aggregates.[172] The morphology of the drop-casted films of **3c**, **4c**, **9c**, and **10c** from MCH solutions (1×10^{-4} mol dm^{-3}) on SiO_2 has been visualized by atomic force microscope (AFM) (Figure 4-16). Interestingly, the AFM image for **10c** exhibited the appearance of globular aggregates uniformly, supporting the formation of microspheres from **10c** at the initial stage of self-assembly by the phase-transfer method. The images of **3c**, **4c**, and **9c** showed the presence of needle-like aggregates as expected from the SEM images of their superstructures.

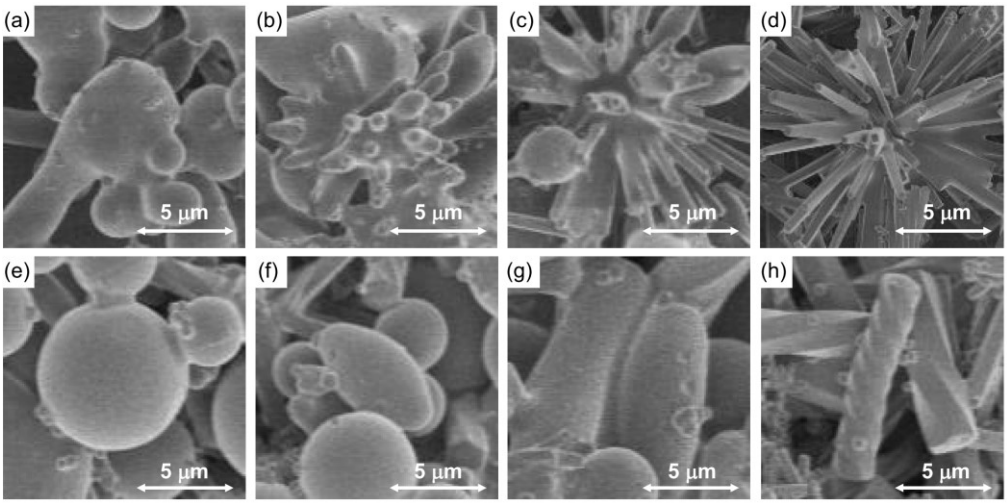

Figure 4-15. Different regions of the SEM images of superstructures of **10c** (a–d) obtained from $CHCl_3$/EtOH system and (e–h) MCH/EtOH system.

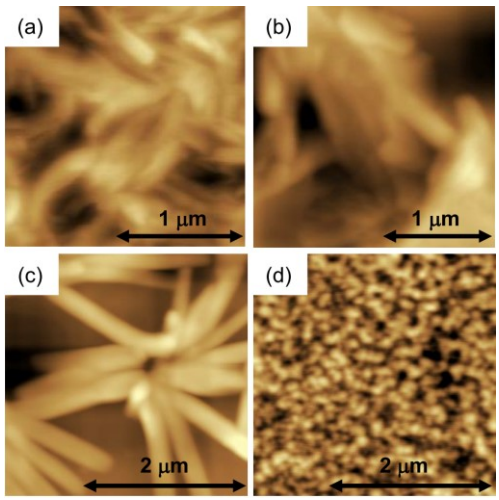

Figure 4-16. AFM images of the drop cast films of (a) **3c**, (b) **4c**, (d) **9c**, and (d) **10c** obtained from MCH solution.

The self-assembled clusters of **3c**, **4c**, **9c**, and **10c** were further investigated by wide-angle X-ray diffraction (WAXD) measurements. The WAXD patterns of the superstructures obtained from $CHCl_3$/EtOH system were shown in Figure 4-17. Although a number of peaks with strong intensity were observed in the region of 2θ = 5–10°, the author could not deduce the molcular-packing mode from these patterns; however, the effects of the length of oligoyne linkages and the topology of the DA moieties on the crystallinity of the

self-assembled clusters are visible from inspection of the peaks around 2θ = 23° (d spacing = 3.8 Å), which corresponds to π–π stacking distance along the growth direction of the cluster, and the results are generally consistent with the SEM measurements. The diffraction pattern of assembled **3c** showed sharp peaks at 2θ = 24.9°, 22.0° and 20.9° (d spacing = 3.6, 4.0. and 4.2 Å, respectively). The assembled **4c** exhibited peaks at 2θ = 25.0° and 21.1° (d spacing = 3.6 and 4.2, respectively). As compared to the assembled **3c**, the WAXD pattern of the assembled **9c** displayed broad peaks at 2θ = 24.1°, 21.6°, and 20.7° (d spacing = 3.7, 4.1, and 4.3 Å). The assembled **10c** showed a significantly broad peak at 2θ = 19–25°. The overall results suggest that the extension of oligoyne linkages decreases the crystallinity of the self-assembled clusters, and the [12]- and [20]DA moieties with a ellipsoidal topology are responsible for the high crystallinity of the suparstructures relative to the [18]- and [30]DA moieties with a triangular topology, respectively.

The WAXD patterns of the superstructures of **3c**, **4c**, and **9c** obtained from MCH/EtOH system are quite similar to the patterns of the corresponding superstructures obtained from $CHCl_3$/EtOH system in a whole region (Figure 4-18). This demonstrates that the molecular arrangement and the crystallinity of the superstructures of **3c**, **4c**, and **9c** are almost independent of the good solvents used for self-assembly as expected from the SEM observations. Interestingly, the assembled **10c** also afforded similar diffraction patterns irrespective of solvents, suggesting that the molecular arrangement in the clusters of **10c** obtained from MCH/EtOH system resembles that obtained from $CHCl_3$/EtOH system in spite of the drastically different morphology depending on the solvents.

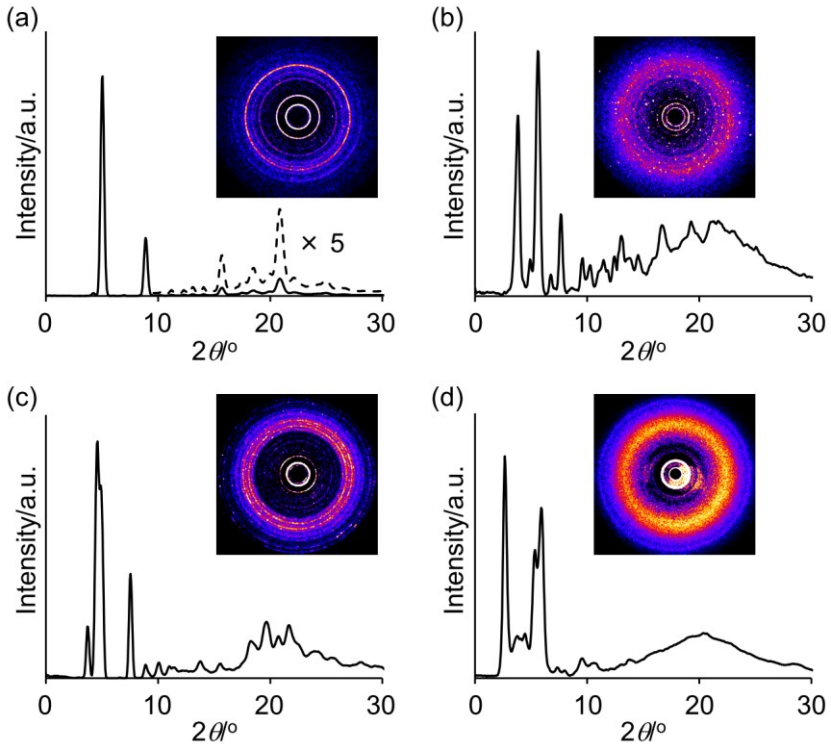

Figure 4-17. WAXD profiles of superstructures of (a) **3c**, (b) **4c**, (c) **9c**, and (d) **10c** obtained from $CHCl_3$/EtOH solvent system at 25 °C.

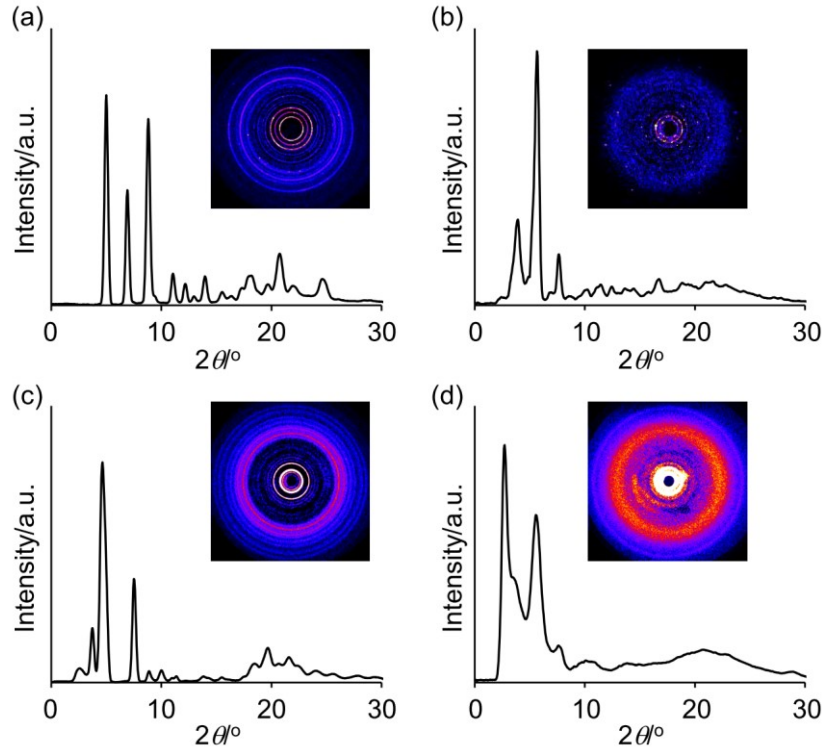

Figure 4-18. WAXD profiles of superstructures of (a) **3c**, (b) **4c**, (c) **9c**, and (d) **10c** obtained from MCH/EtOH solvent system at 25 °C.

4-8. Conclusions

The author has synthesized tetraalkoxyphenanthrene-fused [20]- and [30]DAs **9c** and **10c** possessing octatetrayne linkages together with [12]- and [18]DAs **3c** and **4c** possessing butadiyne linkages. DAs **9c** and **10c** are remarkably stable enough to be readily handled in a neat form, which is in stark contrast to the previously reported macrocycles with an octatetrayne unit. The expansion of DA core by extension of the acetylenic linkages from butadiyne to octatetrayne units decreases the tropicity, and thus **9c** and **10c** are considered to be weakly antiaromatic and nonaromatic, respectively. Both the HOMO and LUMO levels of **9c** and **10c** become lower than those of **3c** and **4c** reflecting the stronger electron withdrawing effect of an octatetrayne unit than a butadiyne unit. DAs **9c** and **10c** were found to self-associate more strongly than **3c** and **4c**. For the first time, the detailed thermodynamic study on self-association behavior of conjugated macrocycles possessing octatetrayne linkages was carried out. The more negative ΔH values for the self-association of **9c** and **10c** than **3c** and **4c** clearly demonstrates that the octatetrayne linkages effectively promote π–π stacking interactions due to their electron-withdrawing ability, which is in line with the polar/π model. The increase in the enthalpic contribution is counterbalanced by increasing the entropic cost, that is, enthalpy-entropy compensation applies. DAs **3c**, **4c**, **9c**, and **10c** produced 1D self-assembled clusters, which differ in the morphology and the crystallinity depending on the length of the acetylenic linkages, the topology of DA core, and the bulkiness of alkoxy groups appended to the phenanthrene moieties. The intriguing supramolecular organization of **10c** depending on the solvent polarity was observed.

4-9. Experimental Section

Preparation of 13c: To a solution of **12c** (4.04 g, 5.58 mmol) in CH_2Cl_2 was added $TiCl_4$ (2.45 mL, 22.3 mmol) at 0 °C under argon atmosphere and the resulting mixture was stirred for 5 min. $MoCl_5$ (3.35 g, 12.29 mmol) was added and the mixture was stirred for 10 min at

room temperature, and then an ice-cold H_2O was added. The organic phase was separated, and the aqueous phase was extracted with CH_2Cl_2. The combined organic phase was washed with H_2O, dried over anhydrous $MgSO_4$, and evaporated under reduced pressure. The residue was purified by silica gel column chromatography (hexane/ethyl acetate, 1:30 to 1:1) to afford **13c** (2.24 g, 3.10 mmol, 55%) as deeply red solids. M.p. 113–120 °C; ^{1}H NMR ($CDCl_3$, 600 MHz): δ 0.90 (t, 6H, J = 7.2 Hz), 0.90 (t, 6H, J = 6.9 Hz), 0.94 (t, 6H, J = 7.2 Hz), 0.98 (t, 6H, J = 7.5 Hz), 1.31–1.58 (m, 32H), 1.75–1.84 (m, 4H), 3.90–3.96 (m, 4H), 4.07 (d, 4H, J = 5.4 Hz), 7.10 (s, 2H), 7.51 (s, 2H); ^{13}C NMR ($CDCl_3$, 150 MHz): δ 11.32, 11.47, 14.20, 23.16, 23.18, 24.05, 29.21, 29.28, 30.70, 30.75, 39.54, 39.64, 71.57, 71.73, 106.93, 112.81, 124.45, 131.30, 149.91, 156.02, 179.38 (21 signals out of 23 expected); UV–vis (CH_2Cl_2): λ_{max}^{abs} (relative intensity) = 293 (0.91, sh), 300 (1.00), 367 (0.29), 518 (0.02) nm; MALDI-TOF-MS (dith, positive): 743.20 $[M+Na]^+$; Elemental analysis calcd (%) for $C_{46}H_{72}O_6$: C 76.62, H 10.06, found: C 76.27, H 9.83.

Preparation of 27b: To a solution of TMSA (1.00 mL, 7.05 mmol) in THF (15 mL) was added dropwise a *n*-BuLi hexane solution (2.69 mol dm^{-3}, 2.49 mL, 6.72 mmol) at −78 °C under argon atmosphere. After stirring at room temperature for 30 min, a solution of **13b** (1.40 g, 1.68 mmol) in THF (10 mL) was added dropwise to the mixture at −78 °C. After stirring at room temperature for 40 min, $(MeO)_2SO_2$ (1.11 mL, 11.8 mmol) was added dropwise to the mixture at −78 °C. After the mixture was stirred at room temperature for 15 h, the resulting mixture was diluted with H_2O. The organic phase was separated, and the aqueous phase was extracted with ethyl acetate. The combined organic phase was washed with H_2O, dried over anhydrous $MgSO_4$, and evaporated under reduced pressure. The residue was purified by silica gel column chromatography (hexane/CH_2Cl_2, 1:1) to afford **27b** (1.18 g, 1.12 mmol, 66%) as yellow oil. ^{1}H NMR ($CDCl_3$, 300 MHz): δ 0.32 (s, 18H), 0.90 (t, 12H, J = 6.6 Hz), 1.30–1.51 (m, 56H), 1.81–1.92 (m, 8H), 3.17 (s, 6H), 4.09 (t, 8H, J = 6.3 Hz), 7.17 (s, 2H), 7.47 (s, 2H); ^{13}C NMR ($CDCl_3$, 75 MHz): δ 0.17, 14.23, 22.80, 22.84,

26.24, 29.52, 29.60, 29.76, 29.81, 31.74, 32.07, 52.29, 69.05, 70.09, 80.99, 94.55, 102.49, 110.72, 115.84, 124.71, 125.37, 147.94, 149.59 (23 signals out of 31 expected); UV–vis (CH_2Cl_2): λ_{max}^{abs} (relative intensity) = 252 (1.0) 320 (0.51) nm; MALDI-TOF-MS (dith, positive): *m*/*z* 1056.74 $[M]^+$; Elemental analysis calcd (%) for $C_{66}H_{112}O_6Si_2$: C 74.94, H 10.67, found: C 74.69, H 10.73.

Preparation of 27c: To a solution of TMSA (1.01 mL, 7.21 mmol) in THF (15 mL) was added dropwise a *n*-BuLi hexane solution (2.65 mol dm^{-3}, 2.61 mL, 6.93 mmol) at −78 °C under argon atmosphere. After stirring at −78 °C for 30 min, a solution of **13b** (1.00 g, 1.38 mmol) in THF (15 mL) was added dropwise to the mixture. After stirring at room temperature for 90 min, $(MeO)_2SO_2$ (0.89 mL, 9.70 mmol) was added dropwise to the mixture at −78 °C. After the mixture was stirred at room temperature for 15 h, the resulting mixture was diluted with H_2O. The organic phase was separated, and the aqueous phase was extracted with $CHCl_3$. The combined organic phase was washed with H_2O, dried over anhydrous $MgSO_4$, and evaporated under reduced pressure. The residue was purified by silica gel column chromatography (hexane/ethyl acetate, 40:1 to 30:1) to afford **27c** (1.10 g, 1.16 mmol, 84%) as yellow oil. ^1H NMR ($CDCl_3$, 400 MHz): δ 0.29 (s, 18H), 0.87–0.98 (m, 24H), 1.27–1.54 (m, 32H), 1.75–1.83 (m, 4H), 3.15 (s, 6H), 3.93–3.96 (m, 8H), 7.12 (s, 2H), 7.43 (s, 2H); ^{13}C NMR ($CDCl_3$, 75 MHz): δ 0.21, 11.37, 11.43, 14.27, 22.82, 23.27, 24.08, 29.27, 29.33, 30.74, 30.80, 31.75, 39.69, 39.80, 52.38, 71.58, 72.33, 81.03, 94.56, 102.60, 110.29, 115.65, 124.48, 125.32, 148.20, 149.95; UV–vis (CH_2Cl_2): λ_{max}^{abs} (relative intensity) = 253 (1.0), 322 (0.28) nm; MALDI-TOF-MS (dith, positive): *m*/*z* 944.84 $[M]^+$; Elemental analysis calcd (%) for $C_{58}H_{96}O_6Si_2$: C 73.67, H 10.15, found: C 73.37, H 10.95.

Preparation of 29b: A mixture of **27b** (800 mg, 0.76 mmol) and K_2CO_3 (209 mg, 1.51 mmol) in THF/MeOH (1:1, 10 mL) was stirred at room temperature for 30 min. After the mixture was diluted with CH_2Cl_2, the insoluble material was removed by filtration and the filtrate was evaporated under reduced pressure. The residue was purified by silica gel column

chromatography (acetone) to give desilylated diyne **28b**. To a suspension of CuCl (75 mg, 0.76 mmol) and *n*-$BuNH_2$ (2.61 mL, 26.4 mmol) in H_2O (20 mL) and CH_2Cl_2 (20 mL) was added $NH_2OH·HCl$ (7 mg, 0.1 mmol) at 0 °C. A solution of **28b** and (2-bromoethynyl)triisopropylsilane (885 mg, 3.39 mmol) in CH_2Cl_2 (10 mL) was then added dropwise to the mixture. After the mixture was stirred at 30 °C for 15 h, H_2O was added to the resulting mixture. The organic phase was separated, and the aqueous phase was extracted with CH_2Cl_2. The combined organic phase was dried over anhydrous $MgSO_4$ and evaporated under reduced pressure. The residue was purified by silica gel column chromatography (hexane/CH_2Cl_2, 1:0 to 1:1) to afford **29b** (877 mg, 0.70 mmol, 92%) as yellow oil. ^{1}H NMR ($CDCl_3$, 600 MHz) δ 0.89 (t, 6H, J = 6.9 Hz), 0.89 (t, 6H, J = 7.2 Hz), 1.13 (brs, 42H), 1.24–1.40 (m, 48H), 1.46–1.52 (m, 8H), 1.82–1.87 (m, 8H), 3.17 (s, 6H), 4.07–4.14 (m, 8H), 7.15 (s, 2H), 7.37 (s, 2H); ^{13}C NMR ($CDCl_3$, 150 MHz): δ 11.45, 14.28, 18.72, 22.86, 26.18, 26.23, 29.50, 29.52, 29.55, 29.59, 29.62, 29.76, 29.81, 29.83, 32.08, 32.09, 52.93, 69.30, 70.04, 73.82, 75.02, 81.68, 85.33, 89.38, 110.53, 116.07, 123.85, 125.17, 148.12, 149.97 (30 signals out of 34 expected); UV–vis (CH_2Cl_2): λ_{max}^{abs} (relative intensity) = 260 (1.0), 321 (0.35) nm; MALDI-TOF-MS (dith, positive): 1273.87 $[M+H]^+$; Elemental analysis calcd (%) for $C_{74}H_{120}O_6Si_2$: C 77.30, H 10.76, found: C 77.18, H 11.13.

Preparation of 29c: A mixture of **27c** (1.11 g, 1.17 mmol) and K_2CO_3 (325 mg, 2.35 mmol) in THF/MeOH (1:1, 10 mL) was stirred at room temperature for 30 min. After the mixture was diluted with CH_2Cl_2, the insoluble material was removed by filtration and the filtrate was evaporated under reduced pressure. The residue was purified by silica gel column chromatography (acetone) to give desilylated alkyne **28c**. To a suspension of CuCl (116 mg, 1.17 mmol) and *n*-$BuNH_2$ (4.07 mL, 41.1 mmol) in H_2O (5 mL) and CH_2Cl_2 (5 mL) was added $NH_2OH·HCl$ (12 mg, 0.2 mmol) at 0 °C. A solution of **28c** and (2-bromoethynyl)triisopropylsilane (1.22 g, 4.70 mmol) in CH_2Cl_2 (5 mL) was then added dropwise to the mixture. After the mixture was stirred at 30 °C for 15 h, H_2O was added to

the resulting mixture. The organic phase was separated, and the aqueous phase was extracted with CH_2Cl_2. The combined organic phase was dried over anhydrous $MgSO_4$ and evaporated under reduced pressure. The residue was purified by silica gel column chromatography (hexane/CH_2Cl_2, 1:1) to afford **29c** (1.20 g, 1.03 mmol, 88%) as yellow solids. M.p. 88–90 °C; ^{1}H NMR ($CDCl_3$, 300 MHz) δ 0.91–0.98 (m, 24H), 1.12 (brs, 42H), 1.32–1.59 (m, 32H), 1.72–1.82 (m, 4H), 3.18 (s, 6H), 3.96 (d, 4H, J = 5.5 Hz), 3.97 (d, 4H, J = 5.4 Hz), 7.13 (s, 2H), 7.35 (s, 2H); ^{13}C NMR ($CDCl_3$, 150 MHz): δ 11.48, 14.26, 18.73, 23.23, 23.25, 24.04, 24.09, 29.23, 29.26, 29.34, 29.39, 30.74, 30.80, 30.83, 39.71, 39.79, 52.97, 71.57, 71.68, 72.23, 72.27, 73.91, 74.96, 81.75, 85.20, 89.44, 110.16, 115.81, 123.59, 125.11, 148.37, 150.33, 150.36; UV–vis (CH_2Cl_2): λ_{max}^{abs} (relative intensity) = 260 (1.0), 332 (0.35) nm; MALDI-TOF-MS (dith, positive): 1161.80 $[M+H]^+$; Elemental analysis calcd (%) for $C_{74}H_{120}O_6Si_2$: C 76.49, H 10.41, found: C 76.43, H 10.41.

Preparation of 30b: To a suspension of **29b** (1.30 g, 1.02 mmol) and $SnCl_2 \cdot H_2O$ (1.14 g, 5.10 mmol) in THF (20 mL) was added H_2SO_4 (1 N, 10 μL) under argon atmosphere. After the mixture was refluxed for 15 h, H_2O was added to the resulting mixture. The organic phase was separated, and the aqueous phase was extracted with CH_2Cl_2. The combined organic phase was dried over anhydrous $MgSO_4$ and evaporated under reduced pressure. The residue was purified by silica gel column (hexane/CH_2Cl_2, 2:1) to afford **30b** (1.00 g, 0.82 mmol, 81%) as yellow solids. M.p. 85–93 °C; ^{1}H NMR ($CDCl_3$, 400 MHz): δ 0.88 (t, 12H, J = 6.6 Hz), 1.15–1.16 (m, 42H), 1.28–1.45 (m, 8H), 1.51–1.58 (m, 8H), 1.89–1.97 (m, 8H), 4.21 (t, 4H, J = 6.6 Hz), 4.22 (t, 4H, J = 6.6 Hz), 7.70 (s, 2H), 7.71 (s, 2H); ^{13}C NMR ($CDCl_3$, 75 MHz): δ 11.54, 14.28, 18.77, 22.87, 26.21, 26.31, 29.28, 29.44, 29.56, 29.66, 29.78, 29.83, 32.10, 69.07, 69.59, 73.84, 83.11, 90.02, 90.62, 105.07, 108.66, 120.91, 124.58, 126.18, 149.75, 150.60 (26 signals out of 33 expected); UV–vis (CH_2Cl_2): λ_{max}^{abs} (relative intensity) = 256 (0.53), 291 (1.0), 306 (0.89), 318 (0.60), 375 (0.43), 395 (0.60), 423 (0.19) nm; MALDI-TOF-MS (dith, positive): 1212.00 $[M]^+$; Elemental analysis calcd (%) for

$C_{80}H_{130}O_4Si_2$: C 79.27, H 10.81, found: C 79.20, H 10.77.

Preparation of 30c: To a suspension of **29c** (1.05 g, 0.90 mmol) and $SnCl_2 \cdot H_2O$ (1.01 g, 4.51 mmol) in THF (10 mL) was added H_2SO_4 (1 N, 10 μL) under argon atmosphere. After the mixture was refluxed for 21 h, H_2O was added to the resulting mixture. The organic phase was separated, and the aqueous phase was extracted with CH_2Cl_2. The combined organic phase was dried over anhydrous $MgSO_4$ and evaporated under reduced pressure. The residue was purified by silica gel column (hexane/CH_2Cl_2, 2:1) to afford **30c** (840 mg, 0.76 mmol, 84%) as yellow solids. M.p. 113–118 °C; ^{1}H NMR ($CDCl_3$, 400 MHz): δ 0.92 (t, 12H, J = 7.0 Hz), 0.99 (t, 6H, J = 7.4 Hz), 1.00 (t, 6H, J = 7.6 Hz), 1.15 (brs, 42H), 1.30–1.64 (m, 32H), 1.83–1.93 (m, 4H), 4.05–4.12 (m, 8H), 7.69 (s, 4H); ^{13}C NMR ($CDCl_3$, 75 MHz): δ 11.41, 11.55, 14.27, 18.76, 23.25, 24.17, 29.27, 29.35, 30.90, 39.43, 39.68, 71.36, 71.77, 73.94, 83.06, 90.06, 90.56, 104.72, 108.33, 120.81, 124.56, 126.12, 150.09, 150.98 (24 signals out of 29 expected); UV–vis ($CHCl_3$): λ_{max}^{abs} (ε) = 292 (62300), 307 (55300), 319 (36700), 376 (27200), 396 (37700), 426 nm (11400 $dm^3\ mol^{-1}\ cm^{-1}$); MALDI-TOF-MS (dith, positive): 1098.85 $[M]^+$; Elemental analysis calcd (%) for $C_{72}H_{114}O_4Si_2$: C 78.63, H 10.45, found: C 78.40, H 10.84.

Preparation of 9c and 10c (Cu-mediated method): To a solution of **30c** (300 mg, 0.27 mmol) in THF (15 mL) was added dropwise a TBAF THF solution (1 mol dm^{-3}, 1.36 mL, 1.36 mmol) at 0 °C. After the mixture was stirring for 15 min at 0 °C, the resulting mixture was diluted with CH_2Cl_2 (20 mL). The mixture was concentrated under reduced pressure to approximately 1 mL. The resulting mixture was purified by silica gel column chromatography (CH_2Cl_2) to give a yellow solution of desilylated diyne **31c**, which was used in the next coupling reaction without further purification due to the instability. To a solution of **31c** in CH_2Cl_2 (27 mL) was added CuCl (135 mg, 1.36 mmol) and TMEDA (0.21 mL, 1.36 mmol) at room temperature. After the mixture was stirred at room temperature for 4 h under air, the suspension was filtrated through a bed of silica gel. The filtrate was evaporated

under reduced pressure. The residue was purified by silica gel column chromatography (CH_2Cl_2/hexane, 1:4) and subsequent recycling GPC eluting with $CHCl_3$ to afford **9c** (120 mg, 0.076 mmol, 56%) and **10c** (11 mg, 0.0046 mmol, 5%) as red solids. **9c**: M.p. 188 °C (decomp.); ^{1}H NMR ($CDCl_3$, 600 MHz, 2.11 × 10^{-2} mol dm^{-3}): δ 0.91 (t, 12H, J = 6.9 Hz), 0.92 (t. 12H, J = 6.6 Hz), 0.97 (t, 12H, J = 7.5 Hz), 0.99 (t, 12H, J = 7.5 Hz), 1.35–1.61 (m, 64H), 1.81–1.87 (m, 8H), 3.94–3.99 (m, 8H), 4.07 (d, 8H, J = 5.4 Hz), 7.16 (s, 4H), 7.54 (s, 4H); ^{13}C NMR ($CDCl_3$, 150 MHz): δ 11.47, 11.53, 14.28, 23.28, 24.14, 24.17, 29.33, 29.38, 30.83, 30.88, 39.58, 39.61, 68.86, 71.13, 71.61, 72.25, 83.23, 85.27, 104.21, 107.56, 124.69, 124.79, 125.05, 150.14, 151.29 (25 signals out of 27 expected); UV–vis ($CHCl_3$): λ_{max}^{abs} (ε) = 262 (122900), 279 (168800), 298 (155000), 337 (53000), 362 (80700), 390 (83700), 493 (41100), 552 nm (7400 dm^3 mol^{-1} cm^{-1}); MALDI-TOF-MS (dith, positive): 1569.46 $[M]^+$; Elemental analysis calcd (%) for $C_{108}H_{144}O_8 \cdot 0.12CHCl_3$: C 81.95, H 9.16, found: C 81.95, H 9.36. **10c**: M.p. 223 °C (decomp.); ^{1}H NMR ($CDCl_3$, 600 MHz, 2.69 × 10^{-3} mol dm^{-3}): δ 0.93 (t, 18H, J = 6.9 Hz), 0.97 (t, 18H, J = 6.9 Hz), 1.03 (t, 18H, J = 7.2 Hz), 1.04 (t, 18H, J = 7.2 Hz), 1.26–1.64 (m, 96H), 1.89–1.92 (m, 12H), 4.09 (brs, 12H), 4.13 (d, 12H, J = 5.4 Hz), 7.61 (s, 6H), 7.65 (s, 6H); ^{13}C NMR ($CDCl_3$, 150 MHz): δ 11.58, 14.29, 14.34, 23.27, 23.33, 24.20, 24.25, 29.40, 29.46, 30.94, 39.60, 39.73, 65.67, 70.67, 71.23, 71.71, 76.26, 83.12, 104.58, 107.76, 120.93, 124.81, 126.07, 150.40, 151.43 (25 signals out of 27 expected); UV–vis ($CHCl_3$): λ_{max}^{abs} (ε) = 290 (183800), 462 (98600), 504 nm (102200 dm^3 mol^{-1} cm^{-1}); MALDI-TOF-MS (dith, positive): 2353.83 $[M]^+$; Elemental analysis calcd (%) for $C_{162}H_{216}O_{12} \cdot 0.35CHCl_3$: C 81.34, H 9.10, found: C 81.35, H 9.47.

Preparation of 10c (Pd-mediated method): To a solution of **30c** (300 mg, 0.27 mmol) in THF (15 mL) was added dropwise a TBAF THF solution (1 mol dm^{-3}, 1.36 mL, 1.36 mmol) at 0 °C. After the mixture was stirring for 15 min at 0 °C, the resulting mixture was concentrated under reduced pressure to approximately 1 mL. The resulting mixture was purified by silica gel column chromatography (THF) to give a yellow solution of desilylated

diyne **31c**, which was used in the next coupling reaction without further purification due to the instability. $[PdCl_2(PPh_3)_2]$ (191 mg, 0.27 mmol), CuI (26 mg, 0.13 mmol), and Et_3N (0.15 mL, 1.09 mmol) were added to a solution of **31c** in THF (9 mL). The resulting mixture was stirred at room temperature for 3 h. After the solvent was removed under reduced pressure, the residue was purified by silica gel column chromatography (CH_2Cl_2/hexane, 1:2) and recycling GPC ($CHCl_3$) to give **10c** (34 mg, 14.4 μmol, 16%) as yellow solids.

Preparation of 17c: To a suspension of **27c** (380 mg, 0.40 mmol) and $SnCl_2 \cdot 2H_2O$ (452 mg, 2.00 mmol) in THF (20 mL) was added H_2SO_4 (1 N, 0.03 mL) under argon atmosphere. After the mixture was reflux for 11 h, brine was added into the mixture. The organic phase was separated, and the aqueous phase was extracted with CH_2Cl_2. The combined organic phase was dried over anhydrous $MgSO_4$ and evaporated under reduced pressure. The residue was purified by silica gel column (hexane/CH_2Cl_2, 5:1) to afford **17c** (300 mg, 0.76 mmol, 84%) as yellow oil. ^{1}H NMR ($CDCl_3$, 300 MHz): δ 0.37 (s, 18H), 0.92 (t, 12H, J = 7.0 Hz), 0.99 (t, 6H, J = 7.6 Hz), 1.00 (t, 6H, J = 7.4 Hz), 1.32–1.64 (m, 32H), 1.85–1.92 (m, 4H), 3.99–4.07 (m, 4H), 4.11 (d, 4H, J = 6.0 Hz), 7.70 (s, 2H), 7.79 (s, 2H); ^{13}C NMR ($CDCl_3$, 150 MHz): δ 0.37, 11.32, 11.51, 14.25, 23.25, 23.29, 24.19, 29.22, 29.35, 30.85, 30.93, 39.48, 39.71, 71.37, 71.80, 103.18, 103.34, 104.82, 108.82, 120.67, 124.24, 125.60, 149.77, 150.42 (24 signals out of 26 expected); UV–vis ($CHCl_3$): λ_{max}^{abs} (ε) = 267 (62800), 298 (40800), 305 (42900), 345 (19600), 360 (25300), 397 nm (6900 $dm^3\ mol^{-1}\ cm^{-1}$); MALDI-TOF-MS (dith, positive): 883.95 $[M+H]^+$; Elemental analysis calcd (%) for $C_{56}H_{90}O_4Si_2 \cdot 0.07CHCl_3$: C 75.51, H 10.17, found: C 75.50, H 10.36.

Preparation of 3c and 4c (Cu-mediated method): A mixture of **17c** (130 mg, 0.14 mmol) and K_2CO_3 (101 mg, 0.73 mmol) in THF/MeOH (1:1, 10 mL) was stirred at room temperature for 30 min. After the mixture was concentrated under reduced pressure to approximately 1 mL, the resulting mixture was purified by silica gel column chromatography (CH_2Cl_2) to give

a colorless solution of desilylated diyne **15c**. The solvent was replaced with CH_2Cl_2 by evaporation followed by dilution, and the solution was used in the next reaction immediately. CuCl (72 mg, 0.73 mmol) and TMEDA (0.1 mL, 0.73 mmol) were added to a solution of **15c** in CH_2Cl_2 (28 mL) was added. The resulting mixture was refluxed for 5 h under a supply of air. After the solvent was removed under reduced pressure, the residue was suspended with $CHCl_3$, and the resulting mixture was washed with H_2O. The organic phase was dried over anhydrous $MgSO_4$ and evaporated under reduced pressure. The residue was purified by silica gel column chromatography ($CHCl_3$/hexane = 1:4) and recycling GPC eluting with $CHCl_3$ to give **3c** (57 mg, 0.038 mmol, 55%) as red solids and **4c** (5 mg, 2.26×10^{-3} mmol, 5%) as yellow solids. **3c**: M.p. 188–190 °C; ^{1}H NMR ($CDCl_3$, 600 MHz): δ 0.91 (t, 12H, J = 7.0 Hz), 0.94 (t, 12H, J = 6.5 Hz), 0.97 (t, 12H, J = 7.5 Hz), 0.99 (t, 12H, J = 7.5 Hz), 1.32–1.62 (m, 64H), 1.81–1.88 (m, 8H), 3.94–4.00 (m, 8H), 4.07 (d, 8H, J = 5.5 Hz), 7.01 (s, 4H), 7.53 (s, 4H); ^{13}C NMR ($CDCl_3$, 150 MHz): δ 11.43, 11.54, 14.26, 14.29, 23.25, 23.28, 24.19, 24.22, 29.36, 29.40, 30.84, 30.91, 39.66, 39.71, 71.18, 71.68, 88.35, 93.94, 104.39, 107.78, 124.49, 124.70, 126.68, 150.07, 150.99; UV–vis ($CHCl_3$): λ_{max}^{abs} (ε) = 275 (85000), 306 (79700), 332 (59800), 347 (86700), 387 (12700), 405 (14300), 473 (26300), 560 nm (1600 dm^3 mol^{-1} cm^{-1}); MALDI-TOF-MS (dith, positive): 1473.10 $[M]^+$; Elemental analysis calcd (%) for $C_{100}H_{144}O_8 \cdot 0.07CHCl_3$: C 81.06, H 9.79, found: C 81.05, H 9.76. **4c**: M.p. 101–104 °C; ^{1}H NMR ($CDCl_3$, 600 MHz): δ 0.88 (t, 18H, J = 7.2 Hz), 0.94 (t, 18H, J = 7.1 Hz), 1.04 (t, 18H, J = 7.4 Hz), 1.05 (t, 18H, J = 7.1 Hz), 1.30–1.68 (m, 96H), 1.87 (sep, 12H, J = 6.0 Hz), 1.93 (sep, 12H, J = 6.1 Hz), 4.18 (d, 12H, J = 5.4 Hz), 4.28 (d, 12H, J = 3.6 Hz), 7.83 (s, 6H), 8.07 (s, 6H); ^{13}C NMR ($CDCl_3$, 150 MHz): δ 11.55, 11.85, 14.22, 14.30, 23.30, 24.20, 24.35, 29.40, 29.50, 30.95, 31.10, 31.12, 39.73, 71.56, 71.67, 82.72, 83.34, 104.89, 109.59, 120.81, 124.69, 126.00, 150.01, 151.35; UV–vis ($CHCl_3$): λ_{max}^{abs} (ε) = 275 (128000), 405 (88900), 426 (92300), 441 (81400) 458 nm (101000 dm^3 mol^{-1} cm^{-1}); MALDI-TOF-MS (dith, positive): 2353.83 $[M]^+$; Elemental analysis calcd (%) for $C_{150}H_{216}O_{12}$: C 81.47, H 9.85,

found: C 81.18, H 10.04.

Preparation of 4c (Pd-catalyzed method): A mixture of **17c** (224 mg, 0.25 mmol) and K_2CO_3 (175 mg, 1.26 mmol) in THF/MeOH (1:1, 10 mL) was stirred at room temperature for 30 min. After the mixture was concentrated under reduced pressure to approximately 1 mL, the resulting mixture was purified by silica gel column chromatography (THF) to give a colorless solution of desilylated diyne **15c**. The solvent was replaced with CH_2Cl_2 by evaporation followed by dilution, and the solution was used in the next reaction immediately. Et_3N (25 mL) was added to a solution of **15c** in THF (25 mL), and the resulting solution was bubbled with argon with stirring for 30 min. $[PdCl_2(PPh_3)_2]$ (17 mg, 0.025 mmol), CuI (9 mg, 0.050 mmol), and *p*-benzoquinone (24 mg, 0.22 mmol) were added to the solution. After the mixture was stirred at 70 °C for 2 h, the suspension was filtered through a bed of silica gel, and the filtrate was evaporated under reduced pressure. The residue was purified by silica gel column chromatography (CH_2Cl_2/hexane = 1:3) and recycling GPC eluting with $CHCl_3$ to give **4c** (20 mg, 9.04 μmol, 10%) as yellow solids.

Chapter 5. Concluding and Future Remarks

In this thesis, the author has described the syntheses, properties, and self-assembling behavior of novel dehydroannulenes **3**–**10** fused with phenanthrene or benzene moieties (Chapters 2–4).

In Chapter 2, the author has described the syntheses of tetraalkoxyphenanthrene-fused octadehydro[12]-, dodecadehydro[18]-, and hexadecadehydro[24]annulenes **3**–**5** by using Cu-mediated or Pd-catalyzed oxidative macrocyclization reactions as key steps and their electronic, optical, electrochemical, and self-assembling properties. X-ray crystallographic analysis of a single crystal of **3a** demonstrated that the molecules were arranged longitudinally in a slipped π-stacked fashion to form a 1D column. ^{1}H NMR and UV–vis spectroscopic and cyclic voltammetric analysis in conjugation with nucleus-independent chemical shift (NICS) calculations for **3**–**5** support that the annulation at the 9,10-positions of phenanthrene to the dehydroannulene (DA) ring enhances the tropicity and decreases the HOMO–LUMO gaps of the molecules relative to the benzannulation and that **3** possesses an antiaromatic character. Self-association behavior due to the π–π stacking interactions in $CDCl_3$ was observed for **3** and **4** and was quantified by concentration-dependent ^{1}H NMR spectroscopic measurements. The self-assembly of **3** and **4** into well-defined 1D superstructures with high aspect ratios was obtained, and the morphology and crystallinity of these compounds were investigated by means of scanning electron microscope (SEM) and wide-angle X-ray diffraction (WAXD) measurements. Furthermore, it was shown that **3b** and **4b** display liquid-crystalline phases by means of differential scanning calorimetry (DSC), polarizing optical microscopy (POM), and variable-temperature WAXD measurements.

In Chapter 3, the author has described the syntheses, characterization, electronic and electrochemical properties, and self-associations of hexadecadehydrodibenzo[20]-, tetracosadehydrotribenzo[30]-, and dotriacontadehydrotetrabenzo[40]annulenes **6**–**8**

possessing octatetrayne linkages. X-ray diffraction analysis demonstrated that the molecules of **7** and *p*-xylene form 2D sheetlike structure. Planar **6** and **7** show significantly weak or almost no tropicity. The extension of the acetylenic linkages from butadiyne to octatetrayne units narrows HOMO–LUMO gaps. The self-association behavior of **7** in solution resulting from effective π–π stacking interactions was observed in contrast with **2a** possessing butadiyne linkages.

In Chapter 4, the author has described the syntheses of tetraalkoxyphenanthrene-fused hexadecadehydro[20]- and tetracosadehydro[30]annulenes **9c** and **10c** possessing octatetrayne linkages and the investigation on their electronic, photophysical, electrochemical, and self-assembling properties together with those of phenanthrene-fused octadehydro[12]- and dodecadehydro[18]annulenes **3c** and **4c**. Various spectroscopic and electrochemical measurements as well as quantum chemical calculations support that planar **9c** and **10c** are weakly antiaromatic and nonaromatic, respectively. The extension of the acetylenic linkages from butadiyne to octatetrayne units lowers both HOMO and LUMO levels. The detailed concentration- and temperature-dependent ^{1}H NMR and UV–vis data of **3c**, **4c**, **9c**, and **10c** provided unambiguous evidence for the enhancement of self-association properties by the extension of the acetylenic linkages. The enthalpic terms of **9c** and **10c** were found to be more negative than those of **3c** and **4c**, and thereby it is reasonably concluded that the extension of the acetylenic linkages withdraws the electron density from the phenanthrene moieties and thus promotes π–π stacking interactions, which is in line with the polar/π model. The entropic cost increases with increase in the enthalpic contribution, and thus enthalpic-entropic compensation applies. DAs **3c**, **4c**, **9c**, and **10c** formed 1D self-assembled clusters and their morphology and crystallinity proved to depend on the length of acetylenic linkages, the topology of DA core, and the bulkiness of alkoxy groups appended to the phenanthrene moieties. The intriguing supramolecular polymorphism of **10c** depending on solvents was observed.

Indacene is a typical 12π antiaromatic, unstable compound, where a [12]annulene moiety is perturbed by two σ-bonds. Indenofluorene derivatives, where the two benzene rings are fused to the indacene moiety, are stable and have attracted attention due to their electrochemical amphoterism and small HOMO–LUMO gap associated with their antiaromatic and quinodimethane substructures embedded in the 20π perimeter (Figure 5-1).[173–175] Based on the studies of phenanthrene-fused DAs described in Chapters 2 and 4, the author designed phenanthrene-fused indacene derivative, since the annulation at the 9,10-positions of phenanthrene to indacene was anticipated to enhance 12π antiaromatic character relative to the benzannulation and hence provide interesting optoelectronic and electrochemical properties of the resulting compounds. The first synthesis of indeno[1,2-*b*]fluorene derivative was achieved by the reaction of dehydrobenzo[12]annulenes ([12]DBA) **1b** with I_2 in the presence of molecular oxygen to form diketone as a key step (Scheme 5-1).[49,50] Inspired by the synthesis of indeno[1,2-*b*]fluorene derivative, the reaction of **3a** using I_2 in $CHCl_3$ was examined (Scheme 5-2), but the reaction did not proceed. The investigation on the different synthetic approach toward phenanthrene-fused indacene is currently underway in our group.

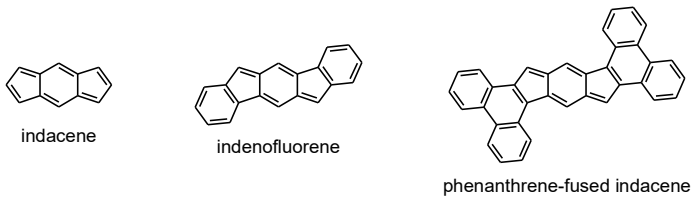

Figure 5-1. Structures of indacene, indenofluorene, and phenanthrene-fused indacene.

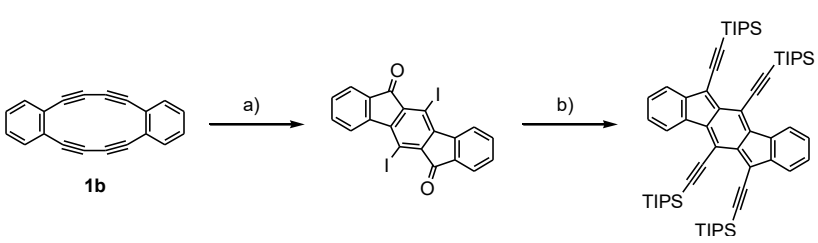

Scheme 5-1. Synthesis of indenofluorene reported in the literature.[48,49] Reagents and conditions: a) 1) I_2, benzene, RT; 2) O_2, benzene, RT; b) 1) TIPS−C≡CH, $[Pd(PPh_3)_2Cl_2]$, CuI, THF/(i-C_3H_7)$_2$NH (1:1 v/v), 60 °C; 2) TIPS−C≡CLi, THF, 0 °C; 3) $SnCl_2$, toluene, 80 °C.

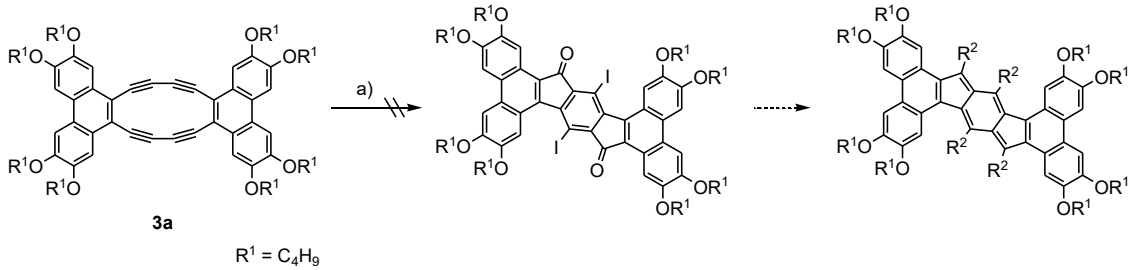

Scheme 5-2. Attempt to synthesize phenanthrene-fused indenofluorene. Reagents and conditions: a) I_2, $CHCl_3$, reflux.

The incorporation of aryl groups into the periphery of π-conjugated framework is an effective way to control over the electronic, photophysical, and electrochemical properties and the self-assembling behavior associated with the extension of π-conjugation.[176–178] Following the work described in Chapter 2, the author designed phenanthrene-fused [12]- and [18]DAs having trialkoxyphenyl groups, which are introduced to the phenanthrene moieties either directly or via an ethynylene spacer (Figure 5-2); the trialkoxyphenyl groups were anticipated to bring about not only the extension of π-conjugation but also the interesting self-assembling properties to form gel, liquid crystal, and/or 1D cluster. These DAs differ in the topology, size, and planarity of π-framework, and hence their extent of π-conjugation, which is apparently responsible for photophysical and electrochemical properties, and self-assembling behavior should be different from each other to some extent. The elucidation of the relationships between tropicity, properties, and self-assembling behavior in these DAs, in particular, the difference of the physicochemical and self-assembling properties stemming from whether the trialkoxyphenyl groups are introduced to the phenanthrene moieties directly or via an ethynylene spacer seems an interesting task. The author has very recently accomplished the syntheses of these novel DAs and undertaken the investigation on their properties and self-assembling behavior. The results will be reported elsewhere.

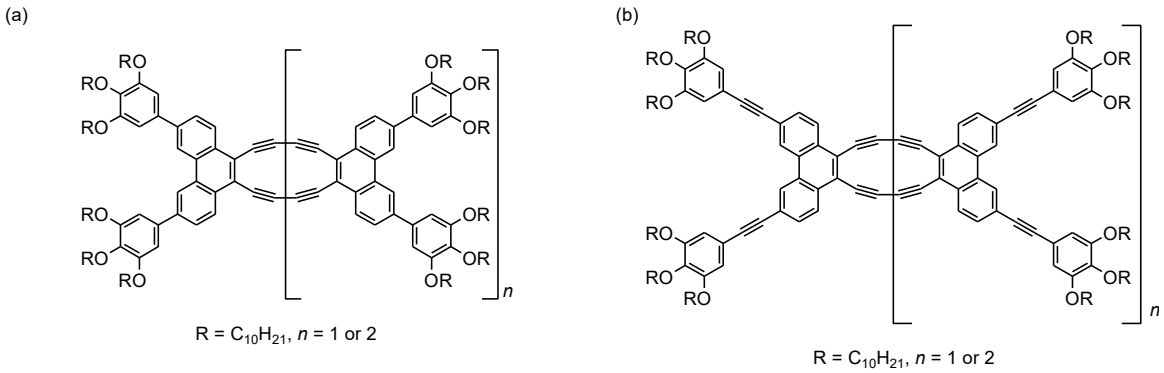

Figure 5-2. Structures of phenanthrene-fused DAs having (a) trialkoxyphenyl and (b) trialkoxyphenylethynyl groups.

Chapter 6. Appendix

6-1. Experimental Methods

General Experimental Methods: Column chromatography and plug filtrations were carried out with SiO_2 60. Thin-layer chromatography (TLC) was conducted on aluminum sheets coated with SiO_2 60 F_{254}; visualization with a lamp (254 or 365 nm). Melting points (M.p.) were measured with a Yanako melting point apparatus and are uncorrected. The NMR spectra were recorded with a JNM-ECS300, JNM-ECS400, or JNM-ECA600 FT NMR spectroscopy (JEOL). Residual solvent or tetramethylsilane signals in the ^{1}H and ^{13}C NMR spectra were used as an internal reference ($CDCl_3$, ^{1}H: δ 7.26; ^{13}C: δ 77.16). Chemical shifts (δ) are given as δ values. The coupling constants (J) are given in Hz. The apparent resonance multiplicity is described as s (singlet), d (doublet), t (triplet), q (quartet), qui (quintet), sex (sextet), sep (septet), m (multiplet), and brs (broad singlet). FAB-MS spectra were recorded with a JMS-HX110A or a JMS-T100CS mass spectrometer with *m*-nitrobenzyl alcohol (NBA) as a matrix. MALDI-TOF-MS spectra were recorded with SHIMADZU AXIMA Performance mass spectrometer with dithranol (dith) or sinapinic acid (SA) as a matrix. The most important signals are reported in *m*/*z* units with M as the molecular ion. The UV–vis spectra were recorded on a SHIMADZU UV-2550 spectrometer. UV–vis spectra were recorded in CH_2Cl_2 or $CHCl_3$ at 10^{-5}–10^{-7} mol dm^{-3}. All peaks followed Beers law, which confirms that the absorption are intrinsic to molecules rather than aggregates. The fluorescence spectra were measured on a HITACHI F-4500 fluorescence spectrophotometer. UV–vis spectroscopic measurements at various temperature were carried by using a HITACHI U-3000 spectrometer with peltier-type temperature controller. The spectra were measured in a cuvette of 0.01, 0.1, or 1 cm. The absorption maxima (λ_{max}^{abs}) is reported in nm with the relative intensity or the molar absorption coefficient in brackets. Fluorescence lifetimes were determined by the time-correlated single-photon

counting method based using a nanosecond laser system that was based on an LED pulse (HORIBA). The absolute fluorescence quantum yields were determined by an integrating sphere system (Hamamatsu Photonics K.K.). Gel-permeation chromatography (GPC) was performed with a LC-918 (Japan Analytical Industry Co., LTD) using JAIGEL-1H (20 × 600 nm) and JAIGEL-2H (20 × 600 nm) columns eluting with $CHCl_3$. Cyclic voltammetry and differential pulse voltammetry (EC FRONTIER, Inc.) were performed by using a cell equipped with a platinum as working electrode, a platinum wire as counter electrodes, and $Ag/AgNO_3$ as a referential electrode. All electrochemical measurements were performed in *o*-dichlorobenzene (*o*-DCB) solution (*ca.* 5×10^{-4} mol dm^{-3}) containing 0.1 mol dm^{-3} *n*-Bu_4NPF_6 at 25 °C. All potentials are referenced to the ferrocene/ferrocenium ion (Fc/Fc^+) couple, used as a standard. SEM images were obtained with a Hitachi field-emission SEM S-4800 operated at 1.0 kV. A Pt-Pd coating was applied using a HITACHI E-1045 ion sputter. WAXD measurements for the materials from dehydro[*n*]annulenes ([*n*]DAs) through a phase transfer method were performed on a Rigaku MicroMax-007HF X-ray diffractometer for which a Cu-Kα radiation (λ = 1.54 Å) was used. The obtained WAXD patterns were recorded using a cooled CCD camera (Hamamatsu Photonics K.K., C4742-98) with an image intensifier (Hamamatsu Photonics K.K., V7739P). AFM measurements were performed on a Shimadzu SPM9600: compounds were drop-casted from a MCH solution on the SiO_2 surface. TG-DTA was performed on a TG/FTA6200 (Seiko Instruments Inc.) at heating and cooling rates of 10 °C min^{-1}. DSC was performed on a PerkinElmer Diamond DSC at heating and cooling rates of 10 °C min^{-1}. Optical textures at cross polarizers were obtained with an OLYMPUS BX50 polarization microscope equipped with a METTLER TOLEDO FP82HT hot stage controller unit. Simultaneous WAXD and DSC measurements for DAs were performed on a Rigaku SmartLab for which a Cu-Kα radiation (λ = 1.54 Å) was used.

Computational Methods: DFT calculations were performed using the Gaussian 09 program package.[100] Geometry optimization was performed with the restricted Becke hybrid (B3LYP) at the 6-31G(d) basis set. Further single-point calculations were performed at the 6-31+G(d,p) basis set to obtain the molecular orbital energies. The NICS values were calculated using the GIAO method at the HF/6-31G(d) or B3LYP/6-311++G(2d,2p) level of theory. The ^{1}H NMR chemical shifts were calculated using the GIAO method at the B3LYP/6-311++G(2d,2p) level of theory. TD calculations were performed at the B3LYP/6-31G(d) level of theory. The calculated UV–vis transitions are vertical. NBO analyses were performed with the B3LYP/6-311G(d,p) level. The ESPs and MEPs were calculated at the B3LYP/6-31+G(d,p) level of theory. PM7 optimization were performed using MOPAC2012.[179]

X-ray crystal structure analysis: The X-ray crystal structures were solved by direct methods (SIR-97)[180] and refined by full-matrix least-squares analysis (SHELXL-97),[181] using an isotropic extinction correction. All non-hydrogen atoms were refined anisotropically; hydrogen atoms were refined isotropically, whereby hydrogen positions are based on stereochemical considerations.

6-2. Procedures for Determination of Association Constants

Monomer–dimer Model:[182] The monomer–dimer model is the model for the description of dimerization. The ^{1}H NMR spectra of DAs and dehydrobenzo[*n*]annulene ([*n*]DBA) were measured at various concentrations. According to the monomer–dimer model, the relationship between the observed chemical shifts (δ_{obs}) and the total concentration (C_T) is expressed as:

$$\delta_{obs} = \delta_{mon} + (\delta_{agg} - \delta_{mon})(4KC_T + 1 - (8KC_T + 1)^{1/2})/4KC_T$$

where K is the association constant, δ_{agg} is chemical shifts of aggregated species, δ_{mon} is

chemical shifts of monomer. The observed chemical-shift data were analyzed by a nonlinear least-squares method fit to Kaleida Graph Program[183] to give best-fit values for variables K, δ_{mon}, and δ_{agg}.

Isodesmic Model (Concentration-dependence):[182] The isodesmic models is the model for the description of extended aggregates. In this model, the aggregates are assumed to be of one dimensional character. For all the binding events *i.e.* the addition of one monomer to another monomer or to any aggregated species, the equilibrium constants are equal. The ^{1}H NMR or UV–vis spectra of DAs were measured at various concentrations. According to the isodesmic model, the relationship between δ_{obs} or observed molar excitation coefficient (ε_{obs}) and C_T is expressed as:

$$\delta_{obs} = \delta_{mon} + (\delta_{agg} - \delta_{mon})(1 - (2KC_T + 1 - (4KC_T + 1)^{1/2})/2K^2C_T^2)$$

$$\varepsilon_{obs} = \varepsilon_{mon} + (\varepsilon_{agg} - \varepsilon_{mon})(1 - (2KC_T + 1 - (4KC_T + 1)^{1/2})/2K^2C_T^2)$$

where K is association constant, ε_{agg} and ε_{mon} are the molar excitation coefficients for the monomer and the aggregated species, respectively. The observed chemical-shift or molar excitation coefficients data were analyzed by a nonlinear least-squares method fit to Kaleida Graph Program[62] to give best-fit values for variables K, δ_{mon} or ε_{mon}, and δ_{agg} or ε_{agg}.

Isodesmic Model (Temperature-dependence):[184] The UV–vis spectra of DAs were measured at various temperatures. According to the isodesmic model, the relationship between ε_{obs} and the temperature (T) is expressed as:

$$\varepsilon_{obs} = \varepsilon_{mon} + (\varepsilon_{agg} - \varepsilon_{mon})(1/(1 + \exp(-0.908\Delta H(T - T_m)/RT_m^2))$$

where ΔH is enthalpic term, R is the gas constant, and T_m is the melting temperature which is the temperature at $\alpha_{agg} = 0.5$. The observed molar excitation coefficient data were analyzed by a nonlinear least-squares method fit to Kaleida Graph Program[62] to give best-fit values for

variables ΔH, T_m, ε_{mon}, and ε_{agg}. The degree of aggregation (α_{agg}) is calculated by ε_{obs}, ε_{mon}, and ε_{agg}:

$$\alpha_{agg} = (\varepsilon_{obs} - \varepsilon_{mon})/(\varepsilon_{agg} - \varepsilon_{mon})$$

From α_{agg}, the number average aggregate (DP_N) can be calculated directly:

$$DP_N = 1/(1 - \alpha_{agg})^{1/2}$$

Furthermore, DP_N is also related to the C_T and K:

$$DP_N = 1/2 + (4KC_T + 1)^{1/2}/2$$

6-3. Transient Absorption Spectra of 3c, 4c, 9c, 10c, 17c, and 30c

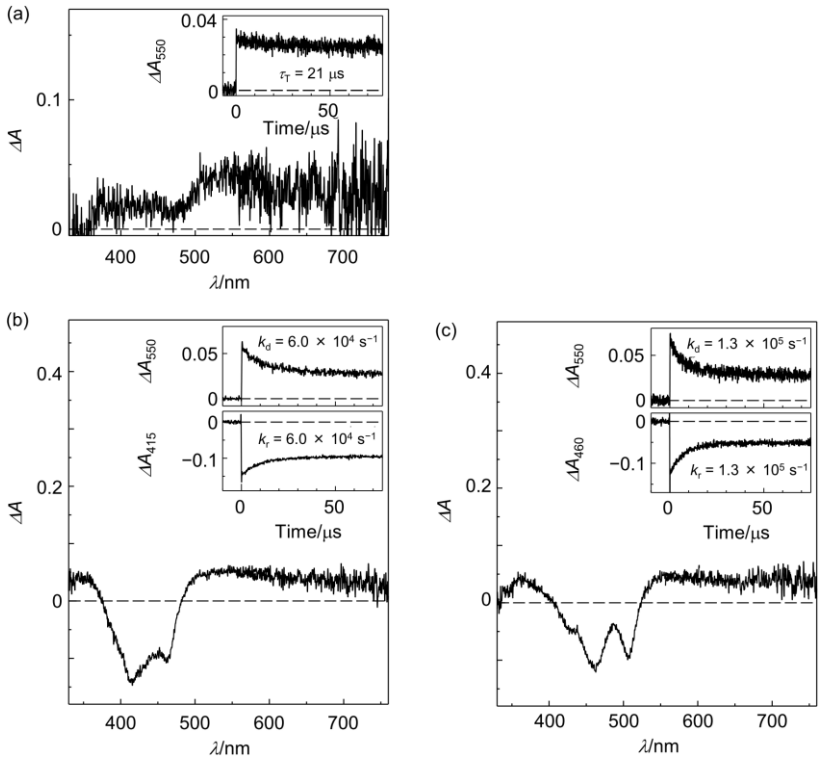

Figure 6-1. Transient absorption spectra of (a) **3c**, (b) **4c**, and (c) **10c** at 100 ns upon 266 nm laser pulsing in Ar–purged $CHCl_3$ solution at 25 °C. Inset; trace at (a) 550 nm, (b) 550 nm (upper), 415 nm (lower), (c) 550 nm (upper), and 460 nm (lower).

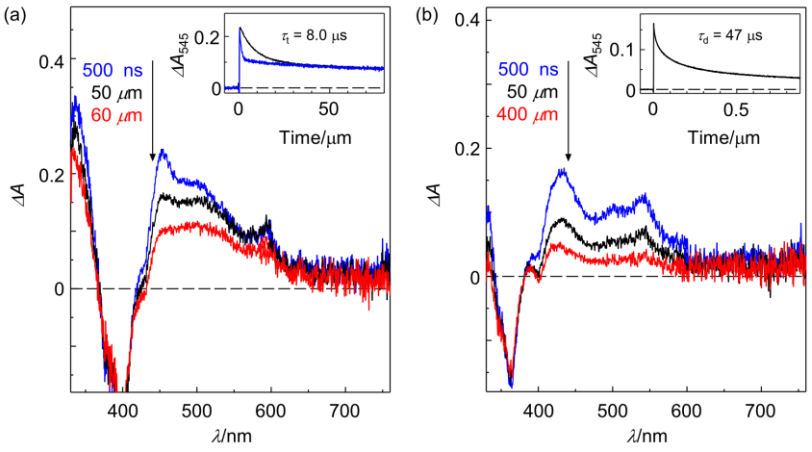

Figure 6-2. Transient absorption spectra upon 266 nm laser pulsing in Ar–purged $CHCl_3$ solution of (a) **30c** and (b) **17c**. Inset; (a) Trace at 545 nm for the Ar–purged (black line) and the aerated (blue line) solution. (b) Trace at 545 nm. The decay profile was independent of the dissolved oxygen.

6-4. Differential Pulse Voltammograms of 3c, 4c, 9c, 10c, 17c, and 30c

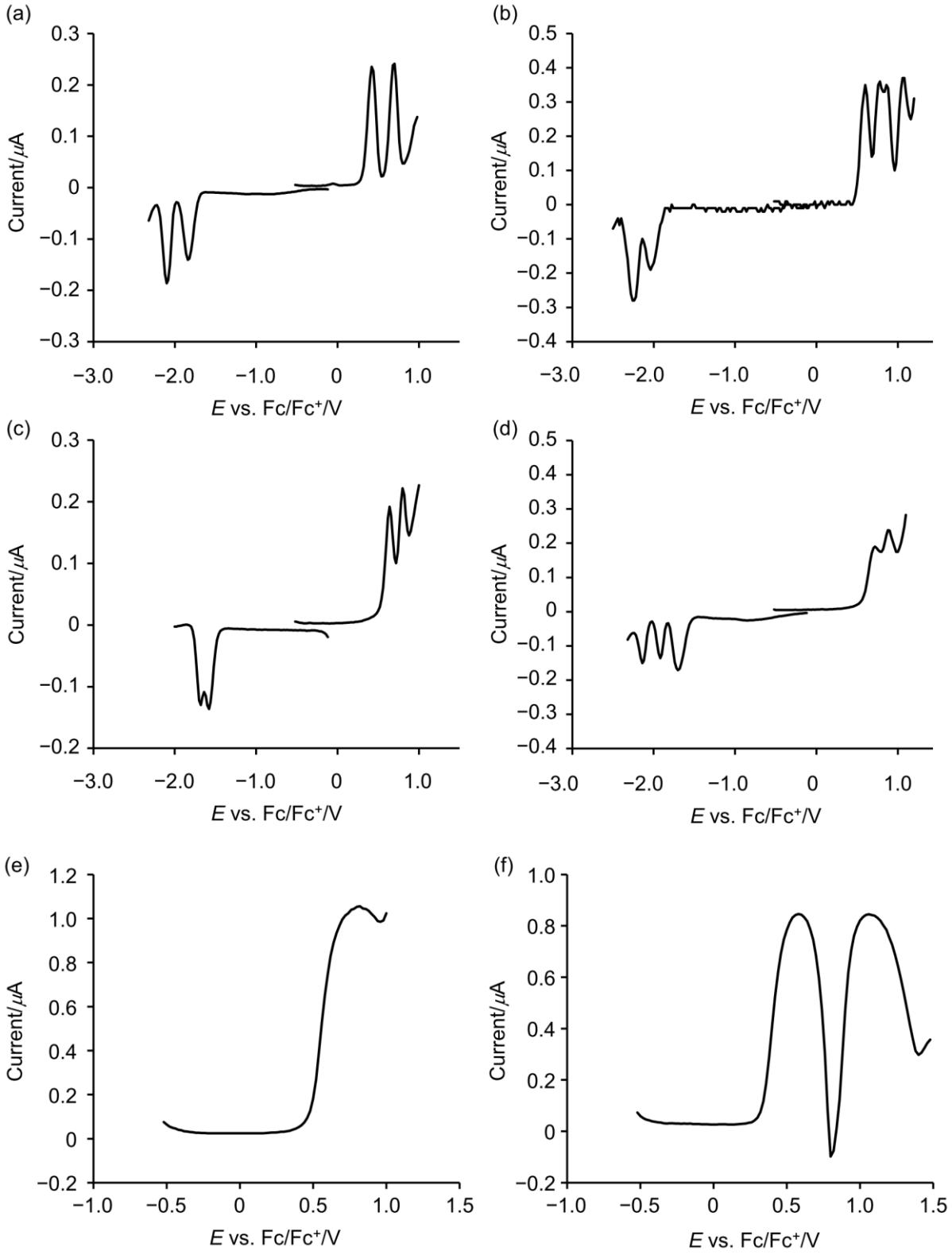

Figure 6-3. Differential pulse voltammograms of (a) **3c**, (b) **4c**, (c) **9c**, (d) **10c**, (e) **17c**, and (f) **30c** measured in *o*-DCB (0.1 mol dm^{-3} *n*-Bu_4NPF_6) at a pulse width of 100 ms over a period of 200 ms.

6-5. van't Hoff Plots of 3c, 4c, 9c, and 10c

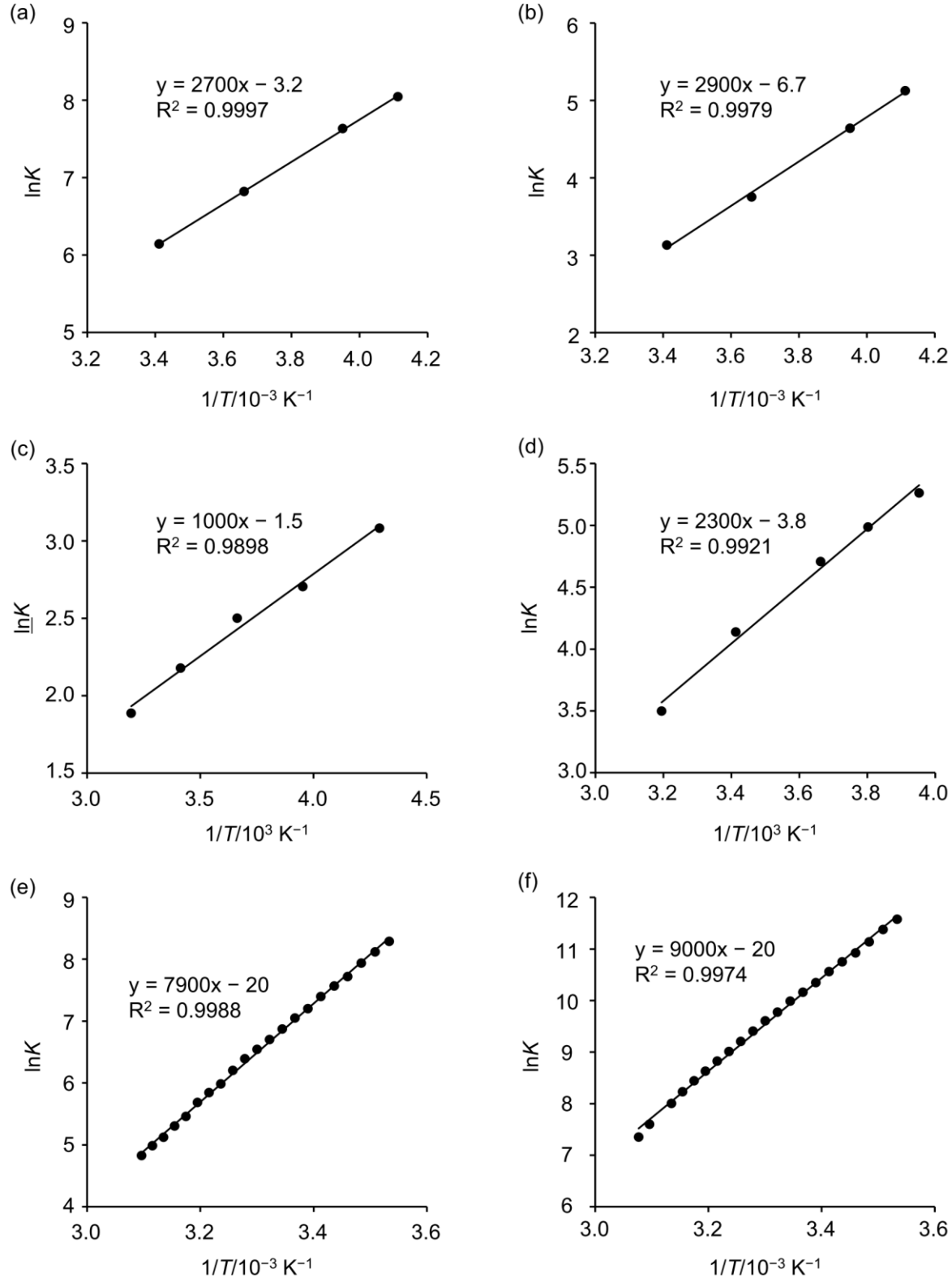

Figure 6-4. van't Hoff plot of (a) **3c** and (b) **4c** in MCH by ^{1}H NMR experiments (concentration dependence) and (c) **9c** and (d) **10c** in $CDCl_3$ by ^{1}H NMR experiments (concentration dependence), and (e) **9c** and **10c** in MCH by UV-vis experiment (temperature dependence).

6-6. ^{1}H and ^{13}C NMR data

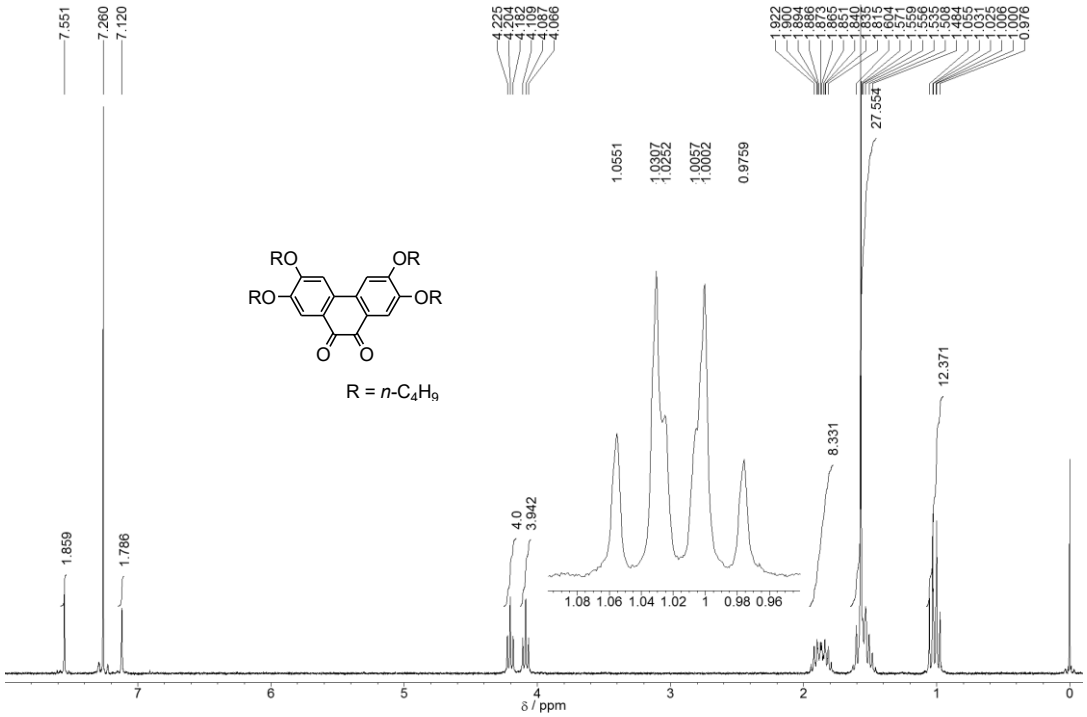

Figure 6-5. ^{1}H NMR spectrum of **13a** in $CDCl_3$ solution (300 MHz).

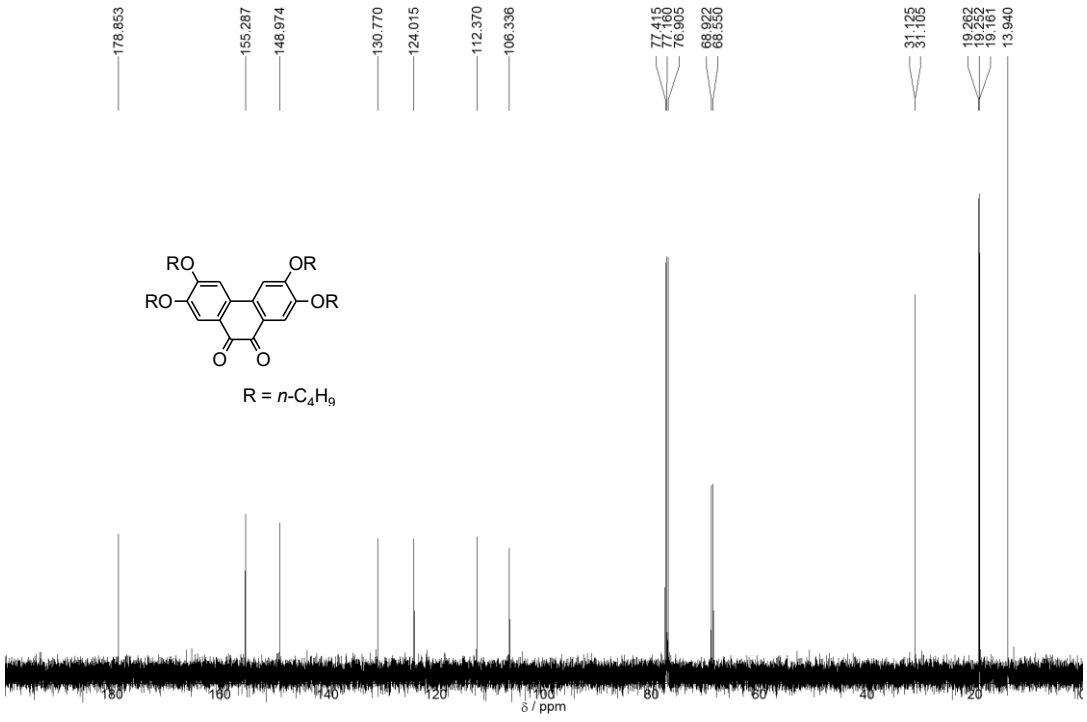

Figure 6-6. ^{1}H NMR spectrum of **13a** in $CDCl_3$ solution (125 MHz).

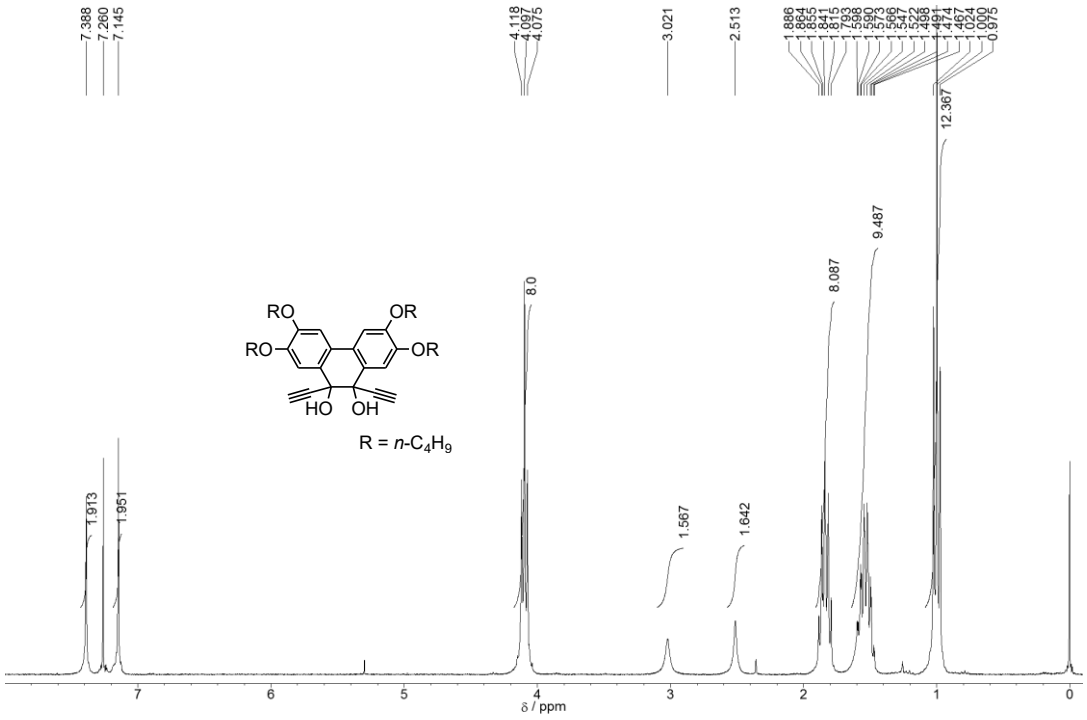

Figure 6-7. ^{1}H NMR spectrum of **14a** in $CDCl_3$ solution (300 MHz).

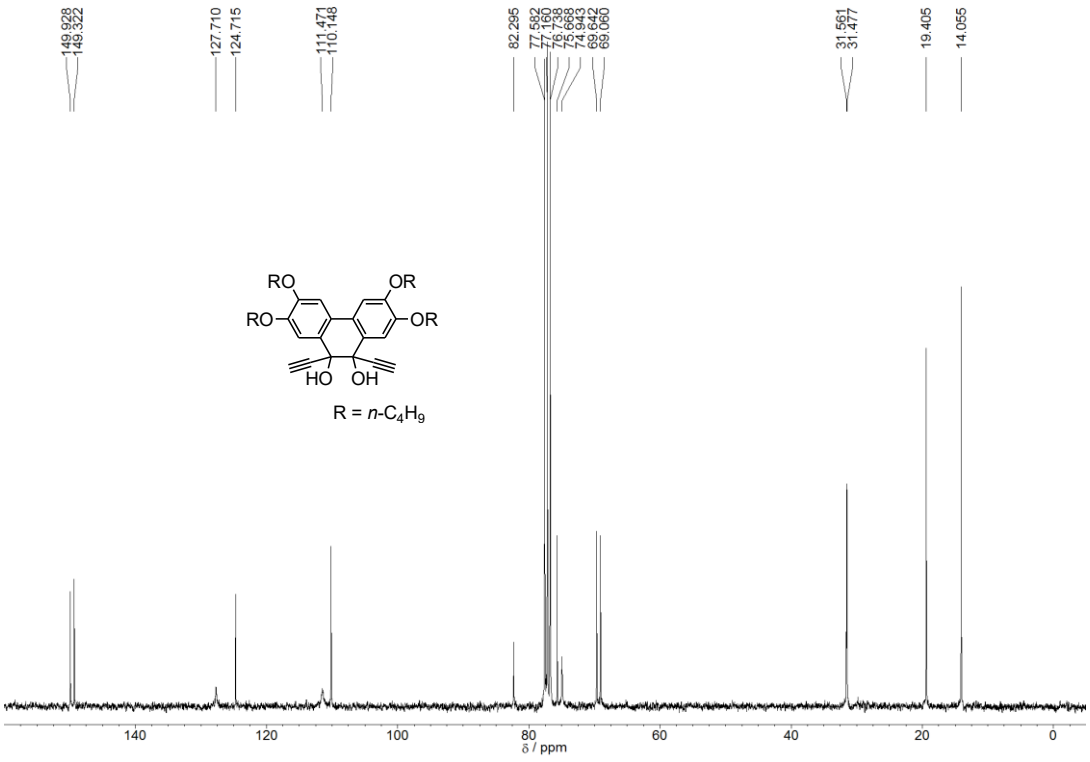

Figure 6-8. ^{13}C NMR spectrum of **14a** in $CDCl_3$ solution (75 MHz).

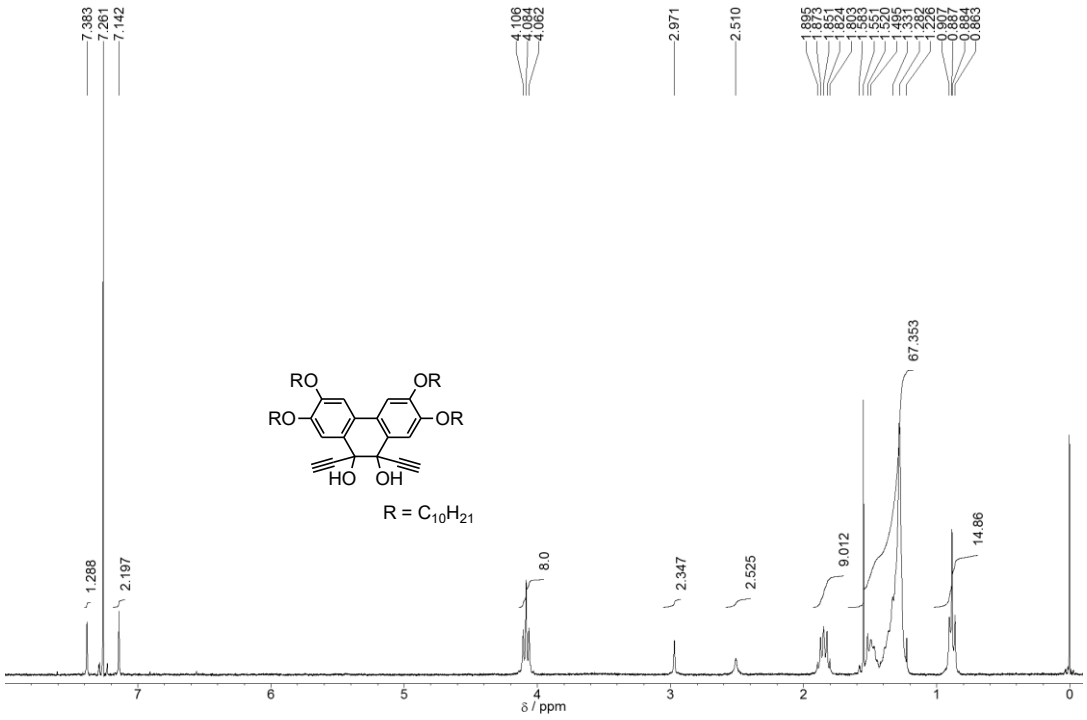

Figure 6-9. ^{1}H NMR spectrum of **14b** in $CDCl_3$ solution (300 MHz).

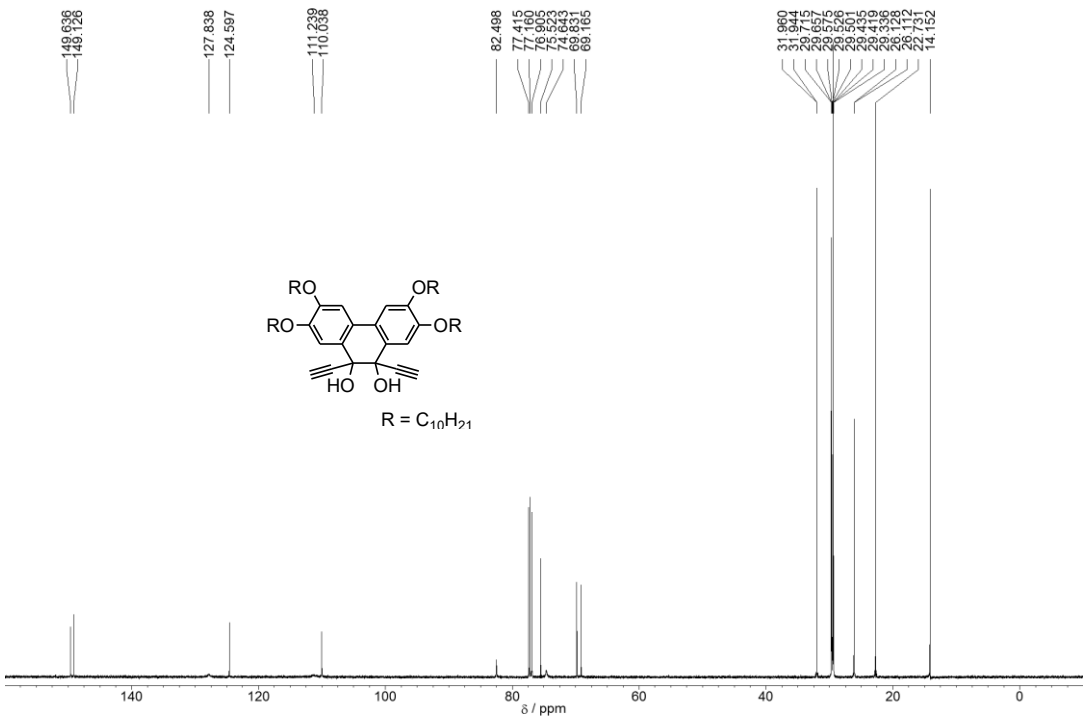

Figure 6-10. ^{13}C NMR spectrum of **14b** in $CDCl_3$ solution (125 MHz).

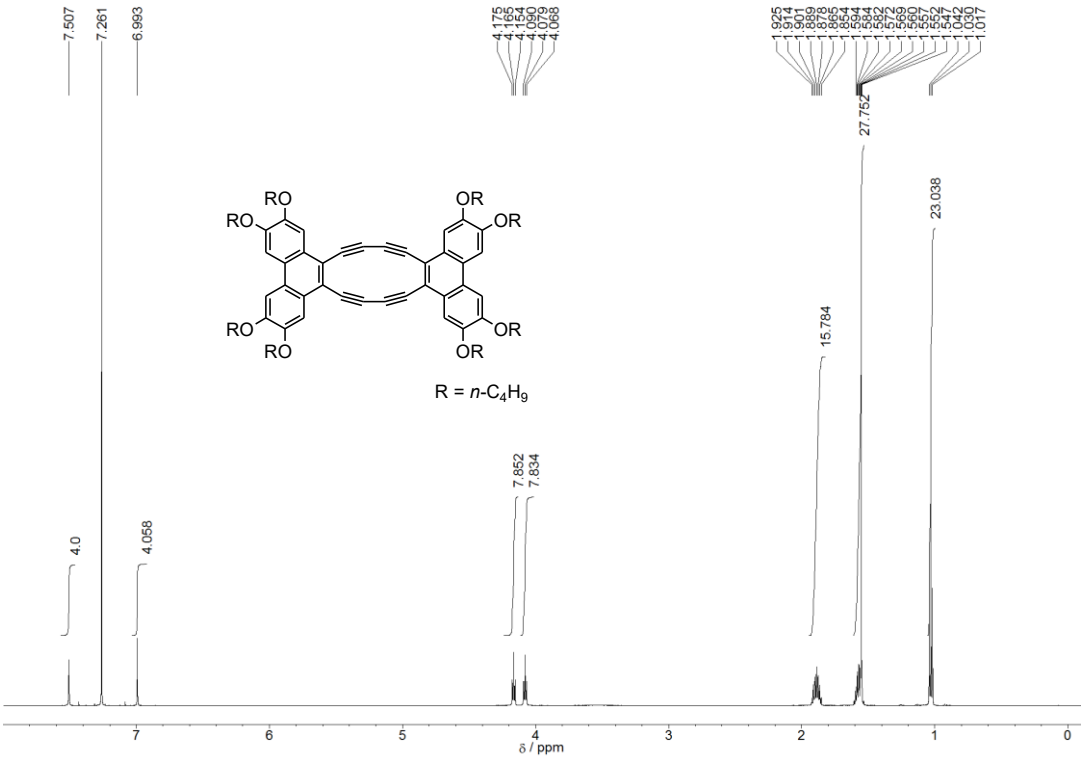

Figure 6-11. ^{1}H NMR spectrum of **3a** in $CDCl_3$ solution (600 MHz, 1.28×10^{-3} mol dm^{-3}).

The ^{13}C NMR spectrum of **3a** could not be obtained due to the low solubility.

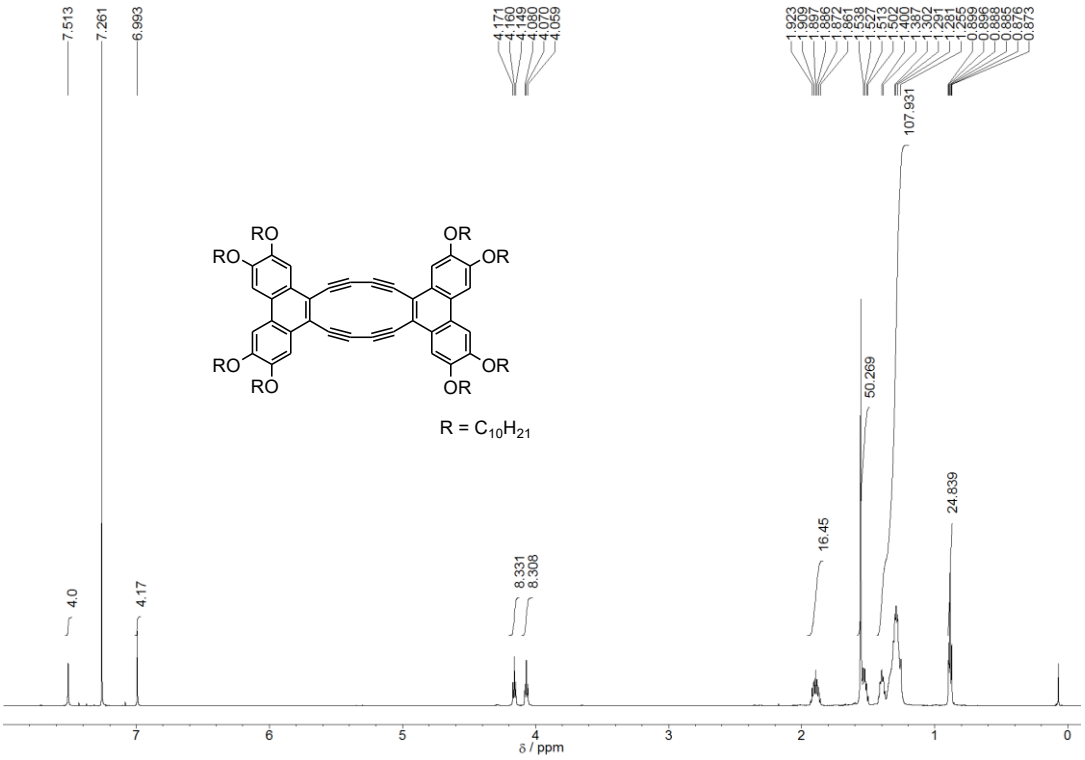

Figure 6-12. ^{1}H NMR spectrum of **3b** in $CDCl_3$ solution (600 MHz, 1.51 × 10^{-3} mol dm^{-3}).

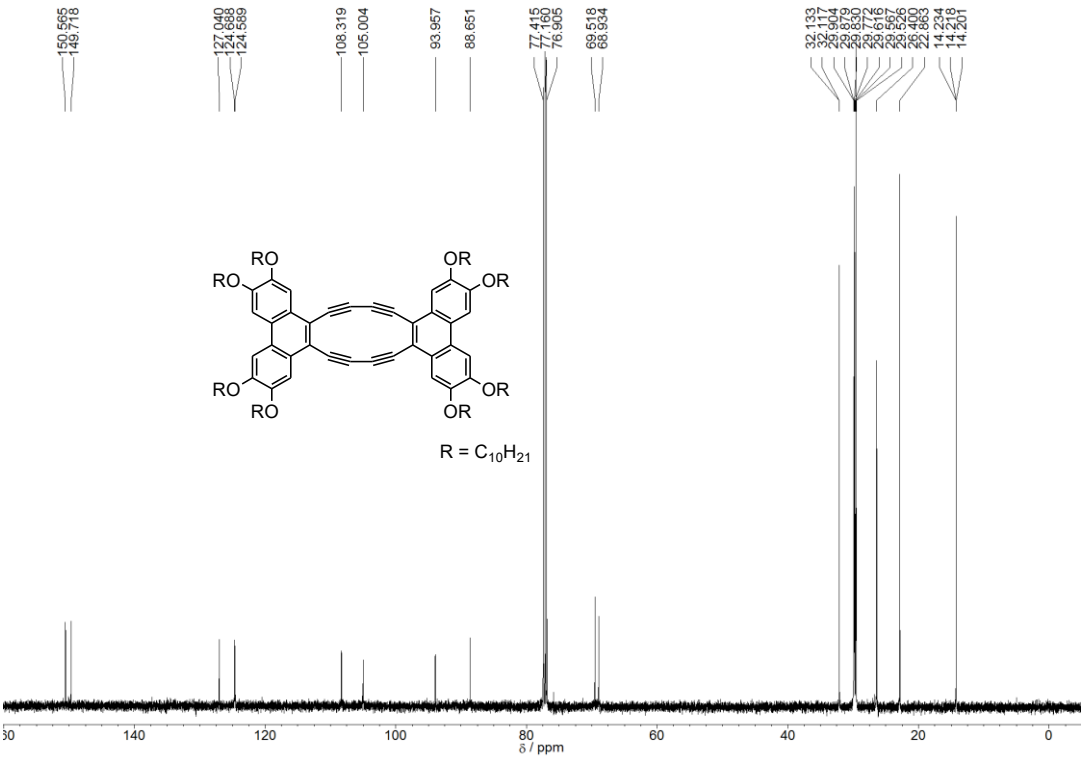

Figure 6-13. ^{13}C NMR spectrum of **3b** in $CDCl_3$ solution (125 MHz, 40 °C).

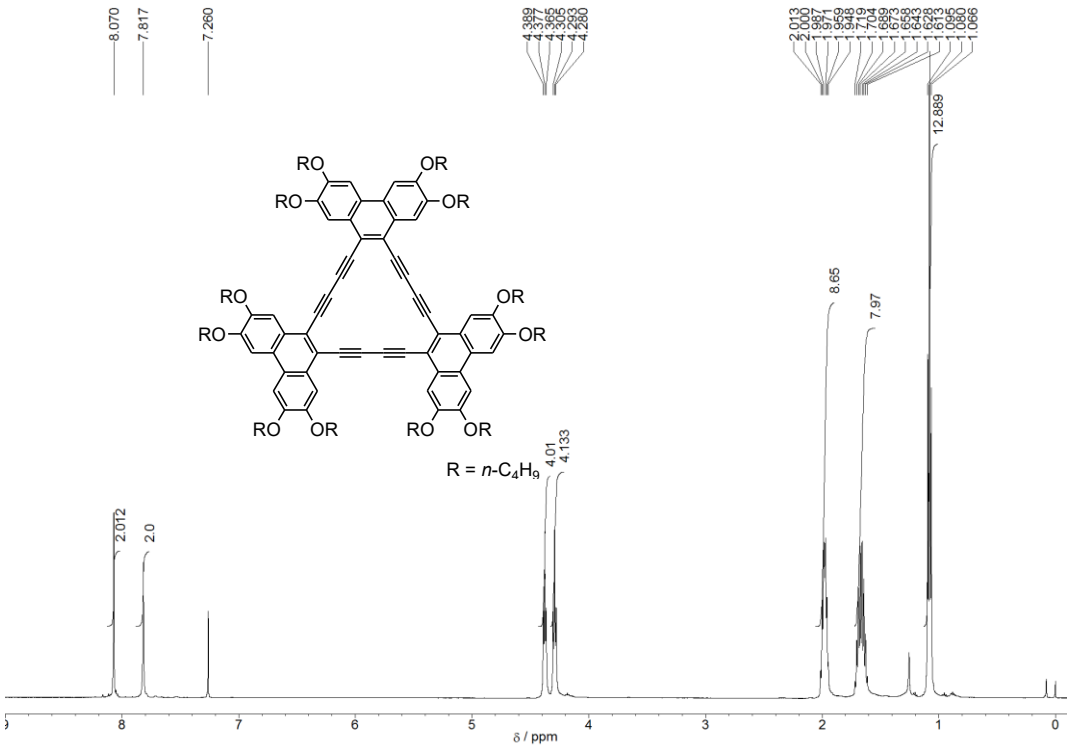

Figure 6-14. ^{1}H NMR spectrum of **4a** in $CDCl_3$ solution (500 MHz, 1.45×10^{-2} mol dm^{-3}).

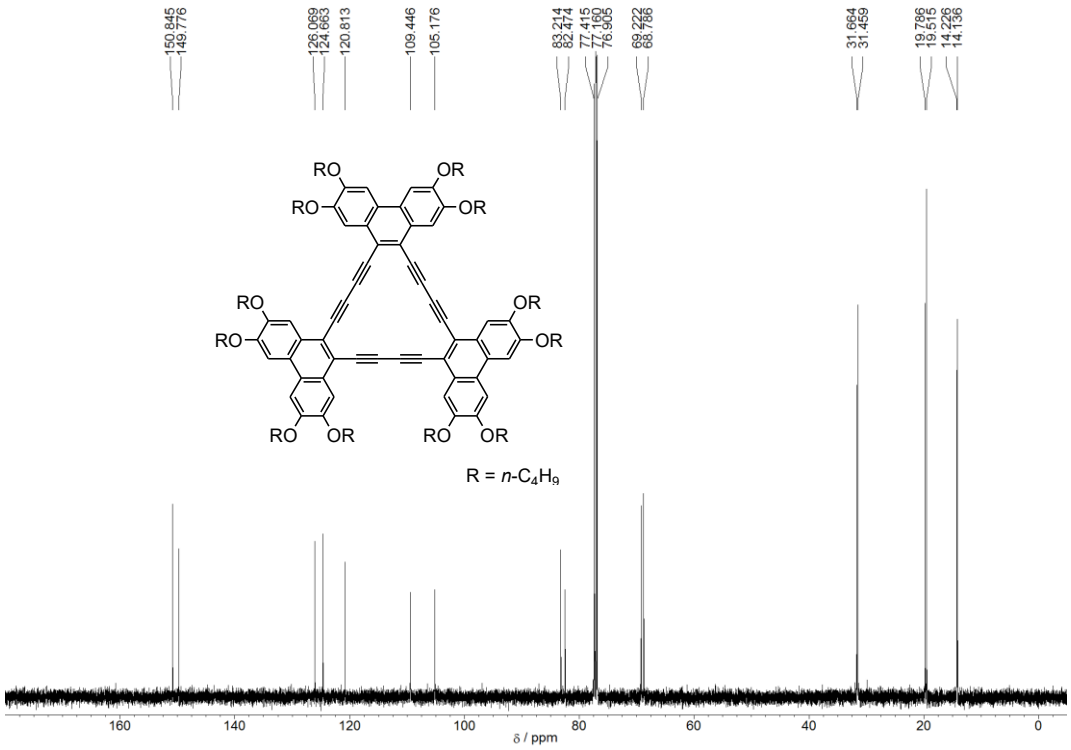

Figure 6-15. ^{13}C NMR spectrum of **4a** in $CDCl_3$ solution (125 MHz).

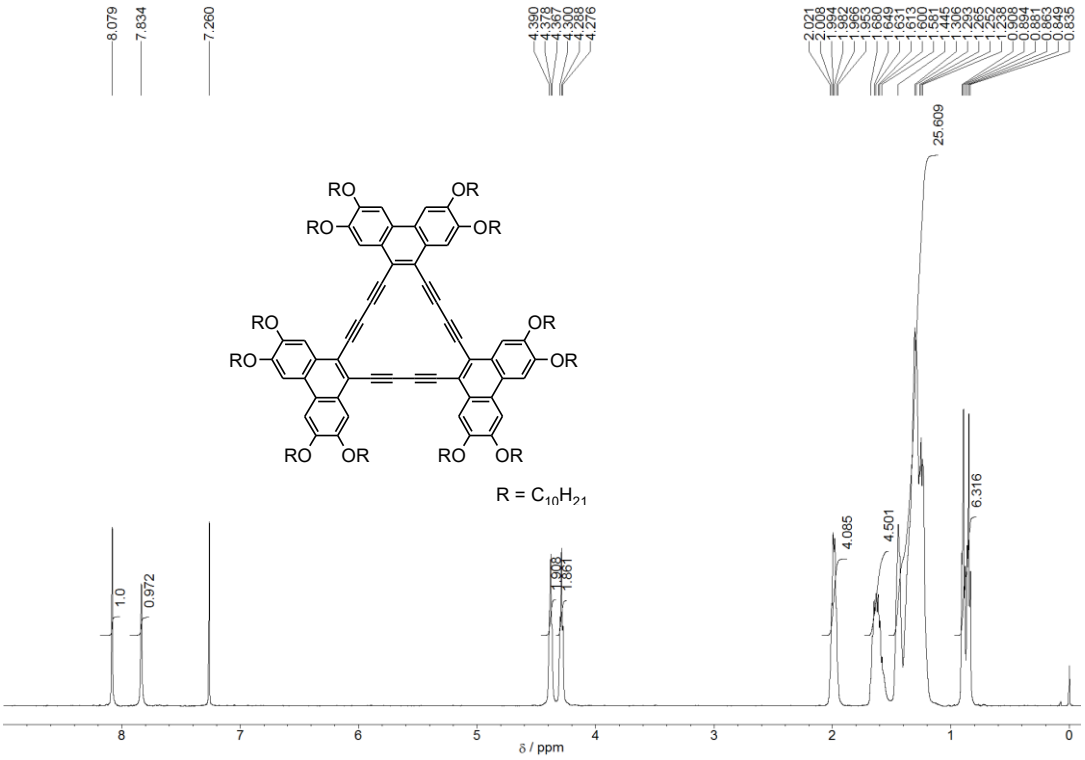

Figure 6-16. ^{1}H NMR spectrum of **4b** in $CDCl_3$ solution (500 MHz, 6.05×10^{-3} mol dm^{-3}).

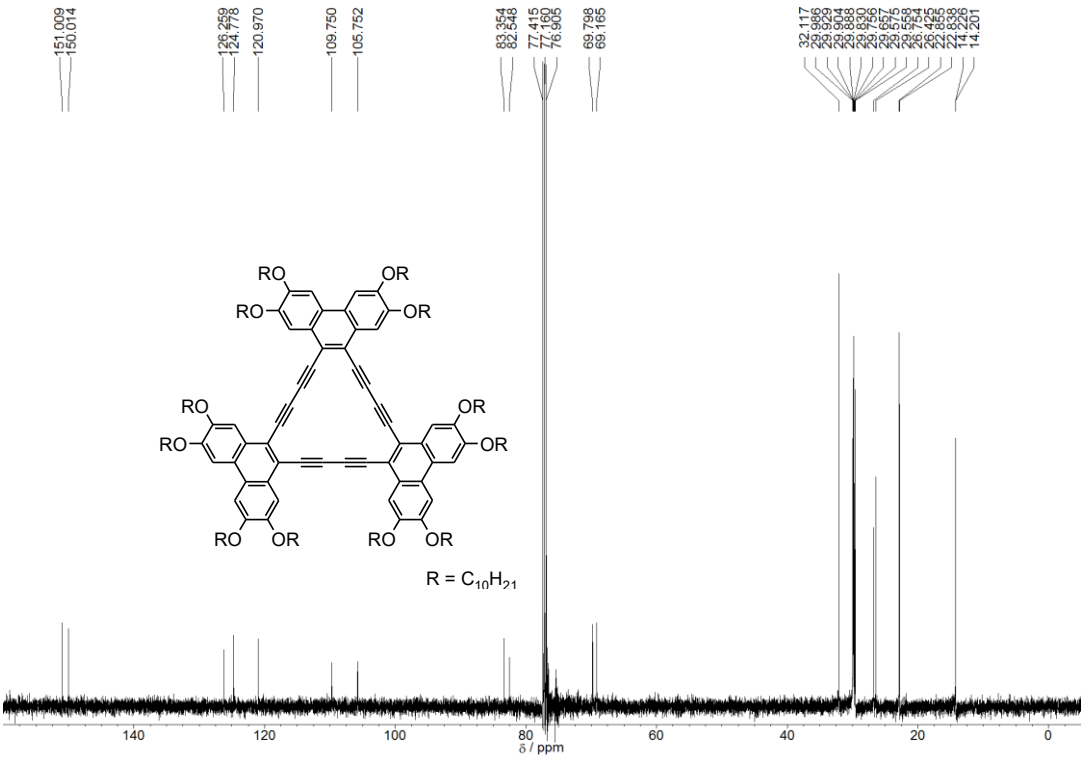

Figure 6-17. ^{13}C NMR spectrum of **4b** in $CDCl_3$ solution (125 MHz).

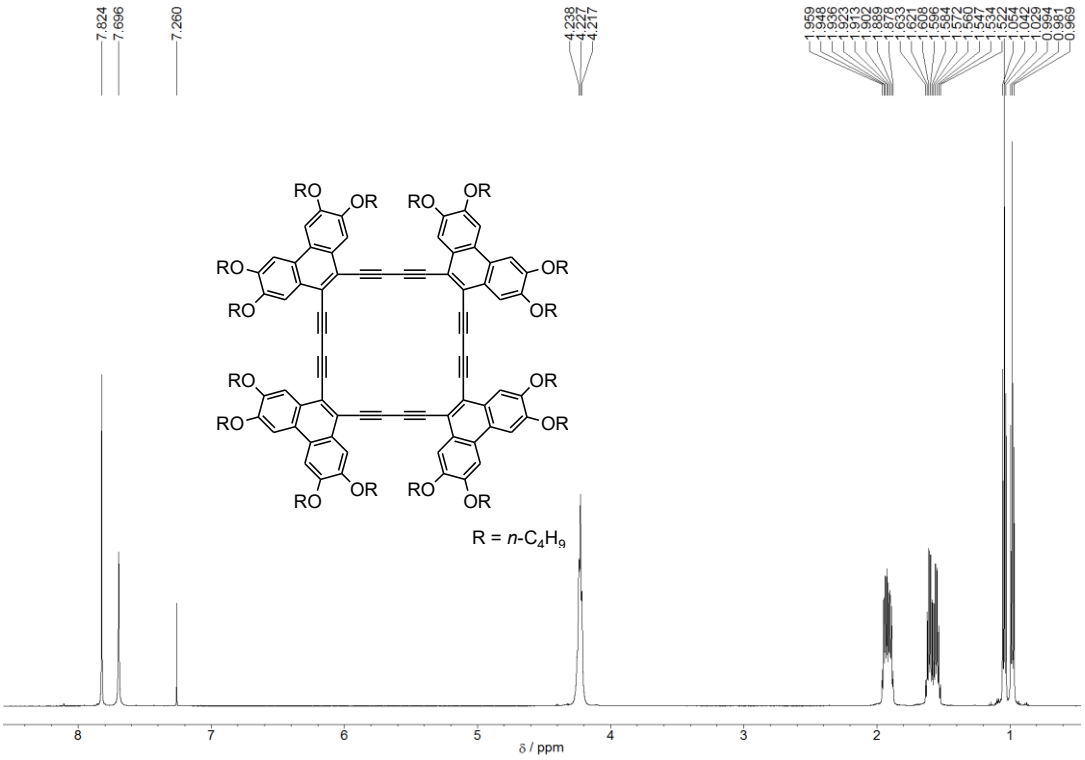

Figure 6-18. ^{1}H NMR spectrum of **5a** in $CDCl_3$ solution (600 MHz).

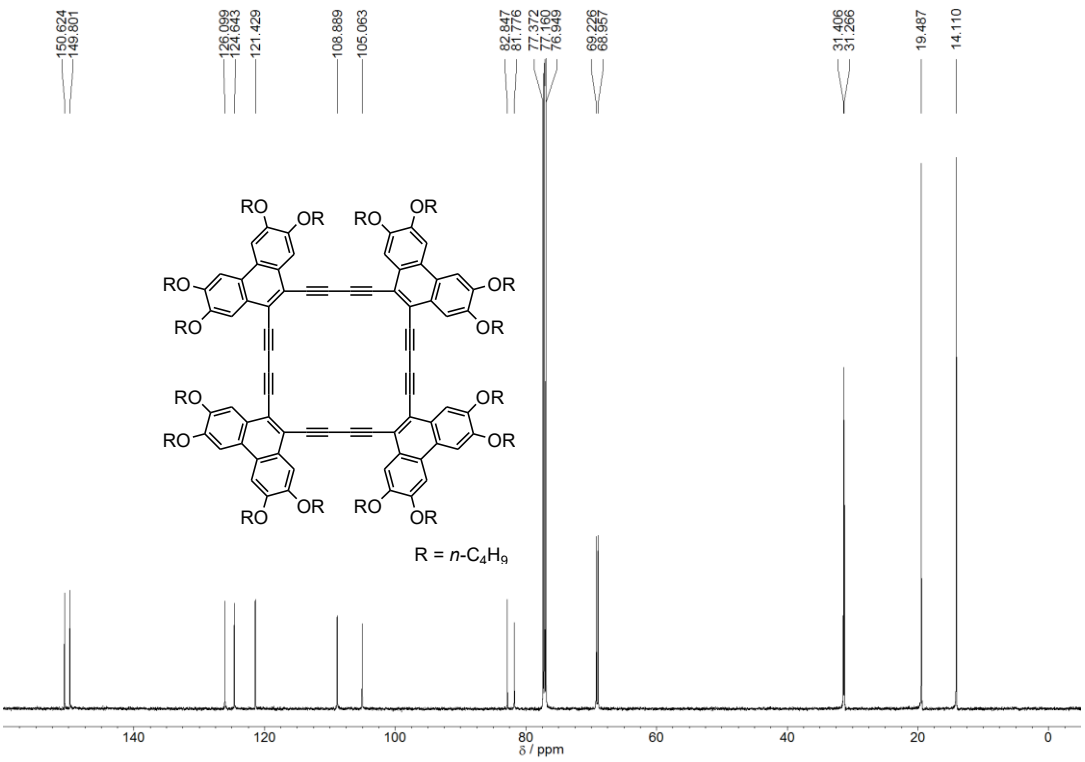

Figure 6-19. ^{13}C NMR spectrum of **5a** in $CDCl_3$ solution (150 MHz).

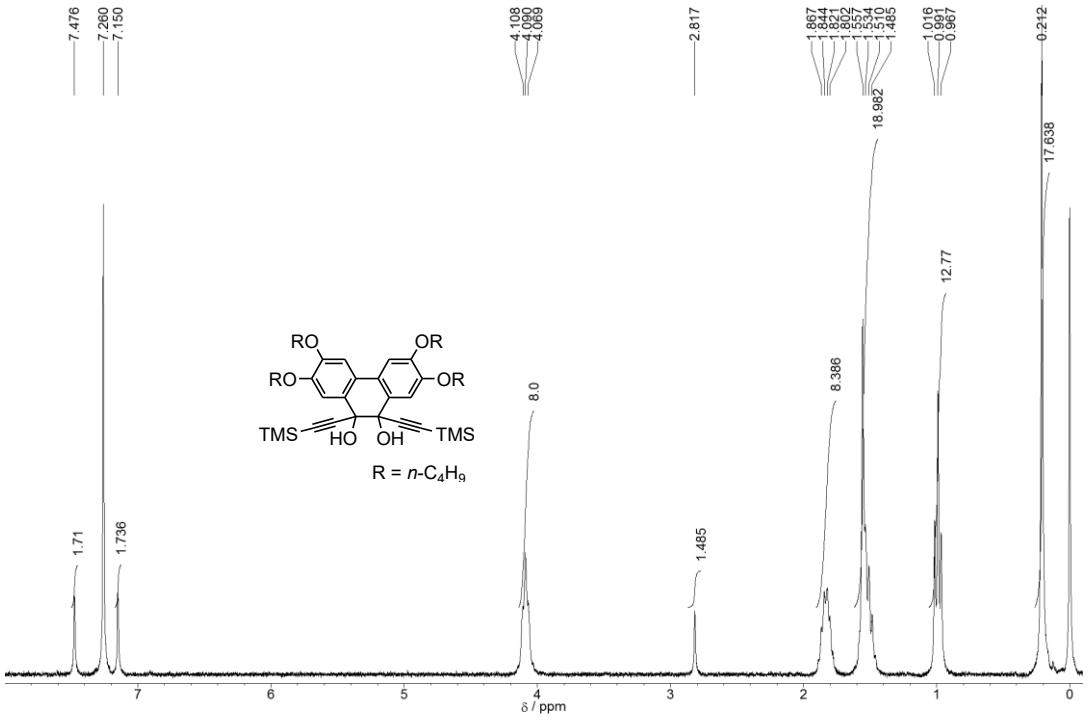

Figure 6-20. ^{1}H NMR spectrum of **16a** in $CDCl_3$ solution (300 MHz).

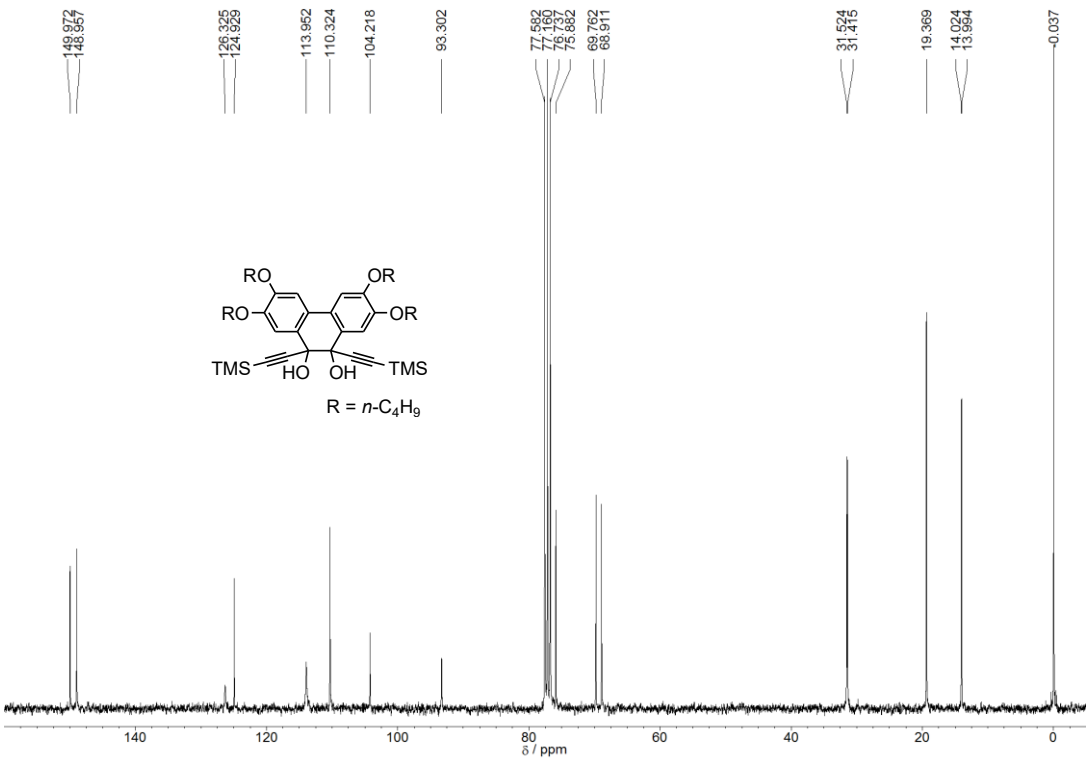

Figure 6-21. ^{13}C NMR spectrum of **16a** in $CDCl_3$ solution (75 MHz).

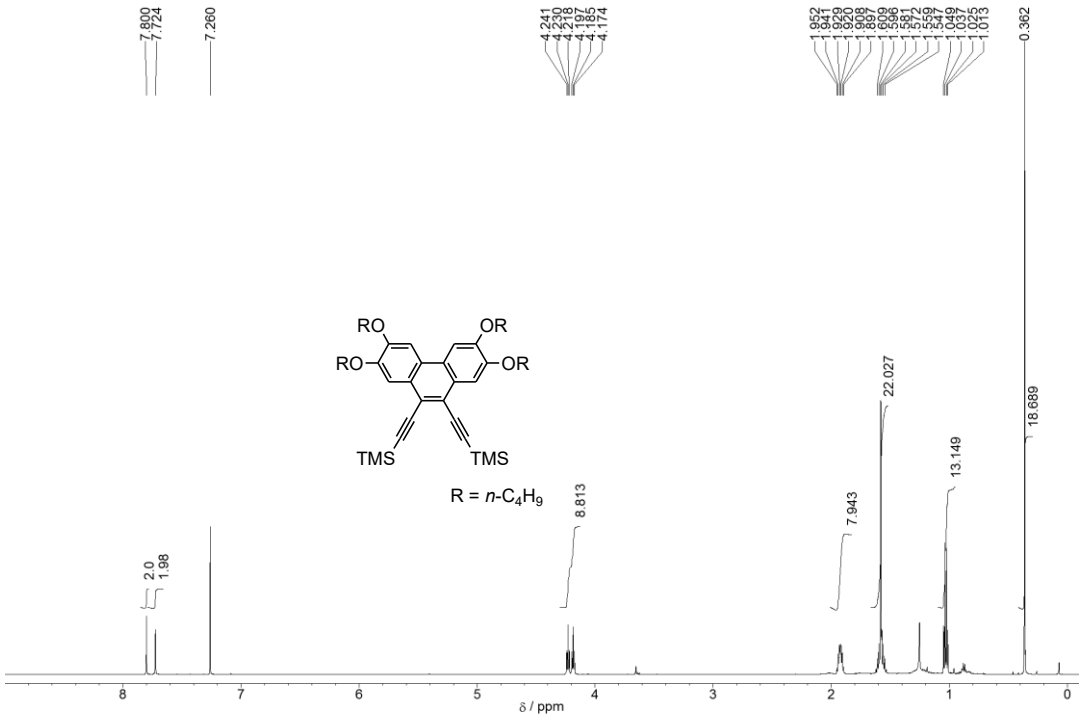

Figure 6-22. ^{1}H NMR spectrum of **17** in $CDCl_3$ solution (600 MHz).

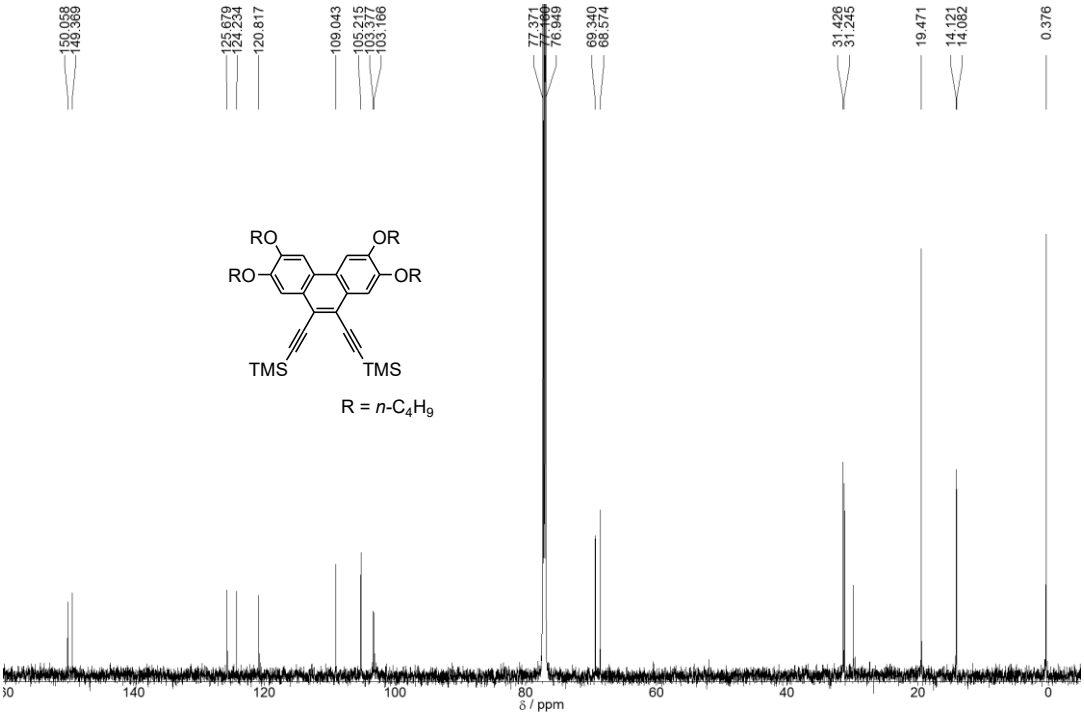

Figure 6-23. ^{13}C NMR spectrum of **17** in $CDCl_3$ solution (150 MHz).

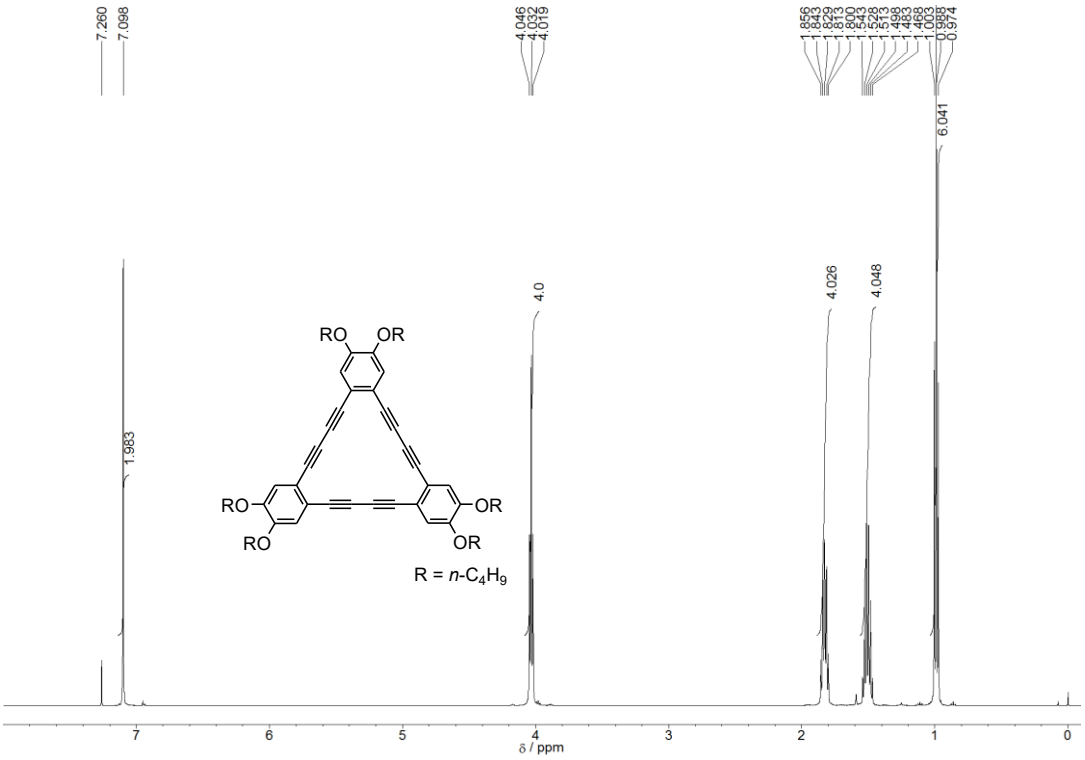

Figure 6-24. ^{1}H NMR spectrum of **2a** in $CDCl_3$ solution (500 MHz).

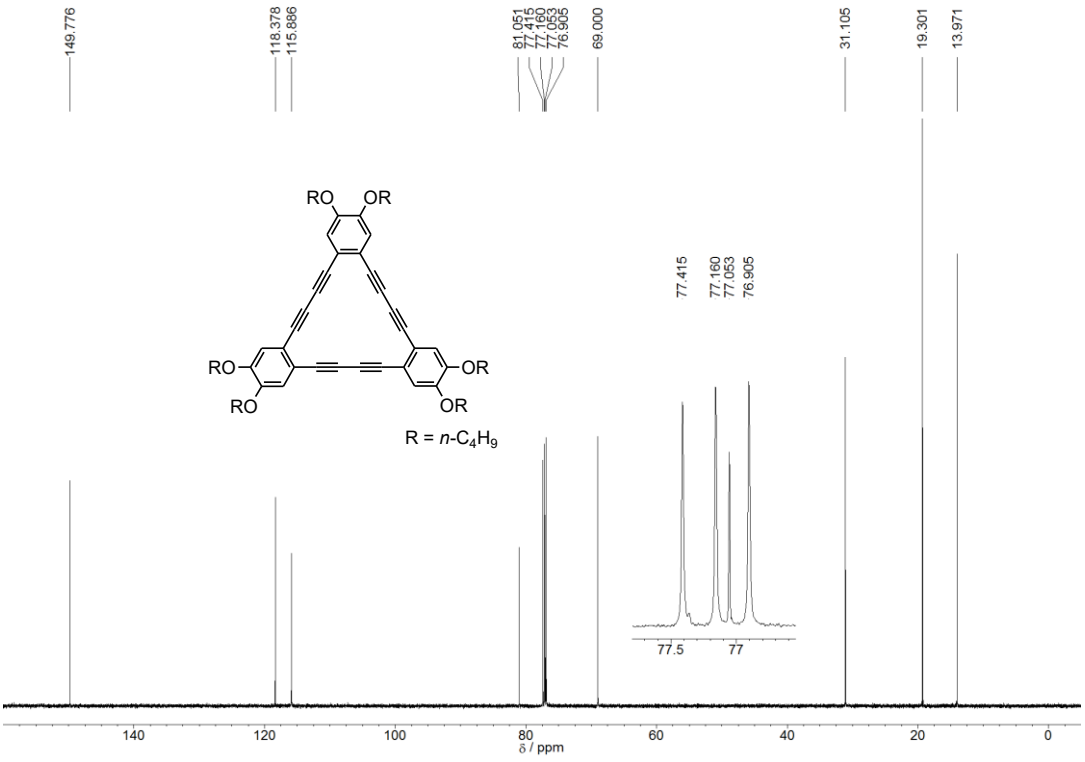

Figure 6-25. ^{13}C NMR spectrum of **2a** in $CDCl_3$ solution (125 MHz).

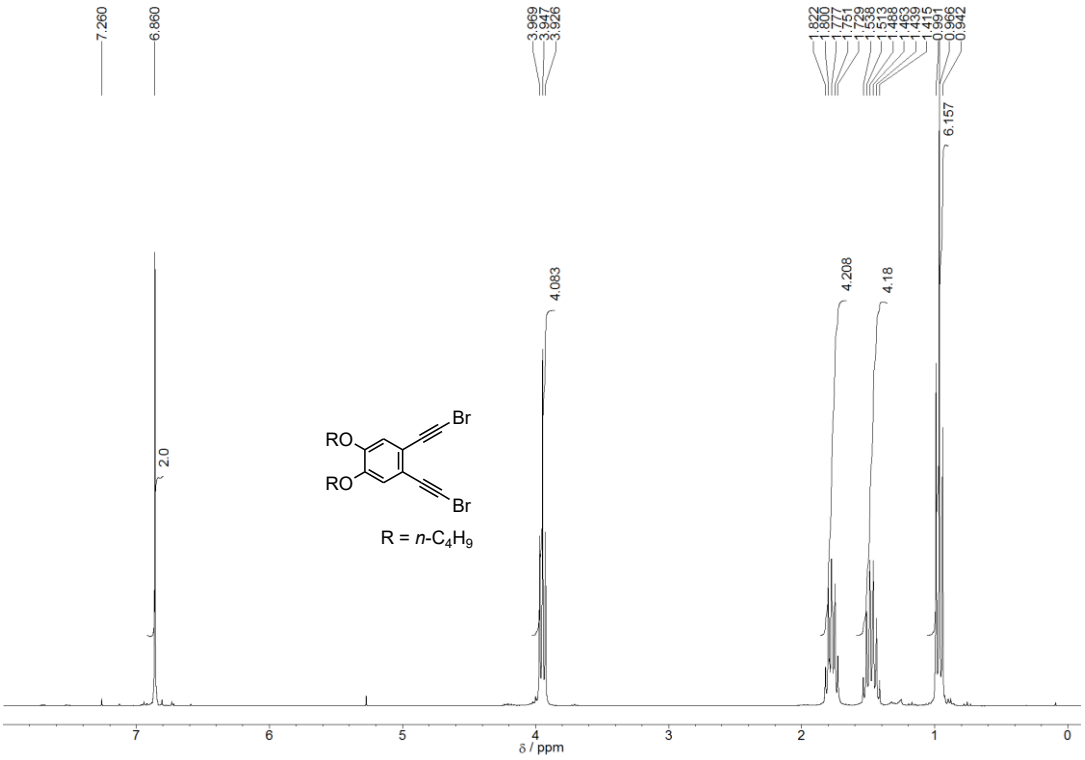

Figure 6-26. ^{1}H NMR spectrum of **24** in $CDCl_3$ solution (300 MHz).

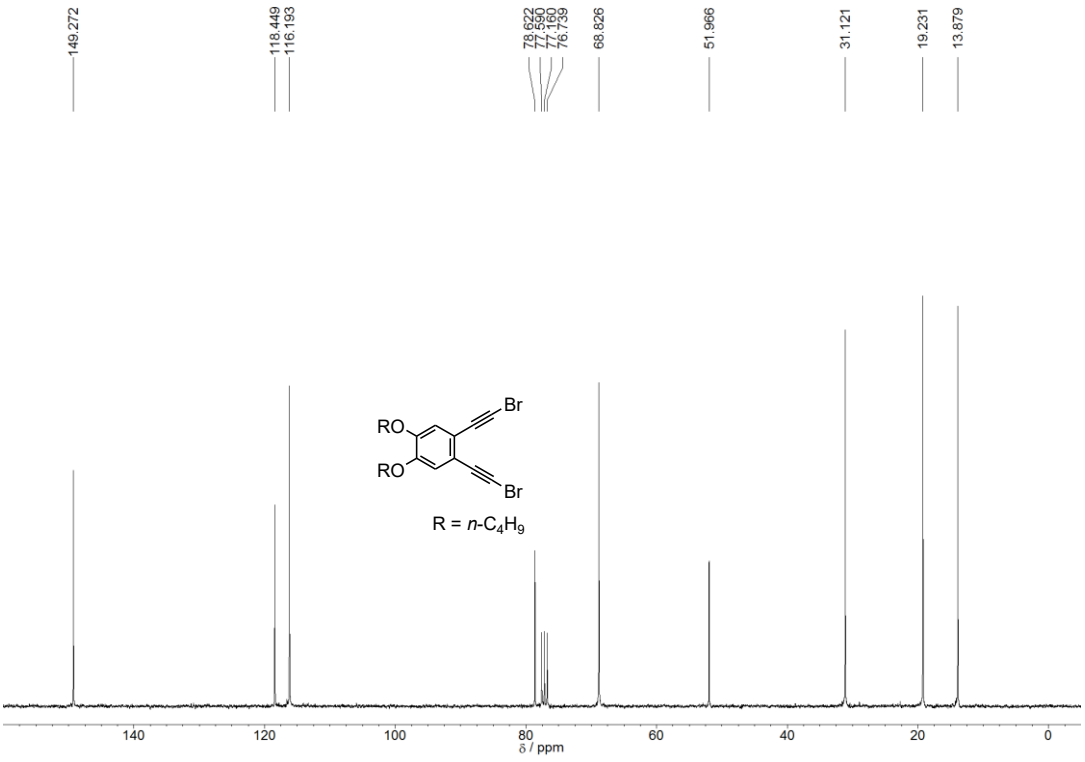

Figure 6-27. ^{13}C NMR spectrum of **24** in $CDCl_3$ solution (75 MHz).

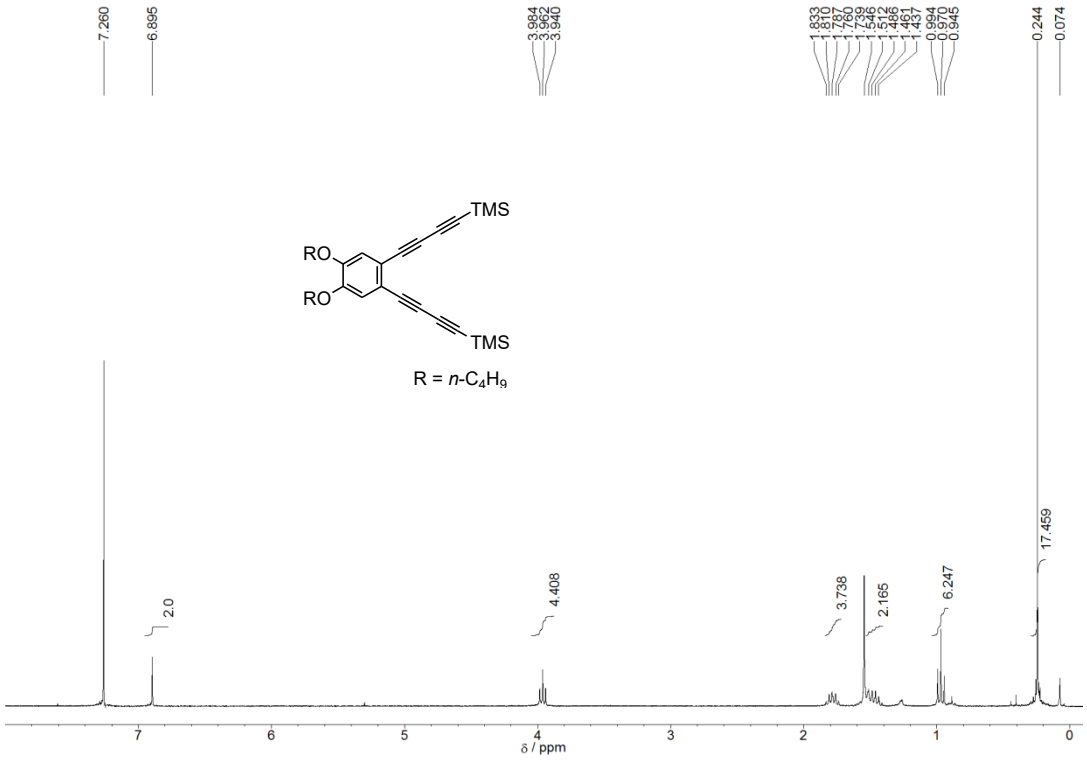

Figure 6-28. ^{1}H NMR spectrum of **25** in $CDCl_3$ solution (500 MHz).

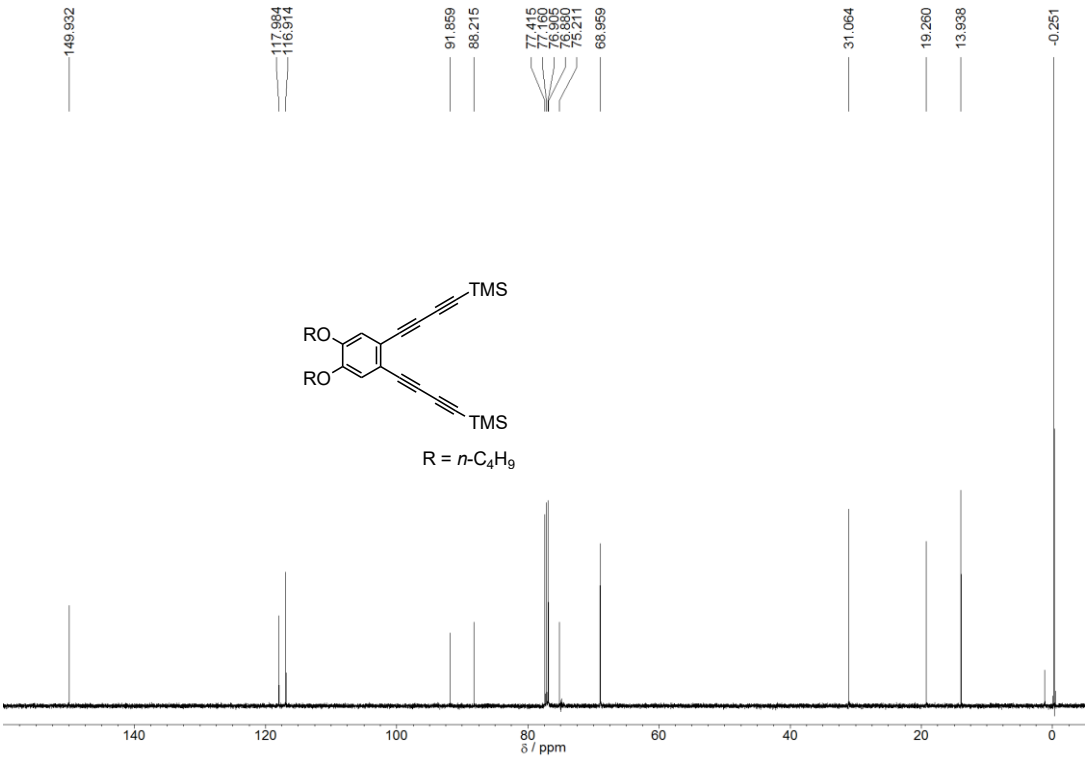

Figure 6-29. ^{13}C NMR spectrum of **25** in $CDCl_3$ solution (125 MHz).

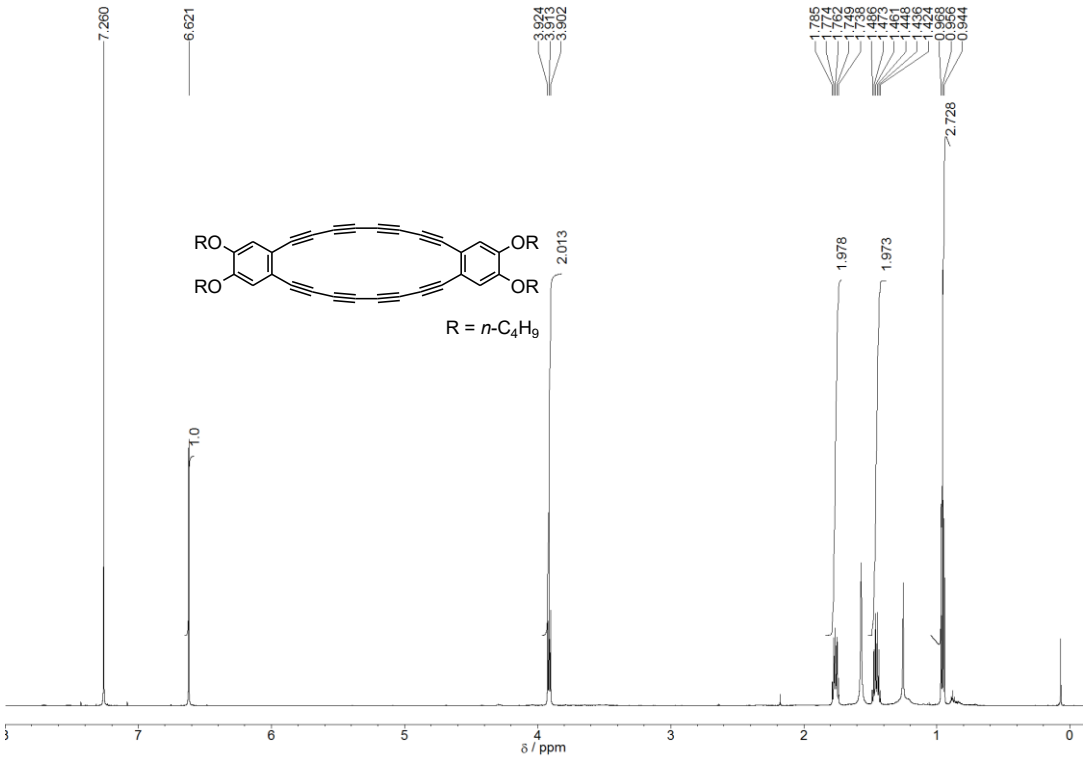

Figure 6-30. ^{1}H NMR spectrum of **6** in $CDCl_3$ solution (600 MHz).

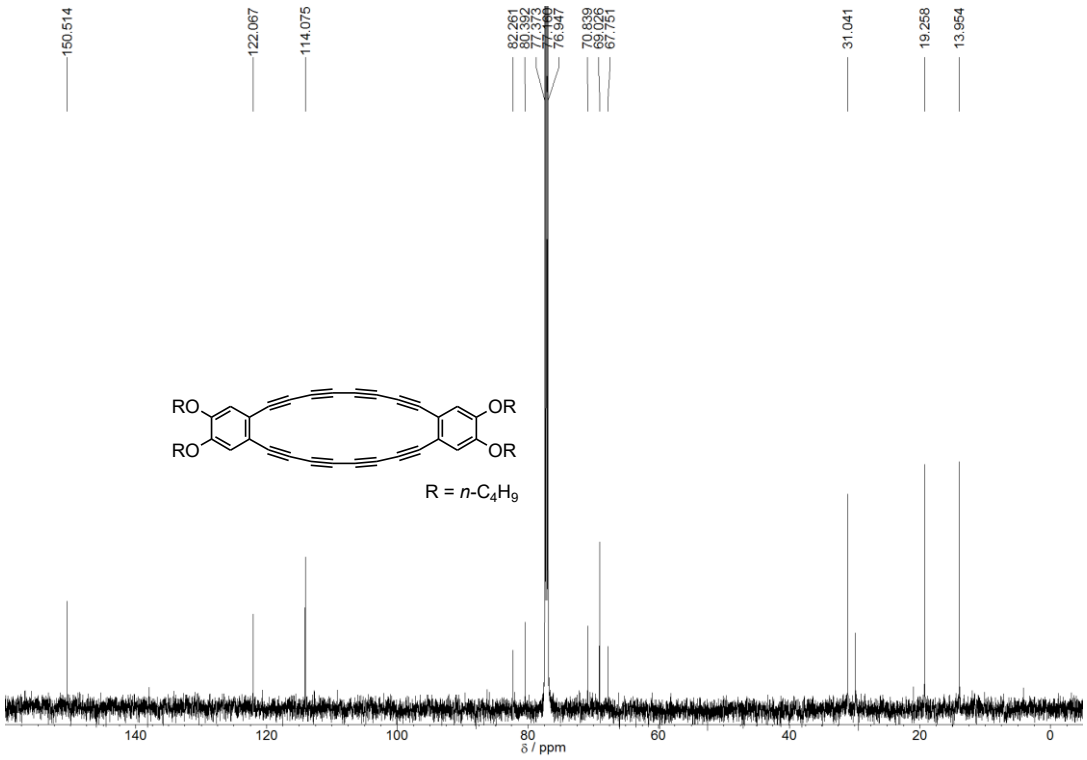

Figure 6-31. ^{13}C NMR spectrum of **6** in $CDCl_3$ solution (150 MHz).

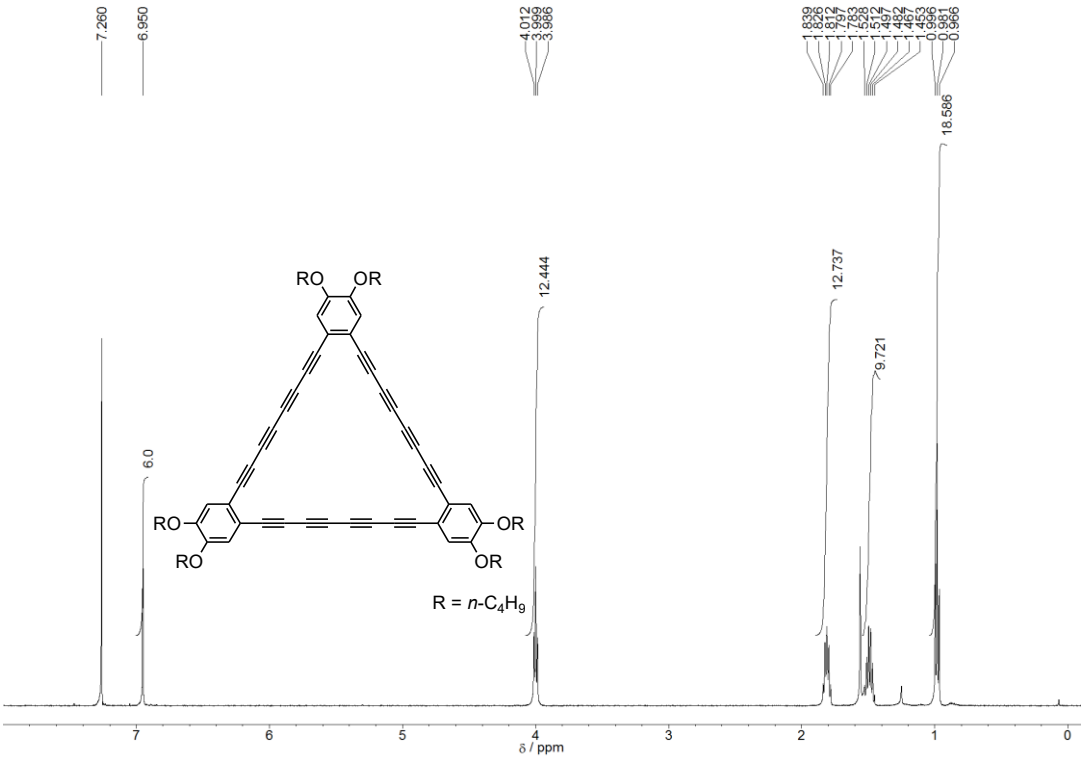

Figure 6-32. ^{1}H NMR spectrum of **7** in $CDCl_3$ solution (2.53×10^{-3} mol dm^{-3}, 500 MHz).

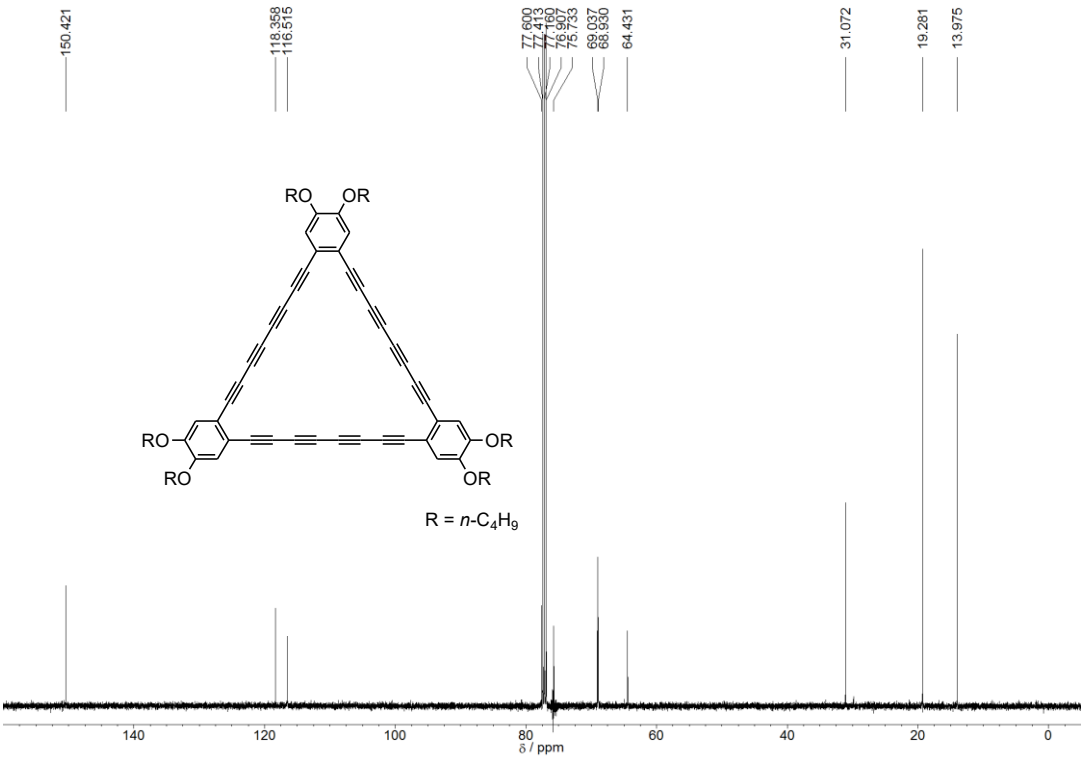

Figure 6-33. ^{13}C NMR spectrum of **7** in $CDCl_3$ solution (125 MHz).

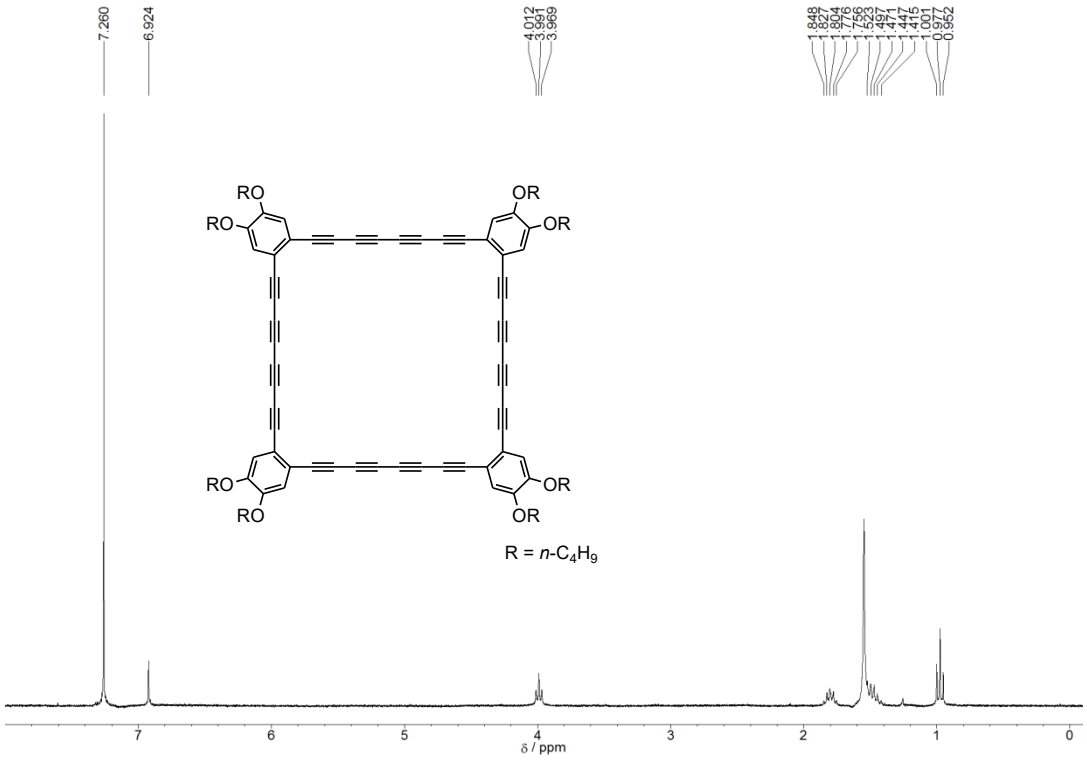

Figure 6-34. ^{1}H NMR spectrum of **8** in $CDCl_3$ solution (500 MHz).

The ^{13}C NMR spectrum of **8** could not be obtained due to the low solubility.

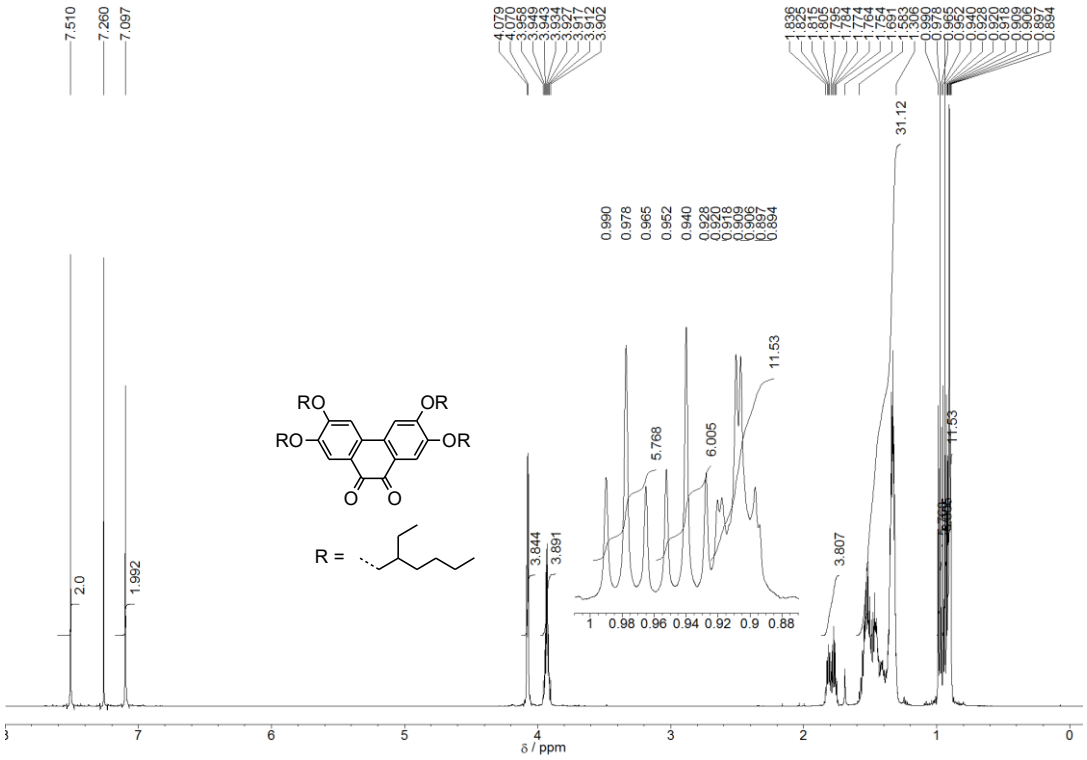

Figure 6-35. ^{1}H NMR spectrum of **13c** in $CDCl_3$ solution (300 MHz).

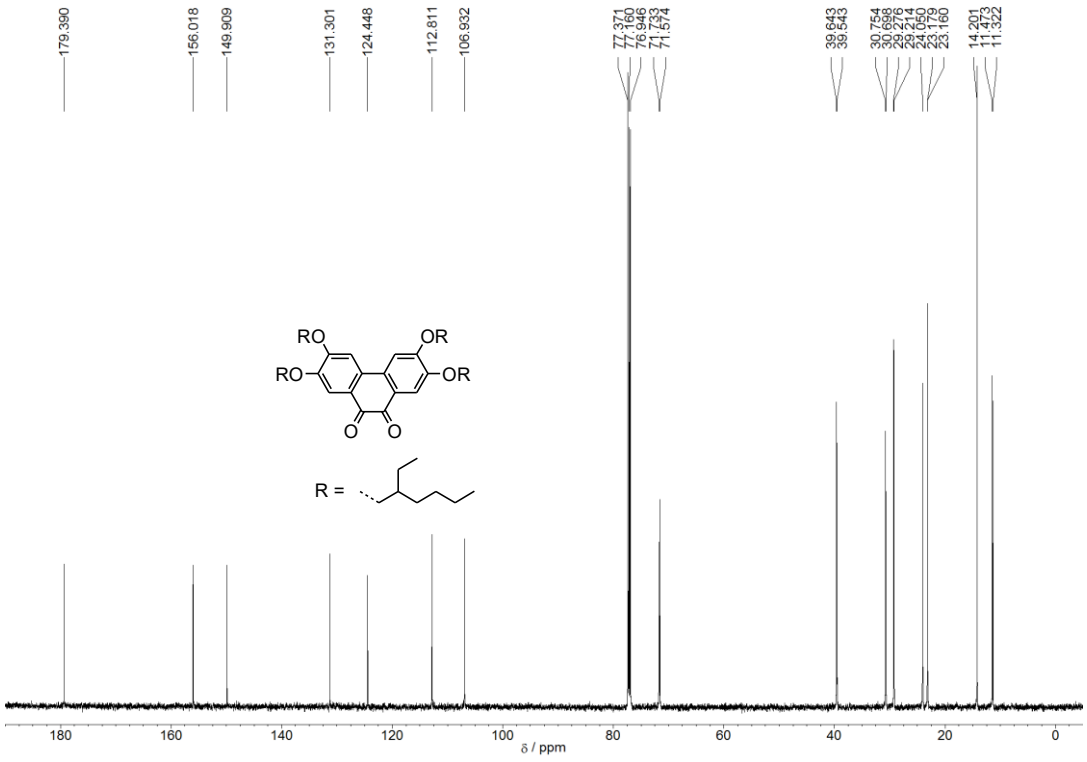

Figure 6-36. ^{13}C NMR spectrum of **13c** in $CDCl_3$ solution (150 MHz).

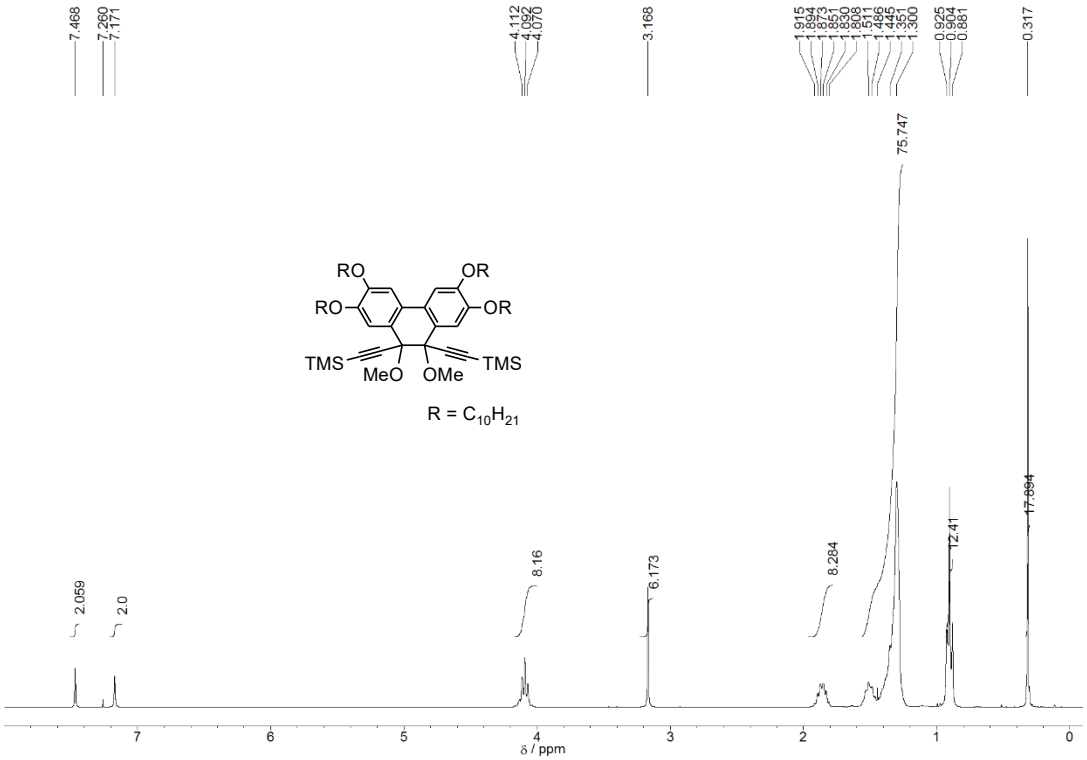

Figure 6-37. ^{1}H NMR spectrum of **27a** in $CDCl_3$ solution (400 MHz).

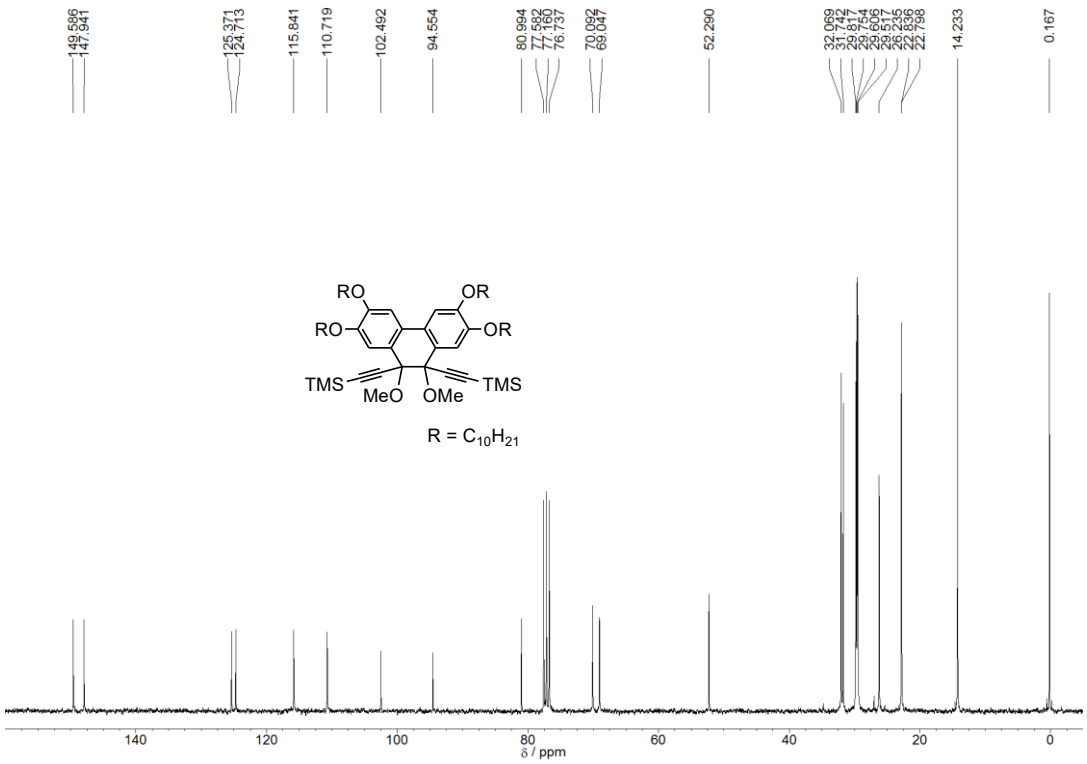

Figure 6-38. ^{13}C NMR spectrum of **27a** in $CDCl_3$ solution (75 MHz).

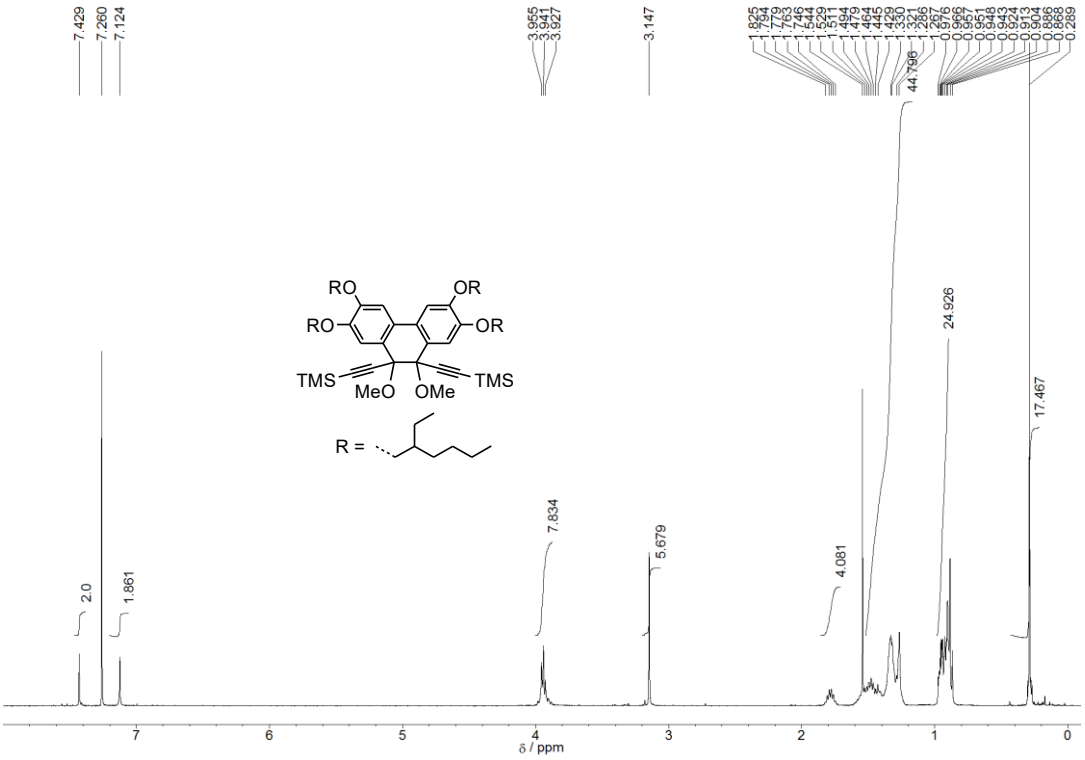

Figure 6-39. ^{1}H NMR spectrum of **27b** in $CDCl_3$ solution (300 MHz).

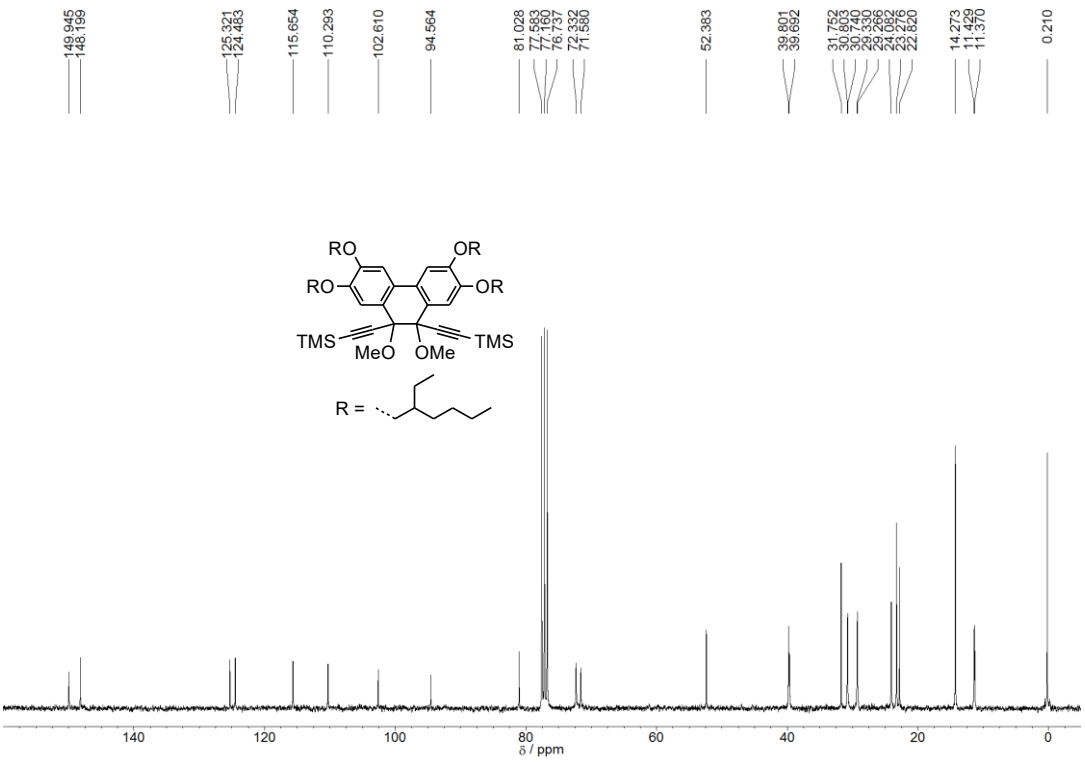

Figure 6-40. ^{13}C NMR spectrum of **27b** in $CDCl_3$ solution (75 MHz).

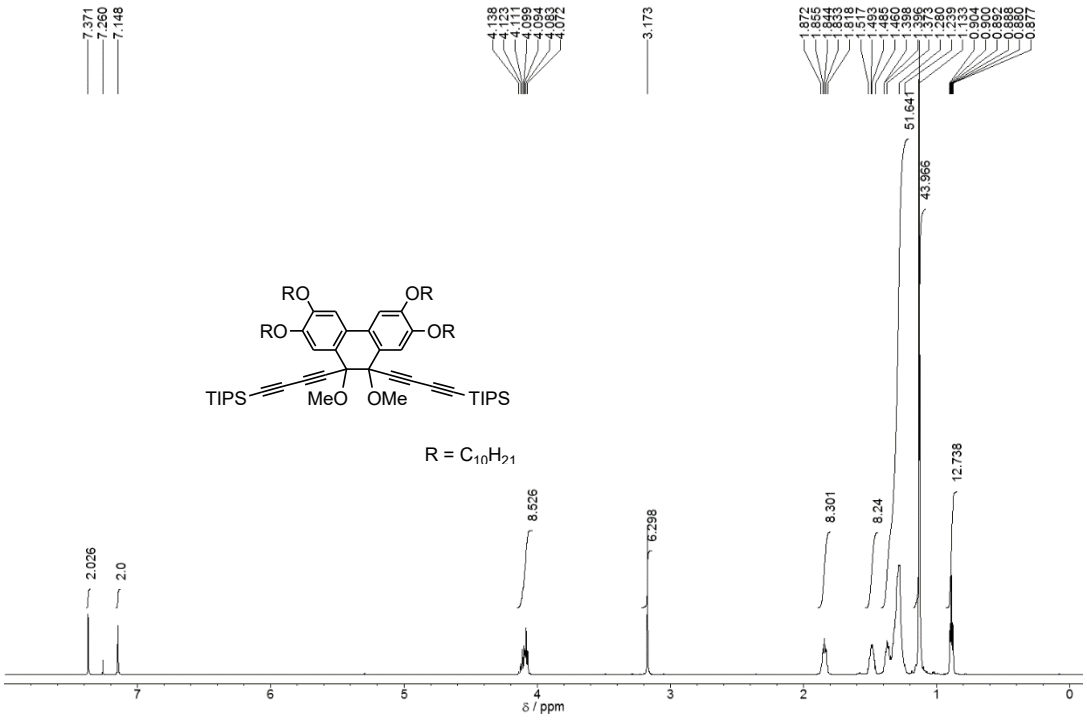

Figure 6-41. ^{1}H NMR spectrum of **29a** in $CDCl_3$ solution (300 MHz).

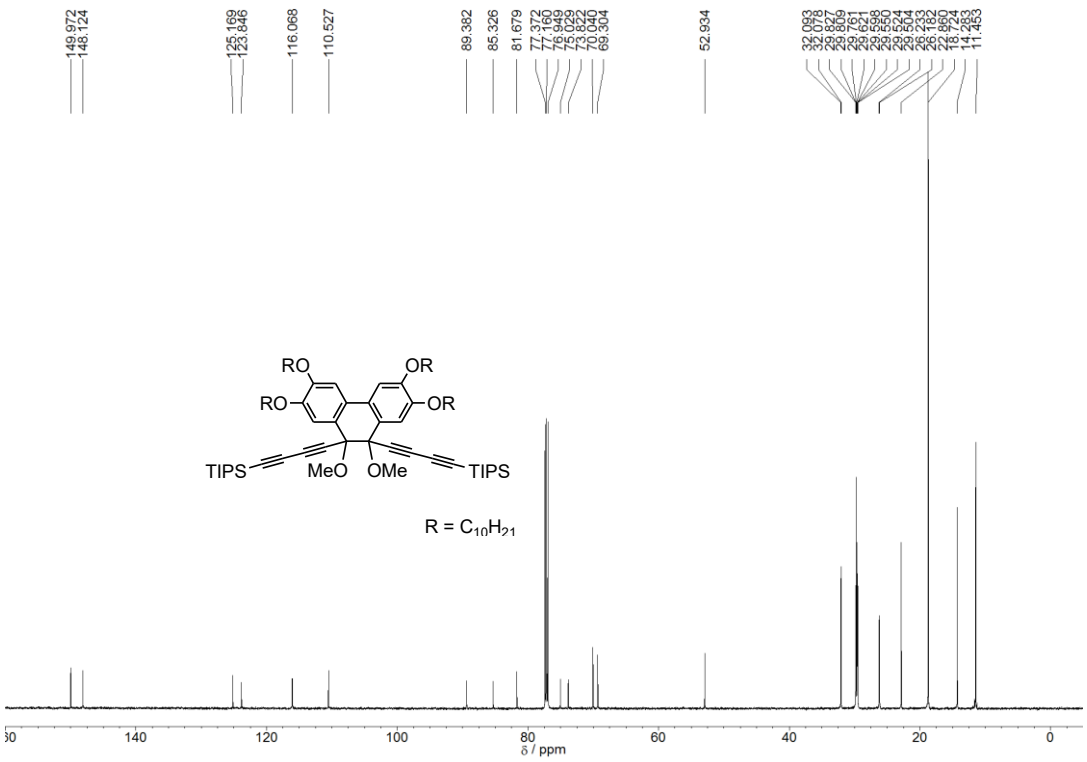

Figure 6-42. ^{13}C NMR spectrum of **29a** in $CDCl_3$ solution (150 MHz).

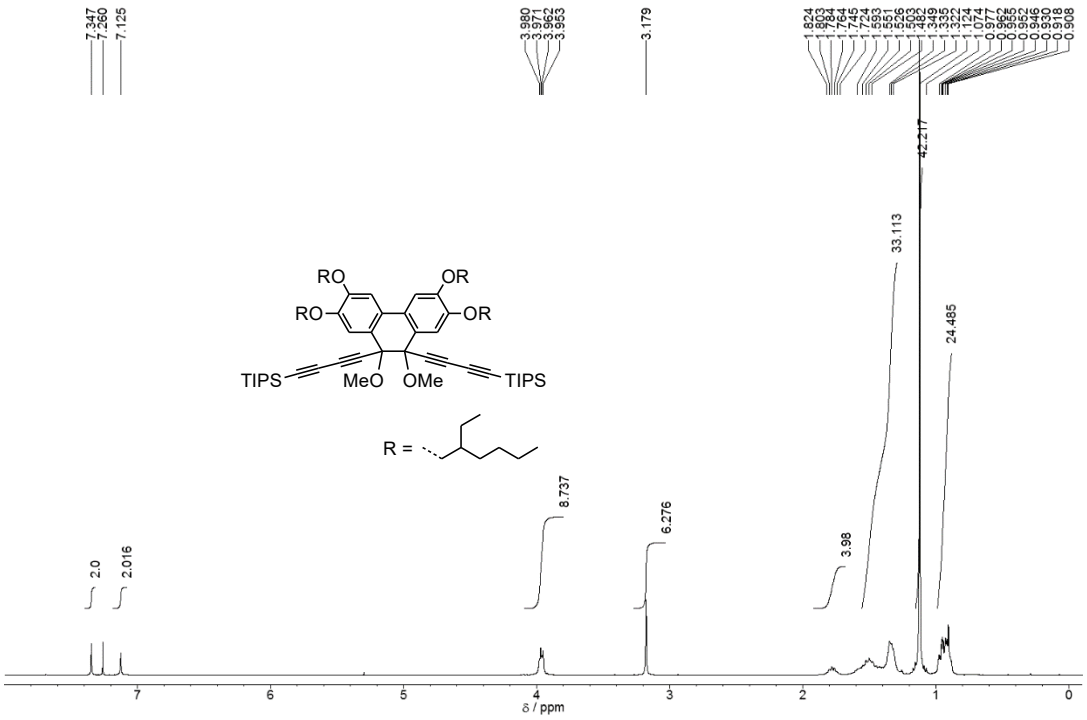

Figure 6-43. ^{1}H NMR spectrum of **29b** in $CDCl_3$ solution (300 MHz).

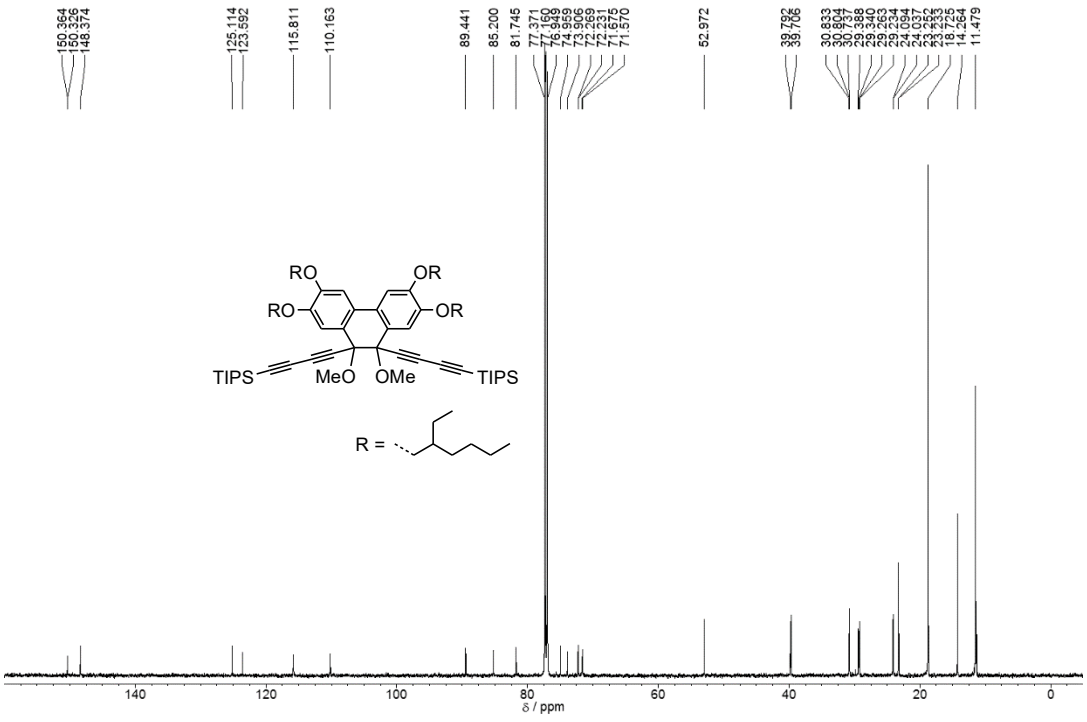

Figure 6-44. ^{13}C NMR spectrum of **29b** in $CDCl_3$ solution (150 MHz).

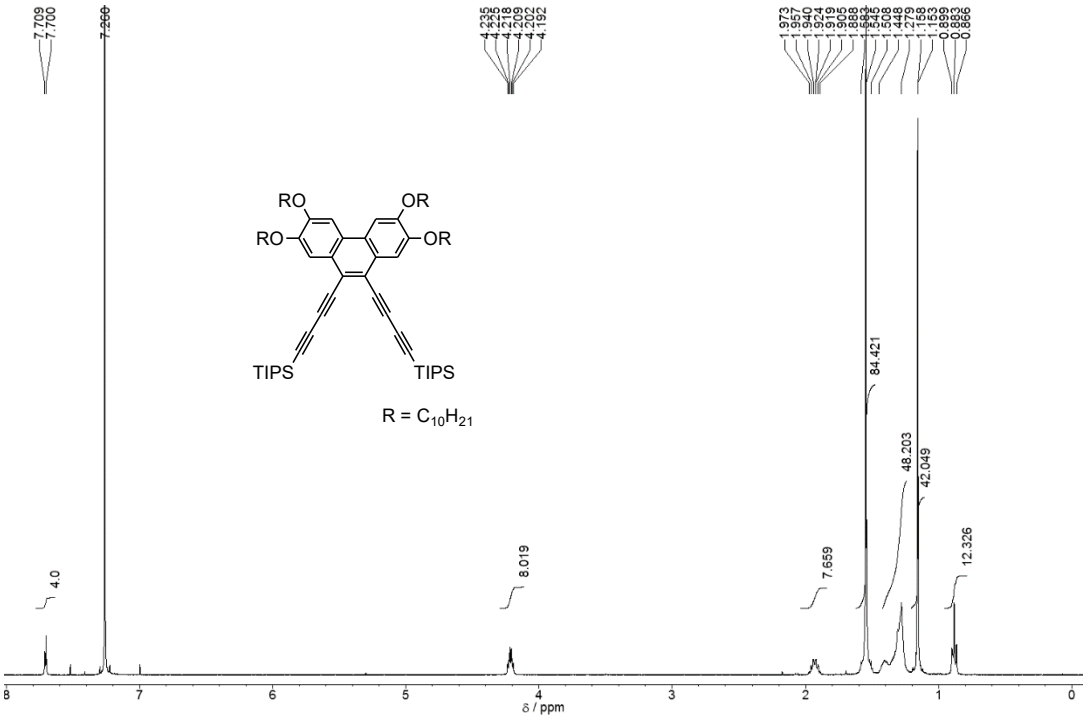

Figure 6-45. ^{1}H NMR spectrum of **30a** in $CDCl_3$ solution (400 MHz).

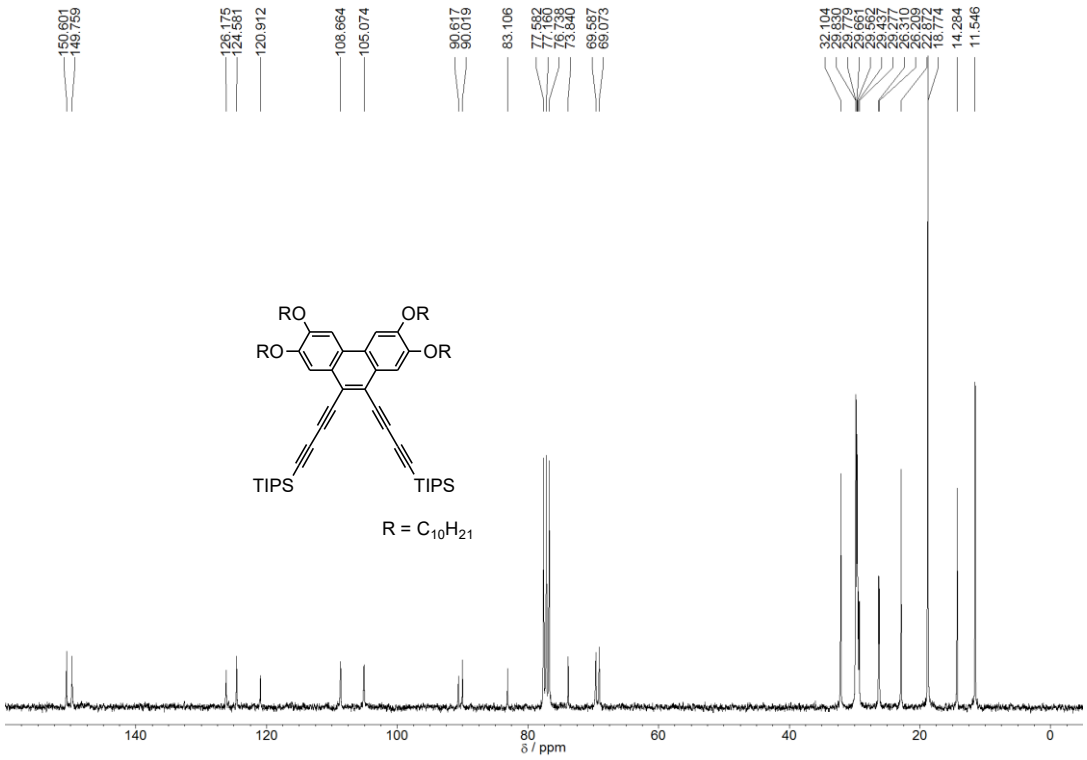

Figure 6-46. ^{13}C NMR spectrum of **30a** in $CDCl_3$ solution (75 MHz).

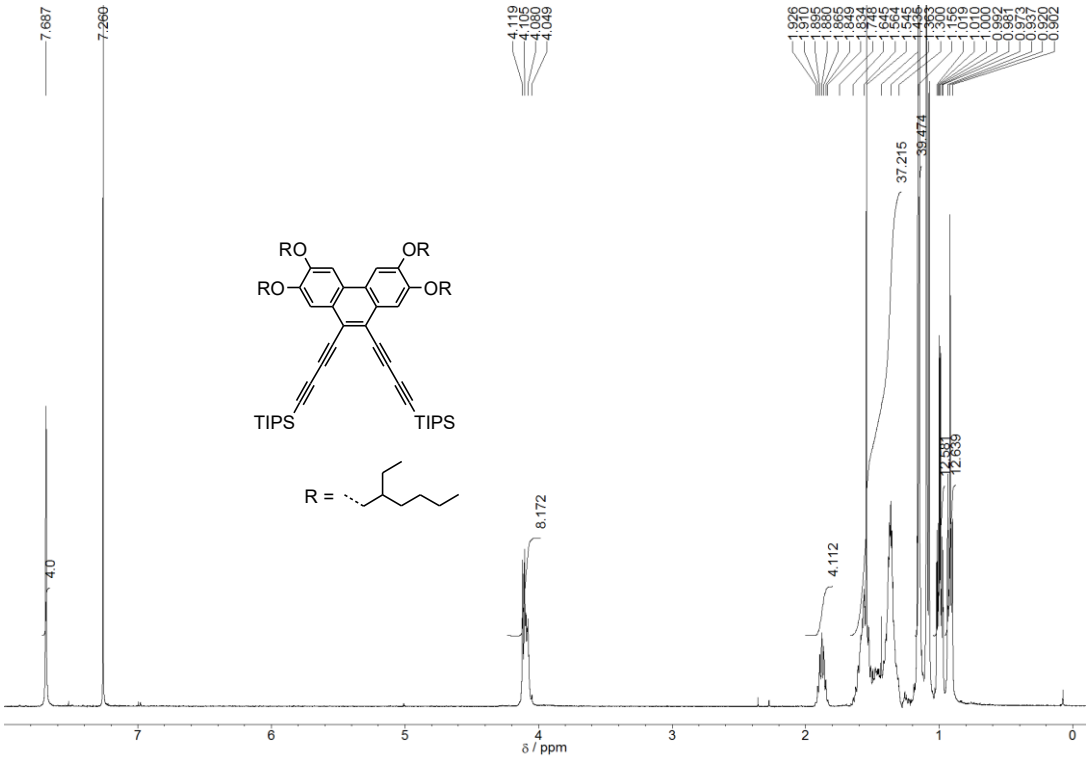

Figure 6-47. ^{1}H NMR spectrum of **30b** in $CDCl_3$ solution (400 MHz).

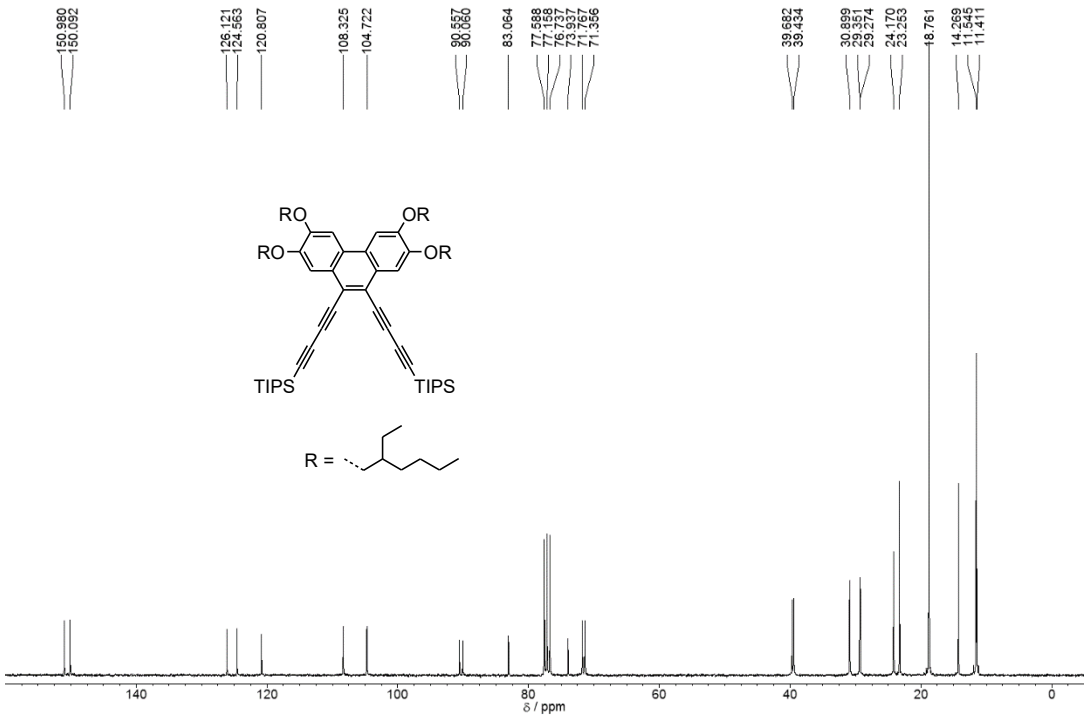

Figure 6-48. ^{13}C NMR spectrum of **30b** in $CDCl_3$ solution (75 MHz).

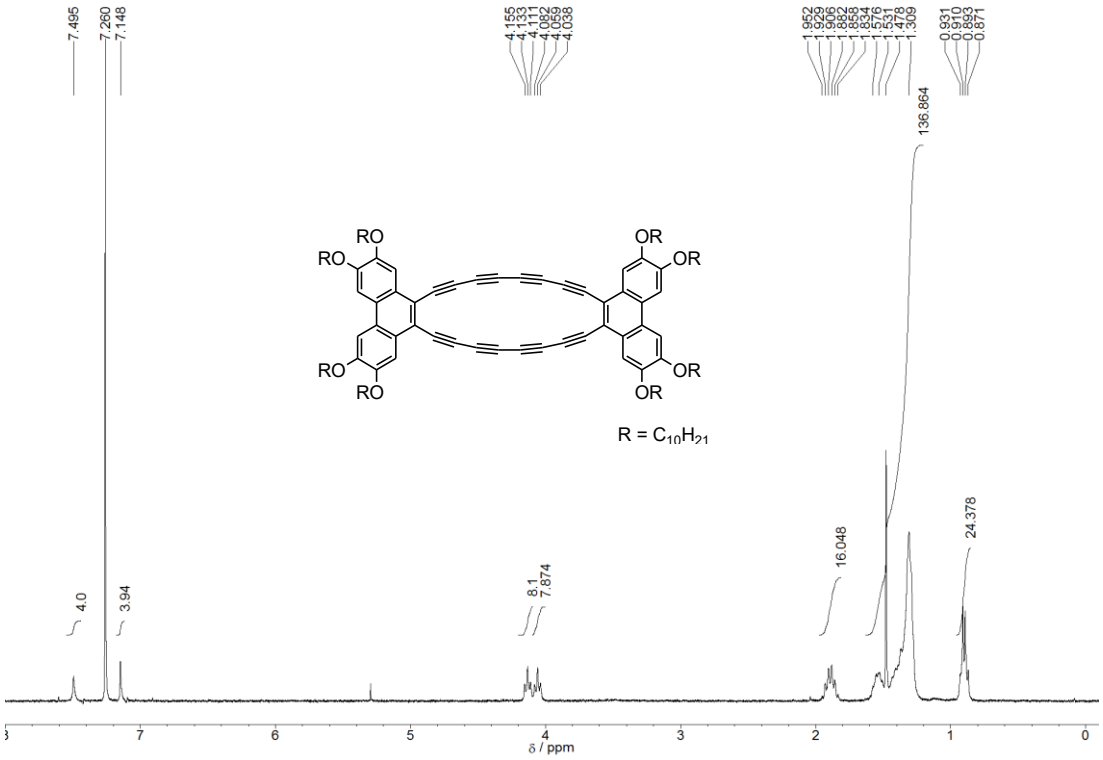

Figure 6-49. ^{1}H NMR spectrum of **9a** in $CDCl_3$ solution (600 MHz, 50 °C).

The ^{13}C NMR spectrum of **9a** could not be obtained due to the low solubility.

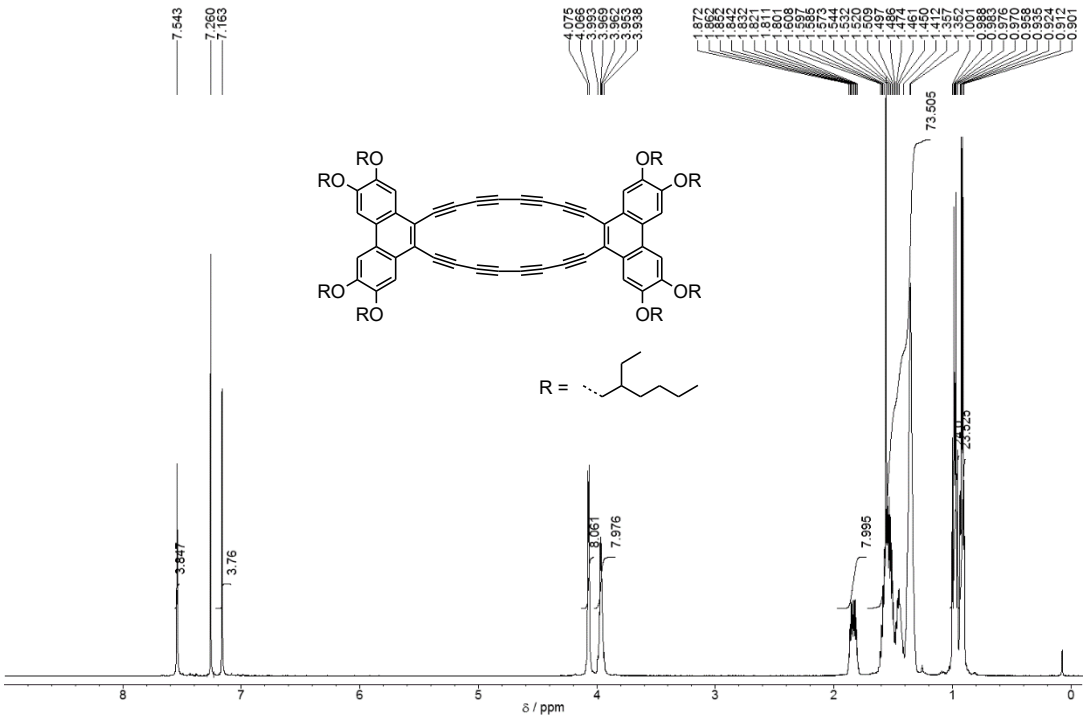

Figure 6-50. ^{1}H NMR spectrum of **9b** in $CDCl_3$ solution (2.11×10^{-2} mol dm^{-3}, 600 MHz).

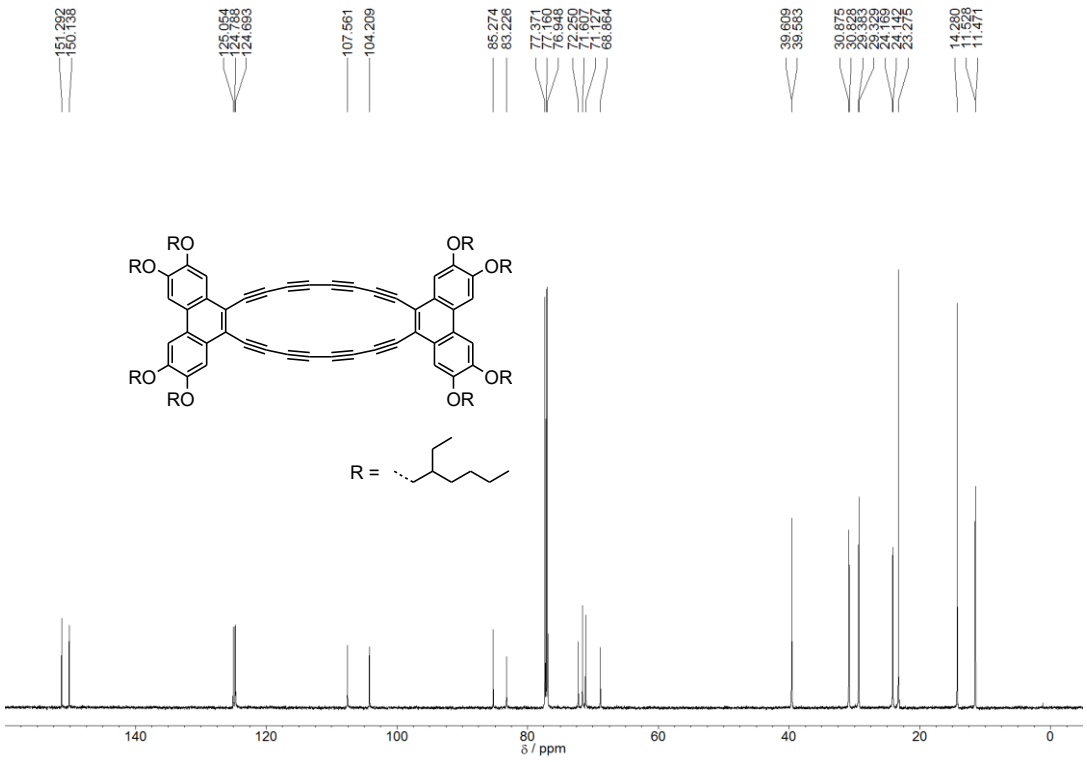

Figure 6-51. ^{13}C NMR spectrum of **9b** in $CDCl_3$ solution (150 MHz).

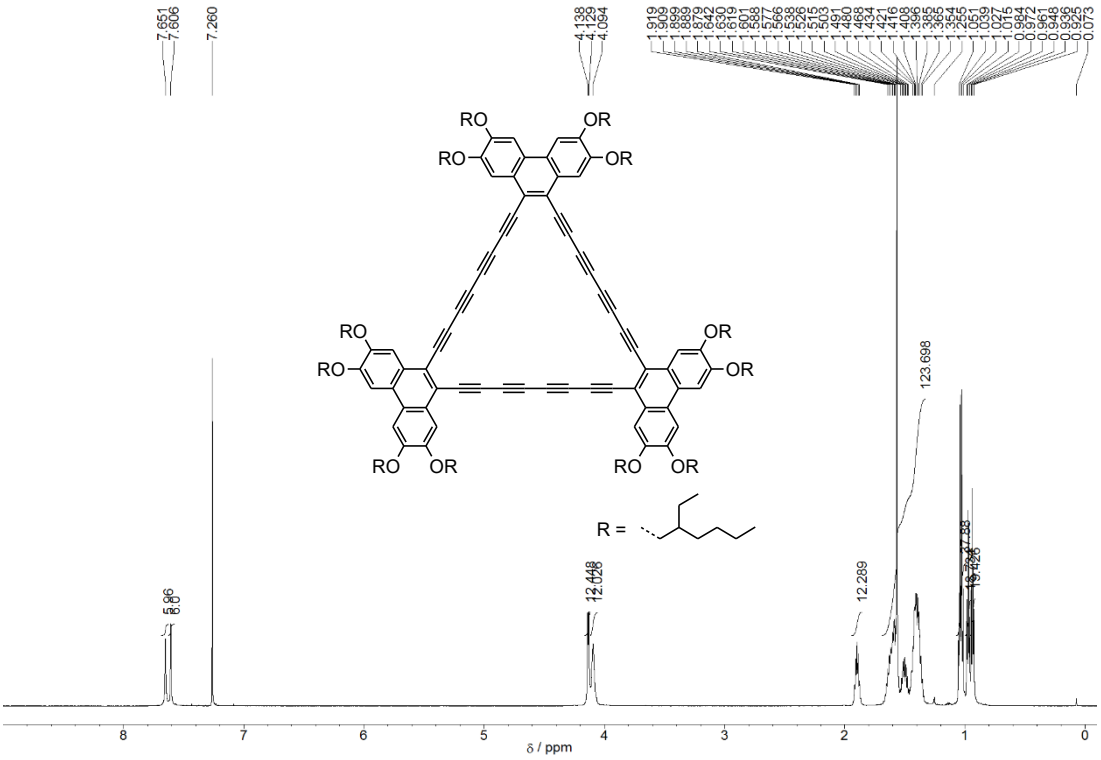

Figure 6-52. ^{1}H NMR spectrum of **10** in $CDCl_3$ solution (2.69×10^{-3} mol dm^{-3}, 600 MHz).

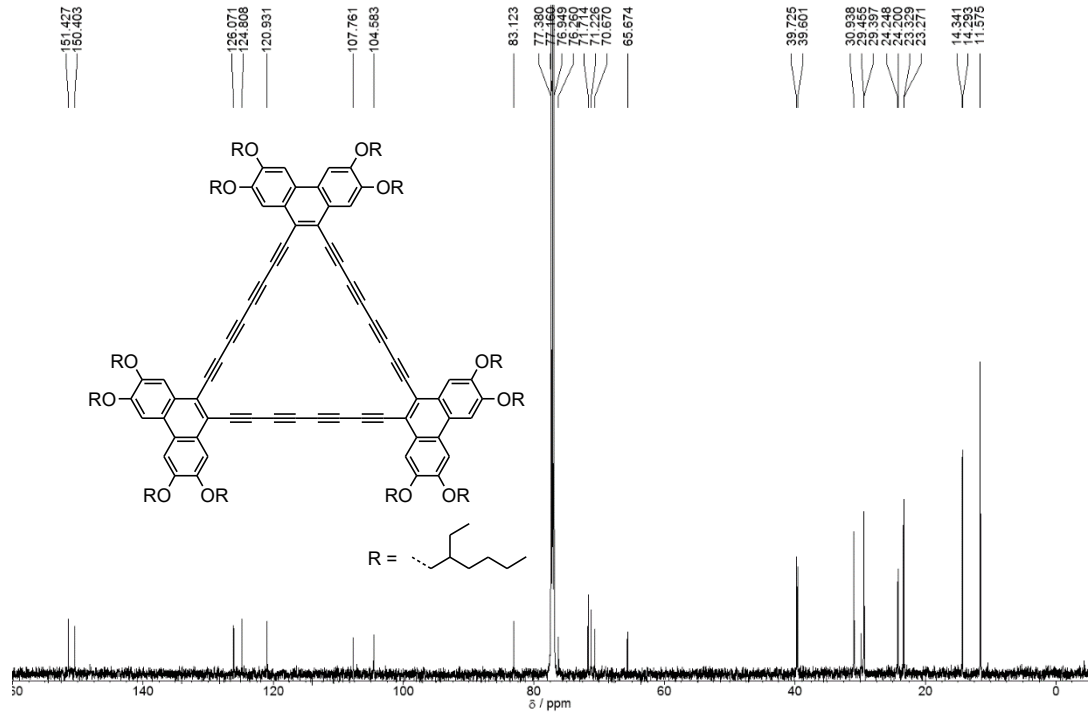

Figure 6-53. ^{13}C NMR spectrum of **10** in $CDCl_3$ solution (150 MHz).

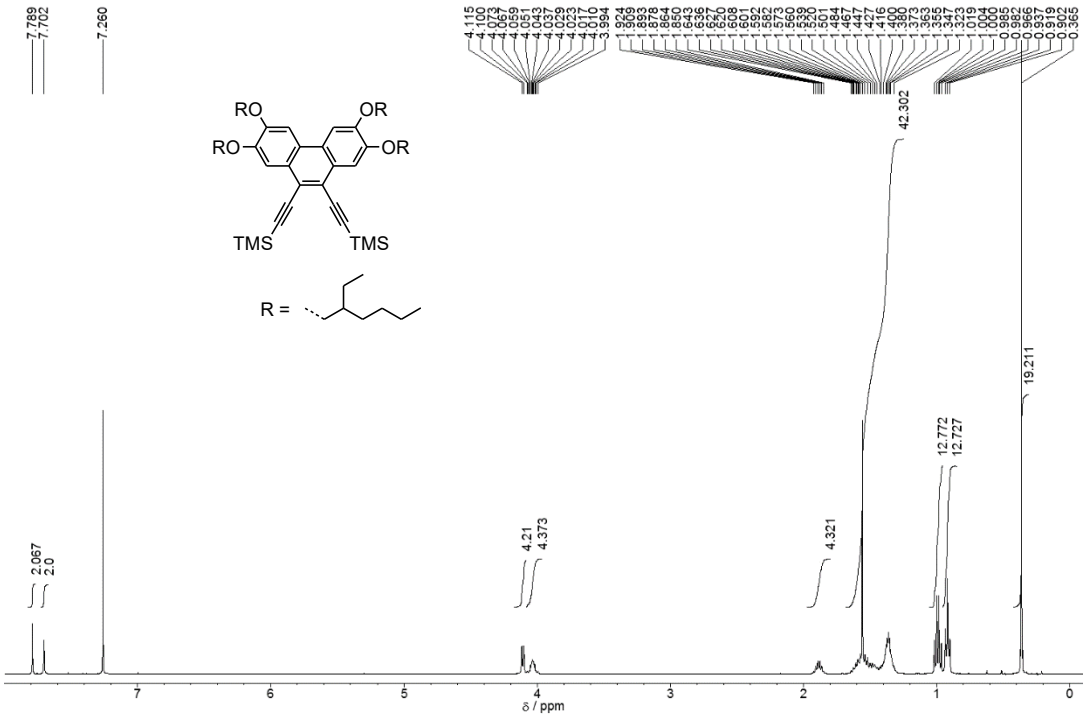

Figure 6-54. ^{1}H NMR spectrum of **17b** in $CDCl_3$ solution (300 MHz).

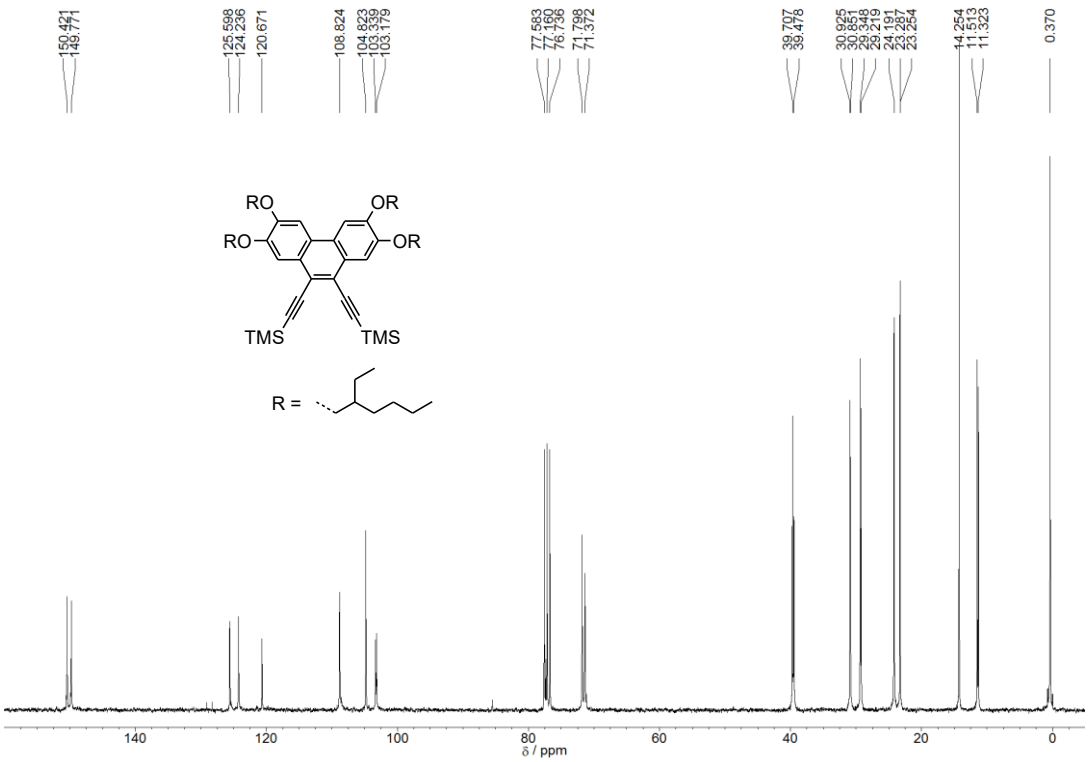

Figure 6-55. ^{13}C NMR spectrum of **17b** in $CDCl_3$ solution (75 MHz).

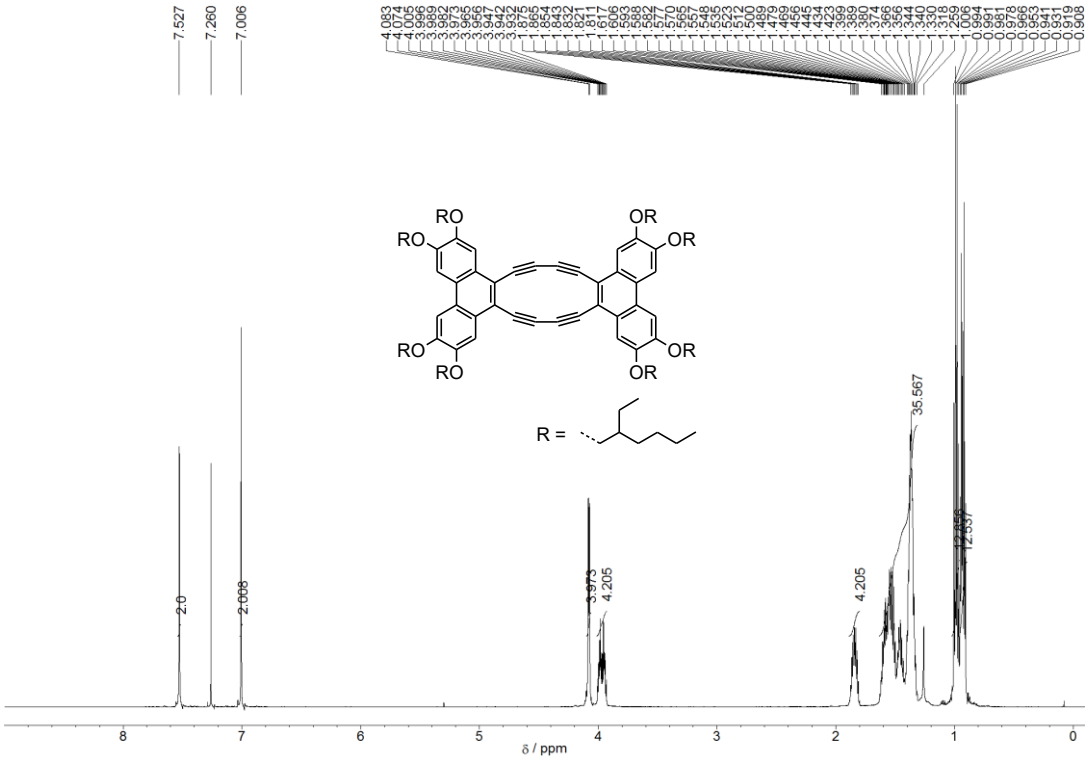

Figure 6-56. ^{1}H NMR spectrum of **3c** in $CDCl_3$ solution (600 MHz).

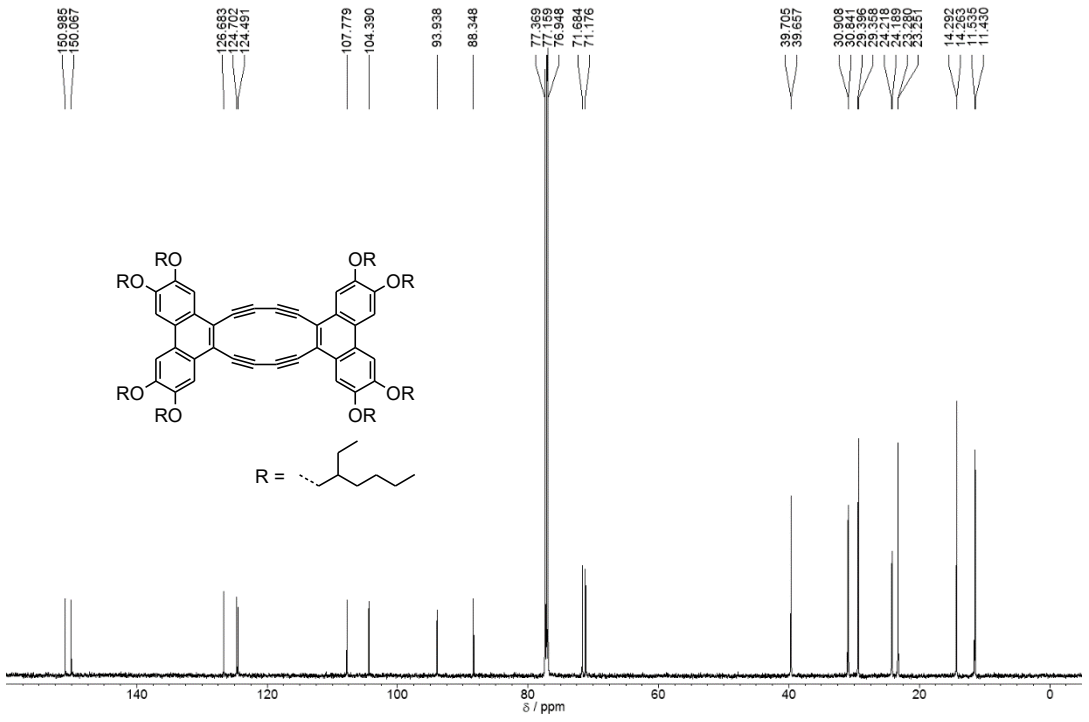

Figure 6-57. ^{13}C NMR spectrum of **3c** in $CDCl_3$ solution (150 MHz).

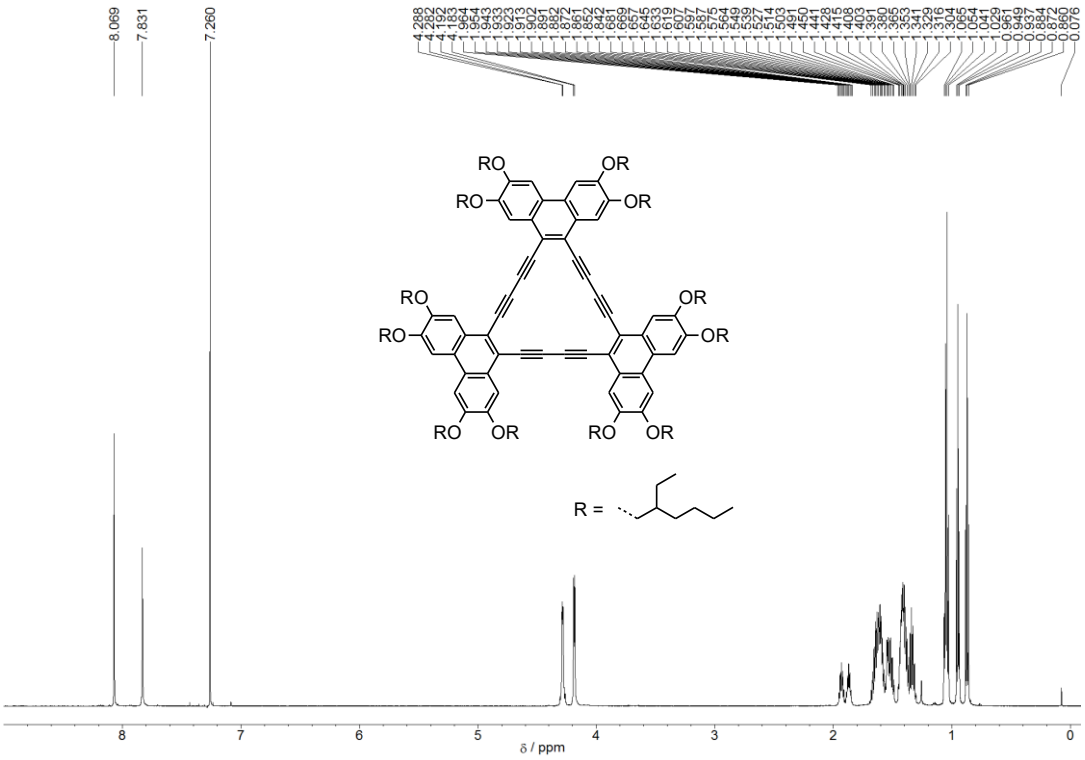

Figure 6-58. ^{1}H NMR spectrum of **4c** in $CDCl_3$ solution (600 MHz).

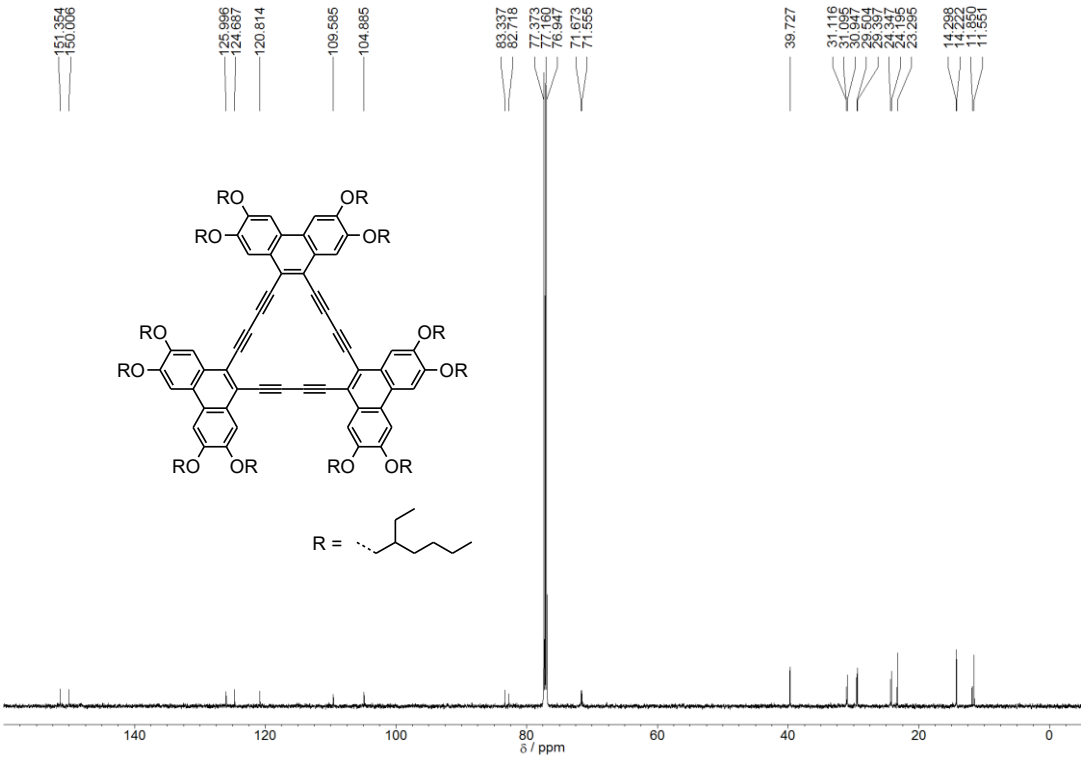

Figure 6-59. ^{13}C NMR spectrum of **4c** in $CDCl_3$ solution (150 MHz).

Chapter 7. References

[1] F. Sondheimer, R. Wolovsky, *Tetrahedron Lett*. **1959**, *1*, 3–6.

[2] F. Sondheimer, R. Wolovsky, *J. Am. Chem. Soc*. **1962**, *84*, 260–269.

[3] W. H. Okamura, F. Sondheimer, *J. Am. Chem. Soc*. **1967**, *89*, 5991–5992.

[4] A. H. Stollenwerk, B. Kanellakopulos, H. Vogler, A. Jurić, N. Trinajstić, *J. Mol. Struct*. **1983**, *102*, 377–389.

[5] M. M. Haley, S. C. Brand, J. J. Pak, *Angew. Chem. Int. Ed*. **1997**, *36*, 836–838.

[6] *Aromaticity* (Ed.: P. J. Garratt), John Wiley and Sons, New York, **1986**.

[7] *Aromaticity and Antiaromaticity* (Eds.: V. I. Minkin, M. N. Glukhovtsev, B. Y. Simkin), John Wiley and Sons, New York, **1994**.

[8] A. D. Allen, T. T. Tidwell, *Chem. Rev*. **2001**, *101*, 1333–1348.

[9] J. A. N. F. Gomes, R. B. Mallion, *Chem. Rev*. **2001**, *101*, 1349–1384.

[10] *Aromaticity and Other Conjugation Effects* (Eds.: R. Gleiter, G. Haberhauer), Wiley-VCH, Weinheim, Germany, **2012**.

[11] *The Chemistry of Annulenes: From the Standpoint of Organic Chemistry* (Ed. M. Nakagawa), Osaka University Press: Suita, Japan, **1996**.

[12] R. T. Weavers, F. Sondheimer, *Angew. Chem. Int. Ed. Engl*. **1974**, *13*,141–142.

[13] H. A. Staab, F. Graf, *Tetrahedron Lett*. **1966**, *7*, 751–757.

[14] H. A. Staab, F. Graf, *Chem. Ber*. **1970**, *103*, 1107–1118.

[15] A. Yasuhara, T. Satake, M. Iyoda, M. Nakagawa, *Tetrahedron Lett*. **1975**, *16*, 895–898.

[16] F. Sondheimer, *Acc. Chem. Res*. **1972**, *5*, 81–91.

[17] F. Sondheimer, *Pure. Appl. Chem*. **1971**, *28*, 331–353.

[18] M. Nakagawa, *Pure. Appl. Chem*. **1975**, *44*, 885–924.

[19] *Annulenes, benzo-, Hetero-, Homo-Derivatives and their valances Isomers* (Eds.: A. T. Balaban, M. Banciu, V. Ciorba), CRC press, Boca Raton, **1987**, Vols. *1–3*.

[20] D. A. Plattner, K. N. Houk, *J. Am. Chem. Soc.* **1995**, *117*, 4405–4406.

[21] M. E. Gallagher, J. E. Anthony, *Tetrahedron Lett.* **2001**, *42*, 7533–7536.

[22] R. H. Mitchell, *Chem. Rev.* **2001**, *101*, 1301–1316.

[23] H. W. Kroto, J. R. Heath, S. C. O'Brien, R. F. Curl, R. E. Smalley, *Nature* **1985**, *318*, 162–163.

[24] W. Krätshmer, L. D. Lamb, K. Fostiropoulos, D. R. Huffman, *Nature* **1990**, *347*, 354–358.

[25] R. C. Haddon, *Acc. Chem. Res.* **2002**, *35*, 997.

[26] D. Tasis, N. Tagmatarchis, A. Bianco, M. Prato, *Chem. Rev.* **2006**, *106*, 1105–1136.

[27] Y.-L. Zhao, J. F. Stoddart. *Acc. Chem. Res.* **2009**, *42*, 1161–1171.

[28] J. C. Meyer, A. K. Geim, M. I. Katsnelson, K. S. Novoselov, T. J. Booth, S. Roth, *Nature* **2007**, *446*, 60–63.

[29] R. Hoffmann, *Tetrahedron* **1966**, *22*, 521–538.

[30] U. H. F. Bunz, Y. Rubin, Y. Tobe, *Chem. Soc. Rev.* **1999**, *28*, 107–119.

[31] R. H. Baughman, H. Eckhardt, M. Kertesz, *J. Chem. Phys.* **1987**, *87*, 6687–6699.

[32] N. Narita, S. Nagai, S. Suzuki, K. Nakao, *Phys. Rev. B* **1998**, *58*, 11009–11014.

[33] J. M. Kehoe, J. H. Kiley, J. J. English, C. A. Johnson, R. C. Petersen, M. M. Haley, *Org. Lett.* **2000**, *2*, 969–972.

[34] M. Sonoda, Y. Sakai, T. Yoshimura, Y. Tobe, K. Kamada, *Chem. Lett.* **2004**, *33*, 972–973.

[35] T. Yoshimura, A. Inaba, M. Sonoda, K. Tahara, Y. Tobe, R. V. Williams, *Org. Lett.* **2006**, *8*, 2933–2936.

[36] Y. Zhou, S. Feng, *Solid State Commun.* **2002**, *122*, 307–310.

[37] K. Tahara, Y. Yamamoto, D. E. Gross, H. Kozuma, Y. Arikuma, K. Ohta, Y. Koizumi, Y. Gao, Y. Shimizu, S. Seki, K. Kamada, J. S. Moore, Y. Tobe, *Chem. Eur. J.* **2013**, *19*, 11251–11260.

[38] W. B. Wan, S. C. Brand, J. J. Pak, M. M. Haley, *Chem. Eur. J.* **2000**, *6*, 2044–2052.

[39] W. B. Wan, M. M. Haley, *J. Org. Chem.* **2001**, *66*, 3893–3901.

[40] J. A. Marsden, M. M. Haley, *J. Org. Chem.* **2005**, *70*, 10213–10226.

[41] F. Diederich, M. Kivala, *Adv. Mater.* **2010**, *22*, 803–812.

[42] M. M. Haley, *Pure. Appl. Chem.* **2008**, *80*, 519–532.

[43] Y. Tobe, T. Fuji, H. Matsumoto, K. Naemura, *Pure. Appl. Chem.* **1996**, *68*, 239–242.

[44] K. P. Baldwin, A. J. Matzger, D. A. Scheiman, C. A. Tessier, K. P. C. Vollhardt, W. J. Youngs, *Synlett* **1995**, 1215–1218.

[45] R. Boese, A. J. Matzger, K. P. C. Vollhardt, *J. Am. Chem. Soc.* **1997**, *119*, 2052–2053.

[46] M. Chakraborty, C. A. Tessier, W. J. Youngs, *J. Org. Chem.* **1999**, *64*, 2947–2949.

[47] G. Babu, A. Orita, J. Otera, *Chem. Lett.* **2008**, *37*, 1296–1297.

[48] F. Xu, L. Peng, A. Orita, J. Otera, *Org. Lett.* **2012**, *14*, 3970–3973.

[49] Q. Zhou, P. J. Carroll, T. M. Swager, *J. Org. Chem.* **1994**, *59*, 1294–1301.

[50] D. T. Chase, B. D. Rose, S. P. McClintock, L. N. Zakharov, M. M. Haley, *Angew. Chem. Int. Ed.* **2011**, *50*, 1127–1130.

[51] T. Takeda, K. Inukai, K. Tahara, Y. Tobe, *J. Org. Chem.* **2011**, *76*, 9116–9121.

[52] D. Malaba, A. Djebli, L. Chen. E. A. Zarate, C. A. Tessier, W. J. Youngs, *Organometallics* **1993**, *12*, 1266–1276.

[53] S. Nobusue, A. Shimizu, K. Hori, I. Hisaki, M. Miyata, Y. Tobe, *Angew. Chem. Int. Ed.* **2013**, *52*, 4184–4188.

[54] S. Nobusue, Y. Tobe, *Chem. Lett.* **2014**, *43*, 1210–1212.

[55] A. Fukazawa, H. Oshima, Y. Shiota, S. Takahashi, K. Yoshizawa, S. Yamaguchi, *J. Am. Chem. Soc.* **2013**, *135*, 1731–1734.

[56] A. Fukazawa, H. Oshima, S. Shimizu, N. Kobayashi, S. Yamaguchi, *J. Am. Chem. Soc.* **2014**, *136*, 8738–8745.

[57] E. L. Spitler, C. A. Johnson II, M. M. Haley, *Chem. Rev.* **2006**, *106*, 5344–5386.

[58] T. M. Figueira-Duarte, K. Müllen, *Chem. Rev.* **2011**, *111*, 7260–7314.

[59] F. Mitzel, C. Boudon, J.-P. Gisselbrecht, P. Seiler, M. Gross, F. Diederich, *Helv. Chim. Acta* **2004**, *87*, 1130–1157.

[60] J. J. Pak, T. J. R. Weakley, M. M. Haley, *J. Am. Chem. Soc.* **1999**, *121*, 8182–8192.

[61] A. Sarkar, J. J. Pak, G. W. Rayfield, M. M. Haley, *J. Mater. Chem.* **2001**, *11*, 2943–2945.

[62] J. A. Marsden, J. J. Miller, L. D. Shirtcliff, M. M. Haley, *J. Am. Chem. Soc.* **2005**, *127*, 2464–2476.

[63] E. L. Spitler, M. M. Haley, *Org. Biomol. Chem.* **2008**, *6*, 1569–1576.

[64] H. N. C. Wong, P. J. Garratt, F. Sondheimer, *J. Am. Chem. Soc.* **1974**, *96*, 5604–5605.

[65] O. M. Behr, G. Eglinton, A. R. Galbraith, R. A. Raphael, *J. Chem. Soc.* **1960**, 5604–5605.

[66] I. D. Campbell, G. Eglinton, W. Henderson, R. A. Raphael, *Chem. Commun.* **1966**, 87–89.

[67] D. Solooki, J. D. Bradshaw, C. A. Tessier, W. J. Young, R. F. See, M. Churchill, J. D. Ferrara, *J. Organomet. Chem.* **1994**, *470*, 231–236.

[68] K. P. Baldwin, J. D. Bradshaw, C. A. Tessier, W. J. Young, *Synlett* **1993**, 853–855.

[69] K. P. Baldwin, R. S. Simon, J. Rose, P. Zimmerman, D. M. Hercules, C. A. Tessier, W. J. Young, *J. Chem. Soc. Chem. Commun.* **1994**, 1257–1258.

[70] M. M. Haley, M. L. Bell, J. J. English, C. A. Johnson, T. J. R. Weakley, *J. Am. Chem. Soc.* **1997**, *119*, 2956–2957.

[71] A. J. Boydston, M. M. Haley, *Org. Lett.* **2001**, *3*, 3599–3601.

[72] M. L. Bell, R. C. Chiechi, C. A. Johnson, D. B. Kimball, A. J. Matzger, W. B. Wan, T. J. R. Weakley, M. M. Haley, *Tetrahedron* **2001**, *57*, 3507–3520.

[73] *Supramolecular Chemistry: Concepts and Perspectives* (Ed.: J.-M. Lehn), VCH, New York, **1995**.

[74] F. J. M. Hoeben, P. Jonkheijim, E. W. Meijer, A. P. H. J. Schenning, *Chem*. *Rev*. **2005**, *105*, 1491–1546.

[75] J. Wu, W. Pisula, K. Müllen, *Chem*. *Rev*. **2007**, *107*, 718–747.

[76] K. Tahara. T. Fujita, M. Sonoda, M. Shiro, Y. Tobe, *J*. *Am*. *Chem*. *Soc*. **2008**, *130*, 14339–14345.

[77] I. Hisaki, Y. Sakamoto, H. Shigemitsu, N. Tohnai, M. Miyata, S. Seki, A. Saeki, S. Tagawa, *Chem*. *Eur*. *J*. **2008**, *14*, 4178–4187.

[78] I. Hisaki, H. Senga, Y. Sakamoto, S. Tsuzuki, N. Tohnai, M. Miyata, *Chem*. *Eur*. *J*. **2009**, *15*, 13336–13340.

[79] I. Hisaki, H. Senga, H. Shigemitsu, N. Tohnai, M. Miyata, *Chem*. *Eur*. *J*. **2011**, *17*, 14348–14353.

[80] I. Hisaki, S. Nakagawa, N. Tohnai, M. Miyata, *Angew*. *Chem*. *Int*. *Ed*. **2015**, *54*, 3008–3012.

[81] S. H. Seo, T. V. Jones, H. Seyler, J. O. Peters, T. H. Kim, J. Y. Chang, G. N. Tew, *J*. *Am*. *Chem*. *Soc*. **2006**, *128*, 9264–9265.

[82] J. Jiang, G. N. Tew, *Org*. *Lett*. **2008**, *10*, 4393–4396.

[83] S. H. Seo, J. Y. Chang, G. N. Tew, *Angew*. *Chem*. *Int*. *Ed*. **2006**, *45*, 7526–7530.

[84] I. Hisaki, H. Shigemitsu, Y. Sakamoto, Y. Hasegawa, Y. Okajima, K. Nakano, N. Tohnai, M. Miyata, *Angew*. *Chem*. *Int*. *Ed*. **2009**, *48*, 5465–5469.

[85] H. Shigemitsu, I. Hisaki, H. Senga, D. Yasumiya, T. S. Thakur, A. Saeki, S. Seki, N. Tohnai, M. Miyata, *Chem*. *Asian J*. **2013**, *8*, 1372–1376.

[86] H. Shigemitsu, I. Hisaki, E. Kometani, D. Yasumiya, Y. Sakamoto, K. Osaka, T. S. Thakur, A. Saeki, S. Seki, F. Kimura, T. Kimura, N. Tohnai, M. Miyata, *Chem*. *Eur*. *J*. **2013**, *19*, 15366–15377.

[87] K. Tahara, S. Lei, J. Adisoejoso, S. De Feyter, Y. Tobe, *Chem*. *Commun*. **2010**, *46*, 8507–8525.

[88] S. Furukawa, K. Tahara, F. C. De Shryver, N. V. d. Auweraer, Y. Tobe, S. De Feyter, *Angew*. *Chem*. *Int*. *Ed*. **2007**, *46*, 2831–2834.

[89] M. Morimoto, S. Akiyama, S. Misumi, M. Nakagawa, *Bull*. *Chem*. *Soc*. *Jpn*. **1962**, *35*, 857–859.

[90] T. Nishinaga, H. Nakayama, N. Nodera, K. Komatsu, *Tetrahedron Lett*. **1998**, *39*, 7139–7142.

[91] S. Ott, R. Faust, *Synlett* **2004**, 1509–1512.

[92] S. Ott, R. Faust, *Chem*. *Commun*. **2004**, 388–389.

[93] E. V. García-Frutos, F. Fernández-Lázaro, E. M. Maya, P. Vázquez, T. Torres, *J*. *Org*. *Chem*. **2000**, *65*, 6841–6846.

[94] M. J. Cook, M. J. Heeney, *Chem*. *Commun*. **2000**, 969–970.

[95] M. J. Cook, M. J. Heeney, *Chem*. *Eur*. *J*. **2000**, *6*, 3958–3967.

[96] R. S. Iglesias, C. G. Claessens, M. Á. Herranz, T. Torres, *Org*. *Lett*. **2007**, *9*, 5381–5384.

[97] H. Enozawa, M. Hasegawa, D. Takamatsu, K. Fukui, M. Iyoda, *Org*. *Lett*. **2006**, *8*, 1917–1920.

[98] A. D. Andersson, K. Kilså, T. Hassenkam, J.-P. Gisselbrecht, C. Boudon, M. Gross, M. B. Nielsen, F. Diederich, *Chem*. *Eur*. *J*. **2006**, *12*, 8451–8459.

[99] N. Saito, R. Terakawa, M. Yamaguchi, *Chem*. *Eur*. *J*. **2014**, *20*, 5601–5607.

[100] Gaussian 09, revision B.01, M. J. Frisch, G. W. Trucks, H. B. Schlegel, G. E. Scuseria, M. A. Robb, J. R. Cheeseman, G. Scalmani, V. Barone, B. Mennucci, G. A. Petersson, H. Nakatsuji, M. Caricato, X. Li, H. P. Hratchian, A. F. Izmaylov, J. Bloino, G. Zheng, J. L. Sonnenberg, M. Hada, M. Ehara, K. Toyota, R. Fukuda, J. Hasegawa, M. Ishida, T. Nakajima, Y. Honda, O. Kitao, H. Nakai, T. Vreven, J. A. Montgomery, Jr, J. E. Peralta, F. Ogliaro, M. Bearpark, J. J. Heyd, E. Brothers, K. N. Kudin, V. N. Staroverov, T. Keith, R. Kobayashi, J. Normand, K. Raghavachari, A. Rendell, J. C. Burant, S. S.

Iyengar, J. Tomasi, M. Cossi, N. Rega, J. M. Millam, M. Klene, J. E. Knox, J. B. Cross, V. Bakken, C. Adamo, J. Jaramillo, R. Gomperts, R. E. Stratmann, O. Yazyev, A. J. Austin, R. Cammi, C. Pomelli, J. W. Ochterski, R. L. Martin, K. Morokuma, V. G. Zakrzewski, G. A. Voth, P. Salvador, J. J. Dannenberg, S. Dapprich, A. D. Daniels, O. Farkas, J. B. Foresman, J. V. Ortiz, J. Cioslowski, D. J. Fox, Gaussian, Inc.: Wallingford, CT, **2010**.

[101] T. C. Walsgrove, F. Sondheimer, *Tetrahedron Lett*. **1978**, 19, 2719–2722.

[102] A. J. Boydston, M. M. Haley, R. V. Williams, J. R. Armantrout, *J. Org. Chem*. **2002**, *67*, 8812–8819.

[103] B. Mohr, V. Enkelmann, G. Wagner, *J. Org. Chem*. **1994**, *59*, 635–638.

[104] A. S. Hay, *J. Org. Chem*. **1962**, *27*, 3320–3321.

[105] P. Siemsen, R. C. Livingston, F. Diederich, *Angew. Chem. Int. Ed*. **2000**, *39*, 2632–2657.

[106] V. E. Williams, T. M. Swager, *J. Polym. Sci. Part A* **2000**, *38*, 4669–4676.

[107] It was reported that [12]DBAs were not detected by TLC and ^{1}H NMR spectroscopic analysis of the crude mixture after Pd-catalyzed macrocyclization of diethynyl benzene derivatives; K. Tahara, C. A. Johnson II, T. Fujita, M. Sonoda, F. C. De Schryver, S. De Feyter, M. M. Haley, Y. Tobe, *Langmuir* **2007**, *23*, 10190–10197.

[108] K. Tahara, K. Inukai, N. Hara, C. A. Johnson II, M. M. Haley, Y. Tobe, *Chem. Eur. J*. **2010**, *16*, 8319–8328.

[109] T. Nishinaga. T. Kawamura, K. Komatsu, *J. Org. Chem*. **1997**, *62*, 5354–5362.

[110] The observed upfield shifts of the aromatic protons in **1a**,**b** may have a substantial contribution from an enhanced anisotropic effect of the butadiyne segments distorted upon the ring formation; see: I. Hisaki, T. Eda, M. Sonoda, H. Niino, T. Sato, T. Wakabayashi, Y. Tobe, *J. Org. Chem*. **2005**, *70*, 1853–1864.

[111] Z. Chen, C. S. Wannere, C. Corminboeuf, P. Puchta, P. v. R. Schleyer, *Chem. Rev*.

2005, *105*, 3842–3888.

[112] P. v. R. Schleyer, C. Maerker, A. Dransfeld, H. Jiao, N. v. E. Hommes, *J. Am. Chem. Soc*. **1996**, *118*, 6317–6318.

[113] Anderson and co-workers have recently pointed out that the bending of butadiynylene bridges in a porphyrin nanoring is responsible for the small HOMO–LUMO gap; see: J. K. Sprafke, D. V. Kondratuk, M. Wykes, A. L. Thompson, M. Hoffmann, R. Drevinskas, W.-H. Chen, C. K. Yong, J. Kärnbratt, J. E. Bullock, M. Malfois, M. R. Wasielewski, B. Albinsson, L. M. Herz, D. Zigmantas, D. Beljonne, H. L. Anderson, *J. Am. Chem. Soc*. **2011**, *133*, 17262–17273.

[114] J. Wirz in *Excited States in Organic Chemistry and Biology* (Eds.: B. Pullman, N. Goldblum), D. Reidal Publishing Company, Dordrecht, **1977**, p283.

[115] The UV–vis spectroscopic analysis and TD-DFT studies of a TMS substituted [12]DA derivative have been reported; see: W. Setaka, S. Kanai, C. Kabuto, M. Kira, *Chem. Lett*. **2006**, *35*, 1364–1365.

[116] K. Suzuki, A. Kobayashi, S. Kaneko, K. Takehira, T. Yoshihara, H. Ishida, Y. Shiina, S. Oishi, S. Tobita, *Phys. Chem. Chem. Phys*. **2009**, *11*, 9850–9860.

[117] B. N. Boden, K. J. Jardine, A. C. W. Leung, M. J. MacLachlan, *Org. Lett*. **2006**, *8*, 1855–1858.

[118] B. He, H. Tian, Y. Geng, F. Wang, K. Müllen, *Org. Lett*. **2008**, *10*, 773–776.

[119] T. Sakida, S. Yamaguchi, H. Shinokubo, *Angew. Chem. Int. Ed*. **2011**, *50*, 2280–2283.

[120] T. Kawase, A. Konishi, Y. Hirao, K. Matsumoto, H. Kurata, T. Kubo, *Chem. Eur. J*. **2009**, *15*, 2653–2661.

[121] R. Dobrawa, M. Lysetska, P. Ballester, M. Grüne, F. Würthner, *Macromolecules* **2005**, *38*, 1315–1325.

[122] R. B. Martin, *Chem. Rev*. **1996**, *96*, 3043–3064.

[123] S. Lahiri, J. L. Thompson, J. S. Moore, *J. Am. Chem. Soc*. **2000**, *122*, 11315–11319.

[124] K. Nakamura, H. Okubo, M. Yamaguchi, *Org*. *Lett*. **2001**, *3*, 1097–1099.

[125] Y. Tobe, N. Utsumi, K. Kawabata, A. Nagano, K. Adachi, S. Araki, M. Sonoda, K. Hirose, K. Naemura, *J*. *Am*. *Chem*. *Soc*. **2002**, *124*, 5350–5364.

[126] J. A. Marsden, J. J. Miller, L. D. Shirtcliff, M. M. Haley, *J*. *Am*. *Chem*. *Soc*. **2005**, *127*, 2264–2476.

[127] E. L. Spitler, J. M. Monson, M. M. Haley, *J*. *Org*. *Chem*. **2008**, *73*, 2211–2223.

[128] P. Terech, R. G. Weiss, *Chem*. *Rev*. **1997**, *97*, 3133–3160.

[129] A. Ajayaghosh, V. K. Praveen, *Acc*. *Chem*. *Res*. **2007**, *40*, 644–656.

[130] K. K. McGrath, K. Jang, K. A. Robins, D.-C. Lee, *Chem*. *Eur*. *J*. **2009**, *15*, 4070–4077.

[131] L. Schmidt-Mende, A. Fechtenkötter, K. Müllen, E. Moons, R. H. Friend, J. D. Mackenzie, *Science* **2001**, *293*, 1119–1122.

[132] S. Xiao, J. Tang, T. Beetz, X. Guo, N. Tremblay, T. Siegrist, Y. Zhu, M. Steigerwald, C. Nuckolls, *J*. *Am*. *Chem*. *Soc*. **2006**, *128*, 10700–10701.

[133] K. Ohta, H. Hasebe, M. Moriya, T. Fujimoto, I. Yamamoto, *Mol. Cryst. Liq. Cryst.* **1991**, *208*, 33–41.

[134] G. Eglinton, A. R. Galbraith, *Proc*. *Chem*. *Soc*. **1957**, 350–351.

[135] A. J. Matzger, K. P. C. Vollhardt, *Tetrahedron Lett*. **1998**, *39*, 6791–6794.

[136] U. H. F. Bunz, V. Enlelmann, *Chem*. *Eur*. *J*. **1999**, *5*, 263–266.

[137] W. B. Wan, D. B. Kimball, M. M. Haley, *Tetrahedron Lett*. **1998**, *39*, 6795–6798.

[138] W. B. Wan, R. C. Chiechi, T. J. R. Weakley, M. M. Haley, *Eur*. *J*. *Org*. *Chem*. **2001**, 3485–3490.

[139] Y. Tobe, I. Ohki, M. Sonoda, H. Niino, T. Sato, T. Wakabayashi, *J*. *Am*. *Chem*. *Soc*. **2003**, *125*, 5614–5615.

[140] G. Wegner, *Macromol*. *Chem*. **1972**, 154, 35–48.

[141] G. Wegner, *Angew*. *Chem*., *Int*. *Ed*. *Engl*. **1981**, *20*, 361–381.

[142] T. Gibtner, F. Hampel, J.-P. Gisselbrecht, A. Hirsch, *Chem*. *Eur*. *J*. **2002**, *8*, 408–432.

[143] Q. Zheng, J. A. Gladysz, *J. Am. Chem. Soc.* **2005**, *127*, 10508–10509.

[144] W. A. Chalifoux, R. R. Tykwinski, *Nat. Chem.* **2010**, *2*, 967–971.

[145] A. Spantulescu, T. Luu, Y. Zhao, R. McDonald, R. R. Tykwinski, *Org. Lett.* **2008**, *10*, 609–612.

[146] J.-P. Gisselbrecht, N. N. P. Moonen, C. Boudon, M. B. Nielsen, F. Diederich, M. Gross, *Eur. J. Org. Chem.* **2004**, 2959–2972.

[147] C. A. Hunter, K. R. Lawson, J. Perkins, C. J. Urch, *J. Chem. Soc.*, *Perkin Trans. 2* **2001**, 651–669.

[148] L. M. Salonen, M. Ellermann, F. Diederich, *Angew. Chem. Int. Ed.* **2011**, *50*, 4808–4842.

[149] J. A. Marsden, J. J. Miller, M. M. Haley, *Angew. Chem. Int. Ed.* **2004**, *43*, 1694–1697.

[150] S. Tokuji, H. Yorimitsu, A. Osuka, *Angew. Chem. Int. Ed.*, **2012**, *51*, 12357–12361.

[151] Y. Hirata, T. Okada, T. Nomoto, *Chem. Phys. Lett.* **1998**, *293*, 371–377.

[152] J. G. Rodriguesz, J. L. Tejedor, A. Rumbero, L. Canoira, *Tetrahedron* **2006**, *62*, 3075–3080.

[153] Y. Xing, X. Xu, P. Zhang, W. Tian, G. Yu. P. Lu, Y. Liu, D. Zhu, *Chem. Phys. Lett.* **2005**, *408*, 169–173.

[154] S.-i. Kato, H. Noguchi, A. Kobayashi, T. Yoshihara, S. Tobita, *J. Org. Chem.* **2012**, *77*, 9120–9133.

[155] J.-K. Fang, D.-L. An, K. Wakamatsu, T. Ishikawa, T. Iwanaga, S. Toyota, D. Matsuo, A. Orita, J. Otera, *Tetrahedron Lett.* **2010**, *51*, 917–920.

[156] L.-O. Pålsson, C. Wang, A. S. Batsanov, S. M. King, A. Beeby, A. P. Monkman, M. R. Bryee, *Chem. Eur. J.* **2010**, *16*, 1470–1479.

[157] Y. Kang, S. Wang, *Tetrahedron Lett.* **2002**, *43*, 3711–3713.

[158] C. Wang, L.-O. Pálsson, A. S. Batsanov, M. R. Bryce, *J. Am. Chem. Soc.* **2006**, *128*, 3789–3799.

[159] M. Biswas, P. Nguyen, T. B. Marder, L. R. Khundkar, *J. Phys. Chem. A* **1997**, *101*, 1689–1695.

[160] A. K. Pati, M. Mohapatra, P. Ghosh, S. J. Garpure, A. K. Mishra, *J. Phys. Chem. A* **2013**, *117*, 6548–6560.

[161] R. M. Adhikari, L. Duan, L. Hou, Y. Qiu, D. C. Neckers, B. K. Shah, *Chem. Mater.* **2009**, *21*, 4638–4644.

[162] A. C. Benniston, A. Harriman, D. J. Lawrie, S. A. Rostron, *Eur. J. Org. Chem.* **2004**, 2272–2276.

[163] J.-K. Fang, D.-L. An, K. Wakamatsu, T. Ishikawa, T. Iwanaga, S. Toyota, S-i. Akita, D. Matsuo, A. Orita, J. Otera, *Tetrahedron* **2010**, *66*, 5479–5485.

[164] D. Ayuk. M. Egbe, E. Birckner, E. Klemm, *J. Polym. Sci. Part A Polym. Chem.* **2002**, *40*, 2670–2679.

[165] M. Kastler, W. Pisula, D. Wasserfallen, T. Pakula, K. Müllen, *J. Am. Chem. Soc.* **2005**, *127*, 4286–4296.

[166] M. Tanaka, T. Ikeda. J. Mack, N. Kobayashi, T. Haino, *J. Org. Chem.* **2011**, *76*, 5082–5091.

[167] C. Shao, M. Grüne, M. Stolte, F. Würthner, *Chem. Eur. J.* **2012**, *18*, 13665–13677.

[168] C. A. Hunter, J. K. M. Sanders, *J. Am. Chem. Soc.* **1990**, *112*, 5525–5534.

[169] X. Wang, M. Liu, *Chem. Eur. J.* **2014**, *20*, 10110–10116.

[170] K. Kim, K. E. Plass, A. J. Matzger, *Langmuir* **2003**, *19*, 7149–7152.

[171] I. D. Tevis, L. C. Palmer, D. J. Herman, I. P. Murray, D. A. Stone, S. I. Stupp, *J. Am. Chem. Soc.* **2011**, *133*, 16486–16494.

[172] H. M. A. Ehmann, R. Baumgartner, D. Reischl, E. Roblegg, A. Zimmer, R. Resel, O. Werzer, *Cryst. Growth. Des.* **2015**, *15*, 326–332.

[173] A. Shimizu, Y. Tobe, *Angew. Chem. Int. Ed.* **2011**, *50*, 6906–6910.

[174] J-i. Nishida, S. Tsukaguchi, Y. Yamashita, *Chem. Eur. J.* **2012**, *18*, 8964–8970.

[175] D. T. Chase, A. G. Fix, S. J. Kang, B. D. Rose, C. D. Weber, Y. Zhong, L. N. Zakharov, M. C. Lonergan, C. Nuckolls, M. M. Haley, *J. Am. Chem. Soc.* **2012**, *134*, 10349–10352.

[176] C. Maeda, M. Masuda, N. Yoshioka, *Org*. *Lett*. **2013**, *15*, 3566–3569.

[177] S. Gomez-Esteban, M. Pezella, A. Domingo, G. Hennrich, B. Gómez-Lor, *Chem*. *Eur*. *J*. **2013**, *19*, 16080–16086.

[178] J. A Hur, S. Y. Bae, K. H. Kim, T. W. Lee, M. J. Cho, D. H. Choi, *Org*. *Lett*. **2011**, *13*, 1948–1951.

[179] MOPAC2012, J, J, P. Stewart, Stewart Computational Chemistry, Colorado Springs, CO, USA, http://openMOPAC.net.

[180] A. Altomare, M. C. Burla, M. Camalli, G. L. Cascarano, C. Giacovazzo, A. Guagliardi, A. G. G. Moliterni, G. Polidori, R. Spagna, *J. Appl. Crystallogr.* **1999**, *32*, 115–119.

[181] G. M. Sheldrick, SHELXL-97, Program for the Refinement of Crystal Structures, University of Göttingen (Germany), **1997**.

[182] Z. Chem. A. Lohr, C. R. Saha-Möller, F. Würthner, *Chem*. *Soc*. *Rev*. **2009**, *38*, 564–584.

[183] Kaleidagraph 3.6, W. Jones, Synergy Software, Pennsylvania, USA.

[184] M. M. J. Smulders, M. M. L. Nieuwenhuizen, T. F. A. de Greef, P. v. d. Schoot, A. P. H. J. Schenning, E. W. Meijer, *Chem*. *Eur*. *J*. **2010**, *16*, 362–367.

List of Publications

1. Tetraalkoxyphenanthrene-Fused Dehydroannulenes: Synthesis, Self-Assembly, and Electronic, Optical, and Electrochemical Properties. S.-i. Kato, N. Takahashi, H. Tanaka, A. Kobayashi, T. Yoshihara, S. Tobita, T. Yamanobe, H. Uehara, Y. Nakamura, *Chem*. *Eur*. *J*. **2013**, *19*, 12138–12151.

2. Hexadecadehydrodibenzo[20]-, Tetracosadehydrotribenzo[30]-, and Dotriacontadehydrotetrabenzo[40]annulenes: Syntheses, Characterizations, Electronic Properties, and Self-Associations. S.-i. Kato, N. Takahashi, Y. Nakamura, *J. Org*. *Chem*. **2013**, *78*, 7658–7663.

Acknowledgement

The author acknowledges Professor Dr. Yosuke Nakamura and Dr. Shin-ichiro Kato for giving the occasion to do this doctoral research and their valuable suggestions and support throughout this work. The author thanks to all the past and present members of the laboratory for their kind corporation.

The author thanks to Professor Dr. Takeshi Yamanobe, Professor Dr. Hiroki Uehara, Mr. Hidekazu Tanaka, Mr. Takumi Sakamura, Ms. Satomi Kato, and Ms. Chihiro Narita for their helpful assistance of scanning electron microscopic measurements and wide angle X-ray diffraction analyses and their useful suggestions. The author thanks to Professor Dr. Seiji Tobita, Dr. Toshitada Yoshihara, and Dr. Atsushi Kobayashi for the measurement of phosphorescence spectrum and the determination of absolute fluorescence quantum yields. The author thanks to Professor Dr. Minoru Yamaji for the measurements of transient absorption spectra and his numerous suggestions.

The author would like to give his special thanks to Professor Dr. Ichiro Matsuo, Professor Dr. Hideki Amii, Professor Dr. Tetsuo Okutsu, and Professor Dr. Shigeki Takeda, for serving on his dissertation committee.

Finally, the author is deeply grateful to his parents and brothers,
Mr. Toshinori Takahashi, Ms. Kiyomi Takahashi, Mr. Hiroaki Takahashi, and
Mr. Yoshiyuki Takahashi for their constant financial support and great affection.